Department of Geomatics Engineering

Real-Time Integration of a Tactical-Grade IMU and GPS for High-Accuracy Positioning and Navigation

(URL: http://www.geomatics.ucalgary.ca/links/GradTheses.html)

by

Mark G. Petovello

April 2003

UNIVERSITY OF
CALGARY

THE UNIVERSITY OF CALGARY

Real-Time Integration of a Tactical-Grade IMU and GPS for

High-Accuracy Positioning and Navigation

by

Mark G. Petovello

A DISSERTATION

SUBMITTED TO THE FACULTY OF GRADUATE STUDIES

IN PARTIAL FULFILLMENT OF THE REQUIREMENTS FOR THE

DEGREE OF DOCTOR OF PHILOSOPHY

DEPARTMENT OF GEOMATICS ENGINEERING

CALGARY, ALBERTA

APRIL, 2003

Abstract

The integration of the Global Positioning System (GPS) and Inertial Navigation Systems (INSs) is often used to provide accurate positioning and navigation information. For applications requiring the highest accuracy, the quality of the inertial sensors required is usually assumed to be very high. This dissertation investigates the integration of GPS with a tactical-grade Inertial Measurement Unit (IMU) for centimetre-level navigation in real-time.

Different GPS/INS integration strategies are investigated to assess their relative performance in terms of position and velocity accuracy during partial and complete data outages, carrier phase ambiguity resolution after such data outages, and the overall statistical reliability of the system. In terms of statistical reliability, the traditional equations used in dynamic systems are redeveloped in light of some practical considerations, including centralized and decentralized filter architectures, and sequential versus simultaneous measurement updating.

Results show that the integrated solution outperforms the GPS-only approach in all areas. The difference between loose and tight integration strategies was most significant for ambiguity resolution and system reliability. The integrated solution is capable of providing decimetre-level accuracy or better for durations of about five or ten seconds when a complete or partial GPS outage is simulated. This level of accuracy, extended over longer time intervals, is shown to reduce the time required to resolve the L1 ambiguities by an average of about 50% or more for data outages as long as 30 seconds when using a tight integration strategy. More importantly, the reliability of the ambiguity resolution process is improved with the integrated

system. Statistical reliability parameters are also dramatically better when using the integrated system with the ability of detecting a single-cycle cycle slip being better and more consistent, relative to GPS-only. The effect of undetected blunders on the final system is also significantly reduced.

Two real-time tests are analyzed and results show that directly resolving the L1 ambiguities is still unreliable in suburban environments, even with the integrated system. However, using the widelane phase observable, sub-decimetre navigation is demonstrated in suburban and pseudo-urban environments, despite the relatively adverse operational conditions encountered.

Acknowledgements

In many ways this dissertation is not only a reflection of myself but also of the many others who have helped me along my journey, both directly and indirectly. My only sorrow is not being able to thank everyone explicitly. However, there are some people whom I could not bear to forget . . .

- My parents. Their unconditional love, support, guidance and understanding over the years is appreciated more than words can express. They should be proud to have done such a great job raising me. Above all others, they are most responsible for my success.

- Victoria Hoyle. Without her ability to make me laugh and put things in perspective, especially during the most difficult times, I question if I would have made it this far. Her support over the last few months is particularly appreciated.

- My initial supervisor, Gérard Lachapelle. Thanks for having the faith to hire me as a summer student way back in '97 — the bait that ultimately got me this far. Since that time your support, encouragement, and frequent "*opportunities*" have given me a breadth of knowledge I can truly be proud of.

- My second supervisor, Elizabeth Cannon. Your knowledge, support and encouragement have always been welcome and appreciated. In particular, thanks for your help with the inertial navigation components of this work.

- My friends since undergrad, particularly James, Amanda, John, Pascale, Mike and Mike. You've been there for me through it all. Thanks in particular for

Dedication

To my parents.

As a small reflection of what they've allowed me to become.

Table of Contents

List of Tables

List of Figures

xvii

Notation

Symbols

$(\bullet)(t)$	... Quantity $(\bullet)$ as a function of time
$(\bullet)_k$	... Quantity $(\bullet)$ at the kth epoch
$(\bullet)^-$	... Quantity $(\bullet)$ before a measurement update
$(\bullet)^+$	... Quantity $(\bullet)$ after a measurement update
$(\bullet)^a$	... Quantity $(\bullet)$ in frame a
$\dot{(\bullet)}$	... Time derivative of quantity $(\bullet)$
$\overline{(\bullet)}$	... Time average of quantity $(\bullet)$
$C_{(\bullet)}$	... Covariance matrix of subscripted quantity $(\bullet)$
F	... Dynamics matrix
	... Skew-symmetric matrix form of vector f
G	... Shaping matrix
H	... Design matrix
H_0	... Null hypothesis
H_a	... Alternate hypothesis
I	... Identity matrix
	... Ionosphere advance or delay
J	... Least-squares cost function
K	... Kalman gain matrix
M	... Multiple blunder mapping matrix

N	...Carrier phase ambiguity
	...Tensor of gravity gradients
$N(a,b)$	...Normal distribution with mean a and (co)variance b
Q	...Process noise matrix
Q_c	...Continuous-time spectral density matrix
R_b^a	...Rotation matrix from frame b to a
R_a	...Rotation matrix about the ath axis ($a = 1,2,3$)
S^b	...Skew-symmetric matrix form of vector $\Delta\theta_{bc}^a$
T	...Test statistic for multi-dimensional blunders
	...Troposphere delay
W	...Weighting function
a	...Acceleration vector
b	...Accelerometer bias (vector)
d	...Degrees of freedom
	...Gyro bias (vector)
$d\rho$	...Satellite orbit error
f	...Specific force vector
f_1	...Frequency of L1 (1575.42 MHz)
f_2	...Frequency of L2 (1227.60 MHz)
g	...Gravity vector
$\tilde{g}$	...Gravitational acceleration vector
ℓ	...Lever-arm from IMU to GPS antenna phase centre
ℓ_m^a	...Measurement from receiver m to satellite a
$m_{(\bullet)}$	...Multipath for subscripted observation
m_i	...Blunder mapping matrix for observation i

n_α	. . . Value of normal distribution at the α significance level
p	. . . L1 C/A Code pseudorange (code) measurement
r	. . . Measurement residual
	. . . Position vector
t	. . . Time variable
	. . . Test statistic for one-dimensional (single) blunders
v	. . . Measurement noise vector
	. . . Velocity vector
w	. . . Random forcing function
x	. . . State vector
x^*	. . . Nominal trajectory vector
$\hat{x}$	. . . Estimated state vector
z	. . . Observation vector
$\Delta(\bullet)$	. . . Change in quantity ($\bullet$)
Δt	. . . Time interval
Δv_f	. . . Velocity increment due to only to specific force measurements
Δx_i	. . . Protection level vector for i^{th} observation
$\Delta\theta_{bc}^a$	. . . Vector of angular increments of frame c, relative to frame b, expressed in frame a
$\Phi_c(t_k, t_j)$	. . . Continuous-time transition matrix from time t_j to t_k
$\Phi_{k,k+1}$	. . . Discrete-time transition matrix from epoch k to $k+1$
Ω_{bc}^a	. . . Skew-symmetric matrix form of vector ω_{bc}^a
α	. . . Probability of committing a Type I error (significance level)
β	. . . Probability of committing a Type II error

$\chi^2(d, \delta_0)$	...Chi-squared distribution with d degrees of freedom and non-centrality δ_0
$\chi_\alpha^2(d, \delta_0)$	...Value of chi-squared distribution at the α significance level
δ_0	...Non-centrality parameter
$\delta(\bullet)$	...Perturbation of quantity $(\bullet)$
δf^b	...Vector of specific force measurement errors
δx	...Perturbation of state vector
δz	...Measurement misclosure
$\delta \omega_{ib}^b$	...Vector of angular rate measurement errors
$\epsilon_{(\bullet)}$	...Measurement noise for subscripted observation
ε	...Misalignment vector
η	...Pitch
γ	...Normal gravity vector
λ	...Geodetic longitude
λ_1	...Wavelength of L1 ($\sim$19 cm)
λ_2	...Wavelength of L2 ($\sim$24 cm)
λ_{WL}	...Wavelength of widelane ($\sim$86 cm)
$\lambda_{m,n}$	...Wavelength of linear combination $\phi_{m,n}$
∇	...Blunder vector
∇_i^{MDB}	...Minimum (Marginal) Detectable Blunder for the ith observation
$\nabla\Delta$	...Double difference operator
ν	...Innovation sequence
ω_{bc}^a	...Vector of rotation rates of frame c, relative to frame b, expressed in frame a
ω_e	...Earth's rotation rate

ϕ	$\ldots$ Carrier phase measurement
	$\ldots$ Geodetic latitude
$\phi_{m,n}$	$\ldots$ Linear combination of carrier phase measurements
$\dot{\phi}$	$\ldots$ Doppler measurement
ψ	$\ldots$ Azimuth
ρ	$\ldots$ Geometric range between receiver and satellite
$\sigma_{(\bullet)}$	$\ldots$ Standard deviation of subscripted quantity
$\sigma^2_{(\bullet)}$	$\ldots$ Variance of subscripted quantity
ξ	$\ldots$ Roll

Abbreviations and Acronyms

ADOP	$\ldots$ Ambiguity Dilution Of Precision
BDS	$\ldots$ Black Diamond System
C/A-code	$\ldots$ Coarse/Acquisition Code
CCIT	$\ldots$ Calgary Centre for Innovative Technology
DGPS	$\ldots$ Differential GPS
DMI	$\ldots$ Distance Measurement Indicator
DOP	$\ldots$ Dilution Of Precision
ECEF	$\ldots$ Earth Centred Earth Fixed
EKF	$\ldots$ Extended Kalman Filter
FASF	$\ldots$ Fast Ambiguity Search Filter
GNSS	$\ldots$ Global Navigation Satellite System

GPS   . . . Global Positioning System

HPL   . . . Horizontal Protection Limit

IMU   . . . Inertial Measurement Unit

INS   . . . Inertial Navigation System

LAMBDA   . . . Least-squares AMBiguity Decorrelation Adjustment

LSAST   . . . Least-Squares Ambiguity Search Technique

MDB   . . . Minimal (or Marginal) Detectable Blunder

NSR   . . . Noise-to-Signal Ratio

OTF   . . . On-The-Fly

P-code   . . . Precise Code

PL   . . . Protection Level

ppm   . . . Part-Per-Million

PRN   . . . Pseudo-Random Noise

RMS   . . . Root Mean Square

SV   . . . Space Vehicle

VPL   . . . Vertical Protection Limit

WL   . . . WideLane

ZUPT   . . . Zero velocity UPdaTe

Nomenclature

The terms Inertial Measurement Unit (IMU) and Inertial Navigation System (INS)
are often confused. An IMU is an instrument that measures specific forces and
angular rates relative to an inertial frame of reference. An INS contains an IMU as

one of its components, but also includes the ability to use the IMU measurements to derive meaningful position, velocity and attitude information. Every effort has been made to use the above terms in their proper context throughout this dissertation.

Chapter 1

Introduction

Satellite-based positioning and navigation systems are playing an ever-increasing role in today's society. Three-dimensional ship navigation in constricted waterways, automobile positioning for en-route guidance and commercial aircraft positioning are just a few examples of the applications for such systems. Unfortunately, to achieve the accuracy requirements for such applications, satellite-based systems are often insufficient and must be augmented with other sensors. Inertial sensors are well suited for integration with satellite-based systems and have been successfully used in this capacity in the past. However, previous investigations have typically used very high quality inertial sensors to meet the most stringent accuracy requirements. This dissertation investigates the integration of medium-performance (tactical-grade) inertial sensors with satellite-based systems for continuous centimetre-level navigation applications.

1.1 Background

Global Positioning System (GPS) navigation has progressed tremendously over the past decade. Originally designed as a military system, it is now driven by the consumer product sector which represents a multi-billion dollar industry annually. The quality of GPS position estimates are basically time-invariant and range from metre-level to centimetre-level (Lachapelle, 1997), depending on the measurements and

methods employed. To this end, the carrier phase observable is the most precise measurement available to GPS users with a resolution of 0.2–1 mm (1σ) (Raquet, 1998). This precision, combined with differential GPS (DGPS) techniques involving two (or more) GPS receivers, is what allows for centimetre-level positioning. However, this level of positioning is only possible using GPS if the carrier phase ambiguities can be resolved to their true integer values. Much research has therefore been directed at resolving the integer ambiguities in as short a time as possible. Several algorithms have been developed for this purpose including the Least-Squares Ambiguity Search Technique (LSAST) (Hatch, 1990), the Fast Ambiguity Search Filter (FASF) (Chen, 1994), and the Least-Squares Ambiguity Decorrelation Adjustment (LAMBDA) (Teunissen and Tiberius, 1994), to name a few. The performance of these and other algorithms is discussed in Hatch (1994), Hein and Werner (1995) and Han and Rizos (1997).

Although the above algorithms provide rapid ambiguity resolution capabilities under certain circumstances, they are still limited by the error sources affecting the GPS measurements. In this regard, the amount of error in the measurements is primarily a function of the spatial decorrelation of the various error sources and inter-receiver separations, both horizontally and vertically, as was shown in Shi and Cannon (1995). Recent work has been done to better model errors in the ionosphere (Skone, 1998), the troposphere (Zhang, 1999) and composite error effects (Raquet, 1998). A method to reduce code and carrier phase multipath, which is unaffected by differential techniques, was developed by Ray (2000). Unfortunately, many of these techniques require extra infrastructure, equipment and/or processing time, none of which may be readily available to many users.

A drawback of GPS in general is the requirement to maintain light-of-sight visibility to the satellites being tracked. Under signal masking conditions, the number of visible satellites can be significantly reduced, leading to a loss of geometric strength in the estimation process and lower position accuracies. However, signal shading effects are particularly bad for carrier phase processing as they can produce non-continuous phase measurements known as cycle slips. Unfortunately, if a cycle slip is detected while the two receivers are separated by a long distance, the ability to resolve the true ambiguity may be compromised by the increased measurement errors and the GPS-only position uncertainty. Methods of mitigating the effect of these errors, or of obtaining a better position estimate, would therefore improve ambiguity resolution times and reliability.

Unlike GPS, Inertial Measurement Units (IMUs) are completely autonomous (self-contained) instruments that sense accelerations[1] and rotation rates in three orthogonal axes relative to an inertial reference frame. An Inertial Navigation System (INS), which contains an IMU as one of its components, integrates the rotation rates to obtain orientation changes, and doubly integrates the accelerations to obtain velocity and position increments (Jekeli, 2000). The integration of the rotation rates implies that vehicle orientation is obtained as a natural byproduct of the navigation solution, thus adding potentially useful information to certain applications (orientation is not usually a product of GPS-only systems). Furthermore, the aforementioned integration process acts as a low-pass filter and thus produces very accurate short-term position and velocity differences.

Also in contrast to GPS, which typically updates position and velocity at 1 to 20 Hz,

---

[1]The IMU actually measures specific forces, which are related to the applied accelerations through the gravity field as discussed in Chapter 3.

IMUs are capable of making measurements at several hundred Hz. Although rarely processed at this rate, output rates of 50 Hz or higher are not uncommon in the literature, see for example Hartman (1988) or Böder and Seeber (1997). Of course, output rates are a function of application requirements, bandwidth and processor limitations.

Despite the above advantages, sensor inaccuracies such as gyro drifts and accelerometer biases cause a rapid degradation in pure-inertial position quality. To this end, higher quality IMUs exhibit significantly slower position degradation. It therefore becomes necessary to provide an INS with regular updates in order to bound the errors to an acceptable level. Traditionally, this was done using zero velocity updates (ZUPTs), as described in Masson et al. (1996) and Jekeli (2000), for example. However, in many applications, aviation being an obvious one, periodic stops of the vehicle are impractical, if not impossible. Such applications therefore require either a very accurate IMU or another means of bounding the errors.

Given the complimentary nature of GPS and INS, their integration arguably represents the best opportunity for meeting the ever-increasing accuracy and availability demands of commercial users. The advantages of GPS/INS integrated systems, relative to GPS or INS only, are reported to be a full position, velocity and attitude solution, improved accuracy and availability, smoother trajectories, greater integrity and reduced susceptibility to jamming and interference, as discussed in Hartman (1988) and Greenspan (1996). Other studies such as Škaloud (1998) and Scherzinger (2000, 2001, 2002b) have also looked at the benefit of using the inertial solution for improving GPS ambiguity resolution performance. These benefits have been exploited for a wide variety of applications including airborne mapping (Da, 1997a;

Grejner-Brzezinska et al., 1998), as-built road surveys (Lapucha, 1990), airborne positioning (Cannon, 1991; Sun, 1994; Sun et al., 1994) and mobile mapping systems (El-Sheimy et al., 1995), to name a few.

Although emphasis has recently been given to integrated GPS/INS systems in interference and jamming environments, most studies to date have focused on system performance under more benign operational conditions. Specifically, position accuracy during complete GPS data outages (i.e. absence of updates) is a direct reflection of system performance, but reported accuracies vary considerably in the literature. For example, reported accuracies include ten centimetres over one second (Yang et al., 2000), decimetre-level accuracy over 20 seconds (Ford et al., 2001) and decimetre-level over approximately one minute (Da et al., 1996; Grejner-Brzezinska et al., 1998), depending on the quality of IMU and method of updating the system. Vehicle dynamics during the data outages is also a critical factor.

Position accuracy between GPS updates is related to the ability of the integrated system to identify and correct GPS cycle slips, via the predicted phase accuracy (Cannon, 1991; Schwarz et al., 1994a; Sun et al., 1994). This concept can also be expanded to include instantaneous resolution of the ambiguities after a full loss of lock or data outage. The general rule of thumb is that immediate ambiguity resolution is possible if the position accuracy (along the line of sight to the satellite) is known to better than half of the wavelength of the ambiguities being resolved (de Jong et al., 2002). Again, studies have shown varying levels of performance in this regard, depending on the quality of the IMU considered. In Schwarz et al. (1994a) successful bridging of data outages lasting 20–30 seconds are quoted when using a high-quality IMU, with a discussion of performance improvements if optimal

smoothing algorithms are used offline. Similarly, Sun et al. (1994) reported success for data outages up to about ten seconds, although the specifications for the IMU were not provided (but it appears to be of relatively high-quality).

Assessments of the ability of an INS to assist in the ambiguity resolution process has also been the focus of recent investigations, as mentioned above. Specifically, theoretical improvements were shown in Škaloud (1998) and Scherzinger (2002b). Operationally, Scherzinger (2000, 2001, 2002b) shows improvements in ambiguity resolution times when using an integrated system approach. Unfortunately, very little other work has been done to quantify the performance improvement observed under operational conditions.

As a final note, the level of integration used in the GPS/INS system will likely be significant depending on the application. Typically, three main levels of integration are defined, namely loose integration, tight integration and ultra-tight (or deep) integration. The latter approach is typically performed at the hardware level and has therefore been implemented by equipment manufacturers only until recently. The other two strategies are used in approximately equal quantities in the literature, although recently the tight integration seems to be gaining popularity. Each approach has its own advantages and disadvantages, but there has been little comparison between the two, and the investigations that have been undertaken showed little or no advantage in performance for either approach (Wei and Schwarz, 1990b; Schwarz et al., 1994b).

1.2 Limitations of Previous Work

The integration of GPS and high-quality IMUs has thus far proven very successful. Specifically, with reference to Table 1.1, navigation-grade IMUs have been primarily used for high-accuracy applications. While such systems provide decimetre-level positioning accuracies during GPS data outages of up to one minute (e.g. El-Sheimy et al., 1995; Grejner-Brzezinska et al., 1998), the costs of these systems places a severe restriction on the number of applications capable of exploiting their benefits. Costs for a navigation-grade IMU can run into the hundred's of thousand's of dollars. However, with the decreasing size and cost of inertial sensors that perform at comparatively low accuracy levels, the need to investigate poorer quality systems for high-accuracy navigation is important. The question arises therefore as to whether a tactical or automotive-grade IMU could be used to obtain some benefits in this regard, albeit not as significant as those quoted using navigation-grade systems.

Using an automotive-grade IMU, Salychev et al. (2000) reported metre-level accuracy for data outages of a few seconds when using DGPS code and Doppler measurements. Yang et al. (2000) quoted decimetre-level accuracy over one-second intervals using fixed carrier phase ambiguity updates with similar quality sensors. Finally, centimetre-level accuracy over one second was also reported in Farrell et al. (2000). Other investigations (e.g. Schwarz and Zhang, 1994) have also used similar quality sensors but have focused on attitude accuracy and not on position performance. In general, these investigations show that automotive-grade IMUs are not well suited for high-accuracy navigation applications because of their rapid position and velocity degradation, even in the short-term.

The use of tactical-grade IMUs for high-accuracy navigation has also been some-

Table 1.1: IMU Classification (Modified from Shin, 2001)

Sensor Error	IMU Grade		
	Navigation	Tactical	Automotive
Gyro Bias [deg/h]	0.005–0.010	0.1–10	100+
Gyro Noise [deg/h/$\sqrt{\text{Hz}}$]	0.002–0.005	0.2–0.5	N/A
Accel Bias [mm/s^2]	0.050–0.100	2–4	12+
Accel Noise [mm/s^2/$\sqrt{\text{Hz}}$]	0.050–0.100	2–4	N/A

what limited, despite its potential for success. In Da (1997b), the analysis of system performance was very limited in terms of position accuracy and no mention of the potential for improving the ambiguity resolution process was made. In Scherzinger (2000) two integration strategies were investigated in terms of ambiguity resolution performance with some summaries of position accuracies. This investigation only considered limited GPS data outage durations and did not compare results to the GPS-only case. Furthermore, comparison of the two integration strategies is not entirely fair, given that each used different GPS processing software. Other investigations by Scherzinger (2001, 2002b) also used a distance measurement indicator (DMI). While the corresponding results are promising, the additional cost of the DMI is generally undesirable and no comment is made as to its benefit (or lack thereof) to the system's performance.

Most investigations to date have operated in post-mission only. Notable exceptions (which include post-mission processing using real-time algorithms) are Scherzinger (2000, 2001, 2002b), Farrell et al. (2000) and Yang et al. (2000). While ideal for system testing and development, offline processing opens the door to optimal smoothing

techniques (as discussed in Schwarz et al., 1994a; El-Sheimy et al., 1995), Kalman filter tuning, and increased modeling and/or processing capabilities (Nassar and Schwarz, 2001) which are unavailable to real-time systems. Therefore, in terms of meeting the growing demands for real-time position and navigation information, some of these techniques will have little use. As a result, system performance may suffer accordingly. A more thorough analysis of GPS/INS systems in real-time environments is therefore needed.

Finally, the operational environment of a navigation system will play a large role in the quality of measurements obtained. Under adverse conditions, for example, GPS receivers may have difficulty tracking satellites, may track a reflected signal or may even track the wrong satellite altogether. Such problems can introduce large measurement errors that can bias the estimated parameters, thus compromising system integrity. Statistical reliability quantifies what magnitude of error can be detected and removed by a system. While reliability in kinematic systems has been investigated in the past (e.g. Teunissen, 1990a; Wei et al., 1990; Lu, 1991; Ryan, 2002), only one study has looked at the reliability of integrated systems, but did not focus on the integration of GPS with inertial sensors (Salzmann, 1990). Consequently, reliability in GPS/INS systems remains largely unexplored despite its direct impact on system performance.

1.3 Objectives and Contributions of This Dissertation

Given the lack of research directed towards the use of tactical-grade IMUs for high-accuracy navigation, this dissertation expands upon the work described in the previous section with the ultimate goal being robust sub-decimetre-level positioning

capabilities at all times. Real-time operation of the system is also a major focus. As the size and cost of tactical-grade IMUs decrease, their inclusion in real-time systems will become abundant thus demanding appropriate and efficient implementations be available.

With regard to the shortcomings outlined in the previous section, the objectives of this dissertation are to investigate the following parameters of the integration of a tactical-grade IMU with GPS

1. *System Positioning Accuracy During GPS Data Outages.* Under operational conditions GPS data outages occur with varying (application and/or environment specific) durations. The duration for which the integrated system can navigate through such data outages with satisfactory accuracy will determine the potential uses for the system. Data outages can vary in severity from complete data outages where no satellite signals are available, to partial data outages where sub-optimal or insufficient satellite visibility is available. Simulation of complete and partial GPS data outages of varying duration is used to assess the performance of the integrated system.

2. *Ambiguity Resolution Improvements.* Once GPS signals become available after GPS data outages, timely and reliable determination of the integer carrier phase ambiguities is required to obtain the highest possible positioning accuracy. The ambiguity resolution performance of the integrated system will be compared to that of GPS-only to determine the possible improvements and limitations. Specifically, can the integrated system reduce the time needed to resolve the ambiguities as integers and/or improve the reliability of the process? If so, at what point does the improvement become insignificant?

3. *System Reliability.* By assessing the ability of a system to reject erroneous observations, the overall robustness of the system can be assessed. Specifically, the magnitude of the smallest detectable blunder can be computed, as well as its affect on the estimated parameters (assuming it passes undetected). Comparing these values using GPS-only and GPS/INS systems will provide valuable insight into the benefit of using the integrated system. Consideration of different measurement update strategies will also be considered in this regard.

4. *Impact of Integration Strategy On Overall System Performance.* While loose and tight integrations are common in practice, the benefits of each approach in operational conditions is not well demonstrated. Consequently, each of the above parameters will be investigated using a loose and tight integration strategy.

Each of the above parameters are investigated with real-time applications in mind. This implies no special post-mission processing of the data be required, even if results are obtained offline.

The major contributions of this dissertation to the general field of positioning and navigation can be summarized as follows

1. Characterization of benefits and limitations of integrating GPS with tactical-grade IMUs for real-time applications. Such a characterization is important given the trends in lower-cost sensors while trying to satisfy increasing user demands. Included in the characterization is a thorough assessment of the

   (a) Integrated system performance during GPS data outages

(b) Improvement in ambiguity resolution time and reliability achieved with a GPS/INS system relative to GPS-only

(c) Integrated system's statistical reliability relative to GPS-only

System characterization is performed using actual field data collected with specific GPS and IMU equipment, and using real and simulated GPS outages.

2. Modification of the statistical reliability equations for use in cascaded filter architectures and for sequential updating of Kalman filters. Normally, statistical reliability algorithms assume all observations are processed together in a single filter. However, computational savings can be realized by processing observations sequentially in groups, or by having multiple filters process data in stages. Given this, the traditional reliability analysis equations are re-worked accordingly.

3. Development and testing of a software program capable of using data from various qualities of IMUs and GPS receivers, and able to implement user selectable processing strategies.

1.4   Dissertation Outline

This dissertation contains nine chapters and six appendices which are organized as described below.

Chapter 1 presents the motivation, objectives and contributions of this dissertation to the integration of tactical-grade IMUs with GPS. Results and shortcomings of previous work are shown and used to justify the scope of the research undertaken.

Chapter 2 discusses the estimation theory used throughout the dissertation. In particular, the Kalman filter algorithm is presented. Statistical reliability theory in the context of Kalman filtering is also presented.

In Chapter 3 the basic GPS and INS methodology is reviewed. Differential GPS errors are discussed in general with attention given those relevant to this research. Ambiguity resolution is also discussed. For inertial navigation, the equations of motion, mechanization equations and error equations are presented.

Chapter 4 presents the various strategies for GPS/INS integration. Details of the GPS-only, INS-only and GPS/INS filters are then presented with attention given to the methods used for selecting the system models and corresponding model parameters. The lever-arm effect is also discussed.

In Chapter 5 some issues relating to real-time processing and performance are raised and addressed. Reducing the update rate of the INS parameters relative to the raw IMU data rate and some practical implementation issues of the Kalman filter algorithm are discussed. Special attention is given to the method of updating the filter with external measurements. Specifically, sequential and simultaneous updates are compared in terms of computational efficiency.

The classical reliability theory from Chapter 2 is re-worked in Chapter 6 to accommodate cascading filters and sequential measurement update strategies.

Offline results of the integrated system are presented in Chapter 7. Specifically, position accuracy during complete and partial data outages, ambiguity resolution performance after these data outages, as well as overall system reliability are investigated. Where possible, comparisons between GPS-only and the integrated system

are made. The above performance parameters are also discussed for the appropriate integration strategies. An assessment of the real-time performance is evaluated in Chapter 8.

Chapter 9 concludes the major results and findings obtained in the previous chapters with reference to the objectives listed in Section 1.3 and makes recommendations for expanding upon the research presented.

The appendices contain various detailed information relevant the dissertation.

Chapter 2

Estimation and Reliability Overview

Basic navigation involves the combination of multiple measurements to estimate a desired set of parameters. For situations where the measurements uniquely observe the unknown parameters, the estimation process becomes relatively trivial. Unfortunately, this situation is rarely encountered in practical situations and so more complicated estimation procedures are required. This chapter reviews the estimation strategies employed in this dissertation. Estimation using measurements only (least-squares) is briefly presented followed by a detailed presentation of estimation in dynamic systems (Kalman filters). Finally, a discussion of blunders, reliability testing and statistical reliability is presented.

2.1 Estimation

This section provides a general overview of estimation theory as applied in later chapters.

2.1.1 Estimation Using Measurements Only

As a starting point, the concept of estimating a set of quantities based purely on measurements is considered. The most common estimation procedure for this purpose in geomatics applications is least-squares. To understand the least-squares principle, consider a measurement (observation) vector, z, that relates to an unknown

parameter (state) vector, x, as follows

$$z_k = H_k x_k + v_k \qquad (2.1)$$

where subscript 'k' represents a quantity at the kth epoch and

H is typically referred to as the design matrix, which contains the "geometry" of the observations, relative to the parameters of interest, and

v is a vector of measurement noise.

The objective of least-squares is to derive an estimate of the parameters, $\hat{x}_k$, in order to minimize the weighted sum of squares of deviations, $(z_k - H_k \hat{x}_k)$ (Gelb, 1974)

$$J_k = (z_k - H_k \hat{x}_k)^T W_k^{-1} (z_k - H_k \hat{x}_k) \qquad (2.2)$$

where

J is the cost function to be minimized, and

W is a weighting function.

The solution, consistent with setting the derivative of Equation 2.2 (with respect to $\hat{x}_k$) to zero and solving for $\hat{x}_k$, is given by

$$\hat{x}_k = (H_k^T W_k^{-1} H_k)^{-1} H_k^T W_k^{-1} z_k \qquad (2.3)$$

whose estimated covariance matrix is given by

$$C_{x_k} = (H_k^T W_k^{-1} H_k)^{-1} (H_k^T W_k^{-1} C_{z_k} W_k^{-1} H_k)(H_k^T W_k^{-1} H_k)^{-1} \qquad (2.4)$$

where C is the covariance matrix of the subscripted quantity. To obtain the minimum variance for the estimated parameters let $W_k = C_{z_k}$ such that Equations 2.3 and 2.4 reduce to

$$\hat{x}_k = (H_k^T C_{z_k}^{-1} H_k)^{-1} H_k^T C_{z_k}^{-1} z_k \tag{2.5}$$

$$C_{x_k} = (H_k^T C_{z_k}^{-1} H_k)^{-1} \tag{2.6}$$

Once the final estimate of the states are obtained, the measurement residuals, r_k, can be computed as the difference between the actual and predicted observations (z_k and $H_k \hat{x}_k$, respectively) as

$$r_k = z_k - H_k \hat{x}_k \tag{2.7}$$

Assuming a correct measurement model, residuals indicate the extent to which the measurements agree with each other and are therefore useful for indirectly assessing the quality of the estimated parameters.

Alternate derivations of the above equations, as well as other least-squares formulations, are shown in Mikhail (1976), Vaníček and Krakiwsky (1986), Krakiwsky (1990).

2.1.2   Estimation of Dynamic Systems

Least-squares estimation, as presented above, is limited to determining the desired parameters based on measurements only. However, it follows that if knowledge of how a particular system behaves over time is available, a better estimate of the desired parameters can be obtained. Specifically, if the parameters to be estimated are not only related to the observations as in Equation 2.1, but are also known to

behave as

$$\dot{x}(t) = F(t)x(t) + G(t)w(t) \tag{2.8}$$

where a dot represents a time derivative and

F is a coefficient matrix describing the dynamics of the system (dynamics matrix),

G is a coefficient matrix used to shape white noise input (shaping matrix),

w is a vector of random forcing functions, assumed to be zero-mean white noise with a Gaussian distribution, and

t is a time variable.

then a Kalman filter can be used to efficiently compute optimal state estimates while exploiting the assumed system dynamics. A Kalman filter is a recursive algorithm that uses a series of prediction and measurement update steps to obtain an optimal, in a minimum variance sense, estimate of the state vector (Gelb, 1974). Only the final form of the discrete-time algorithm is shown here, with details of the derivation as well as the continuous-time algorithm available in Gelb (1974) and Brown and Hwang (1992).

Using the measurement model in Equation 2.1 with the additional assumption that v_k is a zero-mean white noise sequence with a Gaussian distribution, an updated estimate of the state vector and its covariance (assuming values for these are already available) can be obtained as

$$\hat{x}_k^+ = \hat{x}_k^- + K_k \nu_k \tag{2.9}$$

$$C_{x_k}^+ = (I - K_k H_k)C_{x_k}^- \tag{2.10}$$

where superscript "−" and "+" represents a quantity before and after the measurement update respectively, and

K is the Kalman gain matrix given by

$$K_k = C_{x_k}^- H_k^T (H_k C_{x_k}^- H_k^T + C_{z_k})^{-1} \tag{2.11}$$

ν is the innovation sequence given by

$$\nu_k = z_k - H_k \hat{x}_k^- \tag{2.12}$$

The innovation sequence has a form similar to Equation 2.7 and is thus sometimes called the predicted residuals. The innovation sequence can be interpreted as the amount of new information being introduced into the system from the measurements. The gain matrix on the other hand, is a weighting factor indicating how much of the new information contained in the innovations should be accepted by the system. Loosely speaking, it weighs the information from the measurements against the current knowledge of the states. To illustrate, consider a scalar system whose state is directly observable such that $H_k = 1$. In this case, the gain matrix reduces to

$$
\begin{aligned}
K_k &= \frac{\sigma_{\hat{x}_k}^2}{\sigma_{\hat{x}_k}^2 + \sigma_{z_k}^2} \\
&= \frac{1}{1 + \dfrac{\sigma_{z_k}^2}{\sigma_{\hat{x}_k}^2}} \\
&= \frac{1}{1 + \mathrm{NSR}_k}
\end{aligned}
\tag{2.13}
$$

where σ^2 is the variance of the subscripted quantity, and NSR is the Noise-to-Signal Ratio (i.e. the amount of noise in the measurement relative to the current knowledge

of the state/signal). In this way, if the NSR is large the gain will be small, indicating the filter will trust the system model (i.e. the current estimate) more than the measurements. In contrast, a small NSR implies the filter will trust the measurements more than the system model. Although this discussion is not directly applicable to the multi-dimensional case, it serves to illustrate the role of the gain matrix and its reaction to the confidence of the measurements and current state estimates.

Prediction of the state vector and its covariance matrix forward in time can be performed using

$$\hat{x}_{k+1} = \Phi_{k,k+1}\hat{x}_k \tag{2.14}$$

$$C_{x_{k+1}} = \Phi_{k,k+1}C_{x_k}\Phi_{k,k+1}^T + Q_k \tag{2.15}$$

where

$\Phi_{k,k+1}$ is the transition matrix of the system from epoch k to $k+1$, and

Q is the process noise matrix.

For most system models the dynamics matrix is considered to be time invariant for the time interval over which the prediction is to be performed. Even if this is not theoretically valid, resulting errors can be mitigated by further shortening the prediction time interval. The benefit is that under this assumption the transition matrix is obtained as the solution of the system model in the absence of forcing functions, given by (Gelb, 1974)

$$\Phi_{k,k+1} = e^{F\Delta t} \tag{2.16}$$

where Δt is the time interval over which the prediction is to take place. The process noise matrix, which accounts for uncertainty in the system model, is computed as

the solution of (Gelb, 1974)

$$Q_k = \int_{t_k}^{t_{k+1}} \Phi_c(t_{k+1}, \tau)G(\tau)Q_c(\tau)G^T(\tau)\Phi_c^T(t_{k+1}, \tau)d\tau \qquad (2.17)$$

where

$\Phi_c(t_k, t_j)$ is the continuous-time transition matrix between times t_j and t_k (Gelb, 1974), and

$Q_c(t)$ is the continuous-time spectral density matrix of the forcing functions, $w(t)$.

With the above equations, the Kalman filter algorithm can be illustrated as in Figure 2.1. The prediction and update steps described above are clearly indicated. It is noted that the prediction increments can be as large as the update interval, however smaller intervals can be used if desired and/or necessary such that several prediction steps are performed between each update step. Also of note is that the covariance propagation (both for prediction and update) is independent of state and observation vectors. In this way, the state covariance can be propagated offline using assumptions of the process noise and expected measurement updates.
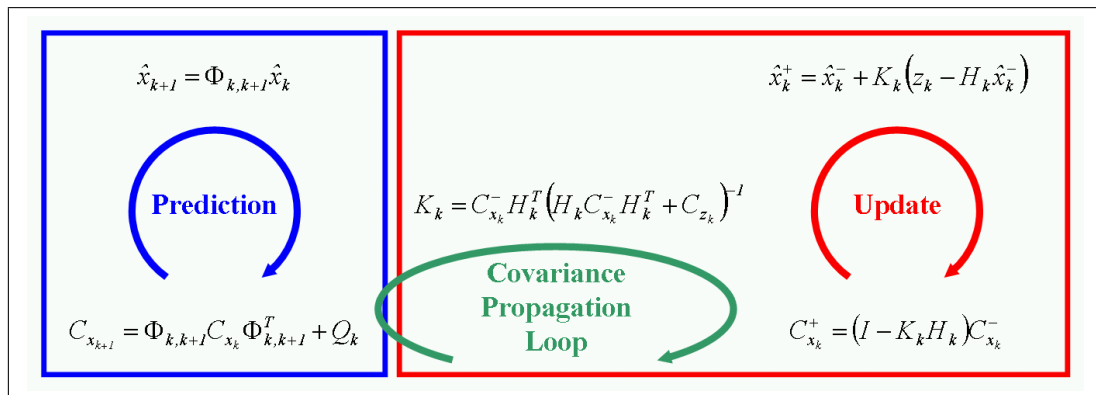
Figure 2.1: Discrete-Time Kalman Filter Algorithm

2.2   Practical Considerations in Estimation

This section discusses some practical considerations of the theoretical development of the previous section.

2.2.1   System Linearization

The system and measurement models of the previous section were assumed to be linear. Unfortunately, in many applications one or both of these models are non-linear and linearization techniques must be applied. The following presentation follows that shown in Brown and Hwang (1992) or Grewal and Andrews (1993).

Non-Linear System Models and the Extended Kalman Filter

To illustrate the linearization process for non-linear system models, consider a slightly modified form of Equation 2.8

$$\dot{x}(t) = f\Big(x(t), t\Big) + G(t)w(t) \tag{2.18}$$

where $f\Big(x(t), t\Big)$ is a (presumably) non-linear function representing the temporal behaviour of the system states. First, a nominal trajectory, $x^*(t)$, is selected such that

$$x(t) = x^*(t) + \delta x(t) \tag{2.19}$$

where $\delta x(t)$ is a perturbation from the nominal trajectory. Note that "trajectory" in this context is meant to represent the time-series of any type of parameter, and need not be restricted to the trajectory of a car, for example. A first order Taylor

series expansion of Equation 2.18 about the nominal trajectory is performed to yield

$$\dot{x}(t) = f\big(x(t), t\big) + G(t)w(t)$$

$$\approx f\big(x^*(t), t\big) + \frac{\partial f\big(x^*(t), t\big)}{\partial x(t)}\bigg|_{x(t)=x^*(t)} \delta x(t) + G(t)w(t)$$

$$= \dot{x}^*(t) + F\delta x(t) + G(t)w(t)$$

$$\dot{x}(t) - \dot{x}^*(t) = F\delta x(t) + G(t)w(t)$$

$$\delta\dot{x}(t) = F\delta x(t) + G(t)w(t) \tag{2.20}$$

where F is now the dynamics matrix for a system whose states consist of the perturbed states, $\delta x(t)$. In this way, the Kalman filter actually estimates the perturbations and then reconstructs the desired states using Equation 2.19.

The remaining step is the determination of the nominal trajectory around which the linearization occurs. Although a nominal trajectory can be computed beforehand, a more common (and practical) procedure is to use the last Kalman filter estimate as the linearization point. This approach is implemented in an extended Kalman filter (EKF). In this approach, the perturbation can also be interpreted as the error in the nominal (i.e. estimated) trajectory. The only difference between a "regular" and an extended Kalman filter is that in the latter, the state vector is reset to zero after each update. This is conceptually valid if one considers that the current Kalman filter estimate is optimal, and that the errors of the estimated stated have zero mean.

Given that the state vector is actually a null vector, the prediction of the state vector is unnecessary. Also, the state update equation (2.9) can be reformulated as

$$\delta\hat{x}_k^+ = \delta\hat{x}_k^- + K_k(z_k - H_k\delta\hat{x}_k^-)$$

$$= (0) + K_k(z_k - H_k(0))$$

$$= K_k z_k \tag{2.21}$$

Finally, the update and prediction of the state covariance is performed as before (see Equations 2.10 and 2.15).

Non-Linear Measurement Model

The concept of linearizing the measurement model is analogous to the development just shown. To begin, re-formulate Equation 2.1 as

$$z_k = h\left(x_k, k\right) + v_k \tag{2.22}$$

where $h\left(x_k, k\right)$ is a (presumably) non-linear function relating the states to the observations. As before, a first order Taylor series expansion of Equation 2.22 about the nominal trajectory is performed to yield

$$
\begin{aligned}
z_k &= h\left(x_k, k\right) + v_k \\
&\approx h\left(x_k^*, k\right) + \left.\frac{\partial h\left(x_k, k\right)}{\partial x_k}\right|_{x_k = x_k^*} \delta x_k + v_k \\
&= z_k^* + H_k \delta x_k + v_k \\
z_k - z_k^* &= H_k \delta x_k + v_k \\
\delta z_k &= H_k \delta x_k + v_k \tag{2.23}
\end{aligned}
$$

where δz_k is termed the measurement misclosure, and H_k is the design matrix relating the misclosures to the perturbed states. Stated differently, the misclosures

act as observations of the perturbed states. If an extended Kalman filter is used in conjunction with a non-linear measurement update, the state update equations can be re-written as

$$
\begin{aligned}
\hat{x}_k^+ &= \hat{x}_k^- + \delta\hat{x}_k^+ \\[2mm]
&= \hat{x}_k^- + \delta\hat{x}_k^- + K_k(\delta z_k - H\delta x_k) \\[2mm]
&= \hat{x}_k^- + (0) + K_k(\delta z_k - H_k(0)) \\[2mm]
&= \hat{x}_k^- + K_k\delta z_k
\end{aligned}
\tag{2.24}
$$

Note that in the case under consideration, the innovation sequence reduces to the misclosure vector.

As already stated, the measurement residuals are important for indirectly assessing the quality of the estimated parameters. However, instead of recomputing them using Equation 2.7, a more efficient implementation is desirable. Given that the residuals are the difference between the actual and predicted observations, based on the updated estimate of the state, they can be formulated as

$$
\begin{aligned}
r_k &= z_k - h(x_k^+, k) \\[2mm]
&= z_k - \left(h(x_k^-, k) + \left.\frac{\partial h(x_k, k)}{\partial x(t)}\right|_{x_k = x_k^-} \delta x_k^+ \right) \\[2mm]
&= \left(z_k - h(x_k^-, k) \right) - H_k \delta x_k^+ \\[2mm]
&= \delta z_k - H_k \delta x_k^+
\end{aligned}
\tag{2.25}
$$

Of course, the computation of the residuals should be performed before the error

states are reset to zero. As a final note, a similar linearization procedure can also be applied to the least-squares concept presented in Section 2.1.1.

2.3   Reliability in Dynamic Systems

Reliability refers to the ability to identify and reject errors (blunders) in the measurements. The actual identification of the blunders is performed via testing of the measurement residuals in the least-squares case, and of the innovation sequence in the case of Kalman filtering. As such, it requires actual measurement and state information. This process will herein be referred to as reliability testing.

In contrast, statistical reliability quantifies the theoretical reliability of a system under certain statistical assumptions, and does not require actual measurements. Instead, statistical reliability can be performed offline using only the necessary co-variance and measurement geometry information, which is readily available from the Kalman filter algorithm (see Section 2.1.2). The concept of statistical reliability can be sub-divided into two categories. First, internal reliability refers to the theoretical magnitude of blunders that can be detected for a given observation. Second, and perhaps more important, external reliability quantifies the effect of these blunders on the estimated states if they were to pass through the system undetected.

Statistical reliability theory was originally developed by Baarda (1967, 1968) for least-squares applications but was expanded to dynamic systems by Teunissen and Salzmann (1989). Since then, many theoretical and practical investigations have taken place. Theoretical development of the equations are shown in Teunissen (1990a,b,c) and Koch (1999), while some practical applications in positioning or

navigation systems are shown in Salzmann (1990), Wei et al. (1990), Lu (1991), Lu and Lachapelle (1992) and Ryan (2002).

This section begins with a brief discussion of the properties of the innovation sequence and how they change in the presence of blunders. Statistical testing is then introduced as a means of identifying such blunders. Finally, statistical reliability is presented.

2.3.1 Reliability Testing of the Innovation Sequence

One of the properties of a Kalman filter is that if the input noise, w and v, are zero-mean white noise sequences with Gaussian distributions, the innovation sequence will have similar properties (Gelb, 1974). Furthermore, it can be shown that the covariance matrix of the innovation sequence is given by

$$C_{\nu_k} = H_k^T C_{x_k}^- H_k + C_{z_k} \tag{2.26}$$

which, with reference to Equation 2.11, is computed as part of the Kalman gain matrix. As such, it is readily available during normal filter operation.

Reliability With Multiple Blunders

However, what if the above assumptions do not hold? Specifically, what happens if the measurement errors are not zero mean? To investigate this, first consider the measurement model (Equation 2.1) under the presence of a blunder vector, ∇

$$z_k = H_k x_k + M_k \nabla_k + v_k \tag{2.27}$$

where M is a known full-rank matrix, mapping the blunders into the observations. The innovation sequence is then constructed as before, as the difference between the

actual and predicted measurements and is therefore biased by the second last term in the above equation. This bias in the innovations is represented as

$$\Delta\nu_k = M_k\nabla_k \tag{2.28}$$

For blunder detection, the null hypothesis (H_0) assumes that the observations are bias-free. The alternate hypothesis (H_a) is that the observations are biased by $M_k\nabla_k$. Under these hypotheses, the innovation sequence is distributed as (Teunissen and Salzmann, 1989)

$$\nu_k|_{H_0} \quad \sim \quad N(0, C_{\nu_k}) \tag{2.29}$$

$$\nu_k|_{H_a} \quad \sim \quad N(M_k\nabla_k, C_{\nu_k}) \tag{2.30}$$

where $N(a, b)$ is a normal distribution with mean 'a' and (co)variance 'b' and it is tacitly assumed that even in the presence of a blunder, the covariance matrix of the innovation sequence remains unchanged. Next, the test statistic used for testing H_0 against H_a is given by (Teunissen and Salzmann, 1989; Koch, 1999)

$$T_k = \nu_k^T C_{\nu_k}^{-1} M_k (M_k^T C_{\nu_k}^{-1} M_k)^{-1} M_k^T C_{\nu_k}^{-1} \nu_k \tag{2.31}$$

However, Equation 2.30 is equivalent to the form of the measurement model in Equation 2.1 where

- the observations are given by the biased innovation sequence with a covariance matrix given by C_{ν_k} (which is both white and Gaussian)

- the design matrix is given by M_k

- the states are the observation blunders

In this light, Equation 2.31 can re-formulated (using Equations 2.5 and 2.6) as

$$
\begin{aligned}
T_k &= \nu_k^T C_{\nu_k}^{-1} M_k (M_k^T C_{\nu_k}^{-1} M_k)^{-1} (M_k^T C_{\nu_k}^{-1} M_k)(M_k^T C_{\nu_k}^{-1} M_k)^{-1} M_k^T C_{\nu_k}^{-1} \nu_k \\
&= \left[(M_k^T C_{\nu_k}^{-1} M_k)^{-1} M_k^T C_{\nu_k}^{-1} \nu_k\right]^T (M_k^T C_{\nu_k}^{-1} M_k) \left[(M_k^T C_{\nu_k}^{-1} M_k)^{-1} M_k^T C_{\nu_k}^{-1} \nu_k\right] \\
&= \hat{\nabla}_k^T C_{\hat{\nabla}_k}^{-1} \hat{\nabla}_k
\end{aligned}
\tag{2.32}
$$

where $C_{\hat{\nabla}_k}$ is the covariance matrix of the estimated observation blunders. The test statistic is distributed under the two hypotheses as

$$
T_k|_{H_0} \sim \chi^2(d, 0)
\tag{2.33}
$$

$$
T_k|_{H_a} \sim \chi^2(d, \delta_0^2)
\tag{2.34}
$$

where d is the degrees of freedom, equal to the number of assumed blunders, and δ_0 is the non-centrality parameter of the distribution given as (Teunissen, 1990b)

$$
\delta_0^2 = \nabla_k^T C_{\hat{\nabla}_k}^{-1} \nabla_k
\tag{2.35}
$$

Consequently, the null hypothesis is rejected in favour of the alternate hypothesis if $T_k \geq \chi_\alpha^2(d, 0)$, at some significance level, α. This represents the basis for reliability testing.

Reliability With a Single Blunder

Focus is now given to the special case where the blunder vector is assumed to consist of a single blunder on a single observation. In this case, the blunder vector reduces to a scalar and the M_k matrix reduces to a column-vector, m_k, of the form

$$
m_{k_i} = \begin{bmatrix} 0 & \cdots & 0 & 1 & 0 & \cdots & 0 \end{bmatrix}^T
\tag{2.36}
$$

where the one is in the ith location, and thus corresponds to the ith observation. Using this new form, the test statistic is re-formulated on an observation-by-observation basis as the square-root of Equation 2.31 to yield

$$t_{k_i} = \frac{m_{k_i}^T C_{v_k}^{-1} \nu_k}{\sqrt{\left(C_{v_k}^{-1}\right)_{ii}}} \tag{2.37}$$

or, using Equation 2.32, as

$$t_{k_i} = \frac{\hat{\nabla}_{k_i}}{\sigma_{\hat{\nabla}_{k_i}}} \tag{2.38}$$

The single-blunder test statistic is denoted using a lower case letter to avoid confusion with the more generic case. Having limited the number of blunders to one and having taken the square-root of the original test statistic (T_k), the single-blunder test statistic is now distributed as (Teunissen, 1990b)

$$t_k|_{H_0} \sim N(0,1) \tag{2.39}$$

$$t_k|_{H_a} \sim N(\delta_0,1) \tag{2.40}$$

where the non-centrality parameter is the square-root of Equation 2.35 and, for the scalar case, is given as

$$\delta_0 = |\nabla_{k_i}| \sqrt{\left(C_{v_k}^{-1}\right)_{ii}} \tag{2.41}$$

The null hypothesis is then rejected if $|t_k| \geq n_{1-\alpha/2}$, where $n_{1-\alpha/2}$ is the point on the X-axis beyond which only $1 - \alpha/2$ percent of the points lie (assuming a Gaussian distribution). Throughout this dissertation, only the single blunder case is assumed. The above testing procedure is therefore implemented herein, with some modifications as discussed below. The testing procedure is shown graphically in Figure 2.2.
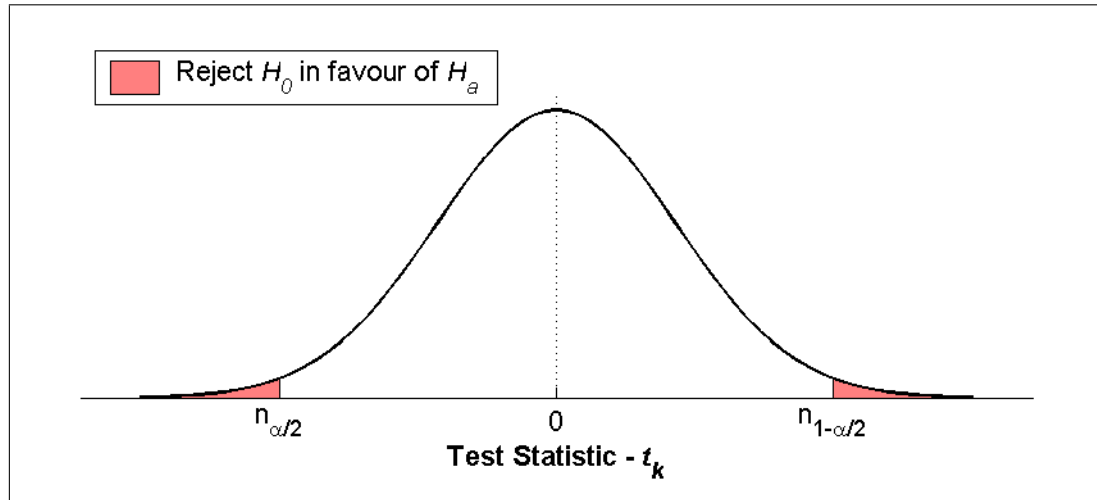
Figure 2.2: Graphical Representation of Reliability Testing

Practical Validity of Single Blunder Testing

Unfortunately, the assumption of a single blunder is not always valid. To detect multiple blunders, several alternate hypotheses are typically required depending on what type of blunders are expected to occur. While such hypotheses can be made for certain situations, they are not likely universally applicable. To alleviate this problem, the testing procedure used herein recursively applies the single blunder test whenever a blunder is detected. Assuming multiple blunders occur simultaneously, the reliability algorithm proceeds as follows

- If multiple blunders are detected (i.e. $|t_{k_i}| \geq n_{1-\alpha/2}$ for multiple observations), the observation with the largest $|t_k|$ is rejected.

- The reliability testing procedure is then repeated with the remaining observations.

- The process is repeated until no more blunders are detected.

Although not theoretically sound, the above approach can be characterized using some statistical assumptions (Koch, 1999). Assuming the first n observations contain blunders, the significance level (see next section for description) is theoretically given by (ibid.)

$$P\left(|t_{k_1}| > n_{1-\alpha/2} \cup |t_{k_2}| > n_{1-\alpha/2} \cup \cdots \cup |t_{k_n}| > n_{1-\alpha/2}\right) = \alpha \qquad (2.42)$$

However, from elementary statistics

$$P\left(A \cup B\right) = P\left(A\right) + P\left(A\right) - P\left(A \cap B\right) \qquad (2.43)$$

Recursive application of this identity to Equation 2.42, assuming the probabilities of the intersections are negligible, yields

$$P\left(|t_{k_1}| > n_{1-\alpha/2}\right) + P\left(|t_{k_2}| > n_{1-\alpha/2}\right) + \cdots + P\left(\cdots |t_{k_n}| > n_{1-\alpha/2}\right) \geq \alpha \quad (2.44)$$

Simplifying the left-hand side gives the following approximation

$$nP\left(|t_{k_i}| > n_{1-\alpha/2}\right) = \alpha \qquad (2.45)$$

$$P\left(|t_{k_i}| > n_{1-\alpha/2}\right) = \alpha/n \qquad (2.46)$$

Heuristically, the above implies that in order to detect n blunders with a significance level of α, the significance level for each individual blunder must be reduced by a factor of n. For the case considered here, the significance level for each individual blunder is assumed constant, implying that the significance level of detecting n is increased by the same factor.

2.3.2 Statistical Reliability

Statistical reliability is a theoretical extension of reliability testing. Whereas reliability testing aims purely at identifying a blunder based on the innovation sequence

and its covariance, statistical reliability aims at quantifying the magnitude of the blunders that can be detected. As a subsequent step, statistical reliability quantifies the effect that the smallest blunder capable of being detected would have on the estimated parameters. In so doing, the extent to which reliability testing can "protect" the system is quantified.

To begin, there are two types of errors that can occur in a statistical test as summarized in Table 2.1 (Vaníček and Krakiwsky, 1986). The first is termed a Type I error and occurs when the null hypothesis is incorrectly rejected. The second error is termed a Type II error and occurs when the null hypothesis is incorrectly accepted. The probability of committing a Type I and Type II error is α and β, respectively.

Internal Reliability

Statistical reliability begins with a selection of the probability of committing a Type I or Type II error. These values are typically selected based on an application's requirements. Next, the non-centrality parameter can be computed as

$$\delta_0 = n_{1-\alpha/2} + n_{1-\beta} \tag{2.47}$$

This is shown graphically in Figure 2.3. Next, under the assumption that a blunder

Table 2.1: Testing of Null Hypothesis H_0 Against Alternate Hypothesis H_a

Actual Situation	Decision Based On Statistical Test	
	Accept H_0	Reject H_0
H_0 Is True	Correct Decision Probability: $1-\alpha$ (Confidence Level)	Type I Error Probability: α (Significance Level)
H_0 Is False	Type II Error Probability: β	Correct Decision Probability: $1-\beta$ (Power of the Test)
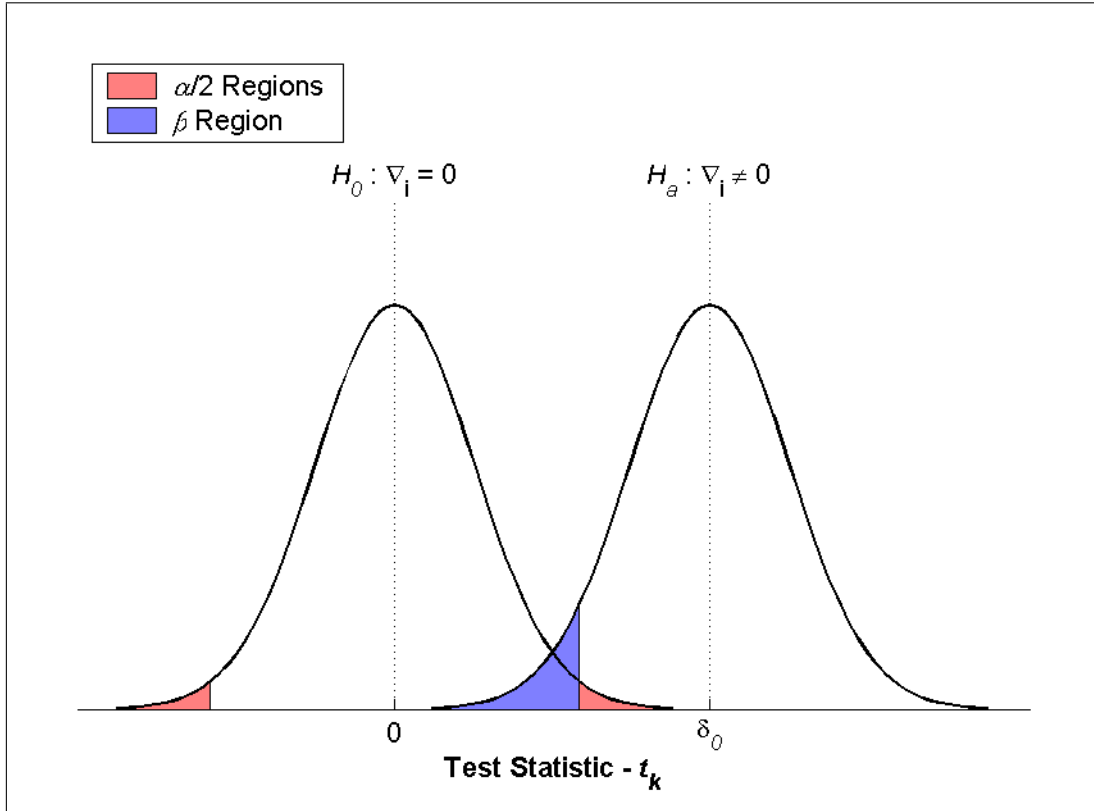
Figure 2.3: Relationship Between Type I and Type II Error Probabilities and the Non-Centrality Parameter

has occurred and the test statistic has failed, the non-centrality parameter can be computed based on the magnitude of the blunder (see Equation 2.41). However, if the problem is reversed and the non-centrality parameter is selected based on some predefined values for α and β, the magnitude of the blunder capable of being detected can be computed. Using this approach, the Minimum (or Marginal) Detectable Blunder (MDB) for the ith observation can be computed as

$$\nabla_{k_i}^{MDB} = \frac{\delta_0}{\sqrt{\left(C_{v_k}^{-1}\right)_{ii}}} \qquad (2.48)$$

Once the MDBs are computed, they should be quoted as "a blunder of magnitude ∇_i^{MDB} can be detected on the ith observation '$1 - \beta$' percent of the time, with

'$1-\alpha$' percent confidence". As a final note, some sample values of the non-centrality parameter are shown in Table 2.2. Since the non-centrality parameter is not unique, it is important that the corresponding α and β parameters are specified, and not just the non-centrality parameter itself.

External Reliability

Once the MDB for a particular observation is detected, its impact on the final estimate of the parameters can be determined. Specifically, since the blunder maps directly into the innovation sequence, its effect on the estimated parameters, $\Delta\hat{x}_k$, is readily seen from Equation 2.9 to be

$$\Delta\hat{x}_{k_i} = K_k m_{k_i} \nabla_{k_i}^{MDB} \tag{2.49}$$

This is termed the external reliability vector. Furthermore, because the MDB represents the smallest blunder that can be detected by the system, its impact on the estimated parameters is also the smallest effect that statistical testing can protect the system against (for the given α and β values). For this reason, the external reliability is called the protection level (PL). If only certain elements of the PL vector are of interest, they can be investigated individually.

Table 2.2: Some Non-Centrality Parameters (Ryan, 2002)

Type I Error (%)	Type II Error (%)	Non-Centrality
5.0	20.0	2.80
2.5	20.0	3.10
5.0	10.0	3.24
2.5	10.0	3.52
0.1	20.0	4.12
0.1	10.0	4.57
0.9	2.5	4.57

As a note, if a vector of MDBs of the form

$$\nabla_k = \begin{bmatrix} \nabla_{k_1}^{MDB} & \nabla_{k_2}^{MDB} & \nabla_{k_3}^{MDB} & \cdots \end{bmatrix}^T \tag{2.50}$$

is available, then the protection level vector can also be computed as

$$\Delta \hat{x}_{k_i} = K_k m_{k_i} m_{k_i}^T \nabla_k \tag{2.51}$$

To summarize, the overall procedure for computing the internal (MDB) and external (PL) reliability parameters for dynamic systems is as follows

1. Select the probability of committing a Type I and Type II error. Typical values in the literature are $\alpha = 0.1\%$ and $\beta = 10\%$ or 20% (Lu, 1991; Ryan, 2002).

2. Use Equation 2.47 to compute the non-centrality parameter, δ_0.

3. For each epoch compute the MDB for the ith observation using Equation 2.48.

4. For each MDB use Equation 2.49 or 2.51 to compute the protection level vector.

Statistical reliability is revisited again in Chapter 6. There, reliability is addressed in light of some of the practical considerations presented in the intermediate chapters.

Chapter 3

Systems Overview

As a precursor to a discussion of the integration of GPS and INS, this chapter reviews the relevant characteristics of each system. GPS is reviewed first with emphasis given to the differential error sources and their magnitudes as well as the ambiguity resolution process. Next, principles of inertial navigation systems are reviewed with focus given to the relevant equations. A brief discussion of the initial alignment procedure concludes the chapter.

3.1 Overview of the Global Positioning System

Developed by the United States Department of Defense, GPS was originally designed for metre-level positioning accuracies (Parkinson, 1996). However, several developments since it was first declared operational in 1993 (Leick, 1995), primarily by the civil community, have made centimetre-level positioning relatively common. This ability to provide a wide range of positioning accuracies under all weather conditions has resulted in GPS revolutionizing modern positioning and navigation.

3.1.1 GPS Signal Structure and Available Measurements

The GPS signal structure is complex and will not be reviewed in detail here. Instead, only the material relevant to this dissertation is provided. For more details on the signal structure, refer to Ward (1996), Spilker (1996) and Misra and Enge (2001).

The GPS signal is comprised of two frequencies, namely L1 (1575.42 MHz) and L2 (1227.60 MHz). Modulated on these carriers are the

- Pseudo-Random Noise (PRN) codes used for ranging measurements

- Navigation data to communicate the satellite's position, time, health, etc. to users in real-time (50 Hz modulation)

Currently, only two types of PRN codes are used, namely the Coarse/Acquisition code (C/A-code) on L1, and the Precise code (P-code) on L1 and L2. Exploiting the characteristics of the signal structure, the following three types of measurements can be obtained from most GPS receivers

- *Pseudorange (code) measurements.* These are derived from the PRN codes and are therefore classified according to code and frequency as L1-C/A, L1-P and L2-P.

- *Carrier phase (phase) measurements.* By measuring the phase of the incoming carrier (L1 and/or L2), the range to a satellite can be measured with an ambiguous number of cycles.

- *Doppler measurements.* The derivative of the carrier phase measurement is the Doppler shift caused by the relative receiver-satellite motion.

In terms of code measurements, the P-code theoretically provides better overall performance. Unfortunately, the P-code signal is currently encrypted in an attempt to limit its use to the military community (including the entire L2 signal). However, codeless and semi-codeless tracking techniques have been developed which allow the

civil community access to these signals (Lachapelle, 1997). Unfortunately, these techniques decrease the signal-to-noise ratio by 14 dB or more and therefore produce considerably noisier measurements than would otherwise be expected. This dissertation only deals with L1 C/A-code measurements, although it is noted that GPS receivers must still implement P-code tracking to obtain the L2 carrier phase measurements.

Linear combinations of the above measurements are also possible, although it is most common with the carrier phase. For example, a linear combination, $\phi_{m,n}$, of the L1 and L2 phase measurements can be formed, with a wavelength of $\lambda_{m,n}$, as

$$\phi_{m,n} = m\phi_1 + n\phi_2 \tag{3.1}$$

$$\lambda_{m,n} = \frac{\lambda_1\lambda_2}{m\lambda_2 + n\lambda_1} \tag{3.2}$$

where subscripts "1" and "2" refer to L1 and L2 respectively. Of particular interest to this dissertation is the widelane (WL) combination ($m = 1, n = -1$) with a wavelength of approximately 86 cm.

3.1.2 GPS Error Sources

Several error sources play a role in GPS applications. To eliminate or mitigate some of these sources of error, differential processing techniques are often implemented. In this approach, two receivers are used; one occupying a known location while the other is located on the vehicle to be positioned. If a measurement from receiver m to satellite a is denoted ℓ_m^a, then a double difference measurement is formed as

$$\nabla\Delta\ell_{m,n}^{a,b} = (\ell_m^a - \ell_n^a) - \left(\ell_m^b - \ell_n^b\right) \tag{3.3}$$

where $\nabla\Delta$ is the double difference operator. Unfortunately, this procedure does not eliminate all sources of error. To illustrate, the double difference measurement equations for code (p), phase (ϕ), and Doppler $(\dot{\phi})$ can be written (without subscripts or superscripts for clarity) as

$$\nabla\Delta p = \nabla\Delta\rho + \nabla\Delta d\rho + \nabla\Delta T + \nabla\Delta I + m_{\nabla\Delta p} + \epsilon_{\nabla\Delta p} \qquad (3.4)$$

$$\nabla\Delta\phi = \frac{1}{\lambda}\left(\nabla\Delta\rho + \nabla\Delta d\rho + \nabla\Delta T - \nabla\Delta I + \nabla\Delta N + m_{\nabla\Delta\phi} + \epsilon_{\nabla\Delta\phi}\right) \qquad (3.5)$$

$$\nabla\Delta\dot{\phi} = \frac{1}{\lambda}\left(\nabla\Delta\dot{\rho} + \nabla\Delta\dot{d\rho} + \nabla\Delta\dot{T} - \nabla\Delta\dot{I} + m_{\nabla\Delta\dot{\phi}} + \epsilon_{\nabla\Delta\dot{\phi}}\right) \qquad (3.6)$$

where a dot represents the time derivative of a quantity and

ρ is the geometric range between the receiver and the satellite,

$d\rho$ is the orbital error of the satellite,

T is the delay due to the troposphere,

I is the delay or advance due to the ionosphere,

m is the multipath error for the subscripted observation,

ϵ is the measurement noise for the subscripted observation,

λ is the wavelength of the carrier on which the measurement is made, and

N is the integer carrier phase ambiguity.

Each of these error sources is briefly discussed below but a more comprehensive overview is found in Raquet (1998) and Ryan (2002), with the latter investigating the undifferenced errors. Details on the troposphere, ionosphere and multipath errors are investigated in Zhang (1999), Skone (1998) and Ray (2000), respectively.

Orbital Errors

In order for the satellite positions to be broadcast in real-time to the user, they are predicted based on the previous motion of the satellites and knowledge of the Earth's gravity field. Given that a satellite's navigation data is updated a maximum of three times per day (Spilker and Parkinson, 1996), the accuracy of these predictions are limited. The magnitude of the errors are about 3.5 m (50th percentile) (Ryan, 2002) and vary slowly with time.

Troposphere

Tropospheric errors are caused by the slowing and bending of GPS signals by the neutral atmosphere. Errors due to the troposphere are about 2.4 m at the zenith and can increase by a factor of about ten for low elevation satellites (Leva et al., 1996). The error is typically broken down into a dry (hydrostatic) and wet part. The hydrostatic part comprises approximately 90% of the delay but can be predicted with an accuracy of about 1% at the zenith using meteorological data. In contrast, the wet term makes up the remaining 10% of the error and can only be predicted with about 10–20% accuracy (de Jong et al., 2002).

Ionosphere

The ionosphere delay or advance is due to the presence of free electrons in the upper atmosphere, typically between 70 and 1000 km above the Earth's surface (Leva et al., 1996). These free electrons in turn influence electromagnetic wave propagation. The presence of free electrons is closely related to the amount of solar radiation and so ionospheric effects show diurnal variations with maximum effects typically occurring at approximately 1400 local time.

The errors listed above are correlated between stations. It is for this reason that the double difference approach can mitigate their effect. However, the extent of this correlation is related to the separation of the two receivers used. Consequently, the above errors are typically quantified in terms of parts-per-million (ppm), where 1 ppm is equivalent to 1 mm of error per 1 km of receiver separation. With this in mind, Table 3.1 summarizes some typical and extreme error magnitudes for spatially correlated errors.

Table 3.1: Magnitudes of Spatially Correlated Double Difference Error Sources

	Error Magnitude	
Error	**Typical (RMS)**	**Extreme**
Orbital	0.1 ppm (Ryan, 2002)	N/A
Troposphere[1]	<1 ppm (Zhang, 1999)	1–3 ppm
Ionosphere	1–3 ppm[2] (Klobuchar et al., 1995; Fortes et al., 2000, 2001)	>10 ppm[3] (Lachapelle et al., 2000)

[1]After applying a tropospheric model.

[2]Effects vary with geographic location and the solar cycle.

[3]For Calgary region. Effects near the equator can be as large as 50 ppm (Wanninger, 1993).

Noise and Multipath

The multipath and noise terms have different effects depending on the observation under consideration. In order to assess their combined effect, a GPS data set was collected between two pillars on the roof of the Calgary Centre for Innovative Technology (CCIT) for just under six hours. NovAtel OEM4 GPS receivers were used with NovAtel 600 antennas. Using the known coordinates of the pillars, the double difference misclosures for each observable of interest was computed. Since the pil-

lars were located only a few metres apart, the only remaining errors are those from multipath and noise (Lachapelle, 1997).

The double difference misclosures were binned according to the lower elevation of the two satellites used in the double difference, in 2.5° increments, and the standard deviation for each bin was computed. The standard deviation for an undifferenced measurement on a high-elevation satellite, σ_{high}, was then computed as half of the standard deviation of the highest elevation bin. This was needed because high-elevation satellites show more uniform behaviour than do low-elevation satellites (see Figures 3.1, 3.2 and 3.3). The undifferenced standard deviations, σ_{ud}, for the other elevation bins were then computed as (Raquet, 1998)

$$\sigma_{ud} = \sqrt{\frac{\sigma_{\nabla\Delta}^2 - 2\sigma_{high}^2}{2}} \tag{3.7}$$

where $\sigma_{\nabla\Delta}^2$ is the variance of the computed double differences for a particular elevation bin. The results of this analysis for the L1 C/A code, L1 carrier phase and L1 Doppler observations are shown in Figures 3.1, 3.2 and 3.3, respectively. As can be seen, the effect of code noise and multipath is at the decimetre-level. However, caution must be exercised when interpreting these results. The multipath environment in which the data was collected was relatively benign in that only short multipath effects are seen. Under more adverse conditions however, the effect of multipath can reach several metres even with high-quality GPS receivers (Ray, 2000).

In contrast to the code observable, the effect of noise and multipath on the L1 carrier phase is at the millimetre-level. This represents one of the greatest advantages of the carrier phase measurement. Specifically, if the carrier phase ambiguities can be resolved as integers (see Section 3.1.3) then the carrier phase measurements act as code observations with considerably better precision. This in turn translates into
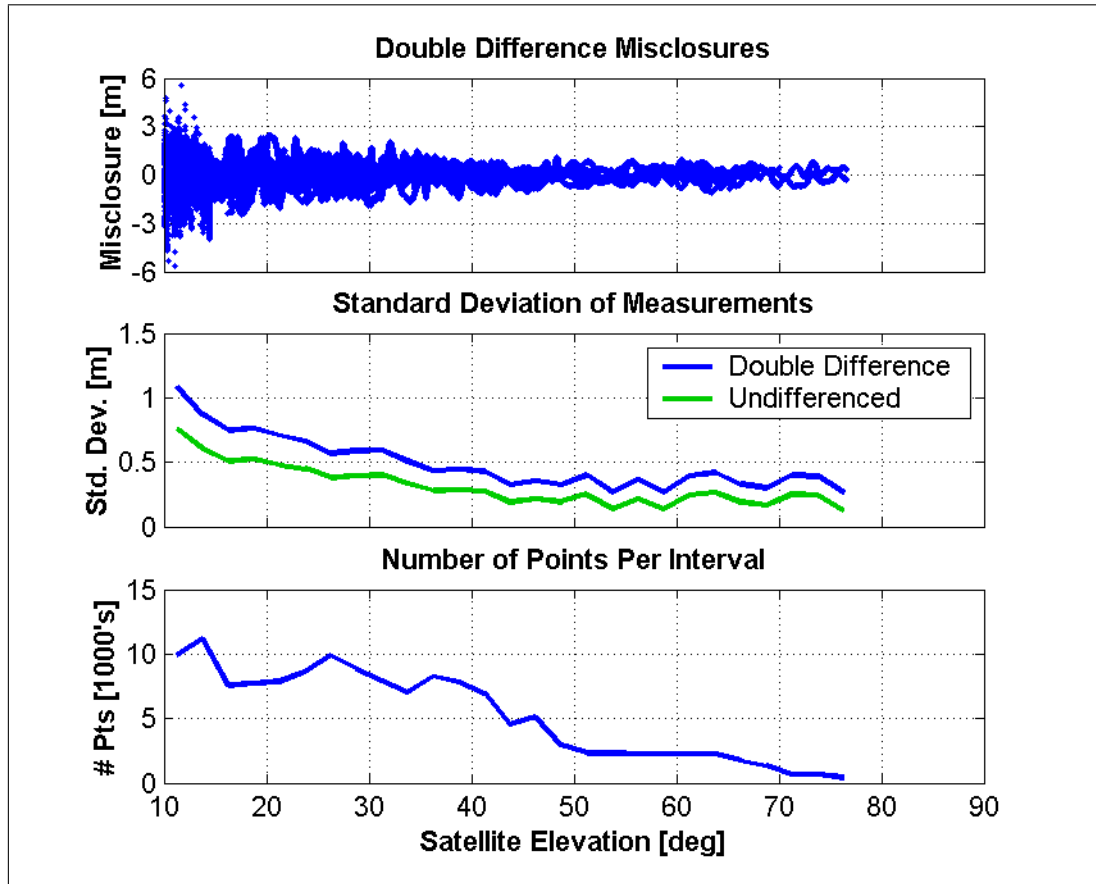
Figure 3.1: Combined Effect of Noise and Multipath for L1 C/A Code

much higher accuracy position estimates. Care must also be exercised in this case since the theoretically largest carrier phase multipath effect on a single measurement is one quarter of a wavelength (about 4.8 cm for L1) (Ray, 2000). Furthermore, because multipath is deterministic, its effect in a double difference can be up to four times its maximum value. Therefore, double difference multipath effects under adverse conditions can reach a magnitude of one full wavelength.

Finally, the results of the Doppler observations show cm/s-level accuracy. However, given that the data were collected in a static environment there are theoretically no multipath effects. Instead, Doppler multipath is a function of the receiver velocity
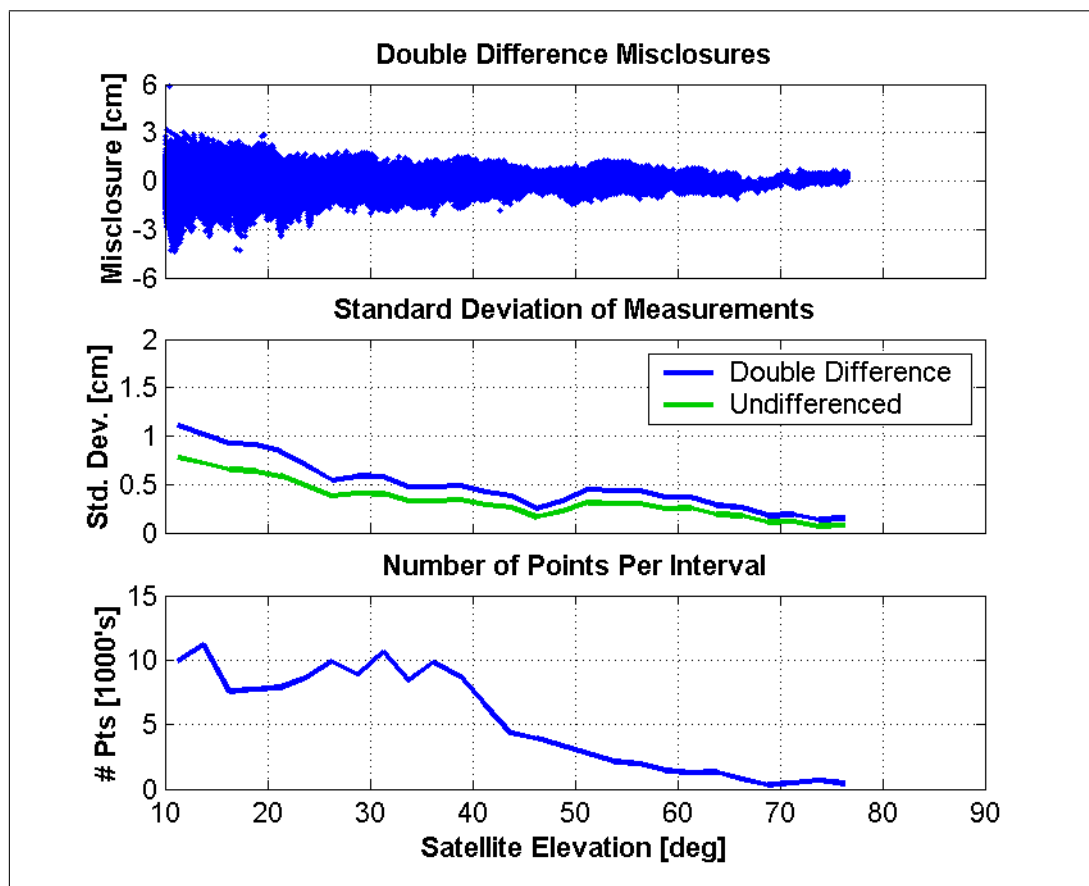
Figure 3.2: Combined Effect of Noise and Multipath for L1 Carrier Phase

and is therefore expected to be larger in kinematic environments.

The findings of this analysis were used for selecting appropriate measurement accuracies for the Kalman filter algorithm. To this end, it is noted that the measurement standard deviations show an increase with decreasing elevation angle. Although expected, this behaviour must be properly accounted for.
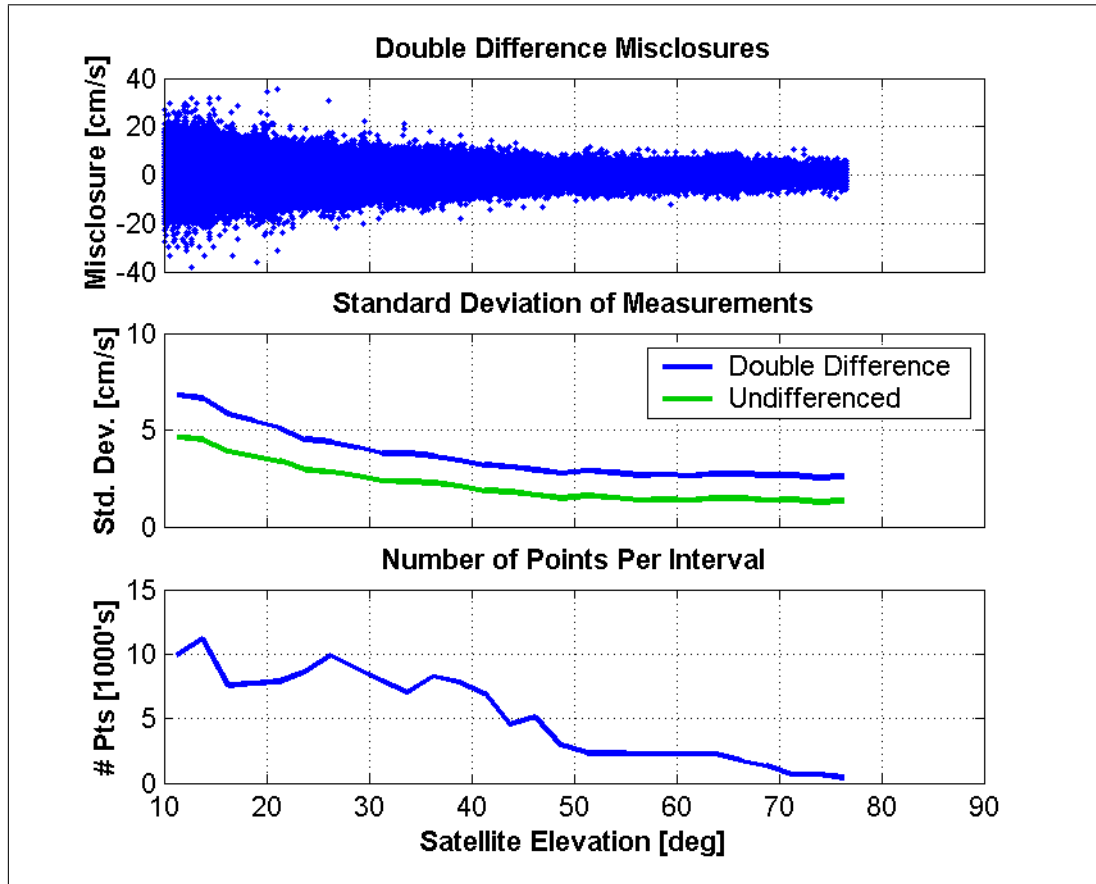
Figure 3.3: Combined Effect of Noise and Multipath for L1 Doppler

3.1.3 Ambiguity Resolution

As shown in the previous section, the carrier phase observable has significantly lower noise and multipath effects than does the code. It follows therefore, that its use in navigation systems is highly desirable. Unfortunately, exploiting the advantages of the carrier phase comes at the cost of having to resolve the ambiguities as integer values. This section very briefly reviews ambiguity resolution in general and its dependence on the above errors. An analysis of using external position estimates for improving the process is also presented.

Resolving the carrier phase ambiguities as integers has been a major focus of many research studies (e.g. Counselman and Gourevitch, 1981; Hatch, 1990; Chen, 1994; Teunissen and Tiberius, 1994). In particular, on-the-fly (OTF) techniques have received much attention because of their requirement in most operational conditions. Most approaches search a range of values for the best set of integers and select the optimal set based on some criteria. The search range (volume) is usually defined in the position or ambiguity domains. Position-domain searches are less common in the literature and are not discussed herein. Some examples of ambiguity-domain searches include the Fast Ambiguity Search Filter (FASF) (Chen, 1994) and Least-Squares Ambiguity Decorrelation Adjustment (LAMBDA) (Teunissen and Tiberius, 1994), to name a couple. The typical steps involved in ambiguity-domain techniques include estimation of the ambiguities as real-values, searching for the optimal ambiguity set, and validation of the selected set.

All ambiguity resolution approaches suffer from differential errors. The errors cause the real-valued estimate of the double difference ambiguity to differ from an integer number of cycles. The larger the errors, the more non-integer the estimate. Errors in the estimated receiver position can also cause a similar effect. Regardless of the source of error, the result is that identifying the correct ambiguity set becomes more difficult.

Effect of Differential Errors

In terms of ambiguity resolution, the magnitude of the differential errors in units of cycles is most important. In Table 3.2 the spatially correlated differential GPS error sources are shown in units of cycles, for L1 and widelane. The symbol f represents the frequency and λ_{WL} is the widelane wavelength. The ratio between L1 and WL

Table 3.2: GPS Error Sources in Units of Cycles For L1 and WL Carrier Phase (Raquet, 1998)

Error	L1 Error [cyc]	WL Error [cyc]	WL / L1 Ratio
Orbital	$\dfrac{\nabla\Delta d\rho}{\lambda_1}$	$\dfrac{\nabla\Delta d\rho}{\lambda_{WL}}$	$\dfrac{\lambda_1}{\lambda_{WL}} \approx 0.221$
Troposphere	$\dfrac{\nabla\Delta T}{\lambda_1}$	$\dfrac{\nabla\Delta T}{\lambda_{WL}}$	$\dfrac{\lambda_1}{\lambda_{WL}} \approx 0.221$
Ionosphere[1]	$\dfrac{1}{\lambda_1}\dfrac{\nabla\Delta Z}{f_1^2}$	$\dfrac{1}{\lambda_1}\dfrac{\nabla\Delta Z}{f_1^2}\dfrac{f_2 - f_1}{f_2}$	$\left|\dfrac{f_2 - f_1}{f_2}\right| \approx 0.283$

[1]Z is the Total Electron Content which is directly proportional to the ionospheric effect.

immediately shows the benefit of the widelane observable, namely it provides about a four-fold improvement in resistance to errors. For this reason, ambiguity resolution with widelane carrier phase measurements is considerably more robust than with L1. For perspective, the rule of thumb for resolving the ambiguities is to have a ranging accuracy of better than one half of a wavelength (de Jong et al., 2002). Therefore, given the relatively short wavelengths of interest here, a four-fold improvement is very significant.

Effect of External Positioning Information on Ambiguity Resolution

The precision of the estimated real-valued ambiguities, as reflected in their covariance matrix, is directly related to the volume of the search space in the ambiguity resolution process. The most common indicator of the search space volume is the

Ambiguity Dilution of Precision (ADOP) (Teunissen and Odijk, 1997) given by

$$ADOP = \sqrt{|C_{\hat{N}}|}^{\frac{1}{m}} \tag{3.8}$$

where $C_{\hat{N}}$ is the covariance matrix of the estimated ambiguities and m is the number of double difference ambiguities being estimated. With this in mind, the objective here is to evaluate the covariance matrix of the ambiguities as a function of the covariance matrix of an external position update. In Škaloud (1998), a closed form of the ambiguity covariance matrix using code, phase and an external position update is derived. Scherzinger (2002b) also showed a similar relationship. Instead of reproducing the details of these works, a slightly more heuristic explanation is given herein. First, it is noted that both of the above references assumed the GPS ambiguities were reset after a GPS data outage. The system was then updated using code, carrier phase and external position information. Here, the updating process is broken into two steps. First, it is assumed that the GPS observations are processed followed by an update from an external position observation. As shown in Appendix A, the results of this two-step approach will be mathematically identical to those of the one-step approach. With this in mind, after the GPS measurements are processed the estimated position and ambiguity states will be correlated with each other. This can be represented mathematically as

$$C_{\hat{x}} = \begin{bmatrix} C_{\hat{r}} & C_{\hat{r},\hat{N}} \\ C_{\hat{N},\hat{r}} & C_{\hat{N}} \end{bmatrix} \tag{3.9}$$

where

$C_{\hat{x}}$ is the covariance matrix of the entire system, assumed to be composed of position and ambiguity states only,

r represents the position states in the filter,

N represents the ambiguity states in the filter, and

$C_{\hat{a},\hat{b}}$ is the covariance matrix between $\hat{a}$ and $\hat{b}$.

The addition of a direct position measurement would then take the form

$$z_r = \underbrace{\begin{bmatrix} I & 0 \end{bmatrix}}_{H} \underbrace{\begin{bmatrix} r \\ N \end{bmatrix}}_{x} + v \tag{3.10}$$

where the first hyper-matrix on the right-hand side acts as the design matrix. Using this design matrix along with Equations 3.9, 2.10 and 2.11, the updated covariance matrices for the position and ambiguity states can be shown to be

$$C_{\hat{r}}^{+} = C_{\hat{r}}^{-} - C_{\hat{r}}^{-}(C_{\hat{r}}^{-} + C_z)^{-1}C_{\hat{r}}^{-} \tag{3.11}$$

$$C_{\hat{N}}^{+} = C_{\hat{N}}^{-} - C_{\hat{N},\hat{r}}^{-}(C_{\hat{r}}^{-} + C_z)^{-1}C_{\hat{r},\hat{N}}^{-} \tag{3.12}$$

From these equations, two conclusions can be drawn. First, the covariance matrix of the position states is directly reduced. This makes sense given the nature of the observation. Second, and more important for the discussion at hand, is that the covariance matrix of the ambiguities is also reduced indirectly through its correlation with the position states. Furthermore, the extent of this improvement depends on two factors, namely

1. The correlation between the position and ambiguity states. This is a function of the satellite geometry after a GPS data outage and is beyond the user's control.

2. The accuracy of the position update used, with more accurate positions providing greater improvement in the ambiguity covariance matrix. Therefore, if the user is capable of obtaining an independent estimate of the position, from an INS for example, then it can be used to reduce the ambiguity search space.

3.2 Overview of Inertial Navigation Systems

In many respects, an Inertial Navigation System (INS) is the perfect complement to GPS. Orthogonally mounted accelerometers and angular rate sensors (gyros) comprise the Inertial Measurement Unit (IMU) which, when combined with the mechanization equations (and system error estimation), comprises the INS itself. This section begins with a review of the coordinate frames used herein and then briefly presents the equations of motion and mechanization equations. The equations are then perturbed to define the INS error equations. Finally, a discussion of the initial alignment process is presented.

3.2.1 Coordinate Frames

Three coordinate frames are used in this dissertation. The discussion of each follows from Schwarz and Wei (1999) and Jekeli (2000).

Inertial Frame (i-frame)

An inertial frame is considered to be non-rotating and non-accelerating relative to far-off galaxies (Schwarz, 1996). Operationally, an inertial frame is realized if the above conditions are met to better than the accuracy of the measurements used to

define the frame in the first place. With this in mind the definition of the i-frame is as follows

Origin : Earth's centre of mass

Z-Axis : Parallel to the Earth's instantaneous spin axis

X-Axis : Pointing towards the mean equinoctial colure in the equatorial plane

Y-Axis : Orthogonal to the X and Z axes to complete a right-handed frame

Earth Centred Earth Fixed Frame (ECEF or e-frame)

The Earth-fixed frame used herein is defined as follows

Origin : Earth's centre of mass

Z-Axis : Parallel to the Earth's mean spin axis

X-Axis : Pointing towards the mean meridian of Greenwich

Y-Axis : Orthogonal to the X and Z axes to complete a right-handed frame

Body Frame (b-frame)

The body frame represents the orientation of the IMU axes. In stabilized platform systems, the IMU can be kept aligned to a particular navigation frame of interest (e.g. the ECEF frame) using external torques derived from the measured angular rates (Jekeli, 2000). However, in a strapdown inertial system such as is used herein, the IMU is rigidly mounted to the vehicle to be positioned and thus can have arbitrary orientation. For convenience, the body frame is assumed to be aligned with the frame of the vehicle with the following convention

Origin : Centre of IMU

X-Axis : Pointing towards the right of the vehicle

Y-Axis : Pointing towards the front of the vehicle

Z-Axis : Orthogonal to the X and Y axes to complete a right-handed frame

3.2.2 Equations of Motion and Mechanization Equations

The mechanization equations are the set of equations used to convert the output of the IMU into useful position, velocity and attitude information. To this end, the output of an IMU can be defined as vectors of rotation rates, ω, and specific force measurements, f. The specific force measurements are related to the total vehicle acceleration, a, via the gravitational acceleration, $\tilde{g}$, as follows

$$f = a - \tilde{g} \tag{3.13}$$

Therefore the raw IMU measurements must be corrected for the gravitational acceleration before the vehicle's actual acceleration can be obtained.

Once the angular rates and accelerations are obtained, inertial navigation can be performed in two basic steps. First, assuming the IMU's initial orientation is known relative to some navigation frame of interest, the angular rates are integrated to obtain the new orientation of the IMU. Second, this new orientation information is used to rotate the accelerations into the navigation frame where they are twice integrated to obtain velocity and position increments. While this is an oversimplified description, it serves to illustrate the general principle of inertial navigation.

Notation

In an effort to clarify the following discussion, the majority of notation used in this section can be summarized as

- A rotation rate vector ω_{bc}^a represents the rotation rate of frame 'c', relative to frame 'b', expressed in frame 'a'.

- A rotation matrix of the form R_b^a transforms a vector from frame 'b' to 'a'.

- A vector denoted x^a represents a quantity, x, in frame 'a'.

Equations of Motion

The equations of motion mathematically describe the motion of the vehicle to be positioned. They can be written in the e-frame as (Schwarz and Wei, 1999)

$$
\begin{bmatrix} \dot{r}^e \\ \dot{v}^e \\ \dot{R}_b^e \end{bmatrix} = \begin{bmatrix} v^e \\ R_b^e f^b - 2\Omega_{ie}^e v^e + \tilde{g}^e - \Omega_{ie}^e \Omega_{ie}^e r^e \\ R_b^e \left(\Omega_{ei}^b + \Omega_{ib}^b \right) \end{bmatrix} \tag{3.14}
$$

where a dot represents a time derivative and

r is the position vector,

v is the velocity vector, and

Ω is the skew-symmetric form of the rotation rate vector ω.

However, exploiting the fact that the combination of the last two terms in the second

equation is the gravity vector, g^e, the above equation can be simplified to

$$
\begin{bmatrix} \dot{r}^e \\ \dot{v}^e \\ \dot{R}_b^e \end{bmatrix} = \begin{bmatrix} v^e \\ R_b^e f^b - 2\Omega_{ie}^e v^e + g^e \\ R_b^e \left(\Omega_{ei}^b + \Omega_{ib}^b \right) \end{bmatrix}
\tag{3.15}
$$

As can be seen, the specific force, f^b, and angular rate measurements, ω_{ib}^b, measured by the IMU act as input to the system.

Mechanization Equations

The mechanization equations are used to solve the equations of motion in order to obtain the necessary position, velocity and attitude increments. These, combined with the initial conditions of the system, provide the information needed for navigation. The mechanization equations consist of four basic steps

1. Correction of raw data for known or estimated errors

2. Attitude update

3. Transformation of specific force to navigation frame of interest

4. Calculation of velocity and position

It is noted that instead of the measured rates, most IMUs will actually output velocity and angular increments (Δv and $\Delta \theta$, respectively) over the interval t_k to t_{k+1}. While this does not affect the validity of the above equations, it will be assumed in the following, which is taken mostly from Schwarz and Wei (1999).

Correction of Raw Data

The errors for which the raw data are corrected typically include biases, scale factor errors and axis non-orthogonalities. These values can be obtained from laboratory or field calibrations, or can be estimated during the navigation process as shown in Chapter 4.

Attitude Update

The total angular increment of the vehicle is the combination of the vehicle's and the navigation frame's rotation relative to inertial space, as shown in the last row of Equation 3.15. While the former is obtained from the IMU directly, the latter is obtained using the known rotation rate vector, ω_e (i.e. Earth rotation rate). The final result is

$$\Delta\theta_{eb}^b = \Delta\theta_{ib}^b - R_e^b \omega_e \Delta t \tag{3.16}$$

where $\Delta t = t_k - t_{k+1}$. The updated rotation matrix can then be obtained to first order approximation as

$$R_b^e(t_{k+1}) = R_b^e(t_k)\left(I + S^b\right) \tag{3.17}$$

where S^b is the skew-symmetric form of the angular increment vector in Equation 3.16. Practically, the approach shown above is rarely used. Instead, the orientation is often parameterized in terms of quaternions because of their robustness against singularities and their computational efficiency (Schwarz and Wei, 1999; Jekeli, 2000). The quaternion can also be uniquely converted into a rotation matrix as necessary for the following development.

Once the updated rotation matrix is obtained, the rotation matrix from the body frame to the local level (l) frame (i.e. the frame centered at the user, with the Y-axis

pointing north, Z-axis pointing up and X-axis completing a right-handed frame) is computed as

$$R_b^l = R_1(90° - \phi)R_3(\lambda + 90°)R_b^e \qquad (3.18)$$

where

ϕ is the latitude of the IMU,

λ is the longitude of the IMU, and

R_i is the rotation matrix about the ith axis.

From this matrix, the attitude parameters can be computed using

$$\xi = -\tan^{-1}\left(\frac{(R_b^l)_{3,1}}{(R_b^l)_{3,3}}\right) \qquad (3.19)$$

$$\eta = -\sin^{-1}\left((R_b^l)_{3,2}\right) \qquad (3.20)$$

$$\psi = \tan^{-1}\left(\frac{(R_b^l)_{1,2}}{(R_b^l)_{2,2}}\right) \qquad (3.21)$$

where

ξ is the roll of the vehicle,

η is the pitch of the vehicle,

ψ is the azimuth of the vehicle, and

$(R_b^l)_{a,b}$ is the element at the ath row and b^{th} column of the R_b^l matrix.

Although the R_b^l matrix is itself unique, practically it is computed assuming a particular order of rotations. The order in which the rotations are assumed to have

occurred will impact the computation of the attitude parameters in Equations 3.19 to 3.21. With this is mind, the rotation matrix is herein assumed to be constructed as follows

$$R_b^l = R_3(\psi) R_1(-\eta) R_2(-\xi) \tag{3.22}$$

Transformation of Specific Force to the Navigation Frame

Before correction and integration, the measured specific force measurements must be rotated from the body frame to the ECEF frame. Instead of using the rotation matrix computed above, the average orientation of the IMU during the interval t_k to t_{k+1} is preferred. With this in mind, the velocity increment in the e-frame is computed using either of the following two equations

$$\Delta v_f^e = R_b^e(t_k) \left(I + \frac{1}{2} S^b \right) \Delta v_f^b \tag{3.23}$$

$$\Delta v_f^e = R_b^e(t_{k+1}) \left(I - \frac{1}{2} S^b \right) \Delta v_f^b \tag{3.24}$$

where the f subscript implies that the velocity increments are due only to the measured specific force.

Calculation of Velocity and Position

The final velocity increment in the e-frame is given by

$$\Delta v^e = \Delta v_f^e - 2\Omega_{ie}^e v^e + \gamma^e \tag{3.25}$$

where γ is the normal gravity, computed using the parameters of a given reference frame. An efficient method of computing this value in the e-frame is given in Schwarz and Wei (1990) or Wei and Schwarz (1990a). The second term in the above equation

is the Coriolis term and is computed using the previous epoch's velocity. Once the velocity increment is computed, the updated velocity is given by

$$v^e\left(t_{k+1}\right) = v^e\left(t_k\right) + \Delta v^e \tag{3.26}$$

Finally, using trapezoidal integration, the position can be incremented as

$$r^e\left(t_{k+1}\right) = r^e\left(t_k\right) + \left(v^e\left(t_k\right) + v^e\left(t_{k+1}\right)\right)\frac{\Delta t}{2} \tag{3.27}$$

3.2.3 INS Error Equations

The mechanization equations discussed in the previous section provide no information about the errors of the system. Instead, they blindly process data received from the IMU to obtain updated navigation parameters without regard to the veracity of these parameters. In practice, it is often required to estimate the system errors in order to improve performance to a satisfactory level. This is commonly done using a Kalman filter. However, given the non-linear nature of the system shown in Equation 3.15, the system must first be perturbed.

Given the complexity of the system at hand, the full derivation of the perturbed system is not shown here. Instead, readers are referred to Schwarz and Wei (1999) or Jekeli (2000) for details. Following steps outlined in ibid., the results of the perturbed system can be expressed as

$$\begin{bmatrix} \delta\dot{r}^e \\ \delta\dot{v}^e \\ \dot{\varepsilon}^e \end{bmatrix} = \begin{bmatrix} \delta v^e \\ -F^e\varepsilon^e + N^e\delta r^e - 2\Omega_{ie}^e\delta v^e \\ -\Omega_{ie}^e\varepsilon^e \end{bmatrix} + \begin{bmatrix} 0 \\ R_b^e\delta f^b \\ R_b^e\delta\omega_{ib}^b \end{bmatrix} \tag{3.28}$$

where a δ in front of a parameter indicates a perturbed quantity and

F is the skew-symmetric matrix of specific force measurements,

ε is a vector of misalignment angles along each axis,

N is the tensor of gravity gradients,

δf^b is the vector of errors in the measured specific force vector, and

$\delta \omega_{ib}^b$ is the vector of errors in the measured angular rates.

3.2.4 Initial Alignment

One of the underlying assumptions used in the presentation of the mechanization equations was that the initial condition of the system was already known. While position and velocity are usually easily input by the user, the initial orientation of the system is not so readily available. For this reason, the INS usually has to execute an initial alignment procedure. Typically, this is performed in two steps; a coarse alignment step and a fine alignment step.

Coarse Alignment

Two known quantities, namely the Earth's rotation rate and gravity vector, are used to provide the initial alignment of the INS. Specifically, under static conditions (i.e. no external acceleration) the gravity vector is used to compute the roll and pitch as

$$\xi \;=\; -\sin^{-1}\left(\frac{\overline{\Delta v_x^b}}{\gamma\,\Delta t_{IMU}}\right) \tag{3.29}$$

$$\eta \;=\; \sin^{-1}\left(\frac{\overline{\Delta v_y^b}}{\gamma\,\Delta t_{IMU}}\right) \tag{3.30}$$

where a bar above a quantity represents a time average, the subscripts represent the axis of interest, and Δt_{IMU} is the data interval of the IMU. The time interval used

for averaging is selected based on the noise of the sensor. For the IMU used for this research, the averaging time used was 90 s. Using a longer interval provided no significant improvement. Using the above quantities, the averaged angular increments can be rotated into a horizontal frame (h-frame) as follows

$$\overline{\Delta\theta_{ib}^h} = R_1(-\eta)R_2(-\xi)\overline{\Delta\theta_{ib}^b} \tag{3.31}$$

The approximate azimuth of the system can then be obtained as

$$\psi = -tan^{-1}\left(\frac{\left(\overline{\Delta\theta_{ib}^h}\right)_x}{\left(\overline{\Delta\theta_{ib}^h}\right)_y}\right) \tag{3.32}$$

Finally, with the roll, pitch and azimuth computed, the rotation matrix from the b-frame to the e-frame is computed as

$$R_b^e = R_3\left(-90° - \lambda\right) R_1\left(\phi - 90°\right) R_3\left(\psi\right) R_1\left(-\eta\right) R_2\left(-\xi\right) \tag{3.33}$$

where ϕ and λ are the latitude and longitude of the IMU respectively.

Fine Alignment

The fine alignment process is used to refine the initial alignment estimates obtained in the coarse alignment process. Also, some sensor errors can be observed so as to improve upon previous calibration values. The process is based on updates of an extended Kalman filter estimating the error states of the system. Equation 3.28 shows the basic system model, with more details given in Chapter 4.

Of all observations typically used for the fine alignment process, zero velocity updates (ZUPTs) are perhaps the most popular and were used herein. A coordinate update was performed upon terminating the fine alignment process. Other possible

observations include the horizontal accelerations (which should be zero if the vehicle is stationary) or an external azimuth reference (Jekeli, 2000).

3.2.5   IMU Quality

The quality of an IMU is typically quoted based on the system's nominal gyro biases. The motivation for this is two-fold (Scherzinger, 2002a). First, the performance of all IMU components will be selected to be commensurate with each other. In other words, all of the system components will contribute in a similar manner to the overall error budget. Second, the gyro biases are the primary factors in the free-inertial position performance. To this end, there are three grades of IMUs, namely navigation-grade, tactical-grade and automotive-grade. A very general comparison of these was given in Table 1.1.

Previous studies have shown that automotive-grade IMUs will be of little benefit to high-accuracy navigation (refer to Section 1.2 for details). Since this dissertation aims at replacing navigation-grade units with tactical-grade units for high-accuracy applications, Table 3.3 compares the specifications for the Honeywell HG1700 AG11 unit used in this dissertation with those of two navigation-grade units. Specifications for the HG1700 unit were obtained from Honeywell (1997), while those of the other two systems were obtained from Mohamed (1999).

As can be seen, the accuracy of the HG1700 is significantly poorer than the two navigation-grade units. Specifically, the accelerometer and gyro biases are up to four and 333 times larger respectively. Large differences in the scale factors and misalignments are also seen. Given these differences, this dissertation aims at characterizing the benefits and limitations of tactical-grade systems for high-accuracy navigation.

Table 3.3: Comparison of Tactical-Grade and Navigation-Grade IMU Specifications

Quantity	Inertial Measurement Unit		
	Honeywell HG1700 AG11	Litton LTN90-100	Honeywell LRF-III
Grade	Tactical	Navigation	Navigation
Accelerometer Errors			
Bias (1σ)	1 milli-G	0.5 milli-G	0.25 milli-G
Scale Factor (1σ)	300 ppm	50 ppm	50 ppm
Misalignment (1σ)	500 μrad	24 μrad	24 μrad
Gyro Errors			
Bias (1σ)	1 deg/h	0.01 deg/h	0.003 deg/h
Scale Factor (1σ)	150 ppm	5 ppm	1 ppm
Misalignment (1σ)	500 μrad	10 μrad	10 μrad

Chapter 4

GPS/INS Integration

Having reviewed the major aspects of GPS and INS in the previous chapter, focus can now be directed to integrating the two systems. To begin, a review of the most common GPS/INS integration strategies is presented with more detail given to those strategies used in later chapters. The details of each Kalman filter used in the various approaches are then presented separately, with attention given to model selection and parameterization. Finally, the required accuracy for the lever-arm between the GPS antenna and the IMU is discussed.

It is noted at the outset that throughout this chapter, real-time processing is assumed. Post-mission processing strategies such as backwards processing, optimal smoothing, and error interpolation between updates (e.g. as in Nassar and Schwarz, 2001) are not discussed here. However, given the potential advantages of these approaches for post-mission applications, they are certainly worth investigating in other contexts.

4.1   GPS/INS Integration Strategies

In general, there are several strategies used for integrating GPS and INS data into a common system. Most differ by the type of information that is shared between individual units. The following four approaches are the most common (Jekeli, 2000; Scherzinger, 2000)

- Uncoupled Integration

- Loose Integration

- Tight Integration

- Deep / Ultra-Tight Integration

In the uncoupled integration, the fact that GPS solutions are typically of high-accuracy is exploited. In this way, if GPS data is available it is used to compute the system output. The GPS data is also used to reset the INS errors to zero, but does nothing to affect the rate of their increase. Consequently, when the INS output is used in the absence of GPS, the accuracy of the system declines very rapidly. For this reason, this approach is not well suited to high-accuracy navigation. For details, see Jekeli (2000).

In contrast, deep integration is very well suited to the problem at hand. In this setup the GPS receiver and INS no longer work as independent systems. Instead, the GPS updates are used to calibrate the INS, while the INS is used to aid the GPS receiver tracking loops during interference or otherwise degraded signal conditions (Sennott and Senffner, 1997). Unfortunately, this approach requires access to a receiver's firmware, or at least the tracking loop information. As such, this strategy is typically only implemented by equipment manufacturers, and is thus not used herein.

The loose and tight integration strategies are the most common in the literature. In both cases, the GPS receiver and IMU operate as separate systems, and differ only in the type of information shared between them. Each approach is described

in detail in the following sections. For convenience, the terms "loosely coupled" and "tightly coupled" will also be used to refer to each strategy.

4.1.1 Loose Integration

In the loose integration strategy, position and velocity are used as observations to an INS-only filter. The position and velocity estimates are obtained either from an external source such as a GPS receiver, or are computed internal to the integrated navigation software. In this way, the integration approach uses a cascading scheme where the raw GPS measurements (code, Doppler and phase) are first processed in a GPS-only filter before being passed along to aid the INS. It is important that the full covariance matrix of the estimated states from the GPS-only filter be passed to the INS-only filter. Failure to do so will corrupt the system statistics and thus its performance. The loose integration concept is illustrated in Figure 4.1.

The advantage of the loose integration strategy is that the dimension of the state vectors (in the GPS-only and INS-only filters) are generally of smaller dimension than in the tight integration case (see Section 4.1.2). This translates into faster processing times. A second advantage is that since the position and velocity information used to update the INS-only filter could be obtained from external sources, the software development and required number of computations could be further reduced.

The disadvantage of the loose integration strategy is that the GPS-only filter essentially operates independent of the rest of the system. While this poses no considerable problem under ideal conditions, if a full filter reset (due to loss of lock, for example) is required, the GPS-only filter is subject to the same shortcomings as a GPS-only system. To help circumvent this problem, Figure 4.1 shows a dashed line from the
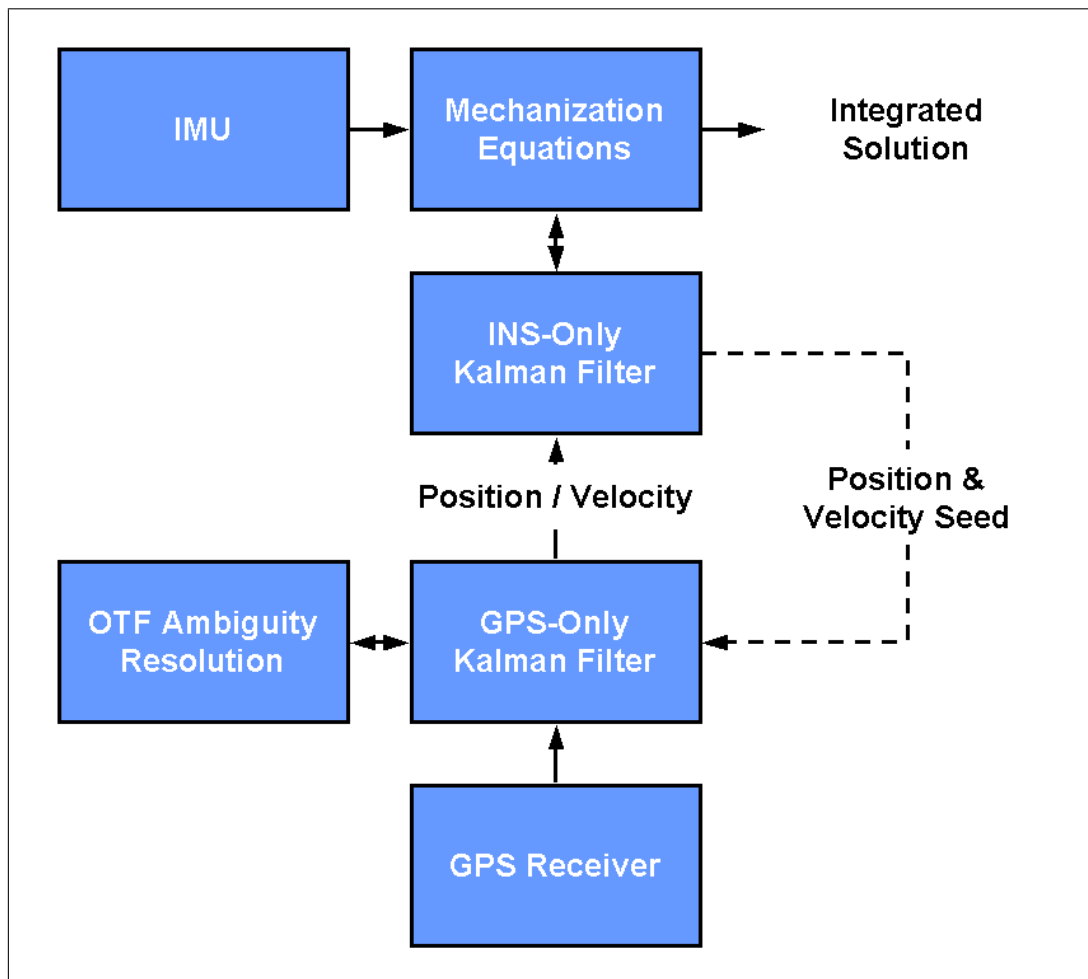
Figure 4.1: GPS/INS Information Flow Diagram for Loose Integration Strategy

INS-only filter to the GPS-only filter. When a full GPS reset is required, the inertial position and velocity (along with the full covariance matrix) can be used to initialize, or seed, the GPS-only filter. In so doing, the GPS-only filter can benefit from the additional information provided by the INS. For clarity, the use of seeding will always be stated explicitly, as in "seeding the GPS filter" or "loose integration with INS seeding". This is done to avoid confusion with the more basic "loose integration" or "loosely coupled" terms in which seeding is not used.

Although listed as an advantage above, having two independent Kalman filters can also be a slight disadvantage. The reason is that process noise must be added to both the GPS-only and INS-only filters (compared to just the GPS/INS filter in the tight integration approach, as discussed below). The "extra" process noise in the GPS-only filter is required to accommodate uncertainties in that filter's dynamic model. However, recall that the Kalman gain matrix ultimately determines how much new information is accepted from new measurements, and thus acts as a "filter" for the observation data. Furthermore, the extent of filtering is a function of the NSR, as shown in Equation 2.13. It follows therefore, that if the process noise increases, the NSR will decrease thus limiting the filtering capability of the system. Ultimately, this will impact system performance.

4.1.2 Tight Integration

Using a tightly coupled integration, the raw GPS observations are passed directly to a combined GPS/INS Kalman filter. The information flow diagram for this approach is shown in Figure 4.2. The grey box and lines in the figure correspond to the loose integration strategy and are included for comparison purposes only. There is no GPS filter in the tightly coupled case.

Having only a single filter means that it must estimate all the states for both the GPS and INS systems. However, this has several advantages. First, it provides a statistically rigourous sharing of information among states (to the extent that the input statistics are correct). Second, because process noise is only added to a single filter, the filtering of the GPS measurements is improved. In fact, as shown in Section 4.2, the reduction in the amount of process noise added relative to the loose
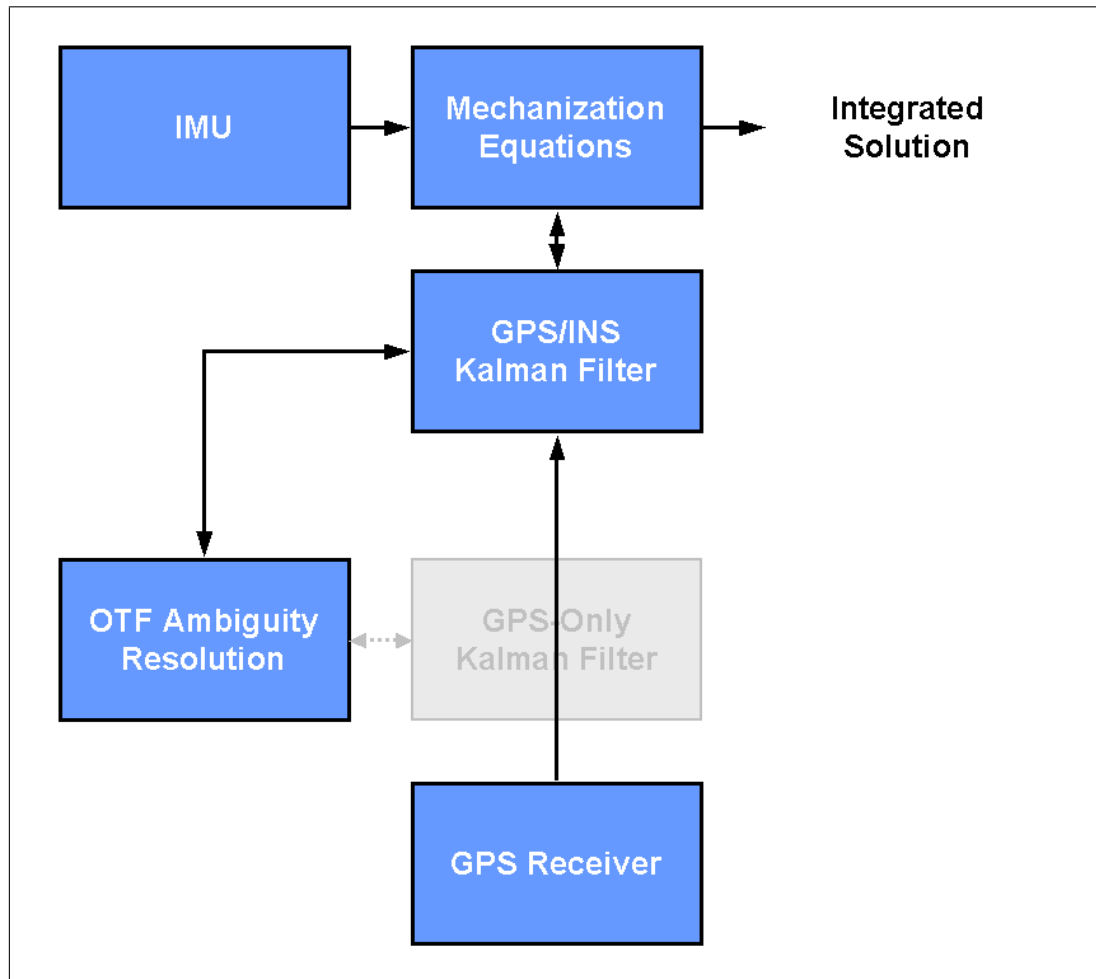
Figure 4.2: GPS/INS Information Flow Diagram for Tight Integration Strategy

integration approach is significant. Finally, having to program only a single Kalman filter can simplify software development and debugging.

The major disadvantage of the tightly coupled versus loosely coupled approach is the increased size of the state vector (in general), which leads to increased computational loads. However, as will be shown in Section 4.2.3, when the GPS ambiguities are fixed, the GPS/INS filter actually reduces to that of the INS-only filter in the loosely coupled case. As a result, the computational burden is actually significantly reduced.

4.2   Details of Specific Kalman Filters

The previous section showed that depending on the integration strategy, either a GPS-only and INS-only filter, or a GPS/INS filter, is required. The following sections outline the details of these individual filters. The system models used as well as the spectral densities are given.

4.2.1   GPS-Only Filter

The GPS-only filter used in the loosely coupled approach can theoretically estimate any state observable using GPS data. Typically, this will include position, velocity and possibly acceleration errors, but may include attitude parameters if multiple receivers are available. To this end, Schwarz et al. (1989) investigated constant velocity and constant acceleration models in kinematic processing. With limited satellite coverage, no significant position differences were obtained while a slight improvement was seen with the constant acceleration model in terms of velocity. For both models, the highest time-derivative states being estimated (i.e. velocity or acceleration) were modeled as a first-order Gauss-Markov processes with a time constant on the order of 10–30 s.

In lieu of the above, the GPS-only filter used in this research estimates position and velocity errors with the latter being modeled as random walk processes. Real-valued double difference ambiguity states are also estimated as needed. Once ambiguities are fixed to integers they are removed from the Kalman filter and are assumed known. The position and velocity states are parameterized in the ECEF-frame and are transformed into the local level frame when necessary. The state vector and

system model can therefore be represented as

$$
x_{GPS}^T = \left[\overbrace{\begin{array}{ccc} \delta r_x^e & \delta r_y^e & \delta r_z^e \end{array}}^{\delta r^{eT}} \quad \overbrace{\begin{array}{ccc} \delta v_x^e & \delta v_y^e & \delta v_z^e \end{array}}^{\delta v^{eT}} \quad \overbrace{\begin{array}{ccc} \delta N_1 & \cdots & \delta N_m \end{array}}^{\delta N^T} \right] \tag{4.1}
$$

$$
\begin{bmatrix} \delta \dot{r}^e \\ \delta \dot{v}^e \\ \delta \dot{N} \end{bmatrix} = \begin{bmatrix} 0 & I & 0 \\ 0 & 0 & 0 \\ 0 & 0 & 0 \end{bmatrix} \begin{bmatrix} \delta r^e \\ \delta v^e \\ \delta N \end{bmatrix} + \begin{bmatrix} 0 \\ w_{GPS} \\ 0 \end{bmatrix} \tag{4.2}
$$

where δN is the vector of double difference ambiguity errors.

The spectral densities for the velocity error states, w_{GPS}, were initially computed using kinematic GPS data collected in open-sky conditions. The time-difference of the estimated velocity states (basically the acceleration) was then used as an indication of the error in the constant velocity model. Taking the standard deviation of the time series of velocity differences gave an initial estimate for the spectral densities. However, since most of the trajectory consisted of approximately constant velocity, this estimate is perhaps conservative. It was therefore decided to raise the spectral densities from the computed values to avoid over-smoothing during periods of higher dynamics. The spectral densities computed from the data as well as the final values are shown in Table 4.1.

Table 4.1: Spectral Densities for Velocity States in GPS-Only Filter

| Axis | Velocity Spectral Density $[\mathrm{m/s^2}/\sqrt{\mathrm{Hz}}]$ | |
	Computed From Data	Final
X	0.63	1.00
Y	0.55	1.00
Z	0.42	1.00

4.2.2   INS-Only Filter

The basis for the INS-only filter was outlined in Section 3.2.3 where the INS error equations were shown. These are reproduced here for convenience.

$$
\begin{bmatrix} \delta \dot{r}^e \\ \delta \dot{v}^e \\ \dot{\varepsilon}^e \end{bmatrix} = \begin{bmatrix} \delta v^e \\ -F^e \varepsilon^e + N^e \delta r^e - 2\Omega_{ie}^e \delta v^e \\ -\Omega_{ie}^e \varepsilon^e \end{bmatrix} + \begin{bmatrix} 0 \\ R_b^e \delta f^b \\ R_b^e \delta \omega_{ib}^b \end{bmatrix} \tag{4.3}
$$

Theoretically, the above equations could be used as is to model the inertial errors. The reason this is not normally done lies with the forcing functions (i.e. the second term on the right-hand side). Specifically, δf^b and $\delta \omega_{ib}^b$ represent the errors in the IMU measurements. In order for the above system of equations to fit the system model used to derive the Kalman filter algorithms (Equation 2.8), these two terms must be zero-mean white noise sequences with Gaussian distributions (the rotation matrices can be considered shaping matrices). Unfortunately, due to systematic errors in the inertial sensors, none of these conditions are met. The sensor error models must therefore be refined accordingly.

A theoretically rigourous model for a resonating beam accelerometer, similar to the kind used herein, is given as (Jekeli, 2000)

$$
\delta f^b = b + c_T \delta T + \sum_{i=1}^{2} c_i a_i + \sum_{i=1}^{3} m_i a_i + sa + w_f \tag{4.4}
$$

where

b is the constant bias of the sensor,

$c_T \delta T$ is the temperature sensitivity effect,

a_i is the acceleration along the ith axis,

$c_i a_i$ are anisoelasticity[1] effects,

m_i are misalignment errors,

s is the scale factor error, and

w_f is the sensor noise.

Similarly, the model for a ring laser gyro is typically given by (ibid.)

$$\delta\omega_{ib}^b = d + c_T \delta T + \sum_{i=1}^{3} c_i B_i + \sum_{i=1}^{3} m_i \omega_i + s\omega + w_\omega \tag{4.5}$$

where

d is the constant bias (drift) of the sensor,

$c_T \delta T$ is the temperature sensitivity effect,

$c_i B_i$ are magnetic sensitivity terms,

ω_i is the rotation rate around the ith axis,

m_i are misalignment errors,

s is the scale factor error, and

w_ω is the sensor noise.

Modeling all of the above states in a Kalman filter is impractical for the application at hand. The observability of all the above states, even if theoretically possible (see Gelb (1974) for details on observability), is virtually impossible under operational

---

[1]Elasticity refers to an object's ability to return to its original size and shape after deformation. Anisoelasticity, thus refers to the non-symmetric nature of this restoration. In this context, anisoelasticity could refer to the actual sensor or to its supports.

conditions due to GPS signal outages, limited vehicle dynamics and short data collection campaigns. Attempting to model all parameters may even weaken the model to a point where the system becomes unstable. Furthermore, given that a real-time system is one of the objectives of this dissertation, adding several more states to the system would increase the computational burden beyond an acceptable level.

In light of the above, both sensors errors are therefore considered to consist of a only bias term and noise, with some temporal variability given to the bias states. The temporal variability is used to account for time-varying parameters in the theoretical models shown above, such as temperature sensitivity, scale factors, etc.. The sensor error models can therefore be written as

$$\delta f^b \;=\; b + w_f \tag{4.6}$$

$$\delta \omega_{ib}^b \;=\; d + w_\omega \tag{4.7}$$

Augmenting the INS error model with these bias states, assuming them to be modeled as first-order Gauss-Markov processes, the final system model in state-space form is

$$
\begin{bmatrix} \delta \dot{r}^e \\ \delta \dot{v}^e \\ \dot{\varepsilon}^e \\ \delta \dot{b}^b \\ \delta \dot{d}^b \end{bmatrix}
=
\begin{bmatrix}
0 & I & 0 & 0 & 0 \\
N^e & -2\Omega_{ie}^e & -F^e & R_b^e & 0 \\
0 & 0 & -\Omega_{ie}^e & 0 & R_b^e \\
0 & 0 & 0 & -diag(\alpha_i) & 0 \\
0 & 0 & 0 & 0 & -diag(\beta_i)
\end{bmatrix}
\begin{bmatrix} \delta r^e \\ \delta v^e \\ \varepsilon^e \\ \delta b^b \\ \delta d^b \end{bmatrix}
$$

$$+ \begin{bmatrix} 0 & 0 & 0 & 0 \\ R_b^e & 0 & 0 & 0 \\ 0 & R_b^e & 0 & 0 \\ 0 & 0 & I & 0 \\ 0 & 0 & 0 & I \end{bmatrix} \begin{bmatrix} w_f \\ w_\omega \\ w_b \\ w_d \end{bmatrix} \tag{4.8}$$

where a more detailed form of the dynamics matrix is included in Appendix B and

δb^b is the vector of accelerometer bias errors,

δd^b is the vector of gyro bias errors,

$diag(\alpha_i)$ is diagonal matrix of time constants for the accelerometer bias models,

$diag(\beta_i)$ is diagonal matrix of time constants for the gyro bias models,

w_b is the driving noise for the accelerometer biases, and

w_d is the driving noise for the gyro biases.

To obtain the Gauss-Markov model parameters for the sensor errors, approximately 15 hours of static IMU data was collected. The IMU used for this purpose was the same one used in the field tests discussed in later chapters, namely a Honeywell HG1700 AG11. Under static conditions, the IMU measures Earth rotation and the reaction force of gravity. However, because these two quantities are constant (for the length of the test considered), any temporal variations in the measurements must be caused by temporal variations in sensor errors, which is to be modeled. Therefore, the autocorrelation function of the raw data was computed and used to determine the parameters for the Gauss-Markov models. The final parameter values are shown in Table 4.2. The corresponding spectral densities can be computed from the values

Table 4.2: Gauss-Markov Parameters for Honeywell HG1700 AG11 IMU

Sensor	Time Constant	Temporal Variance
X Gyro	100 min	0.35 $\deg^2/\mathrm{hr}^2$
Y Gyro	55 min	0.34 $\deg^2/\mathrm{hr}^2$
Z Gyro	84 min	0.47 $\deg^2/\mathrm{hr}^2$
X Accel	170 min	8.0e-8 $\mathrm{m}^2/\mathrm{s}^4$
Y Accel	68 min	2.5e-7 $\mathrm{m}^2/\mathrm{s}^4$
Z Accel	152 min	4.8e-7 $\mathrm{m}^2/\mathrm{s}^4$

in the table as $q = 2\beta\sigma^2$ where β is the inverse of the time constant and σ^2 is the temporal variance.

For computing the sensor noise values that drive the velocity error and misalignment states (i.e. w_f and w_ω), the standard deviation of a few seconds of data was sufficient to obtain a reasonable estimate. This was repeated at several periods in the data set to obtain a representative sample. Longer periods of data were not used so as to avoid any short-term variability that may have been caused by bias instabilities. Unexpectedly, the computed values were approximately one order of magnitude larger than those quoted by the manufacturer, both for the gyros and accelerometers. To refine the computed values, the first of two sets of data collected near Springbank airport was processed with simulated GPS data outages using 36 different combinations of accelerometer and gyro noise parameters (see Chapter 7 for processing details). The final noise parameters were selected as those that gave a standardized error near unity during the data outages (on average). Consideration was also given to the innovation sequence, which shows systematic effects if the process noise value is set too low. The final spectral density values are listed in Table 4.3. The noise value for a particular sensor type is assumed invariant across all three axes.

Table 4.3: Sensor Noise Spectral Densities for Honeywell HG1700 AG11 IMU

Sensor	Spectral Density
Accelerometers	4.1e-3 m/s^2/$\sqrt{\text{Hz}}$
Gyros	5.5 deg/h/$\sqrt{\text{Hz}}$

4.2.3 GPS/INS Filter

The GPS/INS filter used in the tightly coupled integration is the combination of the GPS-only and INS-only filters. It must account for all of the GPS and INS states to be modeled. However, as shown in Sections 4.2.1 and 4.2.2, the two filters share the same position and velocity states. Therefore, the GPS/INS filter is simply the INS-only filter augmented with the double difference ambiguities when they need to be estimated as real-valued quantities. With this is mind, the tight integration approach is actually more efficient (computationally) than the loose integration approach when the ambiguities are fixed (and thus not estimated), since the GPS-only filter is no longer necessary.

The process noise to be added to the filter is also the same as in the INS-only filter above. In other words, the process noise needed for the GPS-only filter is obviated in this case. Given the relatively large magnitude of the spectral densities used in the GPS-only filter, this represents a tremendous improvement.

4.3 Lever-Arm Effect

For a GPS receiver, the point to which all observations refer is the phase centre of the antenna. The analogous point for an IMU is the intersection of the three sensitivity axes. It is immediately obvious that these two points cannot coincide, with the offset

between the two being termed the lever-arm. Denoting the lever-arm vector from the IMU to the GPS antenna phase centre as ℓ, the following equations hold

$$\Delta r^e = R_b^e \ell^b \tag{4.9}$$

$$\Delta v^e = \Omega_{ei}^e R_b^e \ell^b + R_b^e \Omega_{ib}^b \ell^b \tag{4.10}$$

where Δr^e and Δv^e are the differences in position and velocity between the GPS antenna phase centre and the IMU. To determine the required accuracy of the lever-arm, the above equations will be perturbed under the assumption that the rotation matrix is perfectly known and the gyro measurements are errorless. This yields

$$\delta \Delta r^e = R_b^e \delta \ell^b \tag{4.11}$$

$$\delta \Delta v^e = \Omega_{ei}^e R_b^e \delta \ell^b + R_b^e \Omega_{ib}^b \delta \ell^b \tag{4.12}$$

From the first equation, it is obvious that the lever-arm needs be known only to the accuracy of the estimated positions, in this case a few centimetres. However, considering the effect on velocity (primarily the second term), the lever-arm must be known to even better accuracy. Specifically, a turn rate in a ground-based vehicle is capable of reaching $30°/s$ (~ 0.5 rad/s). For a 1 cm error in the lever-arm, this could cause a velocity error of up to 5 mm/s. Since this is only slightly below the level of noise for velocity estimation using GPS, and other errors have not yet been taken into account, the required accuracy for the lever-arm is better than 1 cm.

This accuracy can be achieved using traditional surveying techniques. However, the approach used herein estimated the lever-arm components in the INS-only filter (only the loose integration strategy was used for this purpose). This was done in an iterative manner, using the final solution of one processing run as the starting

point for the next processing run. Typically, four to ten iterations were necessary depending on the accuracy of the initial estimate. Once the final estimate of the lever-arm was obtained it was held fixed for subsequent processing.

Chapter 5

Real-Time Considerations

Operating in real-time imposes some limitations that are not often considered in post-mission software packages. This chapter discusses some of these issues. In particular, some methods to handle data latency from the base station are presented. Next, some of the processing limitations are discussed including the INS output rate, some of the matrix computations in a Kalman filter, and the Kalman filter measurement update strategy.

5.1   Base Station Latency

As shown in Equation 3.3, data from two receivers is needed to form a GPS double difference observation. In order to minimize errors, the data from the two stations should be time matched. In real-time applications however, a finite amount of time is needed to transmit the necessary base station data to the vehicle to be positioned. The latency associated with this transmission is a function of the amount of data to be transmitted and the baud rate of the communication link. Typical latencies experienced in this research were on the order of 0.1–0.2 s. This latency must be properly taken into account, especially when integrating the GPS data with an INS. In this regard there are two options

1. Process the GPS data using non-time-matched data from the base and remote receivers. In this way, "old" base station data can be used such that process-

ing can begin as soon as data from the remote station receiver is available. Alternatively, previously received base station data can be predicted forward using a Kalman filter to approximate time-matched data. These approaches eliminate the latency altogether.

2. Store a time series of IMU/INS information as it becomes available. When latent GPS data is received, the buffered information is restored to the proper time and the update is performed. Finally, the IMU data from the update time to the most recent time is processed. This is diagramed in Figure 5.1.

The first approach offers a relatively simple solution to the situation but is plagued with two practical problems. First, as the data from the base and remote stations becomes less synchronized, the differential errors increase because of their temporal variability. This in turn complicates the ambiguity resolution process. For this reason, non-time-matched data is often only used once the ambiguities are fixed (Neumann et al., 1996). During the ambiguity resolution process the latency must be addressed differently. Second, in this setup it becomes critical that a given epoch of base station data not be used twice. Doing so would mean that the measurement errors are not white and would violate one of the assumptions made in deriving the Kalman filter algorithm. Similarly, if a filter is used to predict the measurements, correlation across multiple epochs will develop. For these reasons, this approach was not implemented.

The second option, while more complicated to implement, provides time-matched GPS double difference observations and removes the possibility of introducing a time correlation in the measurements. As implied above, use of this approach requires information to be stored (buffered) for later use. This information includes the raw
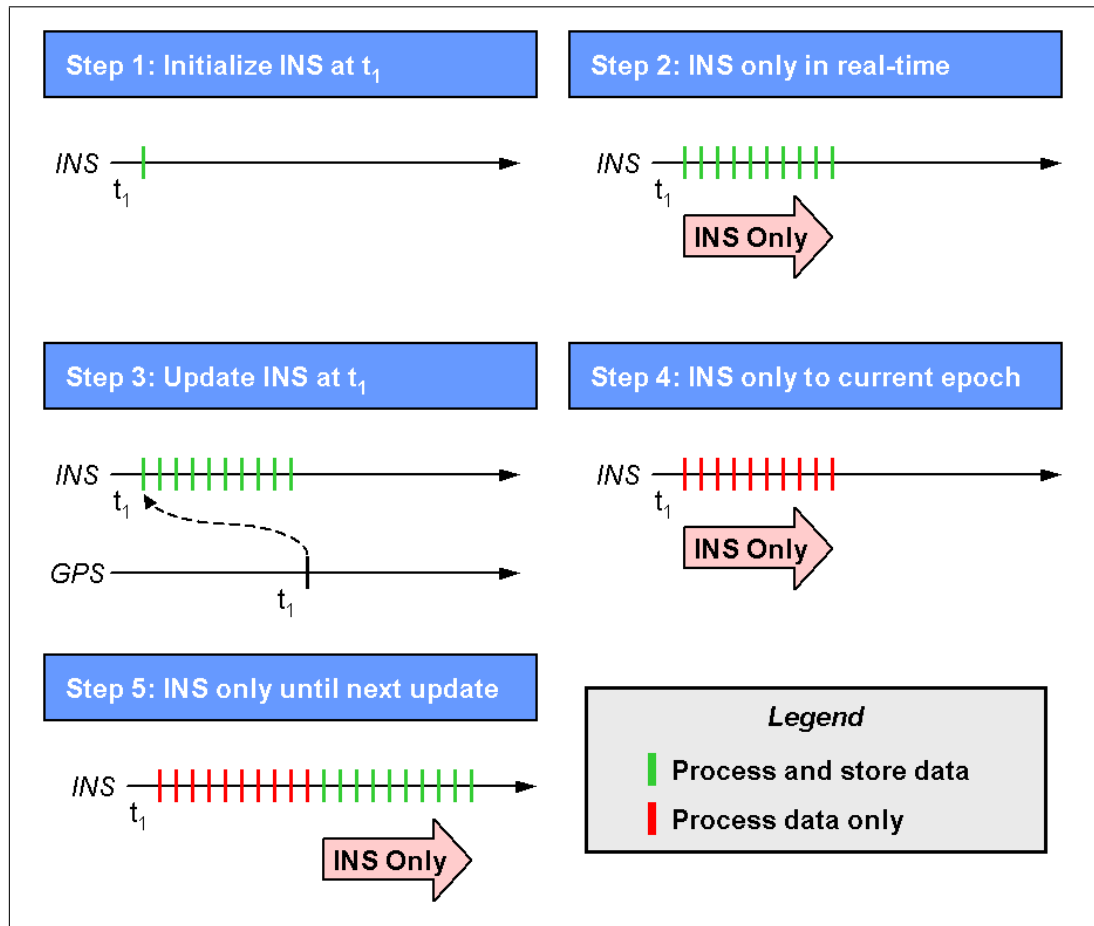
Figure 5.1: Real-Time Processing Strategy With Latent GPS Data

IMU data, the state of the mechanization equations (i.e. current position, etc.) and the INS filter covariance. Practically, only a finite amount of information is stored. If the GPS latency exceeds the maximum time span stored in the buffer, the GPS data is simply not processed.

5.2   Processing Limitations

The most obvious limitation imposed on real-time processing is the amount of computations that can be performed in a given time interval. Having too many operations will mean the system cannot keep up with the incoming data. The objective of real-time processing therefore, is to minimize the amount of computations while maximizing system performance. This section outlines some of the practical issues associated with real-time processing.

5.2.1   IMU Data Rate Versus INS Output Rate

Most IMU data rates exceed 50 Hz with some reaching into the hundreds of Hertz. Processing all of this data in real-time is a significant challenge. Furthermore, propagating the INS filter at this rate becomes even more complex. It is therefore preferred to output the INS solution at a rate lower than the IMU raw data rate.

The mechanization equations presented in Section 3.2.2 assume the data is processed as it is received. For this reason, this approach is not well suited to real-time processing. Instead, the mechanization equations developed by Savage (1998a,b) were implemented (these algorithms are also developed from basic principles in Savage (2000)). These equations are developed assuming a high-rate and low-rate cycle. The high-rate cycle accounts for systematic effects such as coning and sculling while the low-rate cycle is used for updating the position, velocity and attitude. For the equipment used, the high-rate cycle coincides with the 100 Hz IMU data rate while the low-rate cycle is performed at 10 Hz. The INS error filter is also propagated at this lower rate.

5.2.2   Calculation of Kalman Filter Matrices

In Section 2.1.2 the theoretical methods for computing the transition and process noise matrices were given (see Equations 2.16 and 2.17). For many systems however, theoretical evaluation of these equations is impractical and so numerical approximations must be made.

Calculation of Transition Matrix

Computation of the transition matrix can be approximated by expanding Equation 2.16 as a Taylor series

$$
\begin{aligned}
\Phi_{k,k+1} &= e^{F\Delta t} \\
&= I + F\Delta t + \frac{(F\Delta t)^2}{2!} + \frac{(F\Delta t)^3}{3!} + \cdots
\end{aligned}
\tag{5.1}
$$

Practically, truncation of this series after a few terms is often sufficient. The GPS-only filter is time invariant, implying the transition matrix is only a function of the time interval. Assuming no data outages, it can therefore be computed once. Furthermore, the transition matrix is rigourous if a first order expansion is used for a constant velocity model.

For the INS error filter, the dynamics matrix is a function of the measured specific force (see Appendix B) and thus must be evaluated at the filter update rate (i.e. 10 Hz). Although not rigourous, a second order expansion was used to compute the transition matrix for the INS error filter. It was found that increasing the order of expansion beyond two provided no noticeable improvement in results.

Calculation of Process Noise Matrix

Theoretical evaluation of the process noise matrix, as given by Equation 2.17 is often impractical, even for relatively simple systems. A numerical integration approach is therefore required. The algorithm used herein takes the form (Geier, 1998)

$$Q_k = \left(\Phi_{k,k+1} G_k Q_c G_k^T \Phi_{k,k+1}^T + G_k Q_c G_k^T \right) \frac{\Delta t}{2} \tag{5.2}$$

The interval over which the propagation is to take place could also be sub-divided into smaller time intervals such that the above integration is more accurate. However, it was found that for a 0.1 s interval there was no advantage to this approach. Finally, because the process noise matrix is a function of the transition matrix, it must also be computed at the filter update rate.

5.2.3   Kalman Filter Update Strategy

In many applications, groups of observations are often mutually independent. As a result, the covariance matrix of the observations is either diagonal or block diagonal. In these situations, the block diagonal form can be exploited to minimize the number of computations needed in the Kalman filter algorithm by processing the independent groups of observations sequentially (sequential processing) instead of all at once (simultaneous processing). The two methods are shown to be numerically equivalent in Appendix A. To illustrate the potential computational savings, reconsider the equation for the Kalman gain matrix

$$K_k = C_{x_k}^- H_k^T (H_k C_{x_k}^- H_k^T + C_{z_k})^{-1} \tag{5.3}$$

Notice that the dimension of the matrix to be inverted is equal to the number of observations. Consequently, reducing the number of observations to be processed

at a time will reduce the size of the inverse. Given that covariance matrices are positive-definite and symmetric, the inversion is typically done using a Cholesky decomposition for efficiency (Press et al., 1992). The number of floating point operations for this approach (including square roots) is given by

$$\Gamma(N) = \frac{2N^3}{3} + \frac{3N^2}{2} - \frac{5N}{6} \tag{5.4}$$

where N is the dimension of the matrix to be inverted. Now consider the three measurements available from a typical GPS receiver, namely code, Doppler and phase. Most applications assume these measurements to be uncorrelated and thus can benefit from the sequential processing approach. To illustrate the improvement in the number of floating point operations for this case, the following represents the fractional improvement of using the sequential approach over the simultaneous approach

$$\frac{\Gamma(3m)}{3\Gamma(m)} \tag{5.5}$$

where m is the number of double differences, assumed to be the same for all three measurement types. For three to ten double differences, the above ratio ranges from about 6 to 7.2, as shown in Figure 5.2, and thus represents a tremendous computational savings. It is noted that for the computer platform used for generating the results of later chapters, the time saved using the sequential update approach was only about 2 ms. However, for embedded systems where the actual number of floating point operations is critical, the above advantages are still important.
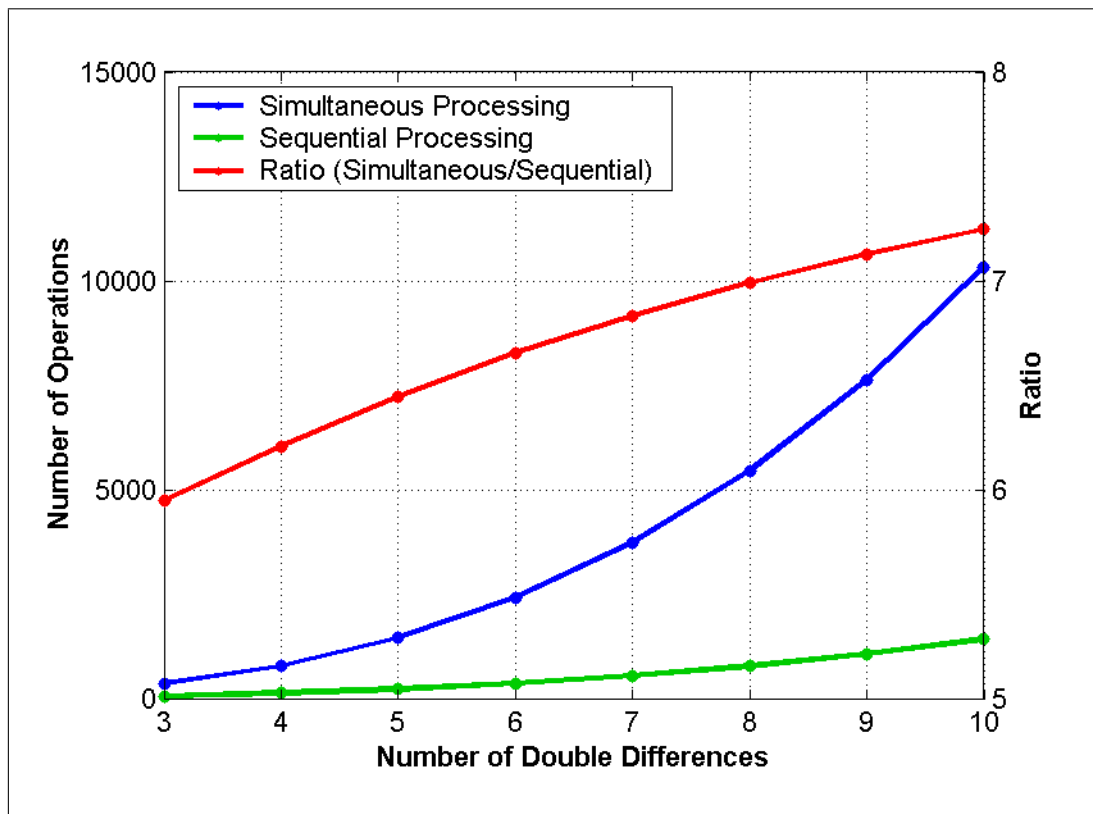
Figure 5.2: Matrix Inverse Operations Count Using Sequential and Simultaneous Updates

Chapter 6

Statistical Reliability in Integrated Systems

The presentation of statistical reliability in Chapter 2 assumed only one filter was used and all observations were processed simultaneously. However, as seen in Chapters 4 and 5, these two assumptions are not always valid. Specifically, the loose integration strategy (with and without seeding) uses two separate filters in a cascading approach, and any filter processing raw GPS observations could possibly process the code, Doppler and carrier phase observations sequentially, instead of simultaneously. This chapter addresses statistical reliability in light of these issues. A summary of all of the major results is included at the end of the chapter.

6.1   Notation

Before proceeding, a more generic notation for the Kalman filter parameters than was used in previous chapters is required. First, the epoch subscript (k) is dropped without loss of generality. Second, observations are assumed to be processed in sets, as in the sequential approach. The new notation can then be summarized as follows

H_i is the design matrix for the ith set of observations,

C_{z_i} is the covariance matrix of the ith set of observations,

$K_{i,F}^{(a,b,...)}$ is the Kalman gain matrix for the ith set of observations, computed by filter F, after having already processed observations a, b, etc.,

$\nu_{i,F}^{(a,b,\dots)}$ is the innovation sequence for the ith observation set from filter F, after having already processed the observation sets a, b, etc.,

$C_{\nu_{i,F}}^{(a,b,\dots)}$ is the covariance matrix of the innovation sequence for the ith set of observations, computed by filter F, after having already processed observations a, b, etc.,

$C_{\hat{x},F}^{(a,b,\dots)}$ is the covariance matrix of the estimated states from filter F after having processed the observation sets a, b, etc., and

$(\bullet)^{(0)}$ is the quantity $(\bullet)$ without having performed any previous updates at that epoch (analogous to the $(\bullet)^-$ notation from before).

The subscript i is omitted in all above locations for the simultaneous update approach. The value of F will be one of the following; G for the GPS-only filter, I for the INS-only filter, or GI for the GPS/INS filter.

The notation for the reliability parameters is also somewhat altered from before. It can be summarized as

$\nabla_{i,F}^{(a,b,\dots)}$ is the internal reliability vector for the ith observation set, computed from filter F, after having already processed observation sets a, b, etc., and

$\Delta\hat{x}_{i,F}^{(a,b,\dots)}$ is the external reliability vector for the ith observation set, computed from filter F, after having already processed observation sets a, b, etc..

As above, the subscript i is omitted when considering simultaneous observation updates.

Instead of trying to show the equations for all possible combinations of filters and update strategies, a simpler approach is desired. For internal reliability computa-

tions, the following notation implies that the MDB vector for the ith observation set is computed using the specified innovations covariance matrix

$$C_{\nu_i,F}^{(j,k,\ldots)} \xrightarrow{\hspace{1.5cm}} \nabla_{i,F}^{(j,k,\ldots)} \tag{6.1}$$

The "transformation" from $C_{\nu_i,F}^{(j,k,\ldots)}$ to $\nabla_{i,F}^{(j,k,\ldots)}$ can be performed using Equation 2.48 and 2.50. Similarly, the external reliability is expressed using

$$\nabla_{i,F}^{(j,k,\ldots)} \xrightarrow{\hspace{0.5cm} K \hspace{0.5cm}} \Delta\hat{x}_{i,F}^{(j,k,\ldots)} \tag{6.2}$$

which implies that the protection level vector is computed by "passing" the specified blunder vector through the (gain) matrix above the arrow. This is performed using Equation 2.49 or 2.51.

6.2 Loose Versus Tight Integration

For contrasting the loosely and tightly coupled integrations in terms of statistical reliability, the most important consideration is that blunders can only enter the system before the first filter. For the case at hand, this implies all blunders occur prior to the GPS-only filter in the loose integration or before the GPS/INS filter in the tight integration. Stated differently, blunders are limited to the raw GPS data. However, regardless of which filter "sees" the blunders first, the external reliability of the final solution is of utmost importance. With this in mind, the major focus of this section is twofold. First, the internal reliability of the filter processing the GPS data is investigated. Second, the external reliability of the final solution is presented. In all cases, simultaneous processing of the observations is assumed.

6.2.1 Internal Reliability

The internal reliability for the loose and tight integration strategies are the same as presented in Section 2.3.2. The only detail is that the MDBs should be computed from the appropriate filter. Therefore, the MDBs for the loose and tight integration cases are respectively given by

$$C_{\nu,G}^{(0)} \quad \longrightarrow \quad \nabla_G^{(0)} \tag{6.3}$$

$$C_{\nu,GI}^{(0)} \quad \longrightarrow \quad \nabla_{GI}^{(0)} \tag{6.4}$$

6.2.2 External Reliability

The external reliability for the tightly coupled integration is the same as shown in Section 2.3.2, and can therefore be denoted

$$\nabla_{GI}^{(0)} \quad \xrightarrow{K_{GI}^{(0)}} \quad \Delta\hat{x}_{GI}^{(0)} \tag{6.5}$$

For the loosely coupled integration, the external reliability is less straight forward. Specifically, applying the traditional external reliability equations to the GPS-only MDB vector will only yield the protection level for the GPS-only filter. The objective however, is to determine the effect after the INS-only filter, since this represents the final system output. Therefore, consider that an undetected blunder from the GPS-only filter will have the effect of biasing the entire GPS-only estimate by an amount given by that filter's PL vector. Since the GPS solution is used as input to the INS-only filter, it follows that the GPS-only PL vector also acts as a (multiple) blunder vector in the INS-only filter. As such, its impact on the state estimates of

the INS-only filter is given by

$$\Delta \hat{x}_I^{(0)} = K_I^{(0)} \Delta \hat{x}_G^{(0)} \tag{6.6}$$

where

$$\nabla_G^{(0)} \xrightarrow{K_G^{(0)}} \Delta \hat{x}_G^{(0)} \tag{6.7}$$

It is important to note that the new notation is not used in Equation 6.6. The reason is that in this case the entire observation vector is assumed to be in error. As such, the GPS-only PL vector must be pre-multiplied by the entire gain matrix, not just a single row as assumed in Equations 2.49 or 2.51.

The above discussion is diagrammed in Figure 6.1. Note that the MDBs for the INS-only filter are not used in this situation. The reason for this is that the basic assumption of statistical reliability, as derived herein, is that only a single blunder exists at any given epoch. However, a single GPS blunder actually biases all of the observations used in the INS-only filter. This situation cannot be reconciled without further algorithm development, which is beyond the scope of this dissertation.

6.3 Sequential Updates

The results of the previous section apply only if all available observations at a given epoch are processed simultaneously. However, as shown in Section 5.2.3, significant computational savings can be achieved if sequential processing of uncorrelated measurements is performed. This section presents the statistical reliability equations assuming sequential measurement processing. The results of this section apply equally to the GPS-only filter in the loose integration or the GPS/INS filter in the tight integration. As such, the filter identifier will be omitted until the end.
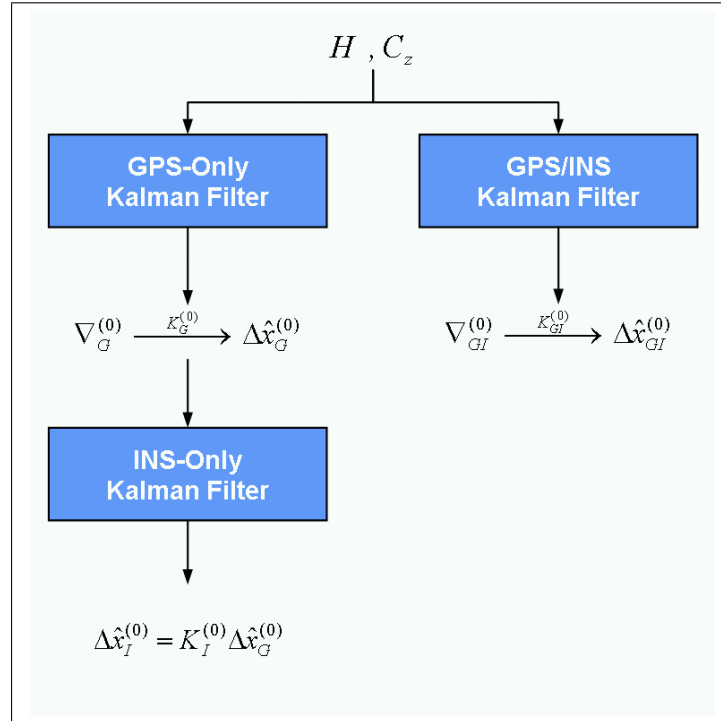
Figure 6.1: Statistical Reliability Parameters for Loose and Tight Integration Strategies Assuming Simultaneous Processing

6.3.1 Internal Reliability

To begin, consider two sets of statistically independent measurements, z_1 and z_2, with covariance matrices given by C_{z_1} and C_{z_2} respectively. The observations can be written as

$$z_1 = H_1 x + v_1 \tag{6.8}$$

$$z_2 = H_2 x + v_2 \tag{6.9}$$

Initially, assume that the first set of observations is processed alone. Using the equations from Chapter 2, the following matrices can be formed

$$C_{\nu_1}^{(0)} = H_1 C_{\hat{x}}^{(0)} H_1^T + C_{z_1} \tag{6.10}$$

$$K_1^{(0)} = C_{\hat{x}}^{(0)} H_1^T \left(H_1 C_{\hat{x}}^{(0)} H_1^T + C_{z_1} \right)^{-1}$$

$$= C_{\hat{x}}^{(0)} H_1^T \left(C_{\nu_1}^{(0)} \right)^{-1} \qquad (6.11)$$

$$C_{\hat{x}}^{(1)} = \left(I - K_1^{(0)} H_1 \right) C_{\hat{x}}^{(0)}$$

$$= C_{\hat{x}}^{(0)} - K_1^{(0)} H_1 C_{\hat{x}}^{(0)} \qquad (6.12)$$

The MDB vector for this set of observations is obtained from Equation 6.10 as follows

$$C_{\nu_1}^{(0)} \quad\longrightarrow\quad \nabla_1^{(0)} \qquad (6.13)$$

Next, assume that the second set of observations are processed to yield

$$C_{\nu_2}^{(1)} = H_2 C_{\hat{x}}^{(1)} H_2^T + C_{z_2} \qquad (6.14)$$

from which the following holds

$$C_{\nu_2}^{(1)} \quad\longrightarrow\quad \nabla_2^{(1)} \qquad (6.15)$$

Repeating the above procedure for subsequent observation sets shows that the following general expression holds for the computation of MDBs in sequential processing

$$C_{\nu_i,F}^{(0,1,\dots,i-1)} \quad\longrightarrow\quad \nabla_{i,F}^{(0,1,\dots,i-1)} \qquad (6.16)$$

Relationship Between Simultaneous and Sequential Updates

Using sequential processing, the covariance matrix of the estimated states decreases after each successive update as (this is the general form of Equation 6.12)

$$C_{\hat{x}}^{(0,1,\dots,i)} = C_{\hat{x}}^{(0,1,\dots,i-1)} - K_i^{(0,1,\dots,i-1)} H_i C_{\hat{x}}^{(0,1,\dots,i-1)} \qquad (6.17)$$

To illustrate the implications of this, consider the case when two sets of observations are available such that $H_i = H_{i+1}$ and $C_{z_i} = C_{z_{i+1}}$. The corresponding innovation covariance matrices are therefore given as

$$C_{\nu_i,F}^{(0,1,\dots,i-1)} = H_i C_{\hat{x}}^{(0,1,\dots,i-1)} H_i^T + C_{z_i} \tag{6.18}$$

$$C_{\nu_{i+1},F}^{(0,1,\dots,i)} = H_{i+1} C_{\hat{x}}^{(0,1,\dots,i)} H_{i+1}^T + C_{z_{i+1}}$$

$$= H_i C_{\hat{x}}^{(0,1,\dots,i)} H_i^T + C_{z_i} \tag{6.19}$$

Comparing Equations 6.18 and 6.19 with the knowledge of Equation 6.17 implies that for a given filter

$$C_{\nu_i,F}^{(0,1,\dots,i-1)} \geq C_{\nu_{i+1},F}^{(0,1,\dots,i)} \tag{6.20}$$

This means that the internal reliability parameters for the $(i+1)^{th}$ set of observations are smaller than those of the ith set, even if they both contain the same information. In general, the last set of observations to be processed in sequential mode has the same internal reliability as if it was processed simultaneously with all previously processed observation sets. To illustrate this, recall the two sets of observations from the start of this section. Assuming $z_{2,1} = \begin{bmatrix} z_2^T & z_1^T \end{bmatrix}^T$, the covariance matrix of the innovation sequence is

$$
C_{\nu_{2,1}}^{(0)} = \begin{bmatrix} H_2 \\ H_1 \end{bmatrix} C_{\hat{x}}^{(0)} \begin{bmatrix} H_2^T & H_1^T \end{bmatrix} + \begin{bmatrix} C_{z_2} & 0 \\ 0 & C_{z_1} \end{bmatrix}
$$

$$
= \begin{bmatrix} H_2 C_{\hat{x}}^{(0)} H_2^T + C_{z_2} & H_2 C_{\hat{x}}^{(0)} H_1^T \\ H_1 C_{\hat{x}}^{(0)} H_2^T & H_1 C_{\hat{x}}^{(0)} H_1^T + C_{z_1} \end{bmatrix} \tag{6.21}
$$

$$
= \begin{bmatrix} C_{11} & C_{12} \\ C_{21} & C_{22} \end{bmatrix}
$$

The internal reliability parameters for observation set #2 depend on the upper left matrix of the inverse of $C_{\nu_{2,1}}^{(0)}$, which is nothing more than $\left(C_{v_2,sim}^{(0)}\right)^{-1}$, where "$sim$" signifies simultaneous processing. Using the inversion lemma in Appendix C

$$
\begin{aligned}
\left(C_{v_2,sim}^{(0)}\right)^{-1} &= \left(C_{11} - C_{12}C_{22}^{-1}C_{21}\right)^{-1} \\
&= \left(H_2 C_{\hat{x}}^{(0)} H_2^T + C_{z_2} - H_2 C_{\hat{x}}^{(0)} H_1^T \left(H_1 C_{\hat{x}}^{(0)} H_1^T + C_{z_1}\right) H_1 C_{\hat{x}}^{(0)} H_2^T\right)^{-1} \\
&= \left(H_2 C_{\hat{x}}^{(0)} H_2^T + C_{z_2} - H_2 K_1^{(0)} H_1 C_{\hat{x}}^{(0)} H_2^T\right)^{-1} \\
&= \left(H_2 C_{\hat{x}}^{(0)} H_2^T - H_2 C_{\hat{x}}^{(0)} H_2^T + H_2 C_{\hat{x}}^{(1)} H_2^T + C_{z_2}\right)^{-1} \\
&= \left(H_2 C_{\hat{x}}^{(1)} H_2^T + C_{z_2}\right)^{-1} \\
&= \left(C_{\nu_2}^{(1)}\right)^{-1}
\end{aligned}
$$

where $(K_1^{(0)} H_1 C_{\hat{x}}^{(0)} = C_{\hat{x}}^{(0)} - C_{\hat{x}}^{(1)})$ from Equation 6.12 was used between the third and the fourth lines. The result confirms that the second observation set processed in sequential mode has the same reliability as if both the observation sets were processed simultaneously. This can be expanded to the general case by assuming three sets of observations are to be processed. However, given the above, the first two sets can be processed together without affecting the final solution. This again leaves two observation sets (i.e. the combination of the first two, plus the third one) which produce the same result if processed sequentially or simultaneously. Recursive application of this logic proves the generic case.

The above conclusion can be explained heuristically as follows. Sets of observations that are processed first do not have "access" to other observation sets that are processed afterwards. In this way, "early" observations have less information to use for identifying blunders. However, by the time the final set of observations are

to be processed, the filter has already acquired the information from the previous observations. Consequently, the last set of sequentially processed observations will have the same reliability as if it was processed simultaneously with all previous observation sets. Unfortunately, this accumulation of information with subsequent observation sets does not affect the internal reliability of earlier observations. The reason for this is that any undetected blunder in earlier observations would have already been incorporated into the filter's state estimate (although, as shown below, the external reliability for a given observation set can be decreased with subsequent observation sets).

A consequence of the above is that, in sequential mode, the order in which observations are processed becomes important (since the order in which a given observation set is processed will affect its MDB). While there is no "correct" processing order, the observations that are most likely to influence the estimated parameters should be processed last. The reason for this is that because these observations are most influential in the estimation process, blunders on these observations will be more pronounced in the final state estimates. However, by processing these observation sets last, their internal reliability improves (i.e. their MDB decreases), which in turn, improves the external reliability of the system.

6.3.2 External Reliability

To determine the external reliability using sequential updates, the fact that both sequential and simultaneous processing of the observations produces numerically identical results, in terms of a final state estimate, is exploited. Assuming only two sets of observations are available, Appendix A shows that the final correction to the

initial state estimate using either processing strategy is given by (see Equation A.13)

$$\chi_{1,2}^{(0)} = \left(I - K_2^{(1)} H_2\right) K_1^{(0)} \nu_1^{(0)} + K_2^{(1)} \nu_2^{(0)} \tag{6.22}$$

where $\chi_{1,2}^{(0)}$ is the correction to the state vector using observation sets 1 and 2 before any other observations are processed. In matrix form, this equation becomes

$$\chi_{1,2}^{(0)} = \left[\ \left(I - K_2^{(1)} H_2\right) K_1^{(0)} \quad K_2^{(1)} \ \right] \begin{bmatrix} \nu_1^{(0)} \\ \nu_2^{(0)} \end{bmatrix} \tag{6.23}$$

where the first matrix is the Kalman gain matrix from the simultaneous processing approach (i.e. $K_{1,2}^{(0)}$ for the example under consideration). Using this notation, the above equation can then be written as

$$\chi_{1,2}^{(0)} = K_{1,2}^{(0)} \ \nu_{1,2}^{(0)} \tag{6.24}$$

Finally, assuming blunders are present

$$\chi_{1,2}^{(0)} = K_{1,2}^{(0)} \left(\nu_{1,2}^{(0)} + \nabla_{1,2}^{(0)}\right) \tag{6.25}$$

From the above, it becomes clear that the blunders are actually propagated into the estimated parameters through the gain matrix from the simultaneous processing approach. Therefore, the following relationship holds

$$\nabla_{1,2}^{(0)} \ \xrightarrow{\ K_{1,2}^{(0)}\ } \ \Delta \hat{x}_{1,2}^{(0)} \tag{6.26}$$

or in matrix form

$$\begin{bmatrix} \nabla_1^{(0)} \\ \nabla_2^{(0)} \end{bmatrix} \ \xrightarrow{\ K_{1,2}^{(0)}\ } \ \begin{bmatrix} \Delta \hat{x}_1^{(0)} \\ \Delta \hat{x}_2^{(0)} \end{bmatrix} \tag{6.27}$$

However, the blunder vectors of interest are those obtained from the sequential processing approach, not from the simultaneous approach as shown above. Fortunately,

the "transformation" from blunder vector to protection level is linear in terms of the blunder vector itself. This means that the MDB vectors in Equation 6.27 can be scaled to match those of the sequential approach. Doing so yields

$$
\begin{bmatrix} \nabla_1^{(0)} \\ \nabla_2^{(1)} \end{bmatrix} \xrightarrow{\quad K_{1,2}^{(0)} \quad} \begin{bmatrix} \Delta\hat{x}_1^{(0)} \\ \Delta\hat{x}_2^{(1)} \end{bmatrix}
\tag{6.28}
$$

Finally, the more general form of the above equation is given by

$$
\nabla_{i,F}^{(0,1,\ldots,i-1)} \xrightarrow{\quad K_{sim,F}^{(0)} \quad} \Delta\hat{x}_{i,F}^{(0,1,\ldots,i-1)}
\tag{6.29}
$$

where $K_{sim,F}^{(0)}$ is the gain matrix assuming all observations are processed simultaneously. Furthermore, Equation 6.29 tacitly assumes that the proper sub-matrix of $K_{sim,F}^{(0)}$ is used for obtaining the protection levels, which is equivalent to considering only a single blunder vector at a time.

Equation 6.29 shows that the MDBs from sequential processing are mapped into the estimated states using the simultaneous processing gain matrix. Essentially, this means that although the MDBs are larger with sequential processing (in general), their effect on the estimated states can be minimized because the blunders are mitigated by other measurements that may be processed afterwards.

So far, consideration has only been given to the external reliability of a given filter. However, applying the findings of Equations 6.6 and 6.7, the external reliability for the loosely coupled case is

$$
\Delta\hat{x}_{i,I}^{(0,1,\ldots,i-1)} = K_{sim,I}^{(0)} \Delta\hat{x}_{i,G}^{(0,1,\ldots,i-1)}
\tag{6.30}
$$

where

$$
\nabla_{i,G}^{(0,1,\ldots,i-1)} \xrightarrow{\quad K_{sim,G}^{(0)} \quad} \Delta\hat{x}_{i,G}^{(0,1,\ldots,i-1)}
\tag{6.31}
$$

6.4   Summary

The results of this chapter can be summarized as in Table 6.1 and 6.2. Respectively, these show the appropriate formulation and equation number for the internal and external reliability parameters, using all combinations of integrations and processing strategies discussed.

Table 6.1: Summary of Internal Reliability Formulas

Update Mode	Loose Integration	Tight Integration
Simultaneous	$C^{(0)}_{\nu,G} \;\rightarrow\; \nabla^{(0)}_{G}$ Equation 6.3	$C^{(0)}_{\nu,GI} \;\rightarrow\; \nabla^{(0)}_{GI}$ Equation 6.4
Sequential	$C^{(0,1,\ldots,i-1)}_{\nu_i,G} \;\rightarrow\; \nabla^{(0,1,\ldots,i-1)}_{i,G}$ Equation 6.16 with $F = G$	$C^{(0,1,\ldots,i-1)}_{\nu_i,GI} \;\rightarrow\; \nabla^{(0,1,\ldots,i-1)}_{i,GI}$ Equation 6.16 with $F = GI$

Table 6.2: Summary of External Reliability Formulas

Update Mode	Loose Integration	Tight Integration
Simultaneous	$$\nabla_G^{(0)} \xrightarrow{K_G^{(0)}} \Delta\hat{x}_G^{(0)}$$ $$\Delta\hat{x}_I^{(0)} = K_I^{(0)}\Delta\hat{x}_G^{(0)}$$ Equations 6.6 and 6.7	$$\nabla_{GI}^{(0)} \xrightarrow{K_{GI}^{(0)}} \Delta\hat{x}_{GI}^{(0)}$$ Equation 6.5
Sequential	$$\nabla_{i,G}^{(0,\dots,i-1)} \xrightarrow{K_{sim,G}^{(0)}} \Delta\hat{x}_{i,G}^{(0,\dots,i-1)}$$ $$\Delta\hat{x}_{i,I}^{(0,\dots,i-1)} = K_{sim,I}^{(0)}\Delta\hat{x}_{i,G}^{(0,\dots,i-1)}$$ Equations 6.30 and 6.31	$$\nabla_{i,GI}^{(0,\dots,i-1)} \xrightarrow{K_{sim,GI}^{(0)}} \Delta\hat{x}_{i,GI}^{(0,\dots,i-1)}$$ Equation 6.29 with $F = GI$

Chapter 7

Field Testing and Post-Mission Analysis

In this chapter, post-mission processing using the real-time algorithms presented in the previous chapters is used to assess the integrated system performance. Details of the data collection and data processing procedures are presented first followed by the results themselves. Results address the objectives listed in Chapter 1 and include position and velocity accuracy during data outages, ambiguity resolution performance and overall system reliability.

7.1 Data Collection

This section presents the details of the field test used to collect the data analyzed later in this chapter.

7.1.1 Equipment

The primary piece of equipment used for this research was NovAtel's Black Diamond System (BDS). The BDS contains a NovAtel OEM4 dual-frequency GPS receiver capable of tracking up to 12 satellites at a time and provides high-quality code, Doppler and carrier phase measurements. The BDS also interfaces with a Honeywell HG1700 AG11 IMU. The IMU data is time tagged with GPS time thus ensuring synchronicity of the data to better than 1 ms. The specifications for the IMU are provided in Table 7.1.

Table 7.1: Specifications for Honeywell HG1700 AG11 IMU (Honeywell, 1997)

Parameter	Value
Accelerometers	
Bias (1σ)	1 milli-G
Scale Factor Accuracy (1σ)	300 ppm
Scale Factor Linearity (1σ)	500 ppm
Axis Alignment Stability (1σ)	500 μrad
Velocity Random Walk (max)	0.0013 m/s/$\sqrt{h}$
Gyros	
Bias (1σ)	1 deg/h
Scale Factor Accuracy (1σ)	150 ppm
Scale Factor Linearity (1σ)	150 ppm
Axis Alignment Stability (1σ)	500 μrad
Angular Random Walk (max)	0.125 deg/$\sqrt{h}$

The IMU was rigidly mounted to the floor of the University of Calgary's test van, a 2002 Dodge Grand Caravan. Specifically, one of the chairs was removed and the IMU was attached to the chair's mounting pins. The GPS antenna was mounted on the roof of the van. The antennas on the van and at the base station were both NovAtel 600 antennas. The lever-arm was measured as discussed in Section 4.3. The base station GPS receiver was also a NovAtel OEM4. For real-time testing (discussed in Chapter 8) a pair of FreeWave DGR-115W data transceivers was used to transmit base station data to the vehicle (remote station). The radio antenna was also mounted on the roof of the van. A picture of the vehicle setup (with radios) is shown in Figure 7.1. Equipment in the vehicle was powered either from the van itself or from additional car batteries.
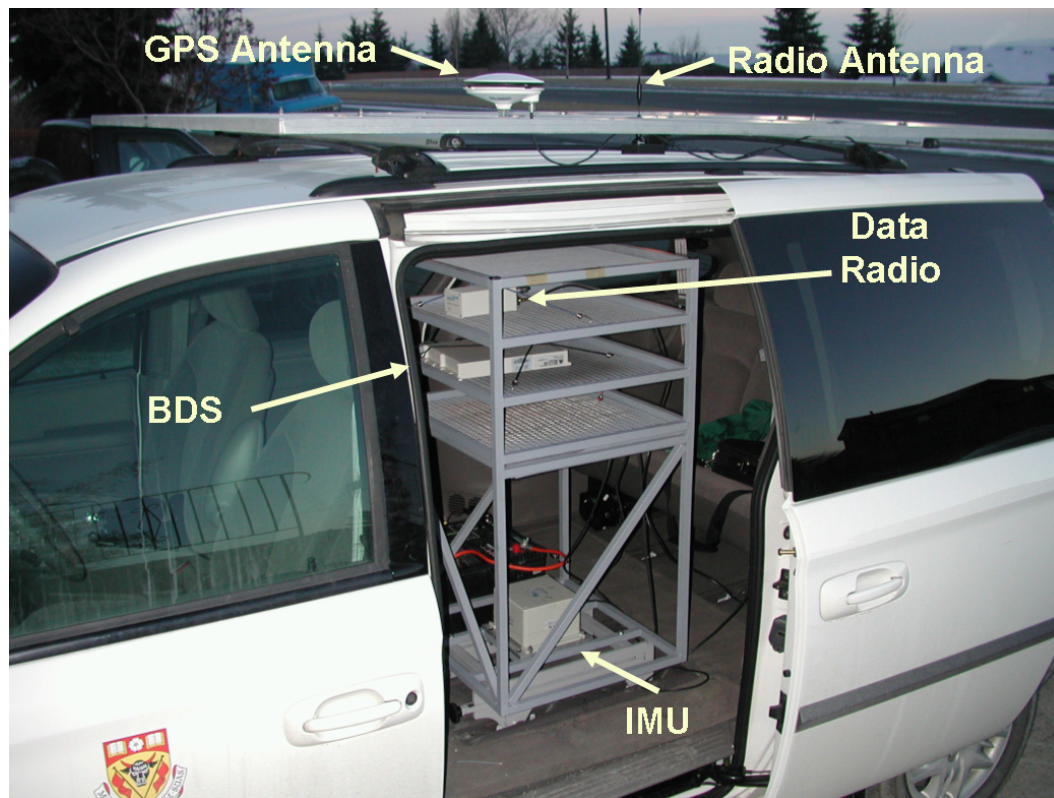
Figure 7.1: Typical Equipment Setup on Test Vehicle

7.1.2 Test Description

The data used for post-mission analysis was collected west of Calgary near Springbank airport on February 1, 2002. This area was selected because it provided excellent GPS satellite visibility. In the area are accessible pillars with known coordinates, one of which was used as the base station. The base station receiver was powered by a gas generator, as was the corresponding logging computer.

Two data collection runs were performed, each beginning with a static initialization period of about 12 minutes followed by about 15–20 minutes of driving. Vehicle speeds varied from 0 to 120 km/h. Vehicle dynamics were somewhat limited, with most of the data being collected at constant velocity. However, the analysis procedure

used (see next section) considers both constant velocity and dynamic portions of the trajectories. In this way, a more realistic assessment of the system is obtained. The distance from the test vehicle to the base station ranged from a few metres during the initialization to about 4 and 7 km during runs one and two respectively. These relatively short distances were selected such that an accurate DGPS solution could be used as a reference for evaluating the integrated system (see the next section for details).

Ionospheric conditions during the test are not considered to be significant. Figure 7.2 shows the Kp index for the day of the test as well as for two days on either side of the test. The Kp index is a global indicator of geomagnetic variation, which is affected by ionospheric activity, measured in eight three-hour segments daily (GFZ-Potsdam, 2003). The Kp index ranges from zero to nine, corresponding to the lowest and highest levels of geomagnetic activity. As shown in the figure, the Kp index for the period of the test is relatively low. However, given that the Kp index is a global average, it cannot accurately account for local variations. Consequently, given that the index is higher on either side of data collection period (within 24 hours), ionospheric activity during the test may also have been higher.

7.2   Analysis Procedure

The post-mission data analysis procedure consisted of two basic steps. First, the necessary truth information was computed for each of the data collection runs discussed in the previous section. Second, GPS data outages of varying duration and severity were simulated in subsequent data processing sessions. The GPS-only and integrated system behaviour during and after these outages was then used to assess
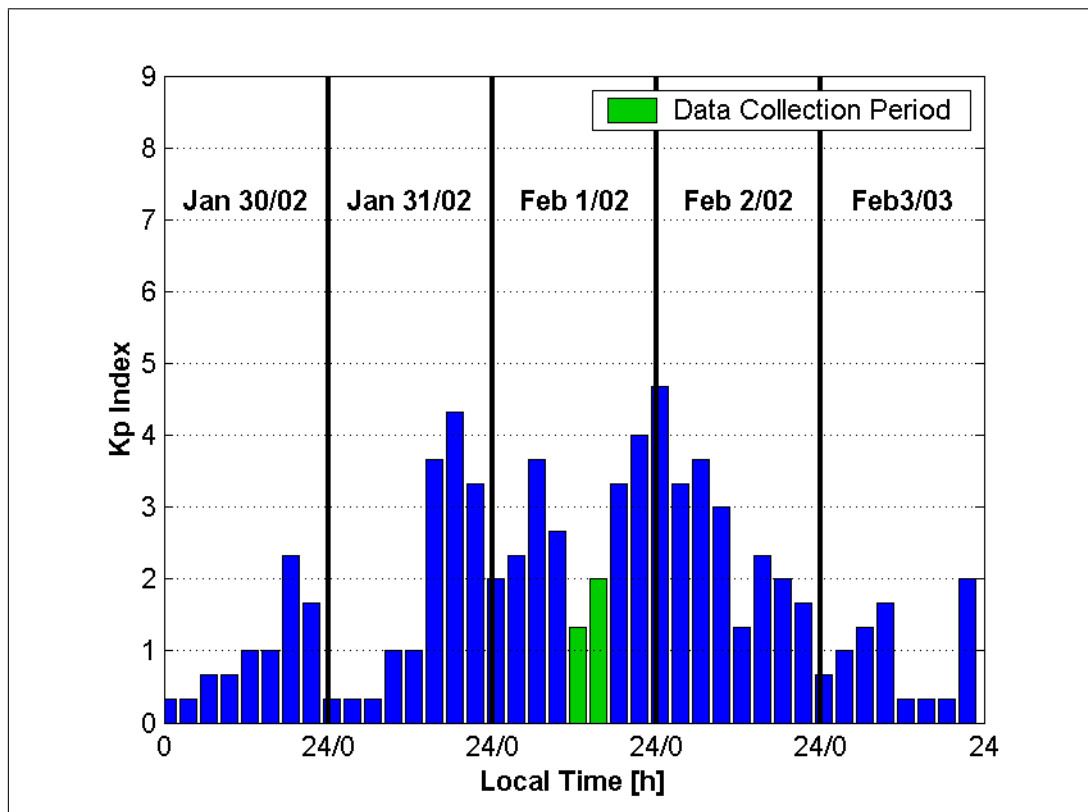
Figure 7.2: Kp Index Before and After Data Collection Period

performance. Comparisons of GPS-only and GPS/INS performance were then used to assess the improvement associated with the integrated system.

This section begins with a description of the software developed for this dissertation. Second, the generation of the truth trajectories as well as an assessment of their quality is presented. Finally, the method used to select the data outages is discussed.

7.2.1 Software Description

As part of this research, a new software package named SAINT™ (Satellite And Inertial Navigation Technology) was developed. Written in C++ using the University

of Calgary's Navigation Development Library (NDL^{TM}), SAINT^{TM} is capable of running in post-mission or real-time and was designed to accommodate high-accuracy applications while maintaining a flexible interface. All three integration strategies presented in Chapter 4 are selectable as are the types of GPS observables to be used for updating the system. Different quality IMUs can also be used by changing the necessary parameters. A basic program flowchart is shown in Figure 7.3.

Processing Parameters

For the results presented herein, C/A code and L1 Doppler measurements were always used to update the system. The carrier phase measurements were either L1 or widelane. The carrier phase will be used to identify the measurements used for a particular processing run. For example, "...the solution obtained using L1 carrier phase updates ..." implies the solution was computed with code, Doppler and L1 phase data. The standard deviations of the undifferenced measurements are listed in Table 7.2.

Table 7.2: Standard Deviations for Undifferenced GPS Observables at the Zenith

GPS Observable	Undifferenced Standard Deviation
C/A Code	50.0 cm
L1 Doppler	3.0 cm/s
L1 Carrier Phase	2.0 cm
L2 Carrier Phase	2.5 cm

The values shown are standard deviations for measurements made at the zenith. These value are scaled by $1/\sin(e)$ where e is the satellite's elevation angle. This scaling closely matches the increase of the undifferenced measurement standard deviation with decreasing elevation angle shown in Figures 3.1, 3.2 and 3.3.
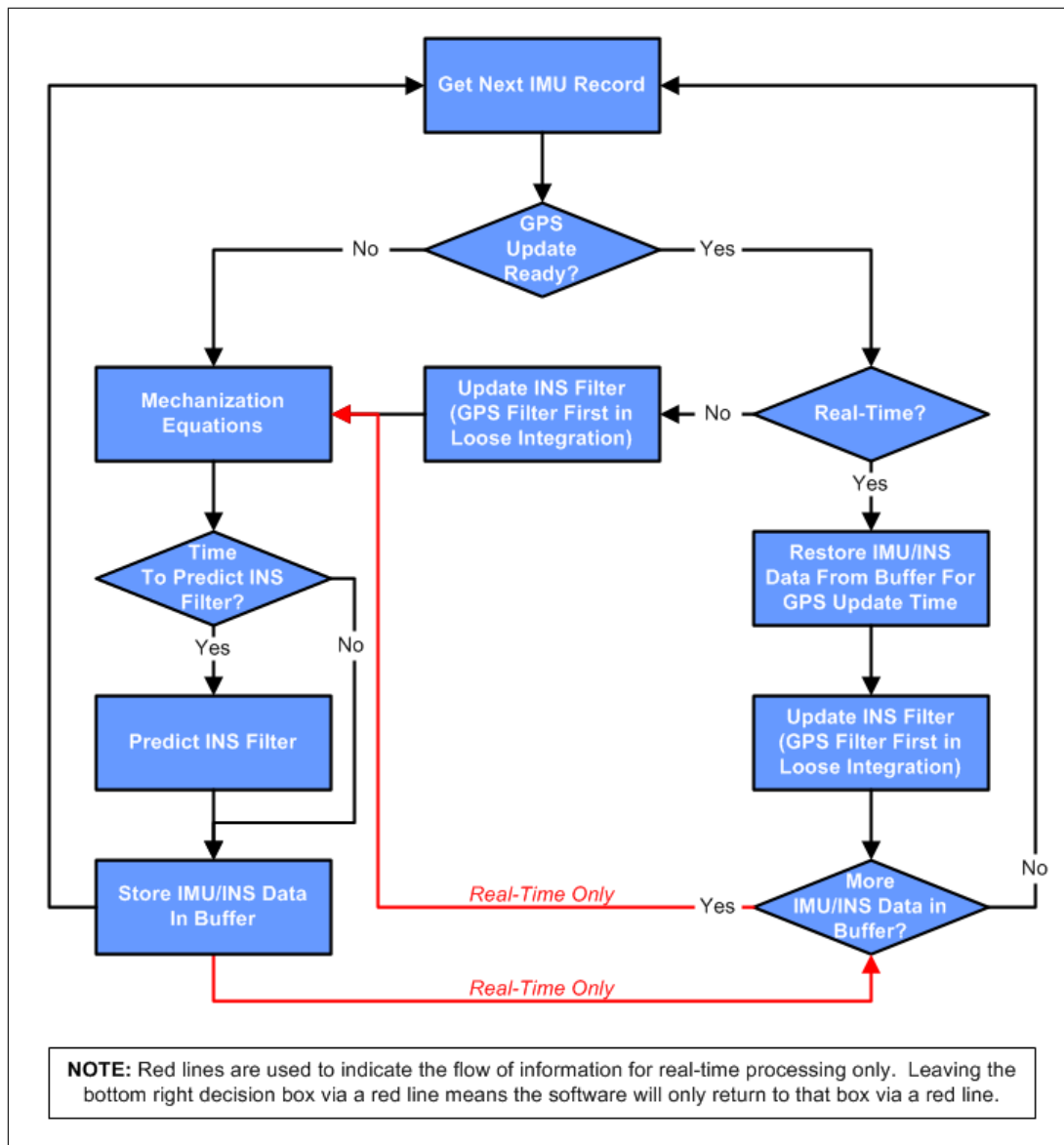
Figure 7.3: SAINT$^{\text{TM}}$ Software Flowchart

Comparing the values from Table 7.2 with those of the "high" elevation satellites from Figures 3.1 to 3.3 shows that the values in the table are larger. The reason for this depends on which observable is being considered. Specifically

- The code misclosures of Figure 3.1 show slowly varying error due to multipath. This implies a temporal correlation of the measurements which must be taken into account. A simple method of doing this is to increase the measurement uncertainty.

- The carrier phase errors due to noise and multipath are at the millimetre-level, but the differential errors could easily exceed 1 cm even for relatively short baselines. The standard deviation was thus increased accordingly.

- Using an uncertainly for the Doppler selected from Figure 3.3 resulted in several observations being rejected by the reliability testing algorithm. The most likely reason for this is that Doppler multipath increases with vehicle speed. However, the results of Figure 3.3 were derived using static data. The final value was thus computed based on having a reasonable number of rejected observations. Better characterization of Doppler noise and multipath effects under kinematic conditions would be required for a more rigourous value to be selected.

Finally, unless stated otherwise, all GPS data was processed with a ten degree elevation mask.

Ambiguity Resolution Fixing Criteria

At some point, the software algorithm must make a decision as to when to fix the ambiguities to integers. In SAINT$^{\text{TM}}$ this decision is made based on weighted sum-

of-squared ambiguity residuals, where the residuals are computed as the difference between an assumed integer ambiguity value and the float estimate. Specifically, the ratio of the weighted sum-of-squared residuals of the second best ambiguity set to that of the best ambiguity set is used. Unfortunately, there are two conflicting considerations affecting the acceptance value for this ratio. On the one hand, ambiguities should be fixed to integers as quickly as possible, suggesting the threshold be a small value. On the other hand, the accuracy of the ambiguity resolution process should be high, suggesting the threshold should be fairly large. A compromise must therefore be made.

The above ambiguity ratio does not technically follow a Fisher-distribution (Teunissen, 1997). However, values from this distribution were found to work well in practice. As such, the threshold value used in SAINT^{TM} is obtained from the Fisher-distribution with a significance level of 10%. The number of degrees of freedom for the distribution is equal to the number of ambiguities trying to be resolved. While a significance level of 10% may seem high, the threshold values for 5–8 satellites are in the range 3.45–2.59. These values agree well with constant threshold value of three used by Liu (2001). However, in contrast to ibid., the Fisher-distribution offers the advantage that when trying to fix fewer ambiguities the threshold value increases to reflect the relative ease of fixing only a few ambiguities. Finally, because Liu (2001) used a constant ratio of three for baseline lengths ranging from 30–400 km, the approach adopted in SAINT^{TM} should be valid for any practical implementation.

7.2.2 Truth Trajectory Generation

Generation of the truth trajectories was accomplished by processing all available GPS and IMU data using the tightly coupled integration strategy. In this way, the trajectory was computed using all available information and should thus be of the highest quality. Optimal smoothing techniques could have been used here but given the expected accuracy of the forward processing run (see the following subsections), little benefit would have been gained.

As stated above, the test area provided very good GPS satellite visibility. This, combined with the very short distance to the base station during the static initialization meant that the GPS ambiguities were resolved before the kinematic portion of the test. The following subsections analyze the quality of the truth trajectories after this initial fix. First, the quality of the GPS-only solutions is investigated followed by an analysis of the integrated solutions. A comparison of the different integration approaches is also included to illustrate their differences.

GPS-Only Solution for First Run

For the first run, the majority of initial ambiguities were maintained throughout the trajectory with only some satellites needing to recompute their ambiguities on-the-fly. As such, the expected position accuracy is expected to be quite high. To help confirm this, Figure 7.4 shows the L1 carrier phase residuals for satellites whose ambiguities are fixed, as computed using GPS-only. Also shown on the figure is the distance of the vehicle from the base station and the number of satellites available.

Baseline lengths of approximately zero occur when the vehicle is stationary next to the base station. During these times, the residuals are on the order of the double

Figure 7.4: Absolute Value of GPS-Only Fixed Ambiguity L1 Carrier Phase Residuals and Baseline Length for Run #1 Without Data Outages

difference standard deviations computed in Figure 3.2, implying that the only remaining errors are those due to multipath and noise. More importantly, it implies the ambiguities are fixed correctly.

As the distance from the base station increases, so does the magnitude of the residuals. This is typical of the increase in differential errors as a function of receiver separation. For the longest baseline ($\sim$4km) the differential errors are at a level of about 5 ppm. Because this value is slightly larger than the typical values quoted in Table 3.1, this suggests that the ionospheric effects are somewhat larger than the Kp index of Figure 7.2 would indicate. However, the apparent decrease in the resid-

uals starting at GPS time 508626 is caused by loss of lock on two satellites, both of which were below 16° (the residuals for these satellites are not shown until 508674 because their ambiguities were not resolved as integers until that time). Given their low elevation, these satellites would be more susceptible to differential errors. This being the case, the remaining satellites show considerably smaller errors. Therefore, the average differential errors for this test are probably lower than the 5 ppm values quoted earlier and are probably closer to 3 ppm. Given the above, the GPS-only solution are considered accurate to 1–2 cm.

GPS-Only Solution for Second Run

The analysis of the second run closely follows that of the first. The L1 carrier phase residuals for those satellites with fixed ambiguities are shown in Figure 7.5, along with the baseline length and the number of visible satellites.

Again, for short baselines, the magnitude of the residuals match those expected from noise and multipath effects. For longer baselines, the residuals show differential effects on some satellites of up to about 9 ppm, but RMS values are probably closer to about 3 ppm. This makes sense since the two runs were collected consecutively, and thus should show similar error behaviour.

There were two problems encountered during this run. First, starting at GPS time 510613 no data from the base station was logged for 13 seconds. During this period, the truth solution is based solely on the INS. Fortunately, after the outage the GPS data showed no signs of cycle slips and so no "recovery" of the ambiguities was needed. The magnitude of the residuals after the data outage confirms this was the case. Second, at GPS time 511291, the vehicle passed underneath a highway sign
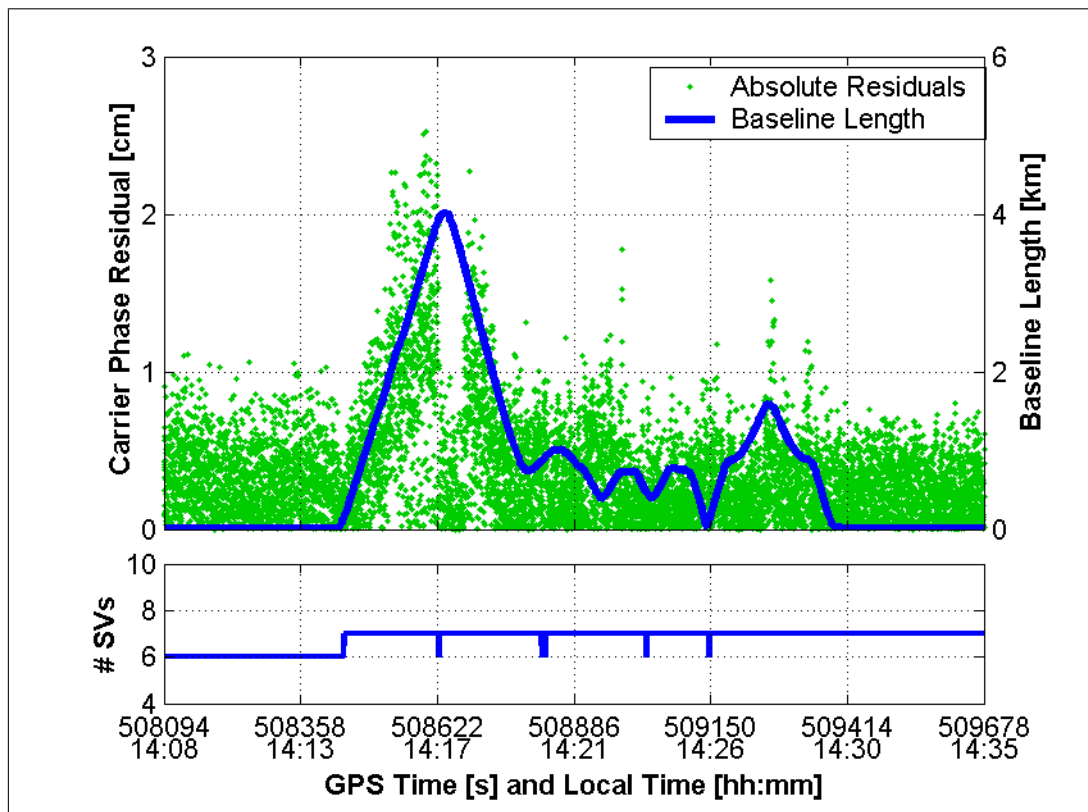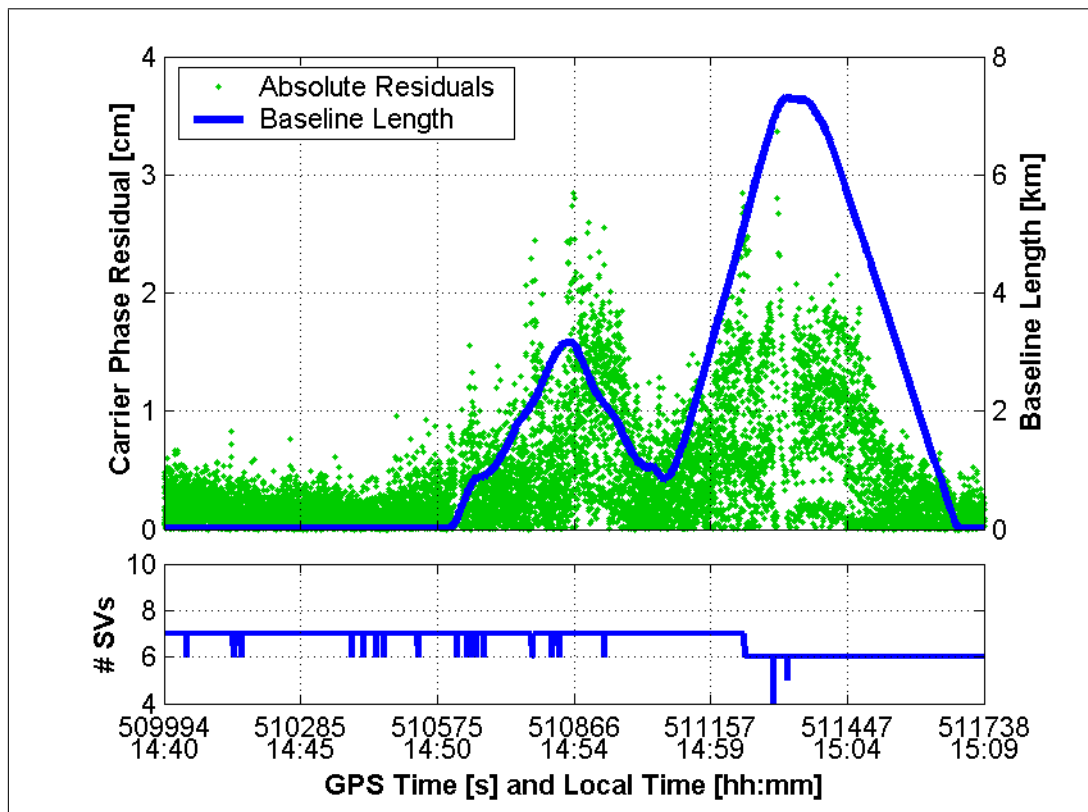
Figure 7.5: Absolute Value of GPS-Only Fixed Ambiguity L1 Carrier Phase Residuals and Baseline Length for Run #2 Without Data Outages

and lost lock on all but four satellites. While this is still sufficient to compute a solution, the relatively long distance from the base station at that time, combined with code multipath errors, will limit system accuracy to several centimetres. This portion of the data set was therefore avoided when selecting locations for simulated data outages (see Section 7.2.3). With the exception of the problematic periods discussed above, the GPS-only solution is again assumed to be accurate to 1–2 cm.

Tight Integration Solution

The above analysis focused on the GPS-only results, since this will ultimately determine the absolute accuracy of the integrated system. However, an assessment

of the integrated system performance is also important. A good indication of the quality of the integrated solution is the magnitude of the corrections applied to the INS position and velocity errors states. Table 7.3 shows the RMS three-dimensional corrections to the position and velocity error states for each run. The problematic sections from the second run were omitted for this analysis. Since the corrections are an indication of the smoothness of the trajectory over time, it can be seen that the trajectories are smooth to about the centimetre-level in position and about 5 mm/s in velocity. Furthermore, since the GPS solutions analyzed above will determine the absolute accuracy of the system, the truth trajectories are assumed to be accurate to 1–2 cm at all times.

Finally, given the high-quality of the position estimates, the fixed ambiguities used to derive these positions can also be considered correct. They will thus be used as a reference when investigating the ambiguity resolution performance in Section 7.5.

Comparison of Loose and Tight Integrated Solutions

This section compares the solutions of the different integration approaches to illustrate their differences under ideal situations. To begin, Table 7.4 shows the difference between the loosely and tightly coupled solutions. As above, the problematic periods of the second run were not used for computing these statistics. The difference between the two solutions is at the millimetre-level. These differences are most likely

Table 7.3: RMS of Corrections to INS Position and Velocity Errors States Using a Tight Integration Without Data Outages

Run	Position	Velocity
1	8 mm	3 mm/s
2	9 mm	4 mm/s

Table 7.4: RMS Difference Between Positions Computed Using Loose and Tight Integration Strategies Without Data Outages

Axis	Run 1	Run 2
North	3 mm	3 mm
East	4 mm	5 mm
Up	4 mm	2 mm

the result of the better ability of the tight integration approach to smooth the GPS data (noise). This concept is addressed again below. The estimated standard deviations for position and velocity using both systems were the same to better than 1 mm and 1 mm/s respectively, with the tight integration giving the more optimistic estimate.

The RMS of the fixed L1 carrier phase residuals for the loose and tight integration solutions are shown in Table 7.5. The residuals are larger when using the tightly coupled approach. This helps confirm that the position differences in Table 7.4 are caused by high-frequency errors on the measurements. Specifically, since the tight integration approach is better able to filter the GPS measurements, more high-frequency measurement error is forced into the residuals, and not the position estimate as with a loose integration. Overall, the two integration approaches can be assumed to be almost equivalent under ideal situations, with the tight integration approach providing the smoother trajectory.

Table 7.5: RMS of Fixed L1 Carrier Phase Residuals Computed Using Loose and Tight Integration Strategies Without Data Outages

Run	Loosely Coupled	Tightly Coupled
1	5 mm	10 mm
2	8 mm	12 mm

7.2.3 Simulated Data Outages

To assess GPS-only and GPS/INS performance in terms of (i) position and velocity accuracy, and (ii) ambiguity resolution during and after data outages (gaps) respectively, six data outages were simulated in each run. The locations of the data outages (during the trajectory) were carefully selected to represent a wide range of vehicle dynamics. This is important because the INS error filter's dynamics matrix is a function of the measured specific force (see Appendix B). As such, the INS error behaviour, and thus the overall INS performance, will vary with vehicle dynamics. By selecting a wide range of dynamics, a more representative assessment of the system's performance will be obtained.

The duration of the data outages varied from 2 to 40 seconds for assessing the ambiguity resolution performance after the outages. The full trajectories with the location of the data outages are shown in Figures 7.6 and 7.7 for the first and second runs respectively. Since a particular outage starts at the same time regardless of its duration, Figures 7.6 and 7.7 show the longest (i.e. 40 second) data outages. The trajectory during each data outage is shown in detail in Appendix D, along with the approximate vehicle accelerations.

Another important criteria for selecting the data outage locations was the vehicle's distance from the base station. The varying baseline lengths will be used in the ambiguity resolution assessment where spatially correlated differential errors are important. To this end, Figures 7.6 and 7.7 show that data outages are simulated anywhere from a few metres to about 7 km from the base station.

The data outages were actually simulated by artificially raising the satellite elevation mask during the selected portions of each trajectory. In this way, the severity of
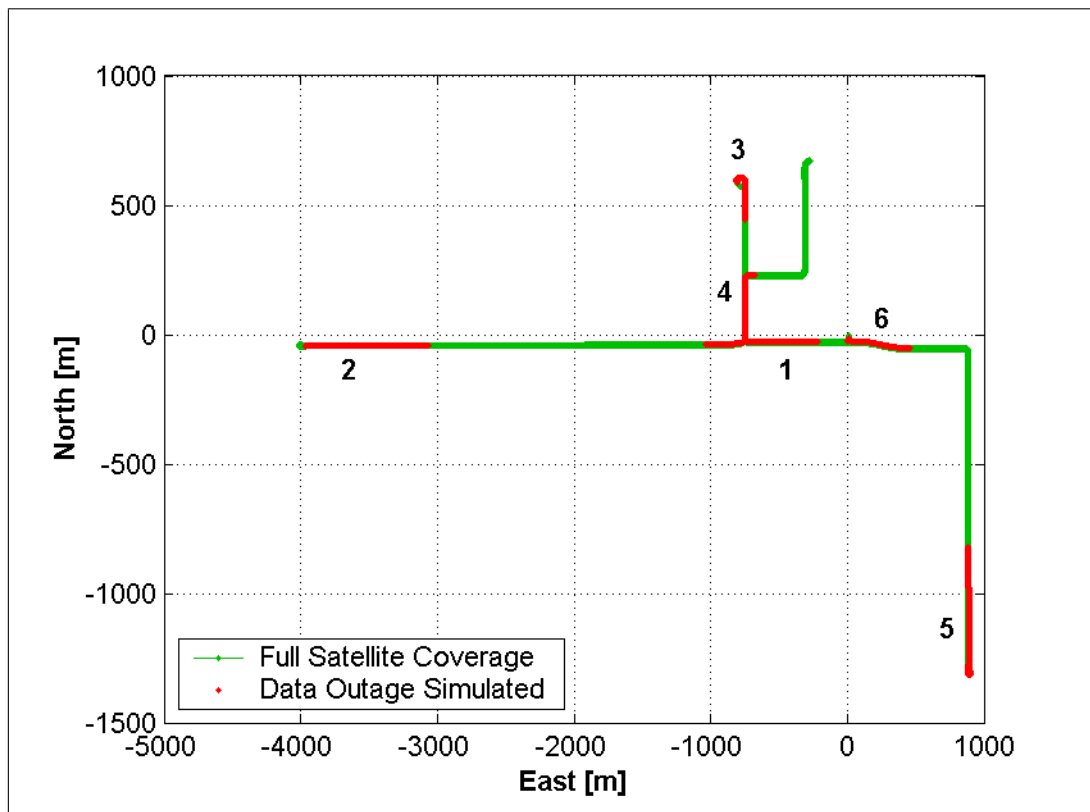
Figure 7.6: Trajectory and Simulated Data Outages for First Run Relative to Base Station

the data outages could be adjusted. For this research, two types of outages were simulated; complete and partial. Complete outages simulate situations where GPS signals are completely unavailable, such as in a tunnel. This was accomplished using an elevation mask of 90°. In contrast, partial data outages simulate situations where fewer than four GPS satellites are available. With so few satellites, a standalone GPS solution is impossible unless a Kalman filter is used. For the first and second runs, the elevation masks used for the partial data outages were 44.5 and 58.0 degrees respectively. The number of remaining satellites was either two or three.

Finally, for the first run, only one data outage was simulated per processing session.
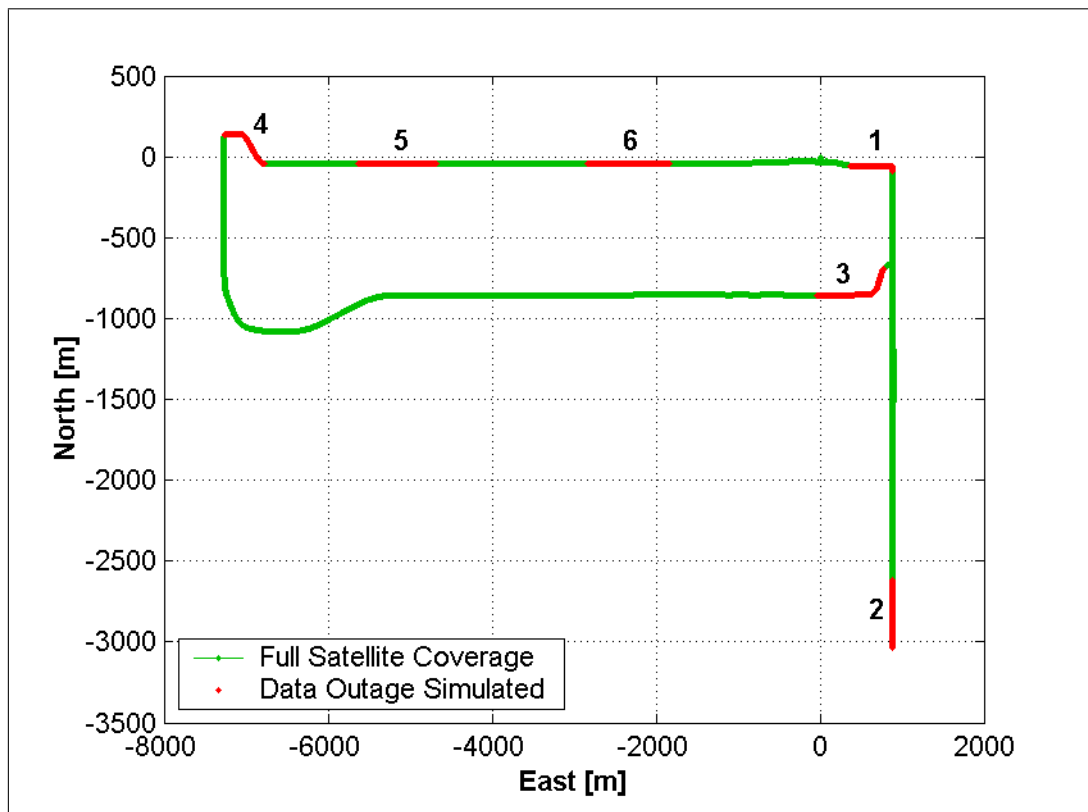
Figure 7.7: Trajectory and Simulated Data Outages for Second Run Relative to Base Station

For the second run, two outages were simulated per processing session with sufficient time between each to ensure the system completely recovers from the first outage before beginning the second.

7.3   Position Accuracy During Data Outages

To assess the positioning accuracy of the integrated system during data outages, the solution obtained during each outage is compared to the reference trajectories of the previous section. Since the reference trajectory is of high-accuracy, the difference between it and the position estimate during the data outage will be mostly due to the

error of the latter solution. As such, this difference represents a direct assessment of the system performance, accurate to the centimetre-level. The following subsections present the results for complete and partial data outages.

It is noted that in order to obtain an assessment of the absolute accuracy of the system, the comparison of the solutions during the data outages should be made with an independent estimate of the trajectory. In the absence of such a trajectory, the reference trajectories of the previous section are used instead. In this way, the following accuracy assessment is only as good as the accuracy of the reference trajectory itself.

Also of note is that prior to the data outages, the carrier phase ambiguities are always fixed to integers. As such, system performance during data outages will be better than in the case where only float ambiguity estimates are available. Similarly, for partial data outages, the ambiguities for those satellites that remain visible during the outage are held fixed. However, the simulations used are still valid in that they simulate situations where extended periods of ideal satellite coverage are temporarily interrupted by partial or complete signal masking, as is often encountered in practical situations.

7.3.1 Complete Data Outages

Since no GPS signals are available during the complete data outages, system performance is due entirely to the free-inertial solution. Instead of assessing the error behaviour on a case-by-case basis, the north, east and up errors for each data outage were computed as a function of time since the last GPS update. Using the resulting 12 time series (i.e. one for each gap over the two runs), the RMS error across all data

gaps was computed. In this way, a statistical assessment of the error as a function of time is obtained. The results using L1 carrier phase data in a tightly coupled integration strategy are shown in Figure 7.8. As shown, the position accuracy degrades quadratically with time. This is expected since any error in the navigation frame (i.e. e-frame) accelerations, due errors in the estimated INS parameters, will be doubly integrated into the position. After about 30 s, the position error is slightly larger than 1 m. Considering that a differential code solution is accurate to approximately the same level, this is significant. Specifically, it can be concluded that the free-inertial solution is as good or better than a differential code solution for data outages lasting up to about 30 s (in an RMS sense). As such, after data outages lasting up to about 30 s, the integrated approach will initialize the position of the system to a more accurate value (relative to GPS alone), which should result in faster filter convergence.

A second potential benefit of the above accuracy improvement (over GPS-only) is a reduction in the GPS ambiguity search space once the GPS data becomes available after the data outage. However, as shown in Section 7.5, such a reduction is dependent on the covariance of the position observation (or error in this context). Consequently, the Kalman filter's estimate of the actual error is important, with the ideal situation being a perfect agreement between the actual error and the estimated error from the filter. To this end, Figure 7.9 compares the three-dimensional RMS position error from Figure 7.8 with the average estimate of the filter's three-dimensional standard deviation (across all 12 outages). As can be seen, the two values agree reasonably well with the filter estimate being slightly pessimistic. However, given that the RMS errors are computed using only 12 samples, this discrepancy is not considered significant. The agreement between the actual and estimated errors confirms
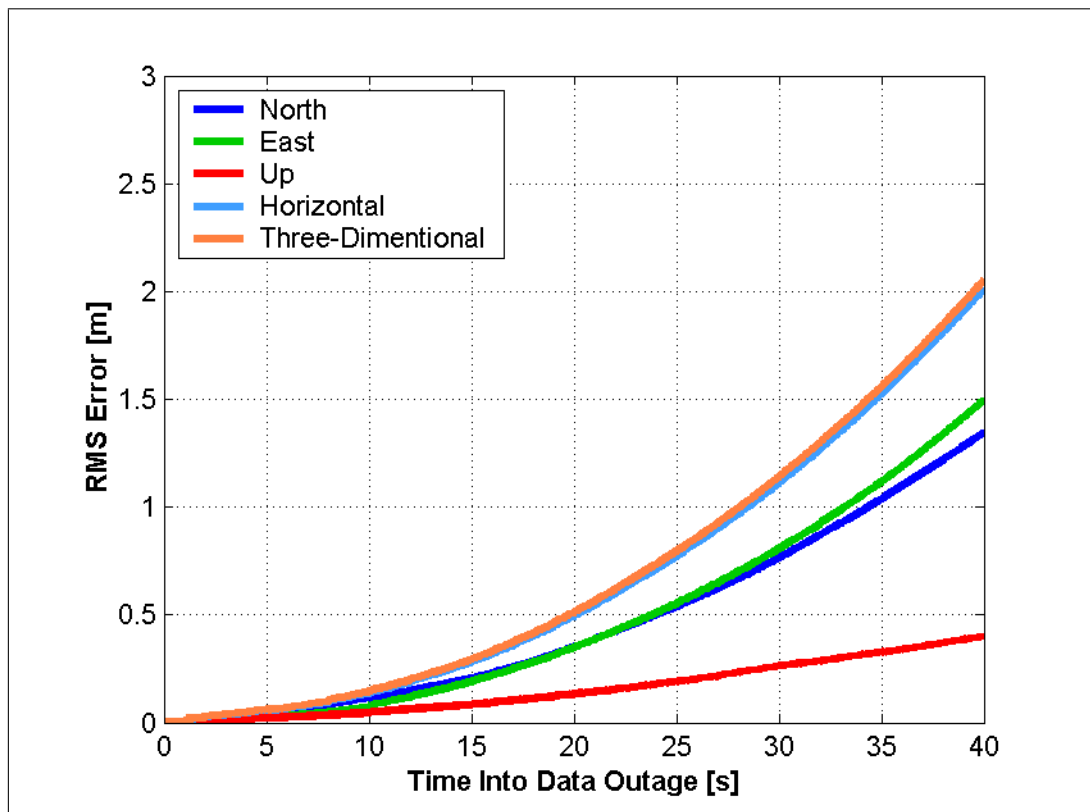
Figure 7.8: RMS Position Error During All Complete Data Outages Using L1 Carrier Phase Updates and a Tight Integration

that appropriate model parameters were used for modeling the system states as well as the measurements. Furthermore, this also means that in the absence of a reference solution, the estimated standard deviation provides a reasonable estimate of the solution's accuracy for scenarios similar to ones used here. In this context, "similar" refers to the magnitude of the differential errors and the inter-antenna distances.

The analysis so far has only considered the use of L1 carrier phase updates with a tight integration strategy. To compare and contrast these results with those obtained using other approaches, Figure 7.10 shows the three-dimensional position errors obtained using all combinations of loose/tight integrations and L1/WL carrier phase
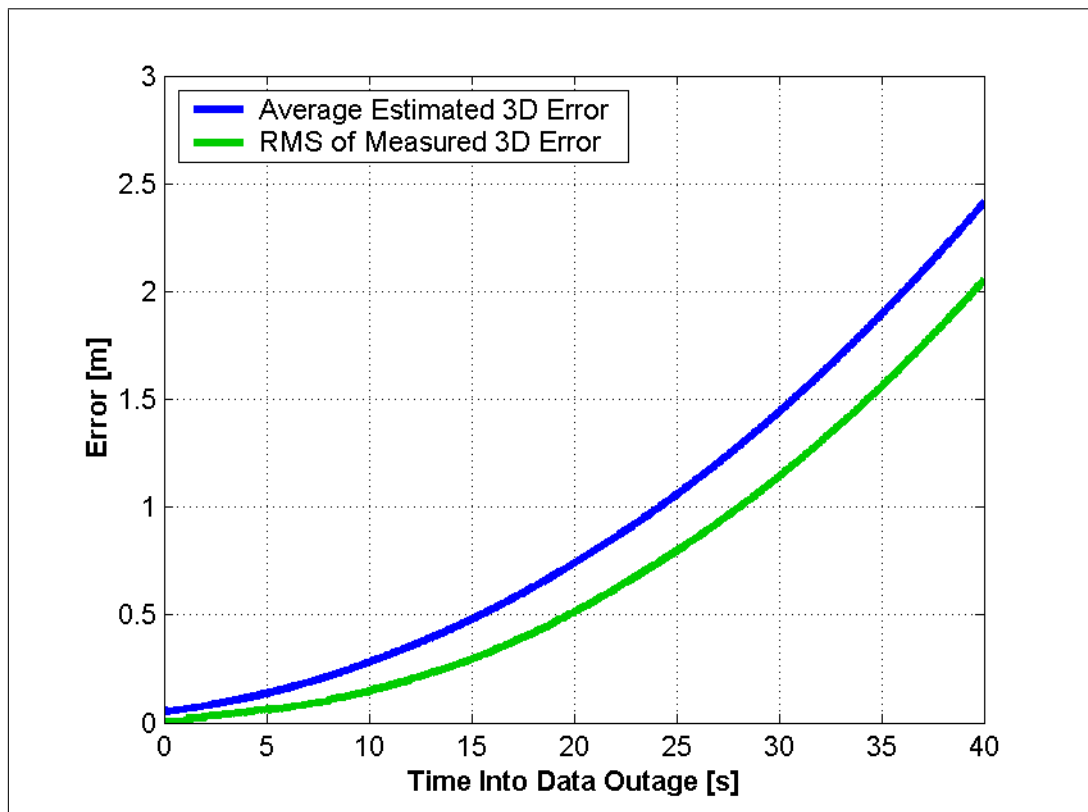
Figure 7.9: Comparison of Three-Dimensional RMS Position Error and Average Estimated Standard Deviations During All Complete Data Outages Using L1 Carrier Phase Updates and a Tight Integration

observations. Note that loose integration with and without seeding are the same in this context. While the overall error behaviour is similar with all approaches, there are some general trends which should be noted. First, for a given carrier phase frequency, the tight integration strategy outperforms the loose integration strategy. While the differences are on the order of about 10 cm after 40 s, the reason is likely because the loose integration approach cannot "calibrate" some of the INS errors as well. This is the result of the additional process noise needed for the GPS-only filter, since the two integration approaches are otherwise the same. Second, the widelane observations are not as useful as L1 for bridging data outages. The reduced accuracy
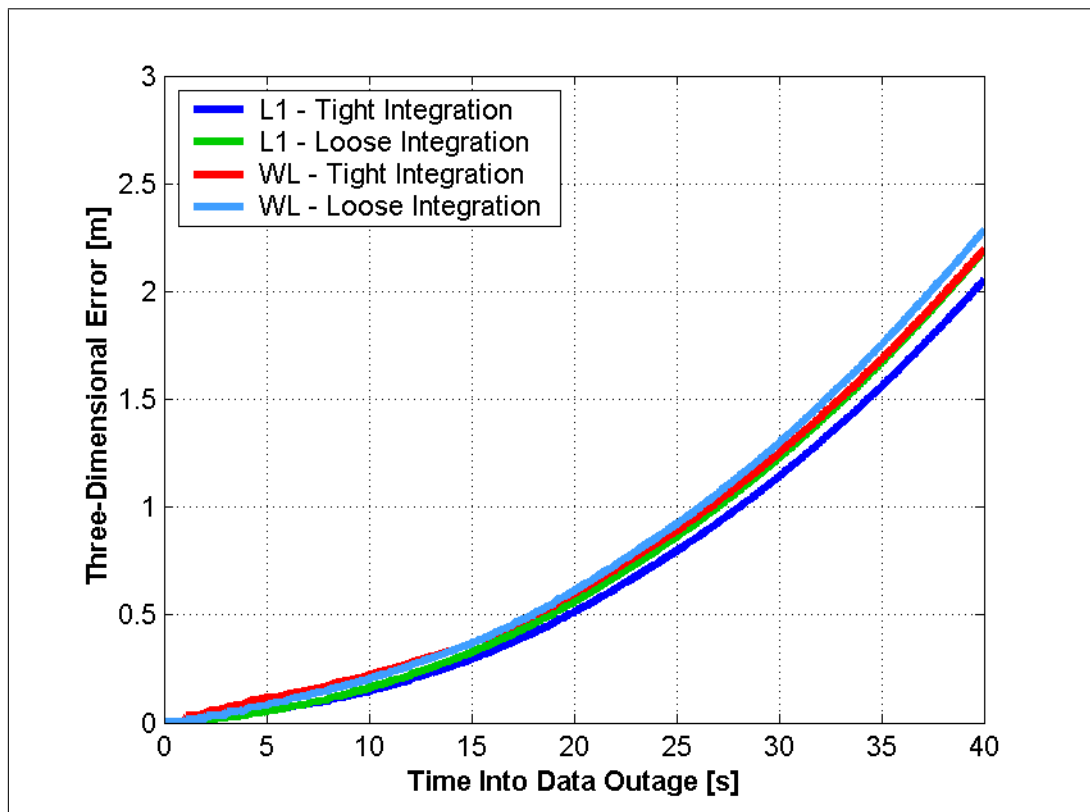
Figure 7.10: Comparison of Three-Dimensional RMS Position Error During All Complete Data Outages Using Different Processing Strategies

of the widelane observations will limit their ability to calibrate the inertial errors, thus causing poorer performance. Finally, the loose integration with L1 and the tight integration with widelane provide approximately the same level of performance.

7.3.2 Partial Data Outages

For partial data outages, the system performance is a function of the inertial errors and the quality of the GPS information/geometry available from the remaining visible satellites. The latter is typically quantified using Dilution of Precision (DOP) values. Unfortunately, for the situation considered here, DOPs cannot be computed

due to the underdetermined nature of the estimation problem. However, since DOPs are an approximation to the estimated standard deviations, the latter will be used instead, since they are still available from the GPS-only Kalman filter. Figure 7.11 shows the estimated position standard deviations as computed using the GPS-only filter. For the horizontal and three-dimensional standard deviations, there appear to be two "groups" of curves. These correspond to the number of satellites in view, either two or three in this case. As can be seen, the three-dimensional GPS-only solution degrades rapidly to 100 m in about 25 or 30 seconds, depending on the available GPS constellation. Furthermore, after only a few seconds, the estimated position accuracy is poorer than the worst case free-inertial error during complete data outages (up to 40 s). The impact of this on the integrated position accuracy is analyzed below.

Figure 7.12 shows the RMS position error as a function of time into a partial data outage, as computed using a tight integration approach with L1 carrier phase updates. The plot has the same scale as those in Section 7.3.1 to facilitate comparison. The position accuracy is considerably better than with complete data outages despite the relatively weak satellite geometry. The position error still grows quadratically, but much more slowly than before. The three-dimensional error is approximately 70 cm after 40 s, compared with over 2 m with complete data gaps.

Although not shown, the agreement of the RMS error and of the filter's estimate of the error is not as good as with complete data outages. The RMS error appears to be a factor of about two smaller than the filter's estimated error. Although not necessarily representative, a pessimistic estimate of the error is better than having an optimistic one as the latter may cause filter divergence.
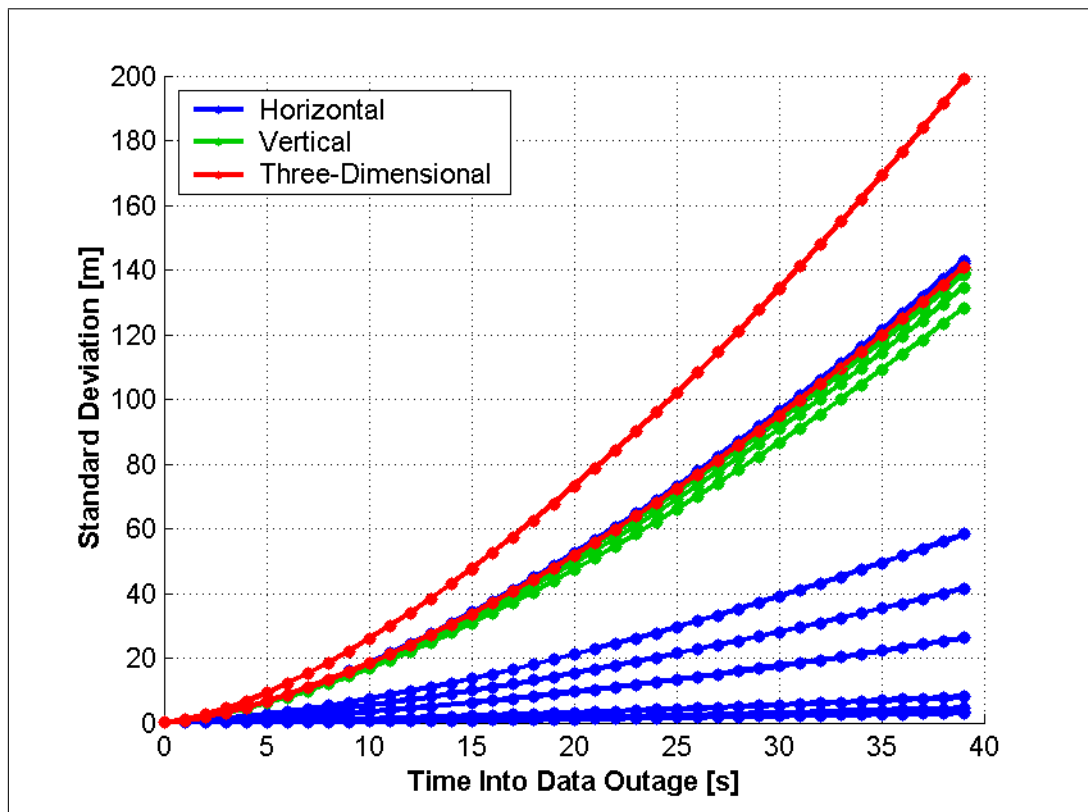
Figure 7.11: Estimated GPS-Only Standard Deviations During All Partial Data Outages Using L1 Carrier Phase Data

Finally, Figure 7.13 compares the results obtained using different integrations and carrier phase updates. As with the complete data gaps, L1 is better than widelane but the difference between the loose and tight integration approaches is much more significant. Specifically, both integration strategies provide very similar behaviour for data outages lasting up to about 20 seconds, at which time the loose integration solutions show a much more rapid degradation in performance. To explain, consider that the results of Figure 7.11 also represent the observation standard deviations for the INS-only filter in the loose integration approach. Given their very rapid increase, due primarily to the amount of process noise being added to the GPS-only filter, the influence of the GPS data on the integrated solution rapidly becomes negligible.
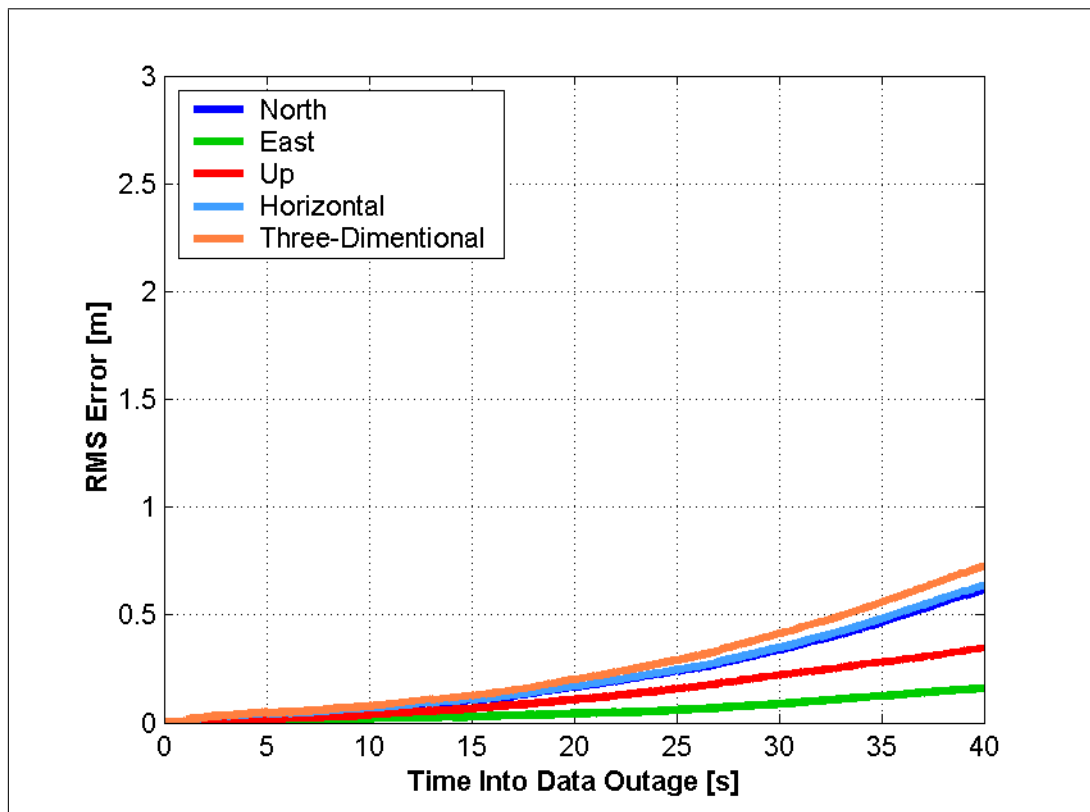
Figure 7.12: RMS Position Error During All Partial Data Outages Using L1 Carrier Phase Updates and a Tight Integration

As such, the final solution will tend towards the case where no GPS updates are available. In other words, as the estimated GPS-only position uncertainty increases, the integrated solution slowly tends to the full data outage case. In contrast, the tightly coupled approach has considerably less process noise and is thus better able to extract the "useful" information from the remaining GPS observations with the ultimate result being improved system accuracy.
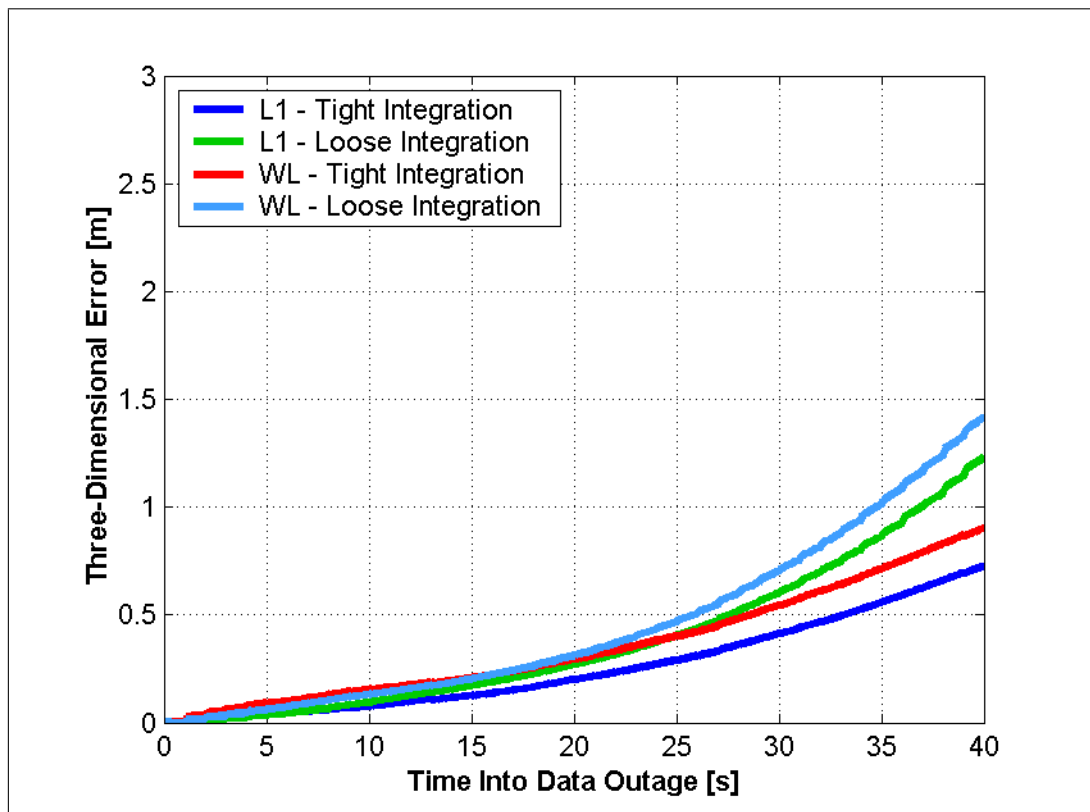
Figure 7.13: Comparison of Three-Dimensional RMS Position Error During All Partial Data Outages Using Different Processing Strategies

7.3.3 Summary

The analysis of the previous sections shows that the integrated system is capable of providing decimetre accuracy during complete and partial GPS data outages lasting approximately 5 and 10 seconds respectively. These results were obtained with ideal satellite measurements and geometry prior to the simulated data outages, and therefore represent a somewhat optimistic situation. Nevertheless, the results give a reasonable expectation of system performance.

Given that the covariance estimate of the filter appears to be a reasonable, if not pessimistic, approximation to the actual error behaviour, the results obtained in

subsequent tests can be assessed from the covariance matrix alone, if necessary.

Finally, the results presented herein are considered to be representative for the quality of system considered. Some improvements may be possible if laboratory and/or field calibrations of the IMU are performed prior to a data collection campaign. However, these procedures are time consuming and may not be practical under normal operational conditions.

7.4   Velocity Accuracy During Data Outages

For certain applications, the more relevant parameter of interest may be the vehicle velocity. To this end, the results of the previous section could be used to infer the accuracy of the estimated velocity during data outages. However, for completeness and clarity, Figure 7.14 shows the RMS velocity errors using L1 carrier phase updates and a tight integration for complete and partial outages. The velocity errors are seen to grow linearly with time, as expected since any biases in the navigation frame accelerations will be integrated only once. The RMS accuracy during complete outages is about 11 cm/s after 40 s, while for partial data outages the accuracy is about 4 cm/s for the same duration. The results of other combinations are approximately the same, with only slight differences. These differences can be inferred from the position accuracy analysis of the previous section, and are therefore not shown here explicitly.
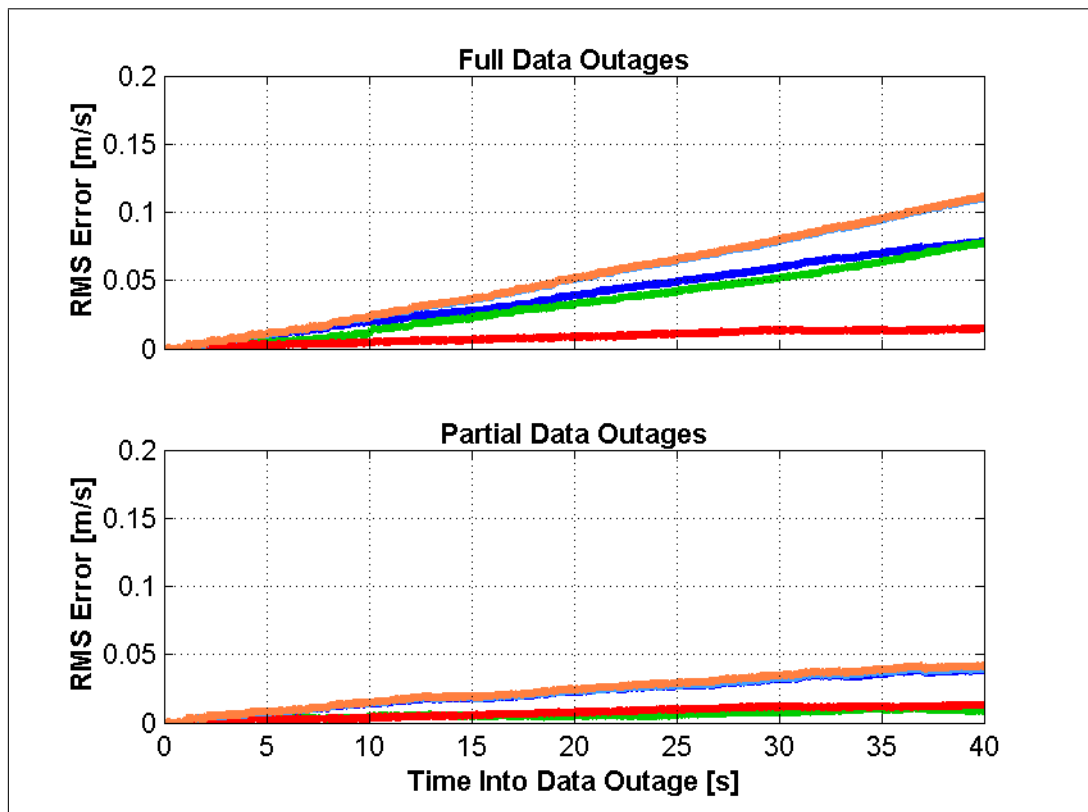
Figure 7.14: RMS Velocity Error During All Complete and Partial Data Outages Using L1 Carrier Phase Updates and a Tight Integration

7.5 Ambiguity Resolution After Data Outages

The ability of a system to recover from complete and partial GPS data outages and return to a correctly fixed integer ambiguity solution is extremely important. Since it is the exploitation of the integer nature of the ambiguities that allows for high-accuracy position estimates in a timely manner, it follows that the ambiguity resolution process is vital to achieving a system's most stringent performance objectives. Furthermore, for an integrated GPS/INS system, it is the GPS solution that provides the absolute accuracy of the system. Therefore, while the inertial information does provide some advantages, the use of inertial data by itself will not

significantly improve the overall system accuracy beyond what the GPS component is capable of delivering. The question therefore becomes, can the ambiguity resolution process be expedited by using the information available from the inertial system?

This section investigates ambiguity resolution performance using standalone GPS and using an integrated approach. In particular, the loose coupling with seeding and tight coupling approaches are compared with GPS-only to assess their improvements and limitations. In this context, there are two main interests

1. The time needed to resolve the ambiguities as integers. The faster the ambiguity resolution process, the faster the system will be able to return to the highest accuracy level.

2. The veracity of the ambiguity fix. Since an incorrect fix of one cycle on one satellite is capable of producing position errors that far exceed the navigation system's estimated accuracy for that position, the accuracy of the ambiguity fix is crucial. Failure to fix the ambiguities correctly can, and likely would, create a serious integrity problem.

The following analysis is performed on a run-by-run basis and investigates the ambiguity resolution performance after complete and partial data outages using various integration strategies and carrier phase measurements. Data outages of different durations are investigated to determine the situations under which the inertial data can be of benefit.

It is noted that the results of this section are to be interpreted in the context of the levels of differential errors and inter-antenna distances experienced in the two data collection runs. For example, baselines longer than 7 km and/or differential error

effects larger than about 3 ppm would likely adversely impact the following results. Nevertheless, the following analysis serves to illustrate the potential benefits and limitations of using an integrated system for ambiguity resolution.

7.5.1 Results From First Run

For the first run, data outages of 2, 4, 6, 9, 12, 16, 20, 30 and 40 seconds were simulated. The following subsections investigate the ambiguity resolution process after all six data outages using each data outage duration. Results after complete data outages are investigated first, followed by those obtained after partial data outages.

Complete Data Outages

As an initial assessment, Figure 7.15 shows the average time needed to fix the L1 ambiguities for each of the six data outages using different integration strategies. In this context, "average" refers to the mean time across all data outage durations. For this particular case, all ambiguity fixes were correct and so the focus of the following will be on the time needed to resolve the ambiguities. Also, note that in terms of ambiguity resolution, the loose integration without feedback is simply the performance of GPS alone, and is therefore denoted accordingly.

The results of Figure 7.15 show two important characteristics. First, the GPS-only solution performs the poorest with either integrated solution providing improvements in all cases, some of which are significant. Specifically, for data outage number three, the average time to fix is reduced by over a minute by simply using the inertial position and velocity to seed the GPS-only filter. Second, the tight integration
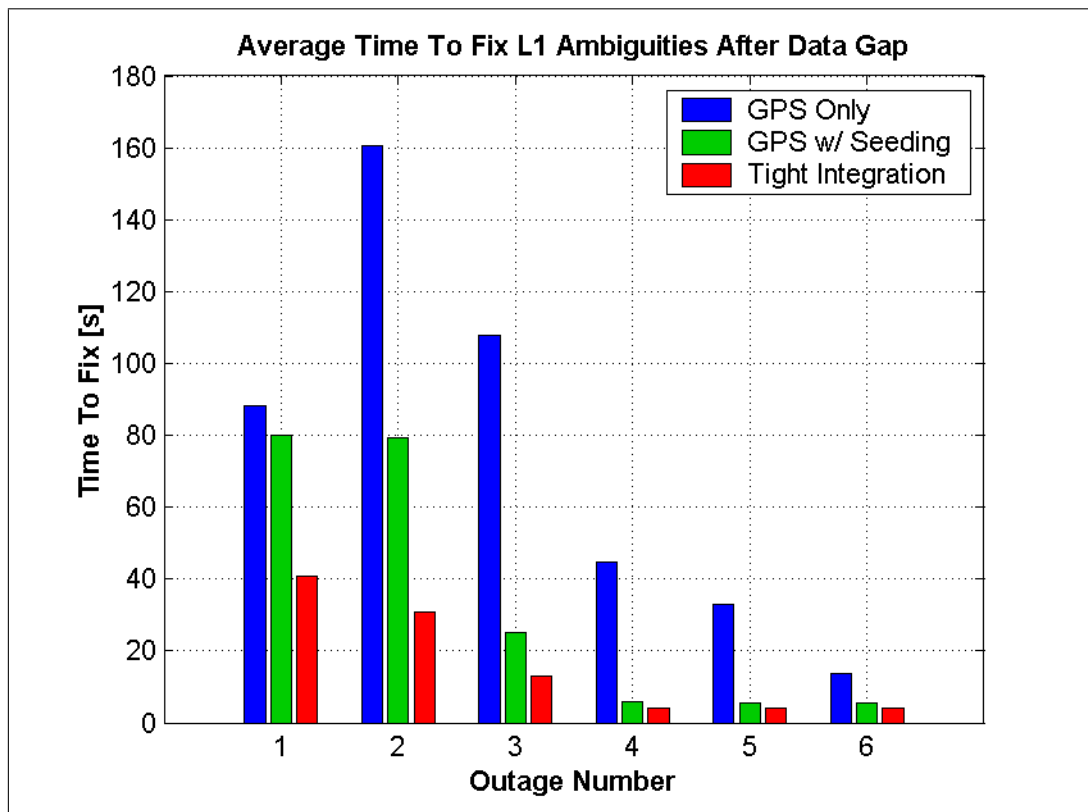
Figure 7.15: Average Time to Fix L1 Carrier Phase Ambiguities After Complete Data Outages for Run #1

approach outperforms the loose integration with seeding. While the improvement is not always significant, certain data outages show average times to fix being reduced by over 30 seconds.

The relative improvement of the tight integration over the loose integration with seeding can be attributed to three factors. First, the reduced amount of process noise in the former approach allows for a faster convergence of filter parameters, including the ambiguities. Second, the tight integration strategy is better able to mitigate code errors. This will be investigated in detail in Section 7.5.2. Third, the correlation between the ambiguity states and the other states being estimated in the

same filter will differ between the two cases. This is illustrated in Figure 7.16, which shows the absolute correlation coefficient between selected L1 ambiguity states and the position states as a function of time since the GPS data was recovered after a data outage. The results shown were generated using only a single data outage but are representative of other cases. Other ambiguities show similar behaviour and are therefore not included here to maintain figure clarity. For each ambiguity, there are three "lines", one for the correlation with each position coordinate. The plot is limited to time intervals of less than 50 seconds since this is longer the average time needed to resolve the ambiguities using the tight integration approach.

Although the correlations do not appear to be consistently larger or smaller for either approach, the individual values are clearly different. The values obtained using a given approach cannot be considered better than those of the other approach, however the fact that they differ will play a role in the ambiguity resolution process. In particular, Equation 3.12 shows that the cross-covariance (correlation) between the position and ambiguity states is important for reducing the ambiguity search space when updating the system with position observations.

Figure 7.17 shows the time needed to fix the L1 ambiguities using all integration strategies after each data outage and for all outage durations. This plot suggests that the average time to fix shown in Figure 7.15 is actually somewhat pessimistic. For example, consider the third data outage. In this case, the tight integration approach can correctly fix ambiguities in ten seconds or less for data outages lasting up to and including 30 seconds. For the 40 second outage however, the time needed to resolve the ambiguities increases to 90 seconds. This increases the average time to fix by ten full seconds. In contrast, the GPS-only performance remains basically
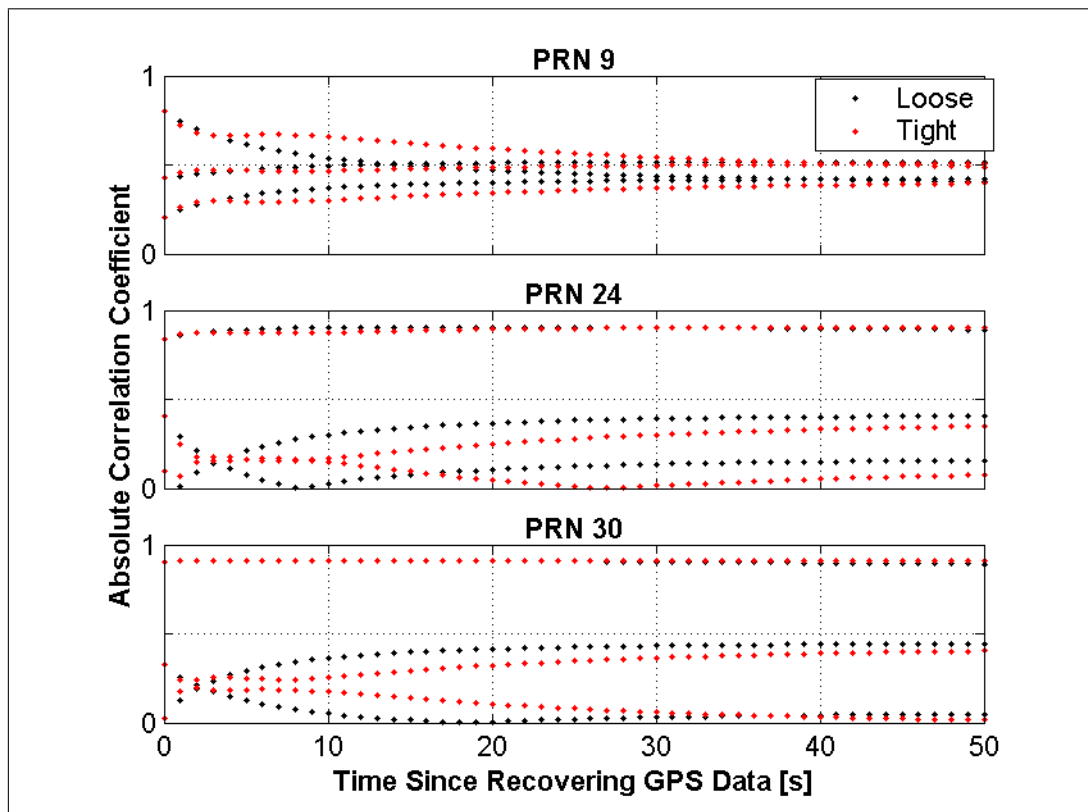
Figure 7.16: Absolute Correlation Coefficient Between Three PRN's Ambiguity States and Position States Using Loose Integration With Seeding and Tight Integration Strategies

constant for all data outage durations. Similar behaviour is also seen in the first two data outages. The reason for this is that, as shown in Section 7.3.1, after about 30 seconds the inertial system provides about the same amount of information as does a differential code solution. In other words, after about 30 seconds the INS does not provide significant improvement over the GPS-only case. As such, the time needed to resolve the ambiguities using the tight integration tends towards the GPS-only case. This provides some insight as to the possible limitations of the inertial system for ambiguity resolution.

A comparison of the relative improvements of the various integration strategies is

Figure 7.17: Time to Fix L1 Carrier Phase Ambiguities After Each Complete Data Outage for Run #1 Using Different Integration Strategies

shown in Table 7.6. The table shows the average percent improvement (across all data outages) in L1 ambiguity resolution times when using the various processing strategies. In this context, a 100% improvement represents an instantaneous fix. As expected, the advantage of using either integration approach is high for short data outages but gradually tends to zero. In this regard, the tightly coupled approach shows a much slower degradation. In general, the loose integration with seeding can provide a 50% reduction for data outages lasting up to about 20 seconds, while the tight integration can extend this performance to 30-second outages. This is also seen in the rightmost column which shows the relative improvement of the tight over the loose approach.

Table 7.6: Average Percent Improvement in L1 Ambiguity Resolution Times After Complete Data Outages Using Different Approaches for Run #1

Outage Duration [s]	Average Percent Improvement		
	Seeding Over GPS-Only	Tight Over GPS-Only	Tight Over Seeding
2	100.0	100.0	0.0
4	95.9	95.9	0.0
6	95.6	96.8	16.7
9	88.7	93.5	44.4
12	67.6	89.9	50.2
16	59.4	84.3	51.8
20	49.3	77.0	46.0
30	11.0	50.8	42.2
40	4.2	12.6	8.8

Figure 7.18 shows the time to fix the widelane ambiguities after all simulated data outages. All ambiguity fixes were correct in this case. Although both integrated solutions provide instantaneous fixing after all data outages, the improvement over the GPS-only case is minimal. Specifically, since GPS-only is capable of resolving the ambiguities in at most one second at all times, saving one second is not necessarily of great benefit. However, in applications where GPS coverage is sporadic, the ability to resolve ambiguities instantly would be desirable.

Partial Data Outages

Before investigating the ambiguity resolution performance after partial data outages, it is noted that loose integration with seeding has no real meaning in this context. The reason is that the seeding of the GPS-only filter was intended for use after complete data outages only. Therefore, both loose integration approaches degenerate to the GPS-only case.
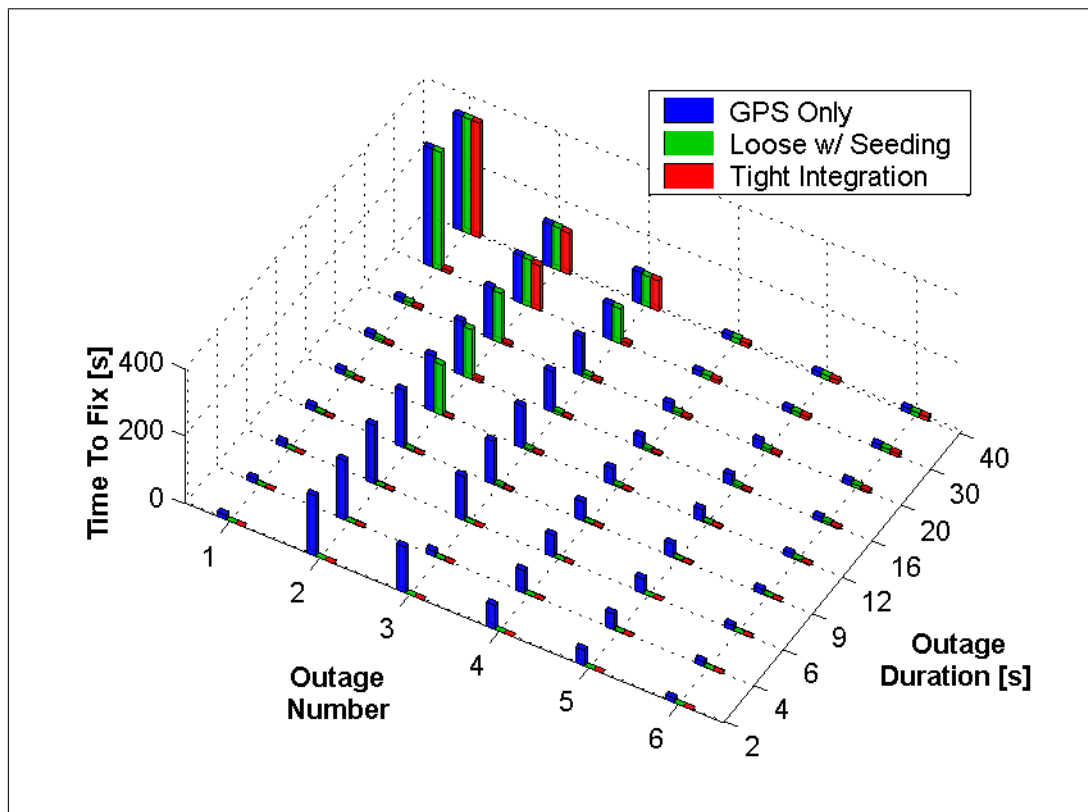
Figure 7.18: Time to Fix Widelane Carrier Phase Ambiguities After Each Complete Data Outage for Run #1 Using Different Integration Strategies

Figure 7.19 shows the L1 ambiguity resolution performance after all partial data outages. Again, no incorrect fixes occurred. Overall, the results parallel those of the complete data outage case shown above. One exception appears to be that for the second data outage, GPS-only performs consistently poorer than in all other data outages. The reason for this is three-fold

1. Recall from Figure 7.4 that at GPS time 508626 two low-elevation satellites experienced cycle slips, with a corresponding reduction in the measurement residuals. Since the data outage in question is simulated at approximately the same time, these two satellites are removed during the outage and their
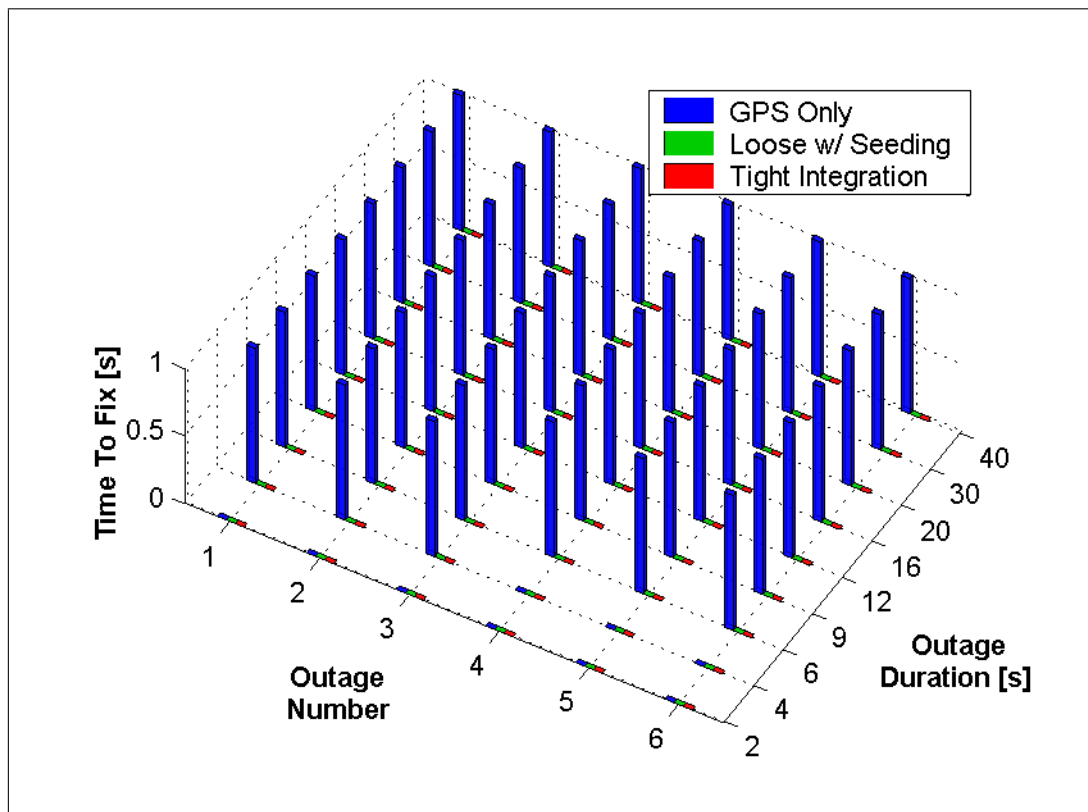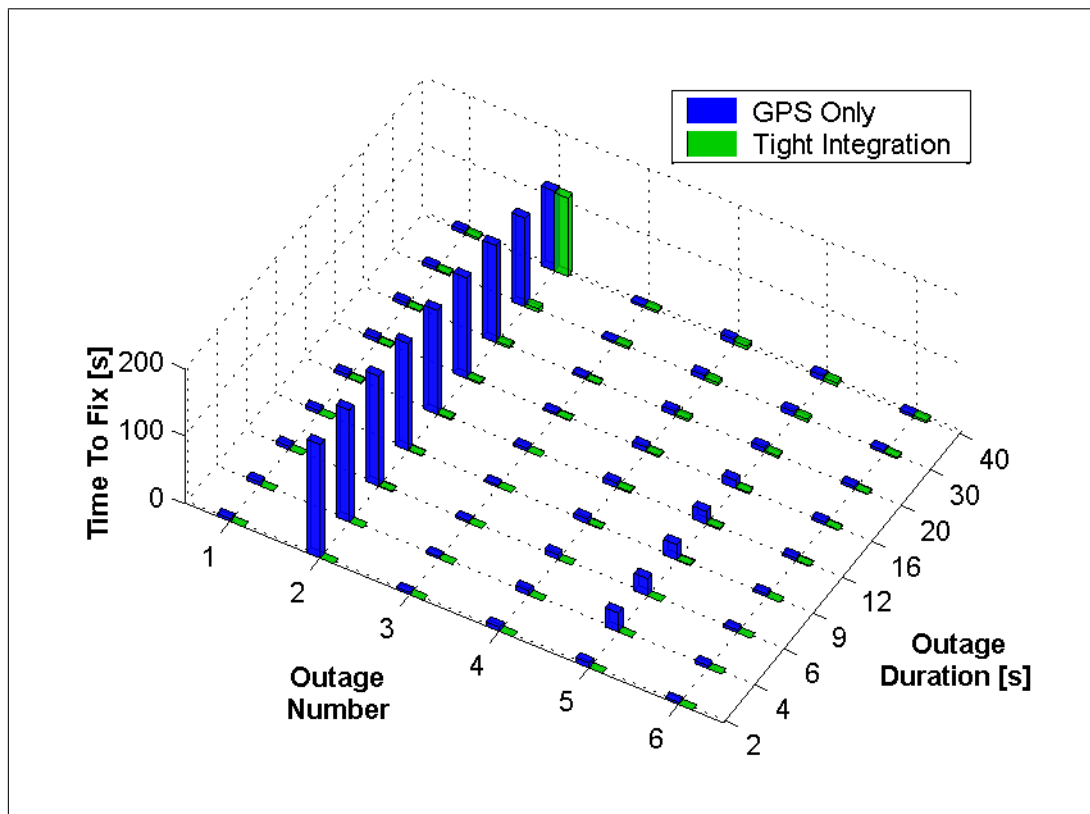
Figure 7.19: Time to Fix L1 Carrier Phase Ambiguities After Each Partial Data Outage for Run #1 Using Different Integration Strategies

ambiguities must be redetermined afterward. Given their relatively large errors, this will hinder the ambiguity resolution process.

2. Even after very short data outages, the GPS-only filter is incapable of providing an accurate position estimate. As such, the GPS-only filter is essentially forced to re-initialize itself after the data outage. Although some fixed ambiguity carrier phase measurements may still be available, their usefulness is limited in providing an accurate three-dimensional position.

3. The threshold value used for deciding when to resolve the ambiguities increases as the number of ambiguities decreases. This, combined with the increased er-

rors discussed in the first point, will adversely impact the ambiguity resolution process.

In contrast, the tight integration approach is capable of bridging the data outage with decimetre-level accuracy. This improved accuracy, combined the reduced process noise in the GPS/INS filter provides significant ambiguity resolution improvements. A summary of the relative improvements of the GPS-only and tight integration approaches are shown in Table 7.7. As with the complete data outages, the improvement of the tight integration slowly degrades with increasing outage duration.

Finally, resolution the widelane ambiguities after the partial data outages was instantaneous for all cases using both the GPS-only and the tight integration approach and so no plot is shown.

7.5.2   Results From Second Run

After analyzing the results of the first run, it was decided that fewer outage durations could be simulated. Consequently, the data outages for this run lasted 2, 5, 10, 15, 20, 30 and 40 seconds.

Complete Data Outages

A plot of the time needed to resolve the L1 ambiguities after all data outages is shown in Figure 7.20. For the most part, the results show characteristics similar to those of the first run. However, for data outages four and five, there are some situations where the GPS-only solution fixes faster than either of the integrated solutions. To help explain this, Table 7.8 shows the number of times the ambiguities were either fixed incorrectly or could not be fixed before the end of the data set.

Table 7.7: Average Percent Improvement in L1 Ambiguity Resolution Times After Partial Data Outages Using a Tight Integration Versus GPS-Only for Run #1

Outage Duration [s]	Average Percent Improvement
2	100.0
4	100.0
6	99.9
9	96.8
12	85.8
16	79.2
20	72.3
30	48.6
40	20.6

Results demonstrate a tremendous advantage when using either the loose coupling with seeding or the tight coupling approaches. Specifically, the inertial system is able to prevent incorrect fixes associated with the GPS-only solution. Unfortunately, only one of these incorrect fixes is actually replaced with a correct ambiguity fix when using an integrated approach. Otherwise, the integrated approach typically prevents the ambiguities from being resolved at all before the end of the data set. Although this is not the most ideal situation, it is far better than the alternative. There are also five situations in which the GPS-only solution could not fix the ambiguities before the end of the data set, that were eliminated using the integrated system.

The GPS-only "problems" listed in Table 7.8 all occurred on data outages four or

Table 7.8: Number of Times the L1 Ambiguities Were Fixed Wrong or Could Not Be Fixed After Complete Data Outages for Run #2

| Problem | Integration Strategy | | |
	GPS-Only	Loose w/ Seed	Tight
Wrong Fix	9	0	0
Could Not Fix	5	9	8
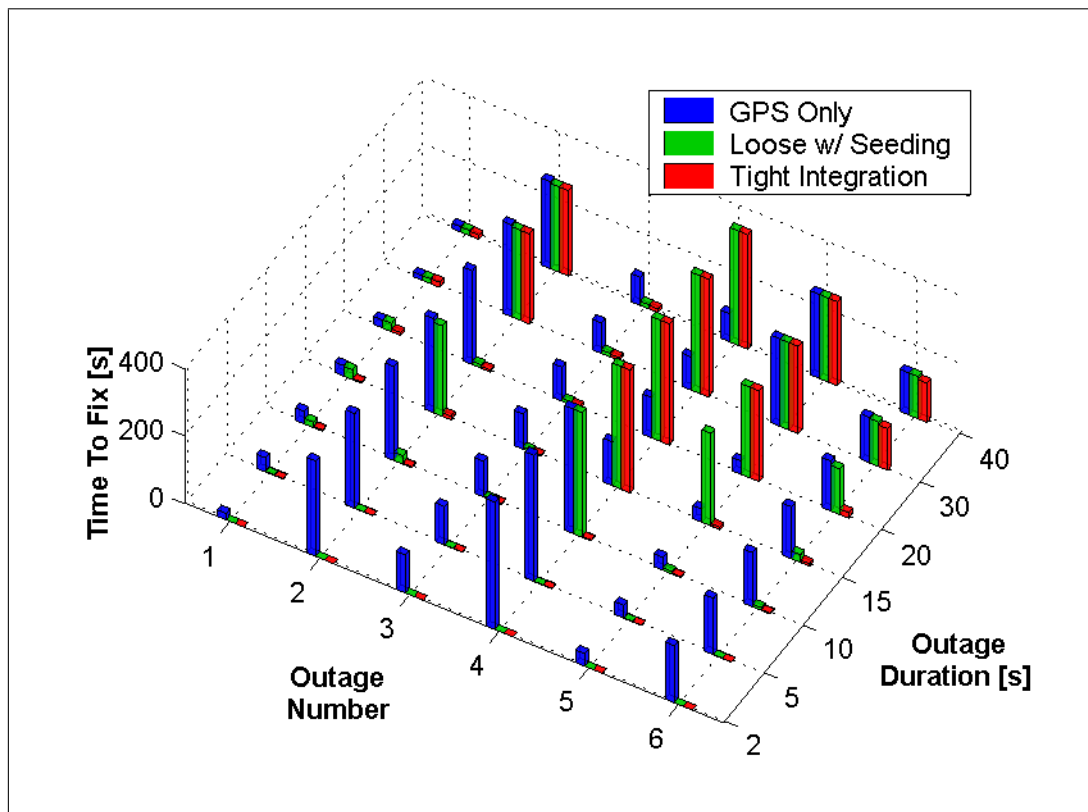
Figure 7.20: Time to Fix L1 Carrier Phase Ambiguities After Each Complete Data Outage for Run #2 Using Different Integration Strategies

five. These two outages occur the farthest from the base station, at a distance of about 7 and 5 km respectively. This suggests that perhaps the differential error sources are playing a role in this regard. From the truth trajectory analysis of this run, the fixed L1 carrier phase residuals near these outage times (GPS time 511360 and 511450) were at the 2 cm level. This represents about 10% of an L1 cycle and is therefore not negligible. Unfortunately, this cannot fully explain the results shown. For clarity, Figure 7.21 shows the ratio used to determine whether the ambiguities should be fixed as integers, as computed for the 20-second long outage for the fourth data gap. The graph starts at the first epoch after the data outage is over (i.e. the first epoch the GPS data becomes available), and continues for five minutes. Also
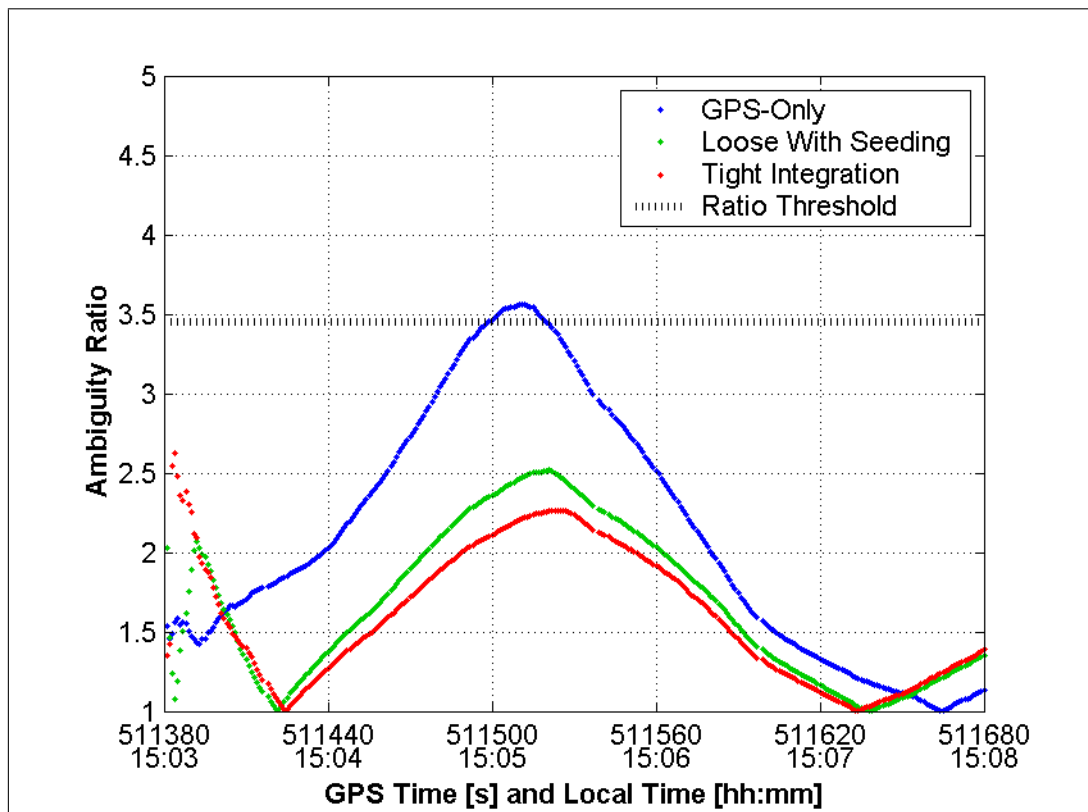
Figure 7.21: Ambiguity Ratio for L1 Carrier Phase Ambiguities After Complete Data Outage #4 Lasting 20 Seconds for Run #2 Using Different Processing Strategies

shown is the ambiguity ratio threshold for the five ambiguities trying to be resolved. Two important comments can be made about this plot. First, only the GPS-only ratio exceeds the threshold, and therefore is the only solution to provide an incorrect ambiguity fix. Second, the ratio using all three approaches shows a clear rise and fall effect, with the peak occurring shortly after GPS time 511500.

The rise and fall of the ratio values is likely caused by code errors. Figure 7.22 shows the GPS-only ambiguity ratio from Figure 7.21 along with the pseudorange residuals for two satellites computed from the truth trajectory. Since the truth solution is accurate to the centimetre-level, the code residuals can essentially be considered
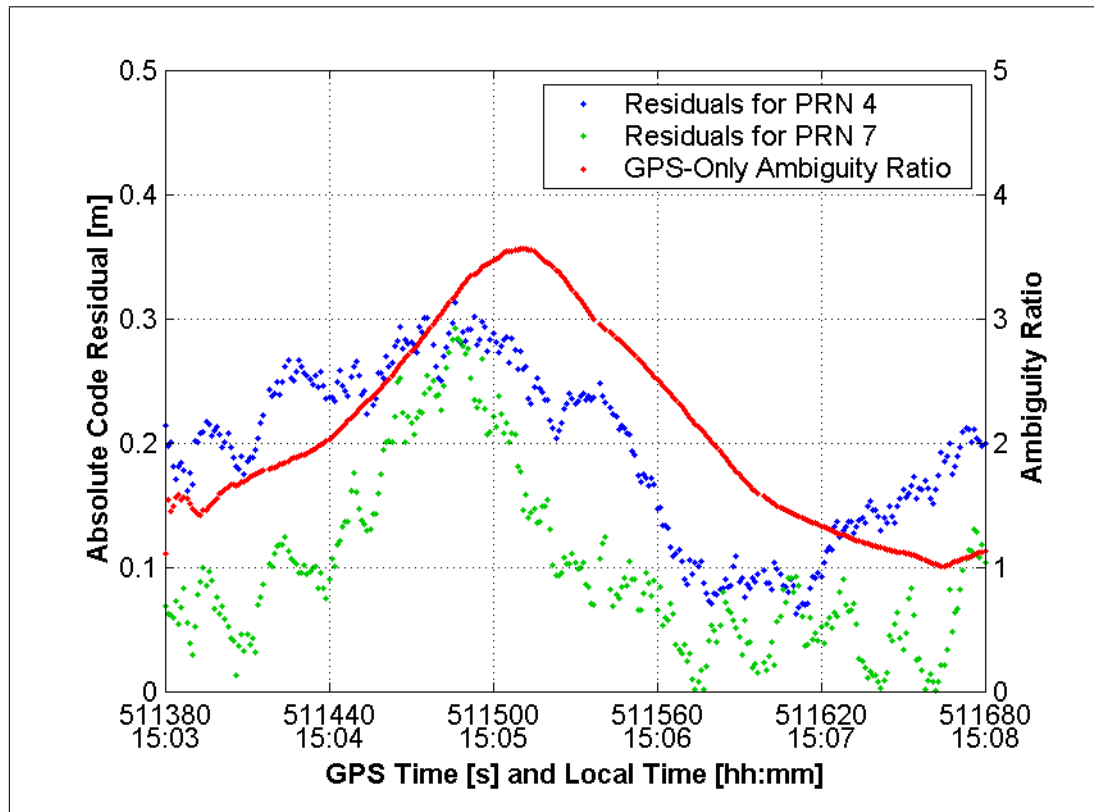
Figure 7.22: Code Residuals and GPS-Only L1 Carrier Phase Ambiguity Ratio After Complete Data Outage #4 Lasting 20 Seconds for Run #2

equivalent to the code errors. This being the case, there appears to be a strong correlation between the code errors and the increased ambiguity ratio. Normally, the ratio is considered to decrease with increasing error. However, caution must be exercised here because the "best" ambiguity set which is driving the ambiguity ratio higher is already known to be incorrect. With this in mind, the increased code error can be interpreted as forcing the ambiguities towards the wrong integer values.

This conjecture can be supported in two ways. First, from Figure 7.21, the maximum ambiguity ratio obtained using the loose and the tight coupled approaches were significantly lower than that of GPS alone. This makes sense since these two approaches

will be less sensitive to code errors because of the additional information provided by the inertial system. Second, Figure 7.23 compares the L1 ambiguity ratios of the 20-second outage shown in Figure 7.21 with the equivalent results from the 40 second data outage. Again, the rise and fall of the ratios is evident in both cases. However, more importantly, the maximum values occur at approximately the same time. This supports the idea that the peak is correlated with systematic effects. Second, the difference between the three processing approaches is considerably reduced for the 40-second data outage. This also agrees with the above because as the data outages increase in duration, the inertial information provides less information to the integrated solutions. In this way, the integrated solutions become more susceptible to code errors. It can be concluded therefore that the integrated ambiguity resolution approaches are more robust against code errors than is GPS alone.

A final note regarding Figure 7.21 (or the top plot in Figure 7.23) is that after about GPS time 511650, the ambiguity ratio for the loose integration with seeding and the tight integration approaches are larger than of GPS alone. Assuming the increase in the ratio is due the correct ambiguity set, this suggests that the integrated solutions would still provide a faster ambiguity resolution time, relative to GPS alone.

A summary of the relative improvements in time needed to fix the L1 ambiguities is shown in Table 7.9. The results were computed without considering the fourth or fifth data outages because of the problems resolving the ambiguities with GPS alone. The results parallel those from the first run and are not be discussed in detail.

The ambiguity resolution results when using widelane carrier phase data are shown in Figure 7.24. As with the first run, the overall improvements are not as significant as with the L1 ambiguities. However, there are some situations in the fourth data
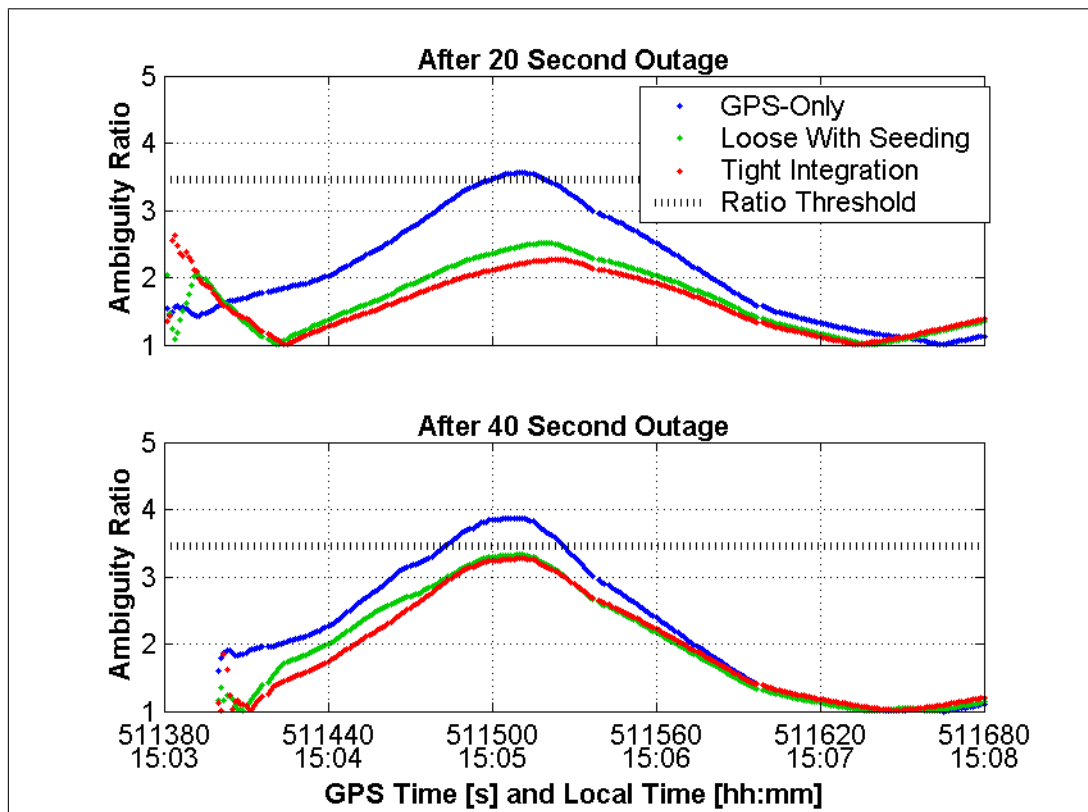
Figure 7.23: Ambiguity Ratios for L1 Carrier Phase Ambiguities After Complete Data Outage #4 Lasting 20 and 40 Second for Run #2 Using Different Processing Strategies

outage where significant performance improvements are seen. This further supports the theory discussed above regarding the effect of the code measurement errors on the ambiguity resolution process. In particular, while the increased code errors were not large enough in this case to cause the WL ambiguities to be fixed incorrectly, they still played a role in the overall ability to identify the true ambiguity set.

Finally, a summary of the improvements in the time needed to fix the WL ambiguities is shown in Table 7.10. As expected, the results using either of the integrated approaches is considerably better than when using GPS alone. Note that the negative improvement of the tight coupling over the loose coupling with seeding (for the 40 s

outage) is due to one data outage where the two approaches fixed in two and one seconds respectively. This represents a 100% degradation (relative to the loose case) which, when averaged across six data outages, gives 16.7%.
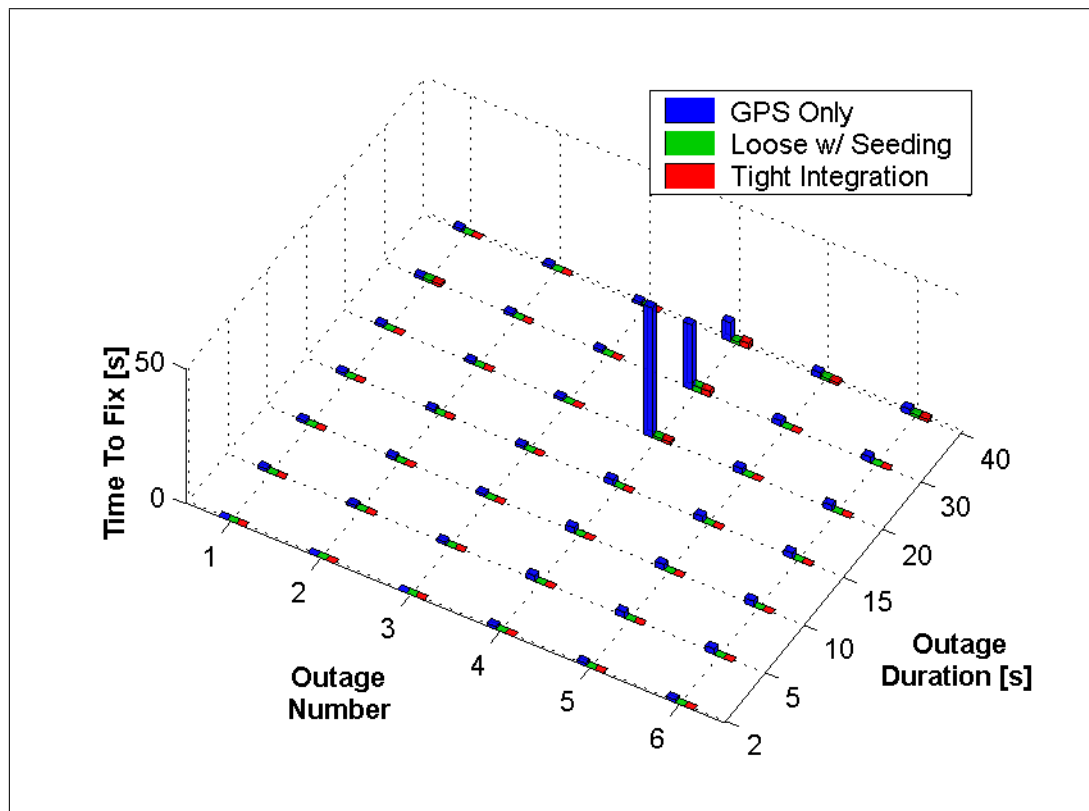

Figure 7.24: Time to Fix Widelane Carrier Phase Ambiguities After Each Complete Data Outage for Run #2 Using Different Integration Strategies

Table 7.9: Average Percent Improvement in L1 Ambiguity Resolution Times After Complete Data Outages Using Different Approaches for Run #2

Outage Duration [s]	Average Percent Improvement[1]		
	Seeding Over GPS-Only	Tight Over GPS-Only	Tight Over Seeding
2	100.0	100.0	0.0
5	98.4	98.4	0.0
10	84.7	95.9	62.6
15	47.2	93.7	73.6
20	48.0	86.9	57.4
30	23.0	23.4	4.5
40	23.4	28.7	7.2

[1]Does not consider data outages four or five.

Table 7.10: Average Percent Improvement in Widelane Ambiguity Resolution Times After Complete Data Outages Using Different Approaches for Run #2

Outage Duration [s]	Average Percent Improvement		
	Seeding Over GPS-Only	Tight Over GPS-Only	Tight Over Seeding
2	50.0	50.0	0.0
5	100.0	100.0	0.0
10	100.0	100.0	0.0
15	100.0	100.0	0.0
20	99.7	99.7	0.0
30	81.9	81.9	0.0
40	81.0	78.6	-16.7

Partial Data Outages

The L1 and widelane ambiguity resolution times after each simulated data outage are shown in Figures 7.25 and 7.26 respectively. For the L1 ambiguities, similar problems to those experienced with the complete data outages were experienced. In this case, the increased code errors did not cause any incorrect fixes, but simply

Figure 7.25: Time to Fix L1 Carrier Phase Ambiguities After Each Partial Data Outage for Run #2 Using Different Integration Strategies

prevented ambiguity resolution for all outage durations for gaps four and five. The WL ambiguity resolution using GPS-only was also hindered by the code errors during the fourth data outage. However, as before, the tight integration performed better and more consistently across all outage durations.

7.5.3 Summary

The analysis of the previous sub-sections shows that using the information provided by the inertial system can dramatically improve ambiguity resolution time and can improve the reliability of the ambiguity fix, relative to GPS-only. In this regard, the
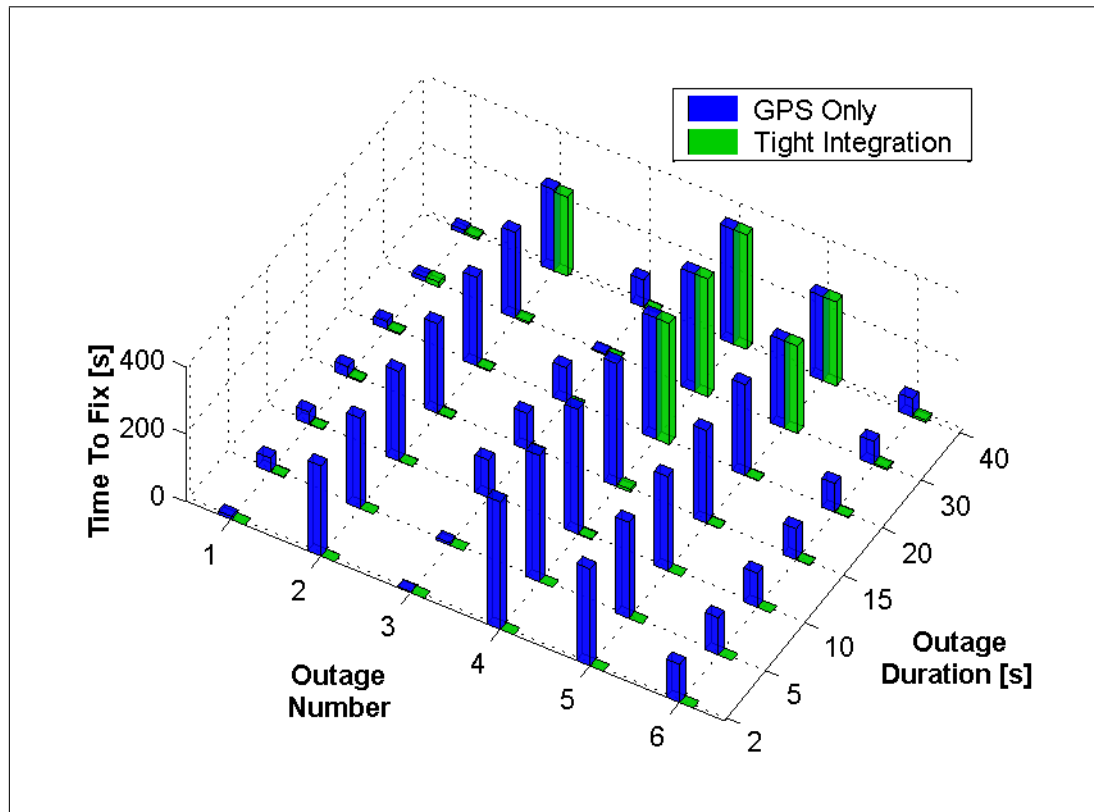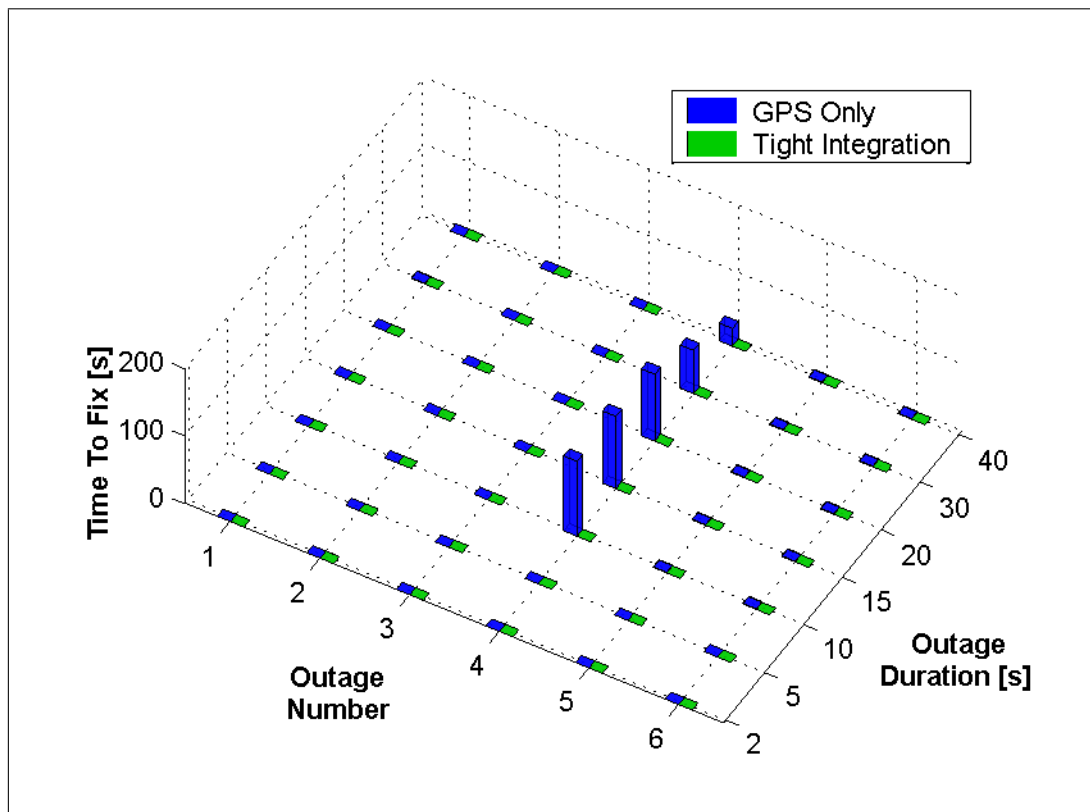
Figure 7.26: Time to Fix Widelane Carrier Phase Ambiguities After Each Partial Data Outage for Run #2 Using Different Integration Strategies

loose integration with INS seeding does not perform as well as the tight integration approach. The difference is attributed mostly to the reduced process noise in the tight integration approach. The slightly slower error drift of the tight integration solution during data outages will also play a role in this regard.

7.6 Statistical Reliability

Statistical reliability parameters can be computed in the absence of actual measurements using only the covariance information from a Kalman filter and an assumed or expected observation geometry and precision. This approach was not used herein

because the dynamics matrix of the INS error states is a function of the measured specific forces. With this in mind, the simulation of a realistic trajectory would therefore be required to obtain useful reliability information. Such a simulation is beyond the scope of this dissertation. Instead, the reliability parameters were computed for the two trajectories analyzed in the previous section. While this represents only a small sample of all possible scenarios, it serves to illustrate the statistical reliability parameters obtained using different integration and measurement updating strategies.

The analysis begins by investigating the internal reliability parameters using GPS-only and the tight integration strategy. Next, the external reliability parameters for GPS-only, loose coupling and tight coupling are compared. Finally, a brief comparison of the reliability using sequential versus simultaneous updates is shown. All analyses assume the following statistical parameters

$$\alpha = 0.1\%$$

$$\beta = 10\%$$

$$\delta_0 = 4.57$$

7.6.1 Internal Reliability

As discussed in Section 6.2, since blunders can only enter the system before the GPS-only filter in the loose integration strategy, the internal reliability parameters for that filter apply equally to the GPS-only and loose integration cases. These values will therefore be referred to as GPS-only values. These will be compared to the corresponding values from the GPS/INS filter using the tight integration strategy.

To simplify the following analysis, all reported values in this section were computed assuming all observations are processed simultaneously. A comparison of the sequential and simultaneous processing strategies is given in Section 7.6.3.

Marginally Detectable Blunders

Figure 7.27 shows the code, Doppler and L1 phase MDBs for all satellites using GPS-only and the tight integration approach, for the first run. The results for the second run are very similar (as shown in Tables 7.11 and 7.12) and are therefore not shown graphically. The graph is not intended to identify individual satellites, but to show the relative improvement when using a tight integration approach. The "outlying" points (e.g. just before 508650) occur when one or more satellites' ambiguities are being estimated in the filter, due to signal masking of low satellites or cycle slips. The advantage of the tight integration approach is minimal when considering the code measurements (the green dots basically cover all of the blue ones). This is because of the relatively high measurement noise of the double difference code observations, which is on the order of 1–2 m. As such, improving the GPS-only filter's predicted covariance from the decimetre-level to the centimetre-level by using the tight integration provides little benefit. The Doppler and carrier phase measurements however, show considerable reductions in the MDBs when using the inertial system.

To better quantify the improvements on a satellite-by-satellite basis, the RMS MDB (over time) for all satellites using GPS-only and a tight integration approach is summarized in Tables 7.11 and 7.12 for the first and second runs respectively. As implied in Figure 7.27, the code MDBs are identical to the centimetre-level. With the Doppler, the MDBs are reduced by as little as about 5 cm/s or as much as about 25 cm/s depending on the satellite. Similar improvements are seen with the phase

Table 7.11: RMS Code, Doppler and Phase MDBs for Each Satellite Using GPS-Only and a Tight Integration for Run #1

PRN	Code [m]		Doppler [cm/s]		L1 Phase [cm]	
	GPS	Tight	GPS	Tight	GPS	Tight
5	4.47	4.47	41.7	27.0	27.9	20.0
7	4.58	4.58	33.5	27.6	22.4	19.8
9	4.53	4.53	32.3	27.3	21.5	19.4
20	5.19	5.19	50.4	31.4	33.7	23.8
24	4.58	4.58	49.6	27.7	33.2	21.2
30	5.22	5.22	46.7	31.6	31.2	23.6

Table 7.12: RMS Code, Doppler and Phase MDBs for Each Satellite Using GPS-Only and a Tight Integration for Run #2

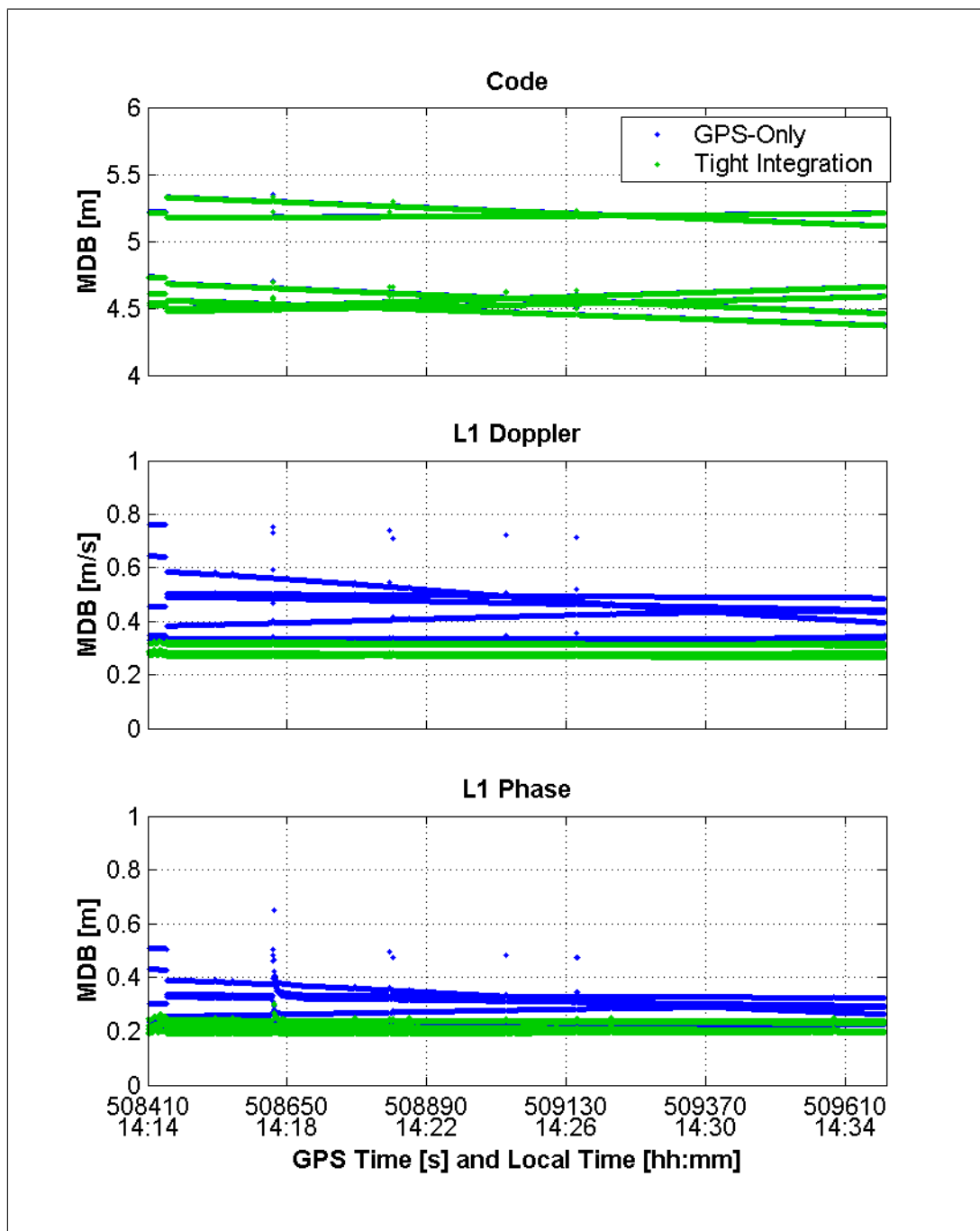| PRN	Code [m]		Doppler [cm/s]		L1 Phase [cm]	
	GPS	Tight	GPS	Tight	GPS	Tight
4	4.23	4.23	32.8	25.5	22.2	18.4
5	4.21	4.20	35.9	25.3	24.0	18.5
7	4.89	4.89	54.3	29.6	37.2	22.5
9	4.80	4.79	53.7	29.0	35.6	22.3
20	5.29	5.29	48.7	32.0	32.6	24.1
24	4.24	4.24	33.1	25.6	22.5	18.5
30	4.88	4.88	48.4	29.6	32.7	22.5

Figure 7.27: Code, Doppler and L1 Phase MDBs for All Satellites Using GPS-Only and a Tight Integration Approach for Run #1

measurements, where reductions of 2–15 cm are evident. These values represent significant improvements, however their impact on the final solution is ultimately of interest. This will be investigated in Section 7.6.2.

Cycle Slip Detection

The carrier phase MDBs of Tables 7.11 and 7.12 can be interpreted as the system's ability to identify cycle slips. In this regard, the most difficult cycle slip to detect is a one-cycle cycle slip, or an approximately 19 cm blunder for L1. The results show that the tight integration approach is capable of detecting blunders on the order of one cycle. However, a more tangible comparison is still desirable. For this, recall Equation 2.48, which is reproduced here for convenience

$$\nabla_{k_i}^{MDB} = \frac{\delta_0}{\sqrt{\left(C_{v_k}^{-1}\right)_{ii}}}$$

This equation is used to compute the MDB for the ith observation, given a non-centrality parameter and the covariance matrix of the innovations. For the analysis at hand, the problem is changed such that the non-centrality parameter is the parameter to be computed assuming a blunder of one cycle and using the innovation covariance matrix. With the non-centrality parameter computed, and assuming a fixed value for α, the value of the normal distribution at the $(1 - \beta)$ point can be computed from Equation 2.47 as

$$\delta_0 = n_{1-\alpha/2} + n_{1-\beta}$$

The above two equations can then be combined to yield

$$n_{1-\beta} = \sqrt{\left(C_{v_k}^{-1}\right)_{ii}} - n_{1-\alpha/2}$$

where it noted that the blunder assumes a value of unity (i.e. one cycle). The above value is then used to compute the corresponding value of $(1-\beta)$, which represents the probability of detecting a one-cycle cycle slip. Using this approach, the probability of detecting a one-cycle L1 cycle slip using GPS-only and the tight integration approach is shown in Figure 7.28 for the first run. This plot shows a tremendous advantage for the tight integration strategy. Specifically, cycle slip detection probabilities for all satellites remain above 50% at all times using the integrated approach. In contrast, GPS-only has some satellites that have less than a 20% chance of having a cycle slip detected. Since an undetected cycle slip is equivalent to an incorrect ambiguity fix, the improved ability to detect a single-cycle cycle slip with the tightly coupled approach is significant. Results of the second run are similar to those shown and are therefore not included.

Results for widelane show that GPS alone is capable of detecting single-cycle cycle slips with better than 99% probability, because of the longer wavelength. While the integrated approach does improve on this, the improvements are not as significant as with L1.

7.6.2   External Reliability

This section investigates the impact of the MDBs presented in the previous section on the estimated parameters. For the GPS-only blunders, the corresponding (GPS-only) external reliability parameters will be computed. However, the effect of these blunders after having passed through the INS-only filter are also computed, as this represents the external reliability of the loosely integrated system. Finally, the tightly coupled protection levels are also investigated. As in the previous sec-
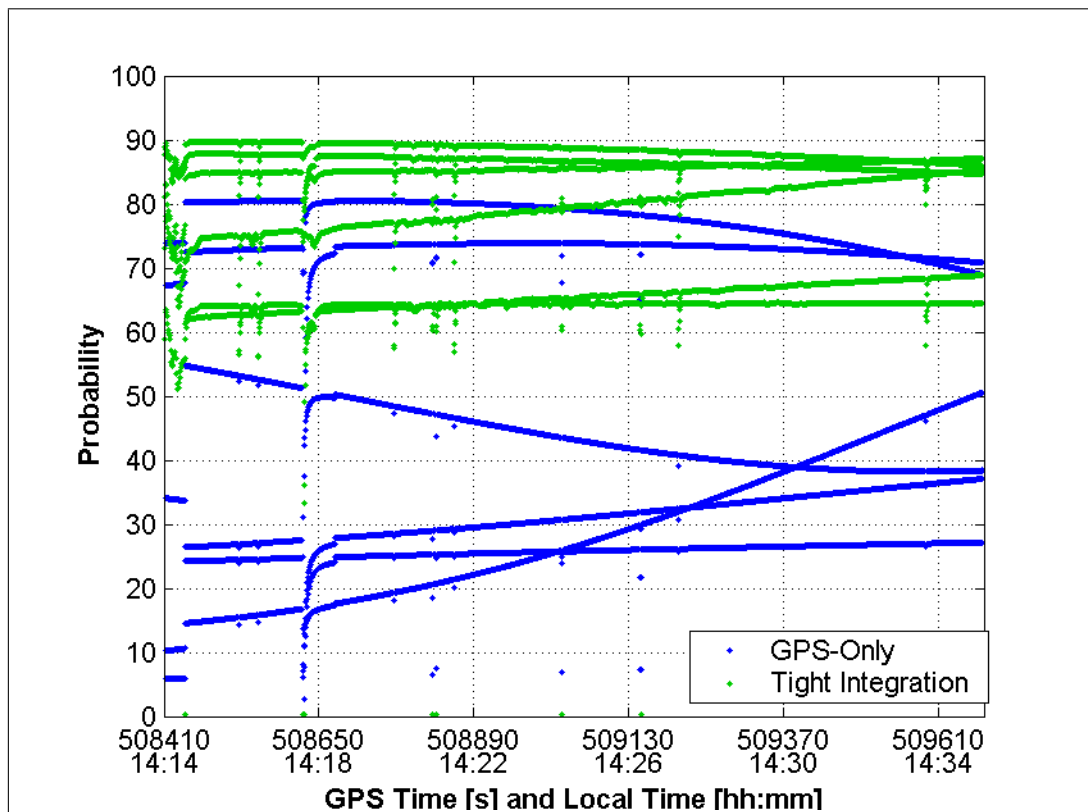
Figure 7.28: Probability of Detecting a One-Cycle L1 Cycle Slip for All Satellites Using GPS-Only and a Tight Integration Approach for Run #1

tion, the blunders used to compute the protection levels were computed using the simultaneous updating approach.

Figures 7.29 to 7.31 respectively show the protection levels for the code, Doppler and carrier phase observations for PRN 5 using GPS-only, loose integration (after INS-only filter) and tight integration. Each figure breaks the protection levels down into horizontal and vertical components. Results for this satellite are shown because they most clearly show (graphically) the difference between the different approaches. Other satellites exhibit the same general behaviour. The following subsections investigate this satellite's PLs for the various observations individually.
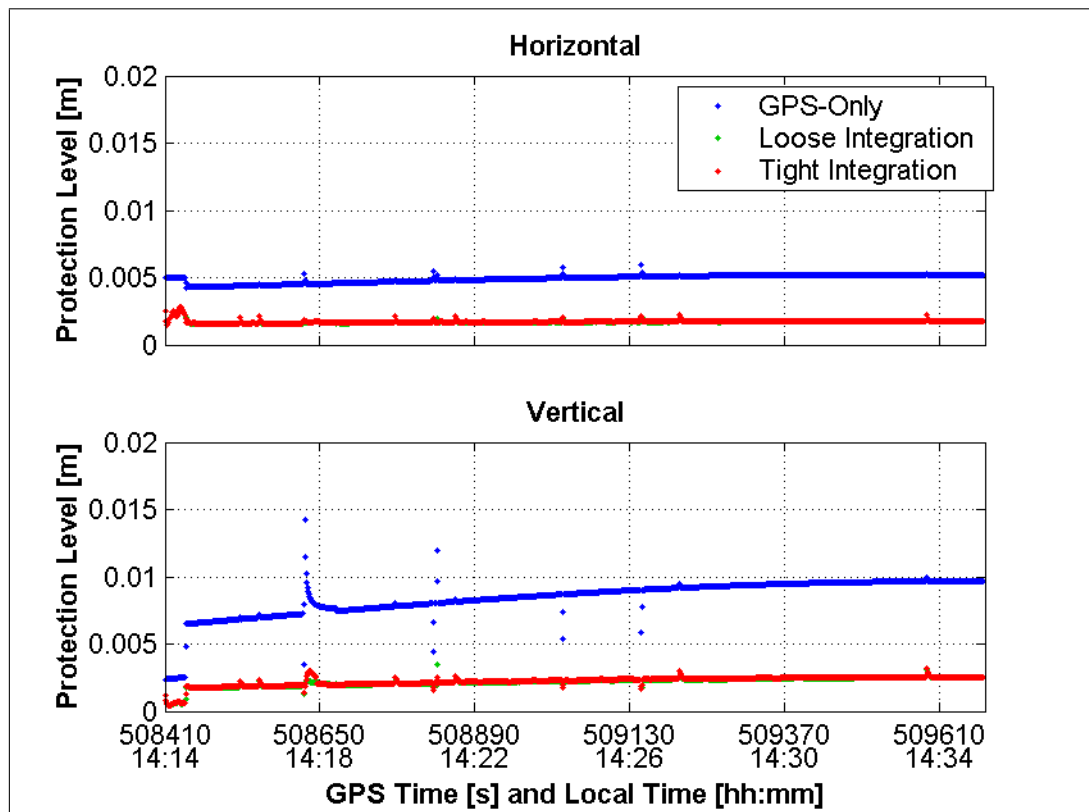
Figure 7.29: Horizontal and Vertical Position Protection Levels for Code MDBs of PRN 5 Using Different Processing Strategies for Run #1

Code

Despite the fact that the GPS-only and tight integration code MDBs are essentially the same, Figure 7.29 illustrates that their protection levels are different. Overall, the PLs are small because of the high accuracy of the carrier phase data. Typical values are lower than 1 cm for GPS-only. However, the tight integration strategy is capable of providing better performance with PLs of less than 5 mm. Finally, the loose and tight integration approaches show very little difference. In general, the effect of code blunders on the final solution is not very significant, even with GPS alone.
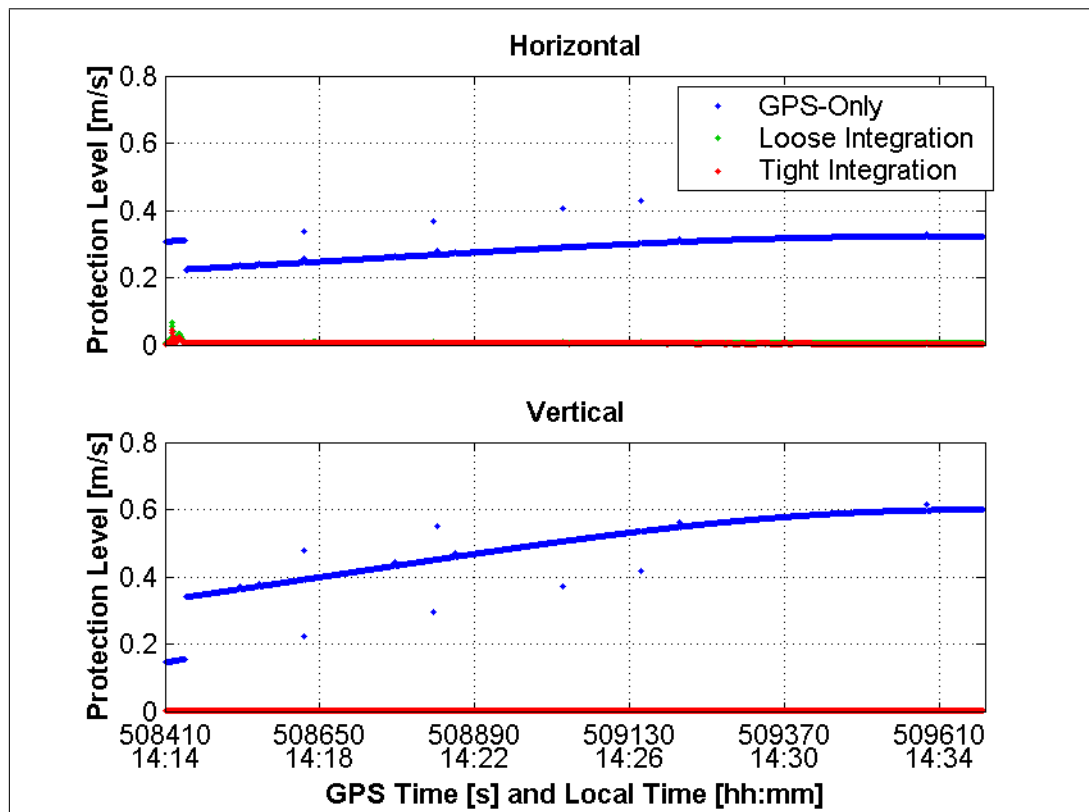
Figure 7.30: Horizontal and Vertical Velocity Protection Levels for Doppler MDBs of PRN 5 Using Different Processing Strategies for Run #1

Doppler

Figure 7.30 shows that the improvement of the velocity protection levels are very significant when using the inertial system. Note that the loose and tight integration strategies are indistinguishable at this scale. In fact, both of these implementations provide protection levels at the millimetre per second level, as shown in the Tables 7.13 and 7.14. This magnitude of improvement over GPS-only, namely decimetres per second, can be attributed to the inertial system's ability to provide very accurate velocity estimates over short time intervals. As such, any error in the Doppler measurements can be effectively filtered out.
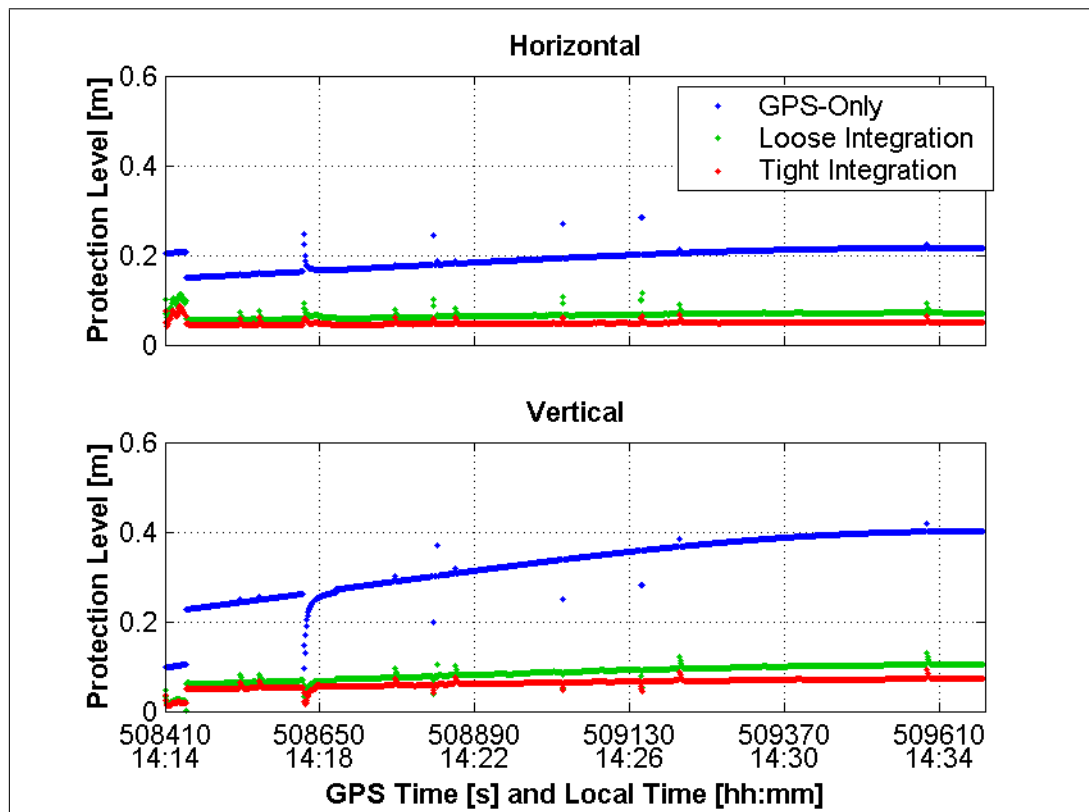
Figure 7.31: Horizontal and Vertical Position Protection Levels for L1 Carrier Phase MDBs of PRN 5 Using Different Processing Strategies for Run #1

Carrier Phase

The L1 phase PLs for the integrated solutions shown in Figure 7.31 also show very significant improvements relative to the GPS-only case. In particular, the GPS-only PLs are improved from the decimetre-level to a few centimetres using either integration approach. Again, the reason for this is that the inertial system can provide very accurate position differences over the short term. The improvement is not as significant as for Doppler measurements because the extra integration introduces more uncertainty into the inertial positions. Also of note is that the tight integration can be seen to offer an advantage over the loose integration of up to a few centimetres.

Summary

To better quantify the protection levels using the different integration strategies, Tables 7.13 and 7.14 show the RMS horizontal (HPL) and vertical (VPL) protection levels for all satellites for the first and second runs respectively. Overall, both runs show similar performance. However, in the second run, the data outage caused by the highway sign (at GPS Time 511291) does cause the GPS-only reliability values to increase considerably for some satellites. The RMS PLs for some satellites are therefore larger than in the first run. For example, the protection levels for PRN 9 show large increases for code, Doppler and carrier phase blunders relative the first run. Fortunately, the integrated approaches are able to keep these protection levels down to a more reasonable level, although still larger than in the first run where fixed ambiguities are maintained throughout.

Otherwise, as stated previously, the protection level for the code observations is generally not of major concern and will not be discussed further. In terms of the effect of Doppler errors on the velocity solution, both integrated solutions provide 1 cm/s reliability, worst case. Relative to GPS-only, this represents an improvement of almost two orders of magnitude in some cases, with better than ten-fold improvements being typical. Also of note is that the tight integration does offer an improvement over the loose integration. Although the improvement is not typically very large, PRN 9 in the second run does show a 50% improvement in the HPL. Nevertheless, the tight integration approach does offer more protection and is therefore more applicable to safety critical applications.

The effect of L1 carrier phase blunders on the position estimate using the integrated approaches is also considerably better than the GPS-only case with decimetre-level

Table 7.13: RMS Code, Doppler and L1 Phase Protection Levels for Each Satellite Using Different Integrations for Run #1

| PRN | HPL | | | VPL | | |
	GPS	Loose	Tight	GPS	Loose	Tight
Code Position Protection Levels [cm]						
5	0.5	0.2	0.2	0.9	0.2	0.2
7	0.3	0.1	0.1	0.2	0.1	0.1
9	0.3	0.1	0.1	0.2	0.1	0.1
20	0.2	0.1	0.1	0.7	0.2	0.2
24	0.6	0.2	0.2	0.7	0.2	0.2
30	0.2	0.1	0.1	0.7	0.2	0.2
Doppler Velocity Protection Levels [cm/s]						
5	28.9	0.7	0.5	50.0	0.2	0.2
7	12.1	0.5	0.4	9.8	0.1	0.0
9	12.0	0.5	0.4	8.8	0.1	0.0
20	13.8	0.8	0.5	40.5	0.3	0.2
24	40.4	0.9	0.5	50.0	0.2	0.1
30	10.7	0.6	0.4	34.2	0.3	0.2
L1 Phase Position Protection Levels [cm]						
5	19.4	6.7	4.9	33.4	8.7	6.3
7	8.2	3.6	3.1	7.1	1.7	1.5
9	8.0	3.4	3.1	5.9	1.5	1.4
20	9.2	4.7	3.3	27.3	7.4	5.2
24	27.0	9.8	6.3	33.8	8.6	5.5
30	7.1	3.8	2.9	22.8	6.3	4.8

improvements being common. As with Doppler observations, the tight integration offers more protection than does the loose integration with improvements of several centimetres in some cases. For example, PRN 9 in the second run shows an improvement of about 3 cm for each of the horizontal and vertical channels when using the tight versus the loose integration. Given that the quoted accuracy of the system under ideal conditions is at the centimetre-level, this level of improvement is not negligible and represents a significant advantage of the tight integration.

Table 7.14: RMS Code, Doppler and L1 Phase Protection Levels for Each Satellite Using Different Integrations for Run #2

PRN	HPL			VPL		
	GPS	Loose	Tight	GPS	Loose	Tight
Code Position Protection Levels [cm]						
4	3.7	0.4	0.2	2.8	0.4	0.2
5	0.4	0.1	0.1	0.7	0.2	0.2
7	1.2	0.2	0.1	0.9	0.2	0.2
9	4.7	0.5	0.2	3.4	0.4	0.2
20	0.2	0.1	0.1	0.5	0.2	0.2
24	1.9	0.3	0.2	1.2	0.1	0.1
30	1.3	0.2	0.2	0.8	0.1	0.1
Doppler Velocity Protection Levels [cm/s]						
4	13.7	0.5	0.4	25.1	0.2	0.1
5	20.6	0.6	0.4	38.6	0.3	0.2
7	23.5	0.9	0.5	45.7	0.3	0.2
9	35.5	1.0	0.5	45.5	0.3	0.2
20	12.1	0.7	0.5	29.1	0.3	0.2
24	19.5	0.6	0.4	15.4	0.1	0.1
30	27.7	0.9	0.5	24.3	0.2	0.1
L1 Phase Position Protection Levels [cm]						
4	10.1	3.7	3.2	19.8	4.7	4.0
5	13.8	5.0	3.8	25.8	7.4	5.8
7	16.3	7.1	4.0	31.9	9.0	5.0
9	23.1	8.6	5.5	30.1	8.4	5.5
20	8.1	4.2	3.2	19.5	5.8	4.4
24	14.7	5.2	4.2	10.2	2.9	2.3
30	19.0	7.7	5.1	17.3	4.7	3.0

7.6.3 Sequential Versus Simultaneous Updates

The previous analysis only considered the case where all observations are processed simultaneously. This section contrasts the above results with those obtained using a sequential updating strategy, assuming a tight integration approach.

Tables 7.15 and 7.16 show the RMS MDBs for all satellites using the different up-dating strategies. As can be seen, the difference between the two approaches is negligible, with the maximum differences being 1 mm/s or 1 mm for Doppler and carrier phase measurements respectively. This being the case, the two approaches are deemed equivalent in a practical sense. Furthermore, because of the small differences in the internal reliability parameters, the external reliability parameters are identical to the millimetre and millimetre per second level and are therefore not shown.

Table 7.15: RMS Code, Doppler and Phase MDBs For Each Satellite Using Sequential (Seq.) and Simultaneous (Sim.) Updating Strategies For Run #1

PRN	Code [m]		Doppler [cm/s]		L1 Phase [cm]	
	Seq.	Sim.	Seq.	Sim.	Seq.	Sim.
5	4.47	4.47	27.0	27.0	20.0	20.0
7	4.58	4.58	27.7	27.6	19.8	19.8
9	4.53	4.53	27.4	27.3	19.4	19.4
20	5.19	5.19	31.5	31.4	23.8	23.8
24	4.58	4.58	27.7	27.7	21.2	21.2
30	5.22	5.22	31.7	31.6	23.6	23.6

Table 7.16: RMS Code, Doppler and Phase MDBs For Each Satellite Using Sequential (Seq.) and Simultaneous (Sim.) Updating Strategies For Run #2

PRN	Code [m]		Doppler [cm/s]		L1 Phase [cm]	
	Seq.	Sim.	Seq.	Sim.	Seq.	Sim.
4	4.23	4.23	25.6	25.5	18.4	18.4
5	4.21	4.20	25.4	25.3	18.5	18.5
7	4.89	4.89	29.7	29.6	22.5	22.5
9	4.79	4.79	29.1	29.0	22.3	22.3
20	5.29	5.29	32.1	32.0	24.1	24.1
24	4.24	4.24	25.6	25.6	18.5	18.5
30	4.88	4.88	29.6	29.6	22.5	22.5

7.7   Summary

This chapter used real-time algorithms in post-mission mode to analyze the performance of an integrated GPS/INS system. By simulating data outages, position accuracy during complete data outages was shown to be better than one decimetre for about five seconds using L1 carrier phase data. Accuracies reached the level of typical DGPS code accuracies after approximately 30 seconds. This improvement in accuracy, relative to GPS-only, was found to improve L1 ambiguity resolution times by up to 50% for data outages lasting up to 30 s when using a tight integration approach. Ambiguity resolution results using a loosely coupled approach with feedback also significantly outperformed GPS alone, but were not as good as with the tight integration approach.

Using either loose integration with feedback or tight integration approaches, the ability to resist code errors during the ambiguity resolution process was shown. In particular, the GPS-only solution was shown to produce several incorrect ambiguity fixes (due to code errors), while the corresponding integrated approaches simply could not resolve the ambiguities as integers before the end of the data set. While this is not an ideal situation, it shows that the integrated system is inherently more robust to code errors and should therefore be considered more reliable.

In terms of system reliability, GPS-only MDBs were reduced considerably when a tight integration approach was employed. In particular, the ability to detected one-cycle cycle slips was shown to be both better and more consistent with the tightly coupled approach. More important than the internal reliability, the external reliability parameters were shown to be better when using either a loose or tight integration approach, relative to GPS-only. Code PLs were shown to be basically the

same in all cases, due primarily to the availability of high accuracy fixed-ambiguity carrier phase data. In contrast, GPS-only Doppler PLs were reduced dramatically from decimetres per second to less than one centimetre per second (RMS). Carrier phase PLs were also shown to be improved considerably, from the decimetre to centimetre level. Overall, the difference between the loose integration and the tight integration were not significant, although some differences were found.

Chapter 8

Real-Time Analysis

The description and results of some real-time tests are given in this chapter. The analysis focuses on assessing the overall system behaviour. Where possible, limitations of the system are also shown and discussed. A comparison of the results obtained in real-time with those obtained offline using GPS-only is made to illustrate the advantage of the integrated system.

8.1 Test Description

The data used for the real-time analysis was collected on January 13, 2003. In total, two runs were collected. The first run used L1 carrier phase data, while the second used the widelane linear combination. The equipment used was the same as for the post-mission data collection, as described in Section 7.1.1. The base station was setup on the roof of the CCIT building on the University of Calgary campus and its data was broadcast to the vehicle over a radio transceiver link. Data latencies were typically on the order of 0.1–0.2 s. The equipment setup was shown in Figure 7.1. The static initialization period at the start of each run was about 12 minutes long. The GPS/IMU lever-arm was determined beforehand using the method described in Section 4.3 and a dedicated test performed in open-sky conditions.

Testing was performed in and around the University of Calgary. The location of each run was selected to reflect more typical, and therefore adverse, operational

environments than those considered in Chapter 7. Specifically, suburban and pseudo-urban conditions were selected. In this context, pseudo-urban conditions represent conditions found around a typical university. Such an environment approximates urban canyon conditions but with overall lower masking angles and with severe masking conditions occurring for significantly shorter durations than in a real urban canyon. The details of the two runs are given in the following sections.

The SAINT$^{\text{TM}}$ software described in Section 7.2.1 was used in real-time mode. The relevant processing parameters were the same as discussed in Chapter 4. The tight integration approach was used due to its improved performance relative to the loose integration case, as demonstrated in the previous chapter. All observations were processed simultaneously.

8.2 Suburban Test

The suburban test was conducted along community roads and some main city routes. Community roads are typically narrow (one driving and one parking lane in each direction) and usually include trees on either side of the street. Given the time of year, the absence of foliage on the trees was beneficial but conditions were still far from ideal in the context of GPS signal tracking. Main city routes are similar to freeway conditions and include fairly open-sky conditions with some overpasses and surrounding concrete structures. As stated above, L1 carrier phase data was used for this test.

Figure 8.1 shows the plan view of the trajectory, relative to the base station. Baseline lengths for this run reach a maximum of approximately 2.4 km implying that dif-
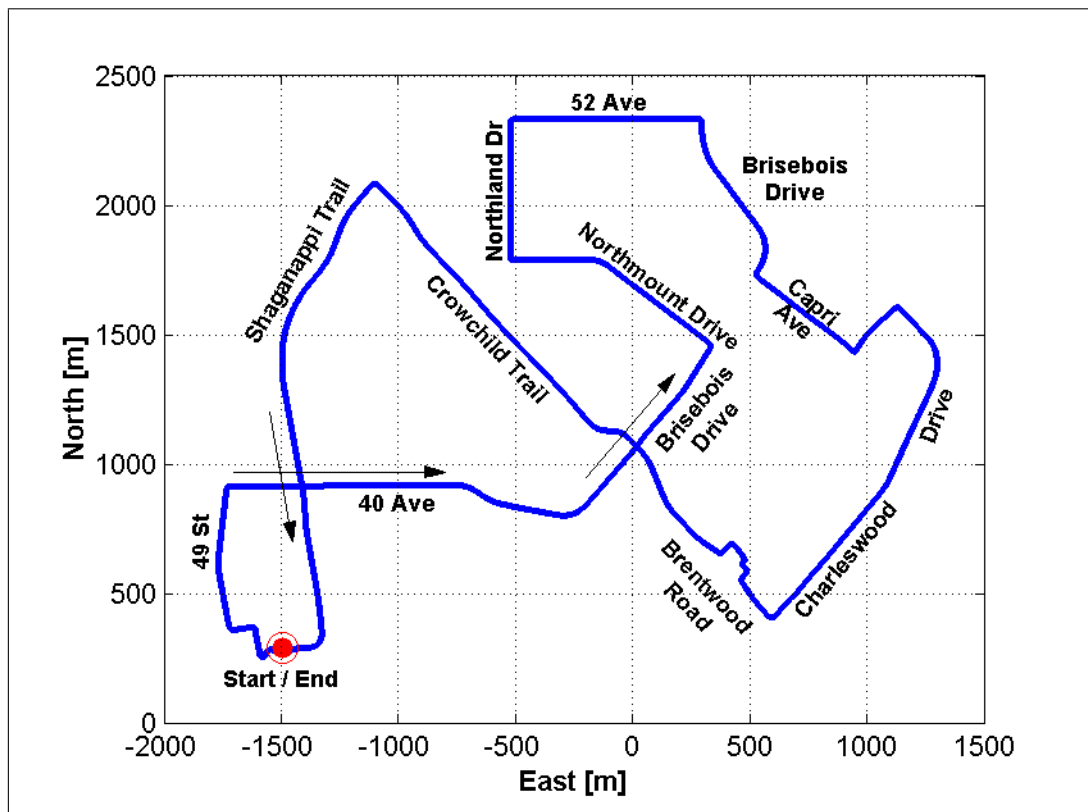
Figure 8.1: Trajectory for First Real-Time Run Relative to Base Station

ferential error sources will be negligible for this case. The run began and ended in the south parking lot of Market Mall shopping centre and proceeded as shown by the arrows. The maximum vehicle speed was approximately 90 km/h with 50 km/h being more common.

Only two complete satellite masking conditions were encountered during the run. First, passing underneath Crowchild Trail from 40 Avenue to Brisebois Drive, a complete data outage lasting five seconds was experienced. Second, traveling northwest on Crowchild Trail, an underpass located at the southward extension of Northland Drive caused a full data outage of three seconds. Otherwise, partial signal masking was caused by trees on either side of the community roads. Trees were most preva-

lent along 40 Avenue just east of Shaganappi Trail, at the west end of Northmount Drive and at the north end of Charleswood Drive. Figure 8.2 shows a picture of Northmount Drive to give an indication of the tree coverage experienced during the test. More pictures from throughout the run are included in Appendix E.

Figure 8.2: Northland Drive Looking Northwest

Figure 8.3 shows the number of satellites tracked and the corresponding DOP values for the horizontal (HDOP) and vertical (VDOP) components. The difference in the
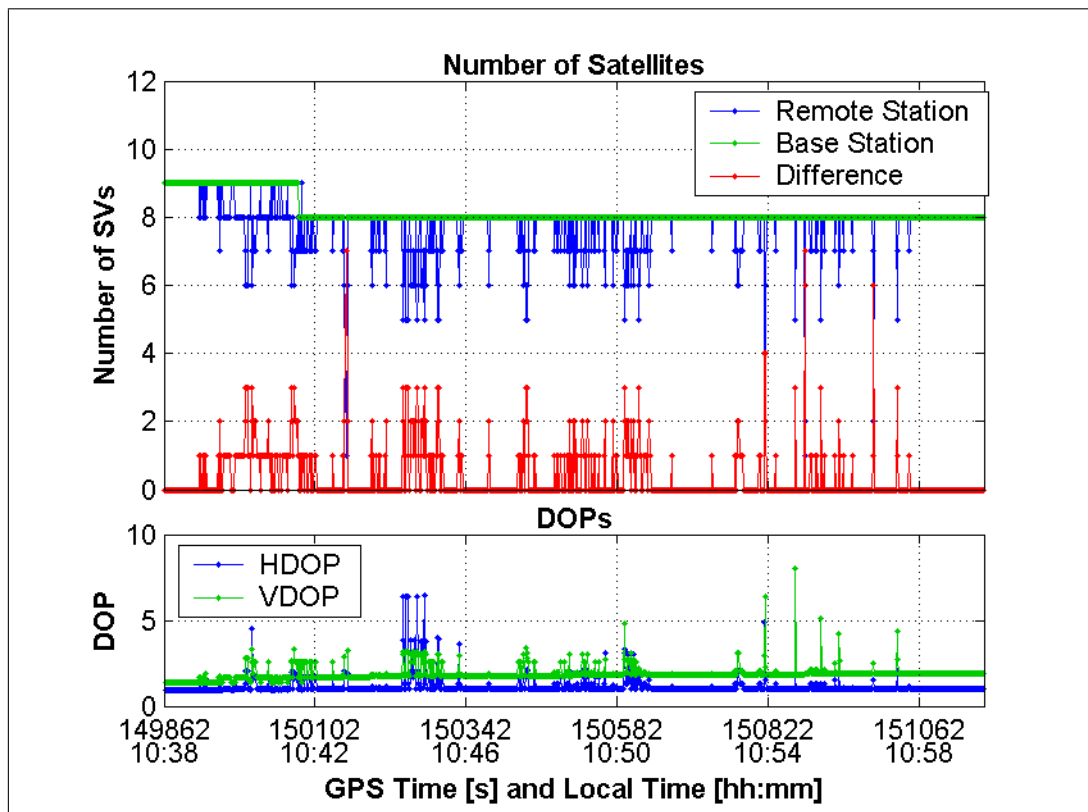
Figure 8.3: Number of Satellites and Dilution of Precision for First Real-Time Test

number of satellites tracked at the base and remote stations gives an indication of the signal masking environment. While not severe by some standards, the level of masking experienced is far from ideal for carrier phase tracking. DOP values were computed using the University of Calgary's C^3NAVG^{2TM} software, an epoch-to-epoch single point or differential code processing program. As such, DOPs are not output when the number of satellites is less than four, which occurred at eight epochs for this run (about 0.6% of the time). As shown, the HDOP is around one for the majority of the test but does exceed five in some cases. The VDOP is typically around two with frequent jumps that exceed three and some as high as eight. Overall, the geometry for the majority of the test is reasonable with some very poor periods.

As an initial assessment of the results, Figure 8.4 shows the double difference L1 carrier phase residuals for those satellite's whose ambiguities are fixed to integers. For the most part, residuals are at the 1–2 cm level. However, there are some situations with considerably larger values. Individual residuals above 2 cm are not of great concern as these could be due to increased multipath effects, which can reach a theoretical magnitude of one cycle for double difference observations (see Section 3.1.2). However, around GPS times 150300 and 150450 there are clear trends where several satellites show increased residuals implying an incorrect ambiguity fix. These correspond to the periods of fluctuating satellite visibility shown in Figure 8.3 which occur at the west end of Northmount Drive and the north end of Charleswood Drive respectively.

To confirm that this is indeed an incorrect fix, the tightly integrated solution using WL carrier phase updates was computed in post-mission. Given the increased wavelength, the likelihood of fixing the ambiguities correctly is greatly improved, as shown in the previous chapter. An analysis of the fixed WL residuals showed no systematic effects, thus supporting the conjecture that the solution is more accurate than the L1 solution. Assuming the WL solution to be correct, the difference between it and the real-time L1 solution can be interpreted as the error in the latter. The comparison of the two solutions is shown in Figure 8.5. There are clear periods where the two solutions are biased relative to each other. In particular, the times with larger L1 carrier phase residuals discussed above show the largest position differences. This helps confirm that the L1 ambiguity fix during these times is likely incorrect. The question arises therefore as to why these incorrect fixes occur, especially in light of the results of the previous chapter that showed the integrated solution as being capable of providing reliable ambiguity fixes.
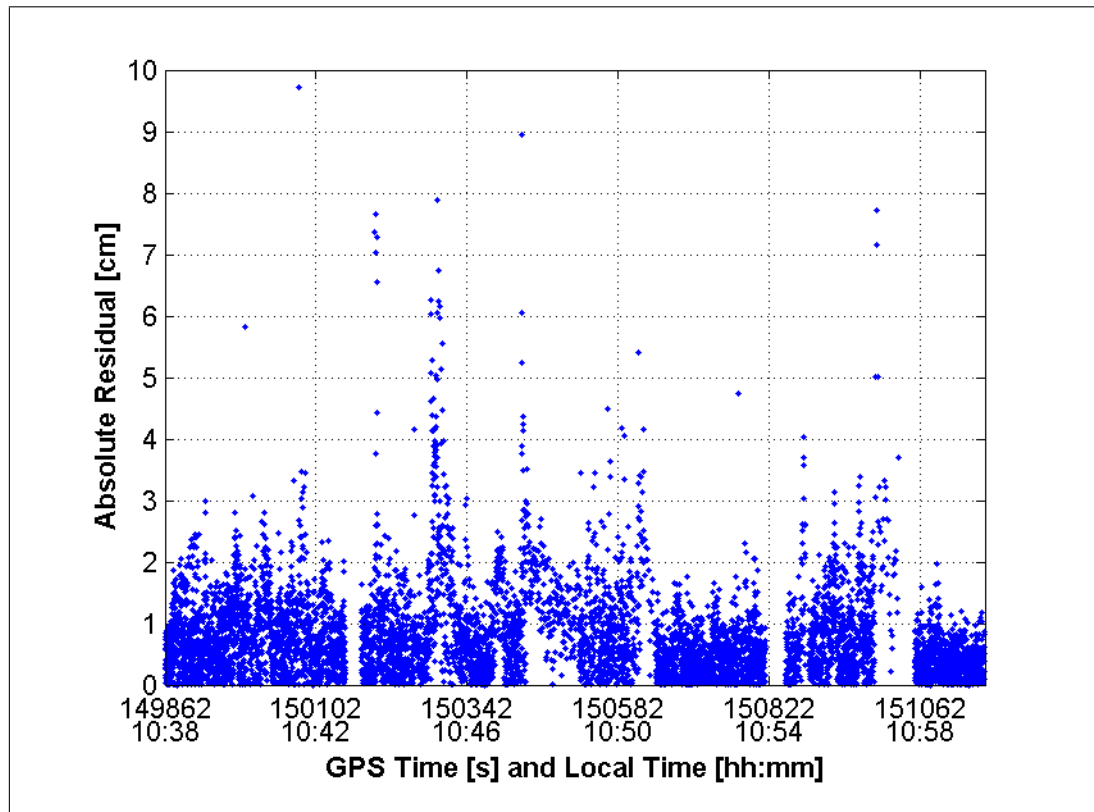
Figure 8.4: Absolute Fixed L1 Carrier Phase Residuals for First Real-Time Test

Unfortunately, this question cannot be answered definitively without further information about the actual vehicle trajectory. This being said, the most probable cause is the increased errors associated with the suburban environment relative to the open-sky environment used for the post-mission analysis. In particular, the multipath in suburban conditions can be severe and highly variable. Furthermore, the degraded satellite geometry will make these errors harder to detect using reliability testing, and any errors that pass undetected will have a larger effect on the estimated parameters than if more satellites were visible. The impact of these effects on the integrated system will therefore include

- Reduced ability of the system to properly calibrate the inertial navigation
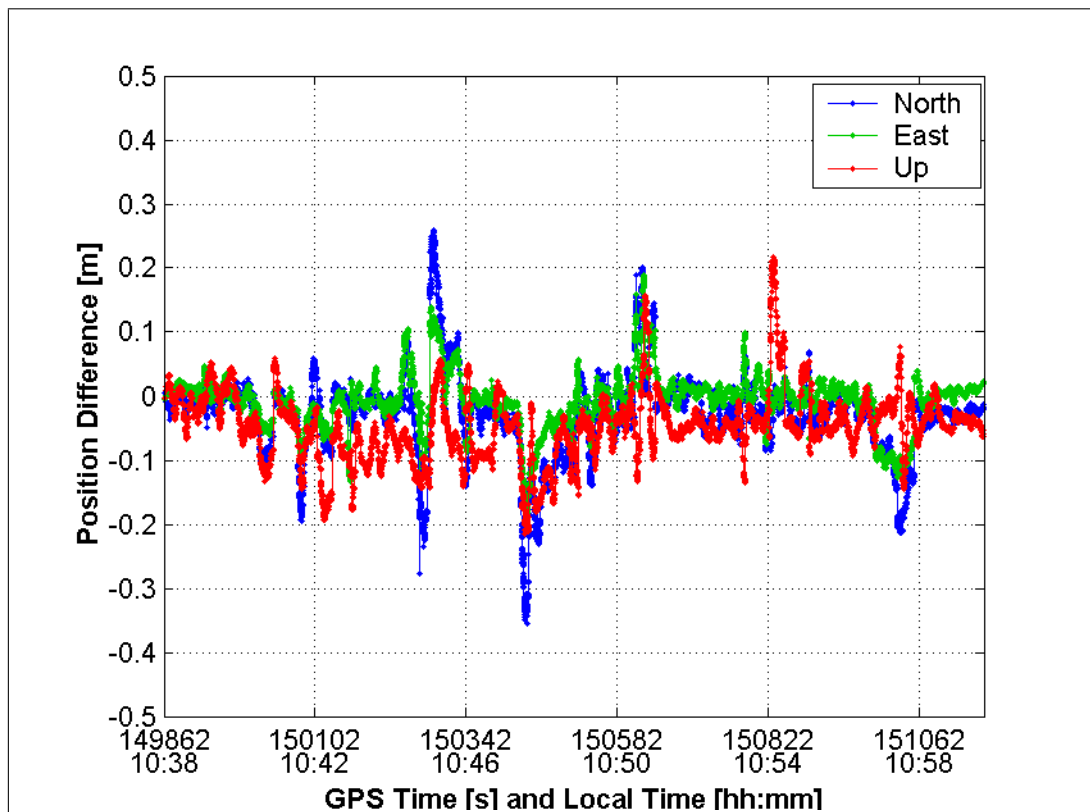
Figure 8.5: Difference Between Real-Time L1 Integrated Solution and Post-Mission Widelane Integrated Solution for First Real-Time Test

system. In particular, small biases in the measurements due to multipath will adversely impact the estimates of the INS error states. While these errors may not appear large, they could impact system behaviour during data outages, thus limiting the benefit of the inertial system in recovering the ambiguities.

- Increased system error immediately prior to data outages when multipath errors are likely to be higher as the GPS signals reflect off, or refract around, the masking object. These errors could then contaminate the estimated parameters prior to the data outage leading to poorer inertial behaviour.

- More difficulty in resolving the ambiguities after data outages, regardless of

the accuracy of the inertial solution. Recall that in Section 7.5.2 code errors were shown to limit the ability of the integrated system to quickly resolve the ambiguities after a data outage. It follows therefore that if the code errors are larger (which is highly probable in this case), the benefit of the inertial system will be reduced.

The above L1 results are clearly not ideal, but serve the important purpose of identifying a possible limitation of the integrated system. Specifically, it illustrates that direct resolution of the L1 carrier phase ambiguities in the suburban environment considered is difficult and may require more accurate inertial sensors.

Although the above results show that the real-time L1 only solution is not always correct, there is still an advantage to using the inertial system. To illustrate, Figure 8.6 shows the difference between the GPS-only L1 solution and the WL integrated solution, both obtained in post-mission. Assuming the difference between the two solutions is due to the error in the GPS-only L1 solution, its performance is considerably poorer than that of the integrated L1 solution obtained in real-time. The errors are at the metre-level versus the decimetre-level with the integrated solution. Furthermore, processing of the data collected in real-time is based on models developed under considerably more favourable conditions. A better characterization of the errors in suburban environments may yield even further benefit for the integrated solution. Unfortunately, such an analysis is beyond the scope of this dissertation.

Assuming the WL solution obtained in post-mission is accurate, its estimated position covariance can be used to obtain a rough estimate of the overall system performance. Figure 8.7 shows that the estimated standard deviations in each of the coordinate directions is bounded within 20 cm with typical reported accuracies being
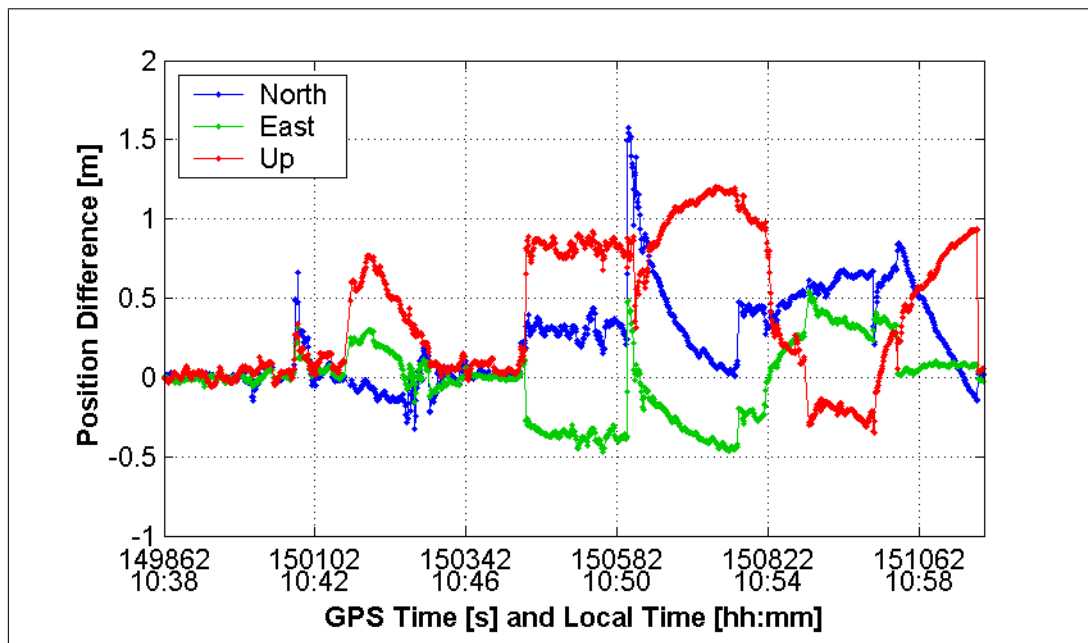
Figure 8.6: Difference Between Post-Mission L1 GPS-Only and Post-Mission Wide-lane Integrated Solution for First Real-Time Test

below 10 cm. While an L1 solution could improve upon this, the WL solution would still meet the sub-decimetre objective set forth in Section 1.3 most of the time.

8.3 Pseudo-Urban Test

As mentioned above, the term "pseudo-urban" is intended to represent conditions similar to those found in an urban canyon environment, with the difference being the severity and duration of periods during which satellite visibility is restricted. For example, in an urban canyon environment three or fewer satellites may remain visible for periods of several minutes. This, combined with large multipath errors would make for a very demanding, if not unreasonable, environment for the system under consideration. As a compromise, the pseudo-urban test was conducted in
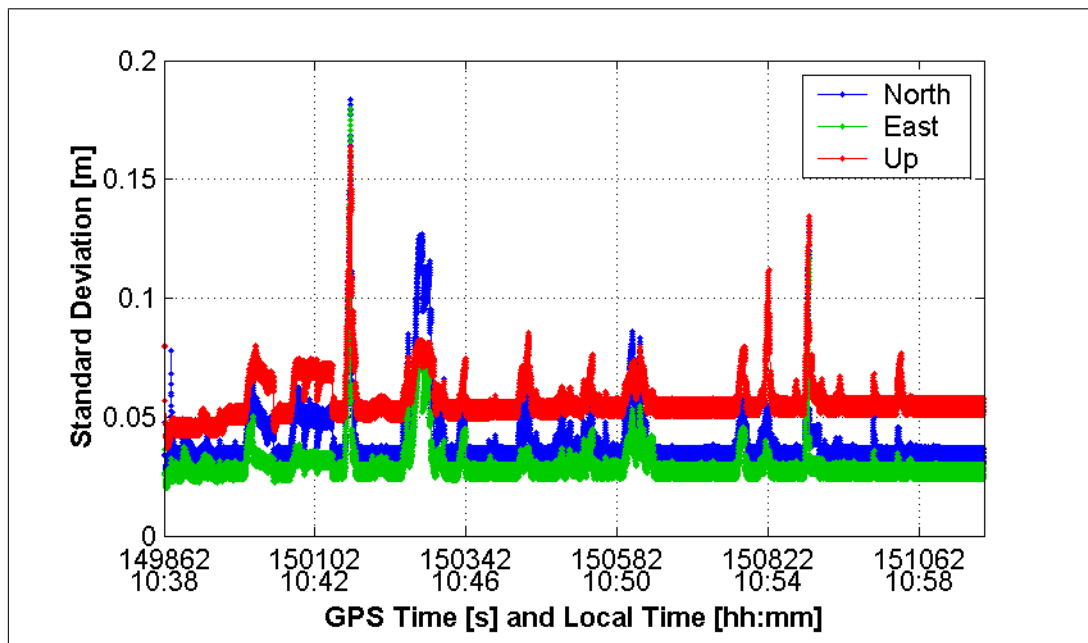
Figure 8.7: Estimated Position Standard Deviations From the Widelane Integrated Solution for First Real-Time Test

and around the University of Calgary campus. In this way, periods of satellite signal masking and multipath conducive environments are interlaced with periods of reasonable satellite visibility. This is considered to be a relatively severe operating environment given the quality of the inertial sensor used and the high-accuracy of the desired solution. The test was therefore performed using widelane carrier phase measurements to improve overall robustness.

The trajectory of the pseudo-urban test is shown in Figure 8.8. Again, the distance of the vehicle from the base station remained small thus limiting the effects of differential errors. The test began in the parking lot in front of the CCIT building and then proceeded as indicated by the arrows. Vehicle speeds remained below 60 km/h at all times.

The Calgary research park (north of 32 Avenue) was used for the first part of the test
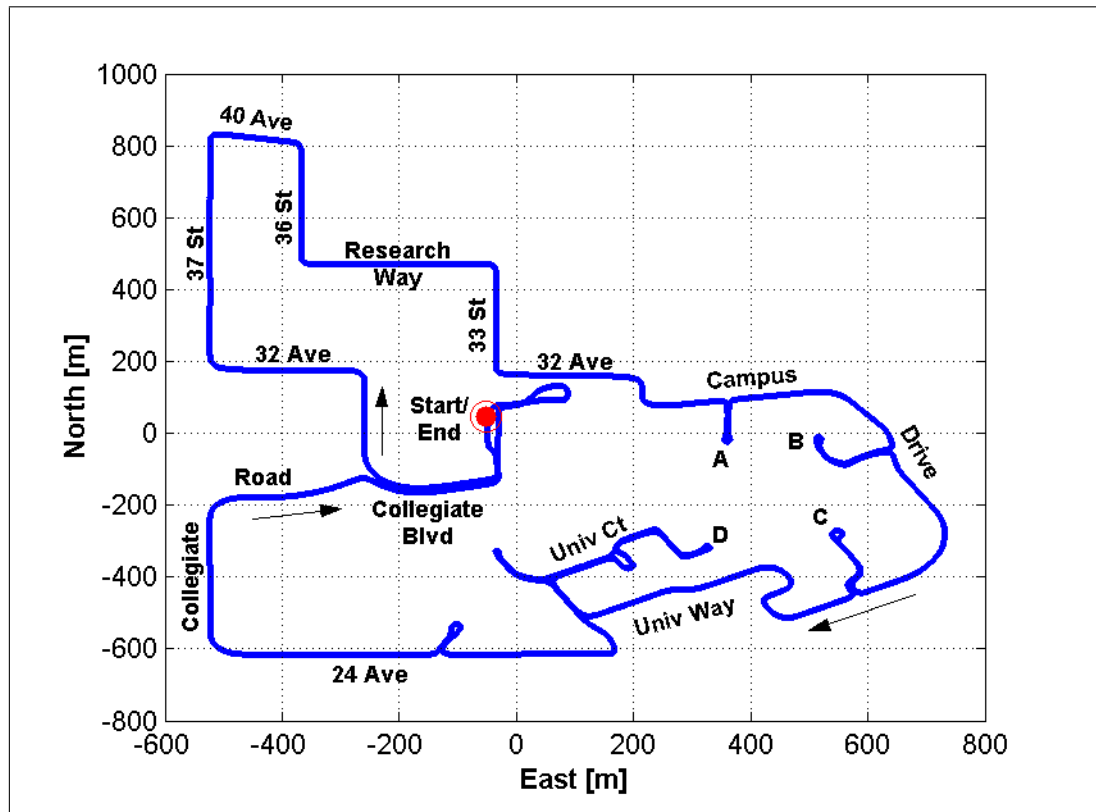
Figure 8.8: Trajectory for Second Real-Time Run Relative to Base Station

as it offered tree lined roads. The test then continued onto the University campus. The locations marked "A" through "D" are areas where the vehicle passed very close or even between several buildings simultaneously and therefore approximates an urban canyon environment. Furthermore, all of these locations except "D" are accessed only after passing under an enclosed walkway which causes a complete data outage. Otherwise, satellite visibility around campus was reasonable although partial signal masking from trees was moderate. Figure 8.9 shows a picture of the masking conditions at the point labeled "B" in Figure 8.8. Other pictures from various locations within the run are shown in Appendix F.

Figure 8.9: Point "B" Looking South

The number of visible satellites and the corresponding DOP (when four or more satellites are visible) is shown in Figure 8.10. Typically, the number of visible satellites is five or greater but there are five periods in which two or fewer satellites remain visible. Overall, the satellite geometry is reasonable with HDOP and VDOP values near one and two respectively. This being said, HDOP values of four or higher are not uncommon. Furthermore, there are 60 epochs for which DOPs could not be computed due to lack of satellite visibility. This represents approximately 4.4% of all epochs, implying that satellite masking was significant. Consequently, the geometry for this test is deemed to be considerably poorer than that of the suburban test analyzed in the previous section.
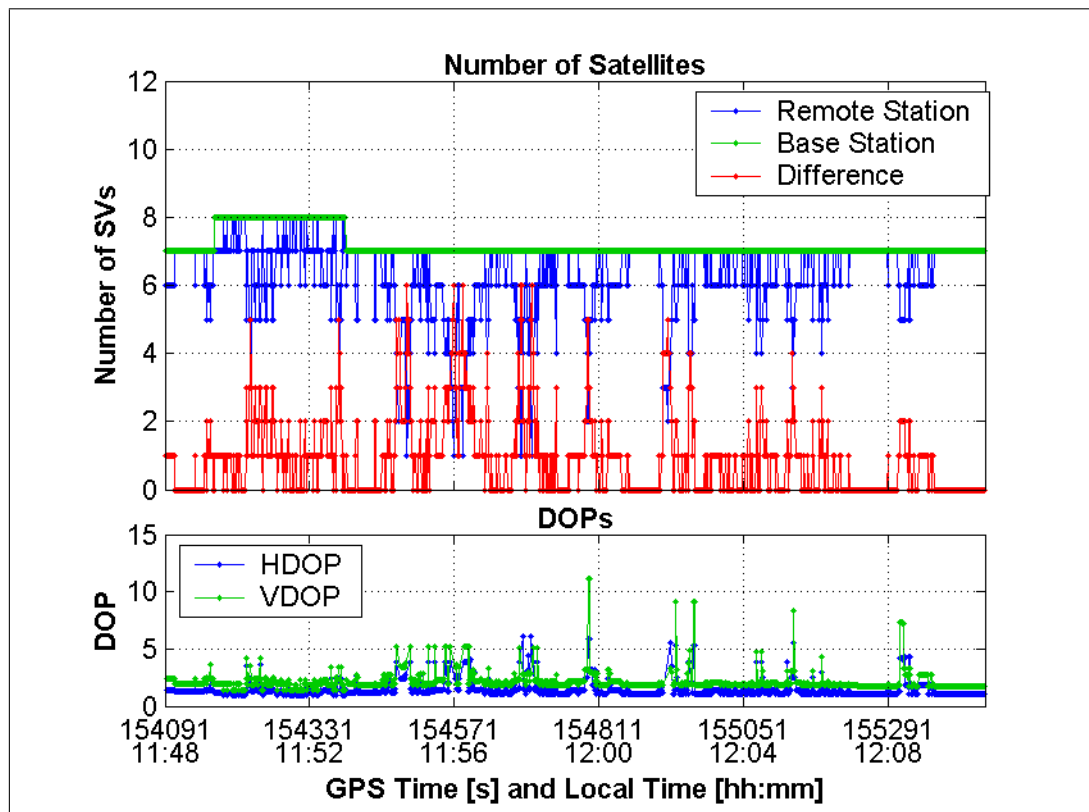
Figure 8.10: Number of Satellites and Dilution of Precision for Second Real-Time Test

The carrier phase residuals for those satellites with fixed ambiguities are shown in Figure 8.11. Overall, the magnitude of the residuals is lower than about 5 cm. While considerably higher than the fixed L1 carrier phase residuals (see analysis of post-mission truth trajectories in Section 7.2.2), this is typical of the increased noise of the WL carrier phase observations. Furthermore, the filtering effect due to the tight integration strategy will cause the residuals to appear slightly larger than when using GPS alone. The above analysis implies that the carrier phase fixes were correct for the entire data set. Also, since Figure 8.11 only shows residuals for fixed ambiguity measurements, the percentage of the time that at least one fixed ambiguity carrier phase measurement exists is seen to be quite high.
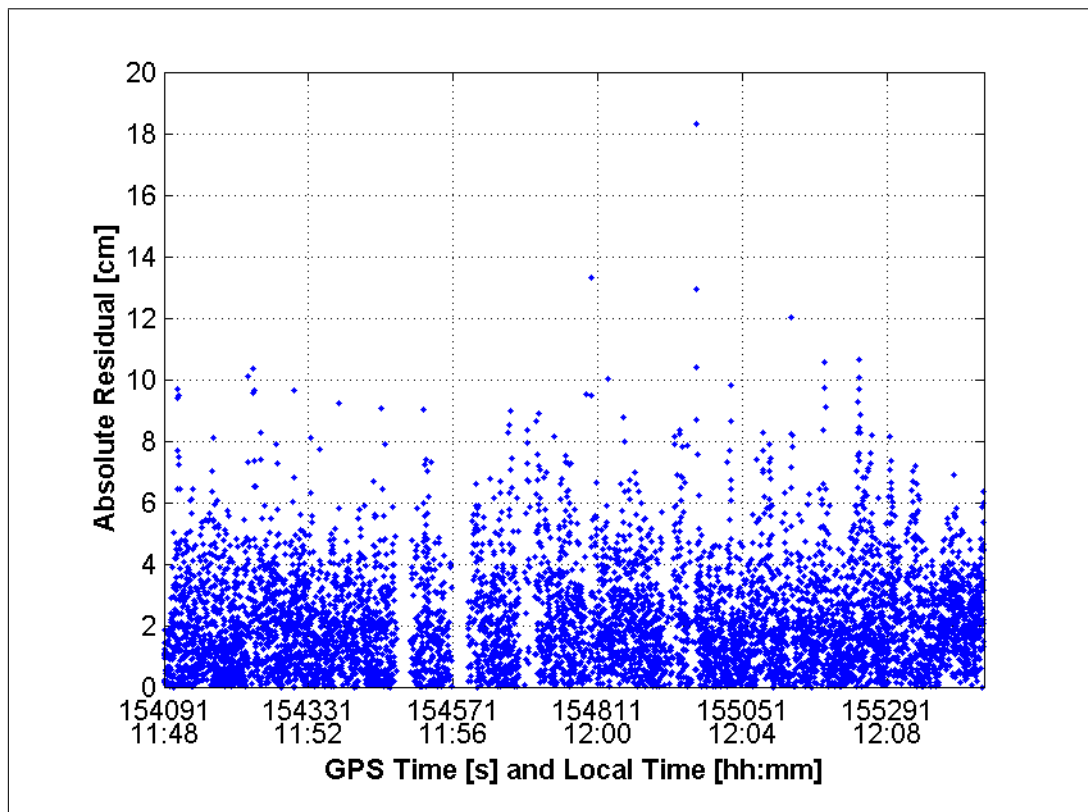
Figure 8.11: Absolute Fixed Widelane Carrier Phase Residuals for Second Real-Time Test

The difference between the real-time integrated solution and the post-mission GPS-only solution (also using WL carrier phase) is shown in Figure 8.12. Sustained position differences between the solutions are as high as one metre in each coordinate direction. Sporadic differences of several metres were also found but were cut off in the figure to better illustrate the low-frequency "biases". The GPS-only carrier phase residuals did not show any significant problems thus making it difficult to assess which of the two solutions was correct. To assist in this regard, Figure 8.13 shows the three-dimensional position PL values for the code and WL carrier phase measurements for the GPS-only and integrated solutions. As can be seen, the code PLs show large variations with the GPS-only approach. The largest PL values can be
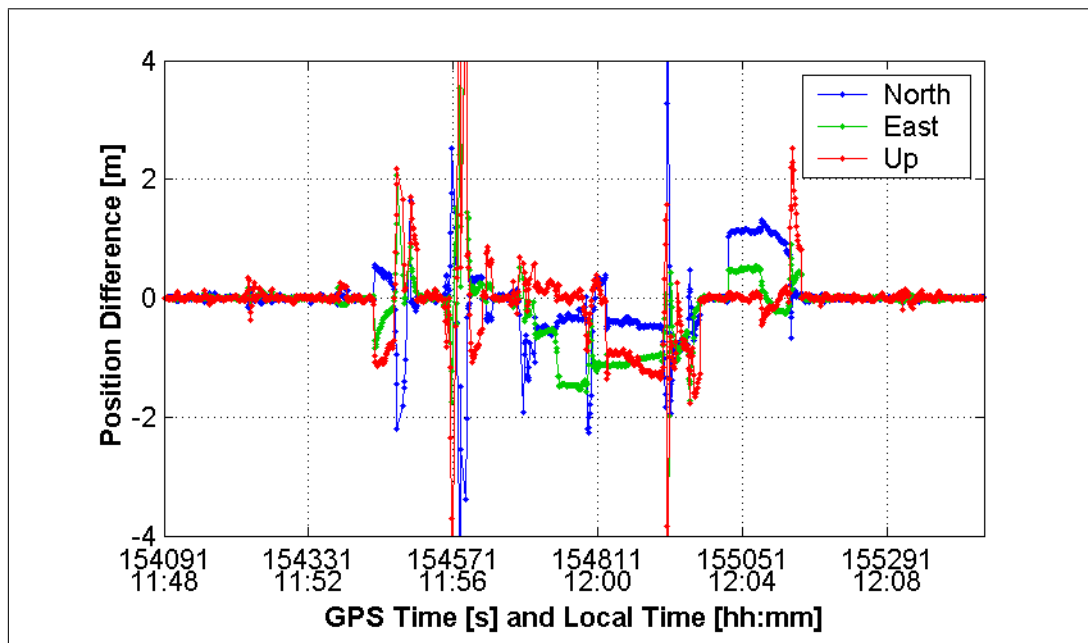
Figure 8.12: Difference Between Real-Time Integrated Solution and Post-Mission GPS-Only Solution for Second Real-Time Test

shown to occur after data outages and can reach 30 m or more (not shown to better show the integrated solution's code PLs). Also, after such data outages, the code measurements are used to re-initialize the GPS-only filter since no knowledge of the ambiguities is available. Given the importance of the code measurements after data outages and their relatively poor reliability (for the GPS-only filter), it is very likely that the code observations are biasing the GPS-only solution and possibly causing an incorrect ambiguity fix. The integrated solution also shows degradation in the code protection levels after data outages, but to a much smaller degree. The carrier phase protection levels for the GPS-only solution are also considerably poorer than with the tightly integrated solution. Finally, cross-referencing the PLs in Figure 8.13 with the position differences in Figure 8.12, it can be seen that changes in position differences correlate well with large increases in the PL values. Given that the GPS-
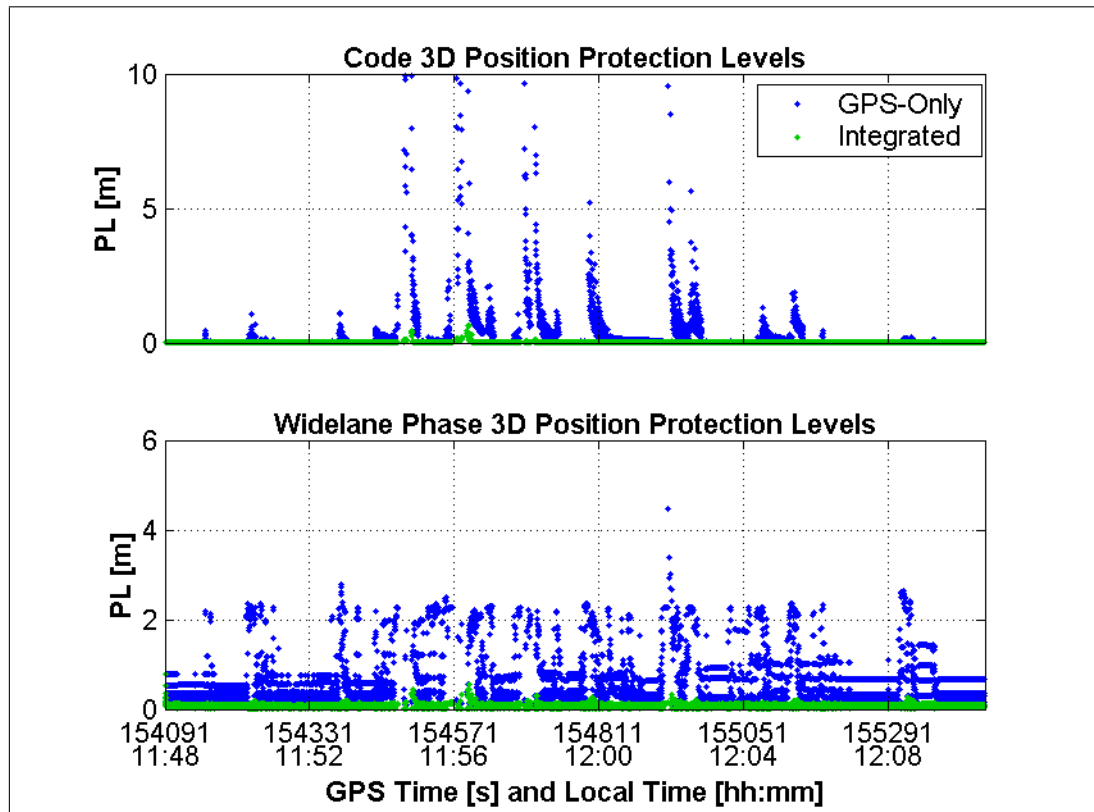
Figure 8.13: Code and Widelane Phase Three-Dimensional Position Protection Levels for GPS-Only and Tight Integration Solution for Second Real-Time Test

only solution is much less reliable than the integrated solution, this supports the idea that the GPS-only solution is in error.

To further confirm this conjecture, Figure 8.14 shows the code residuals for the two approaches. Residuals are colour-coded on a PRN-by-PRN basis for convenience. Overall, both approaches yield reasonable code residuals with some exceptions. First, around GPS time 154450 the GPS-only solution shows larger code residuals, relative to the integrated solution. This corresponds with the first major difference between the two position estimates in Figure 8.12. Second, the time period 154800–155160 also shows some increased residuals. These periods are important as they indirectly
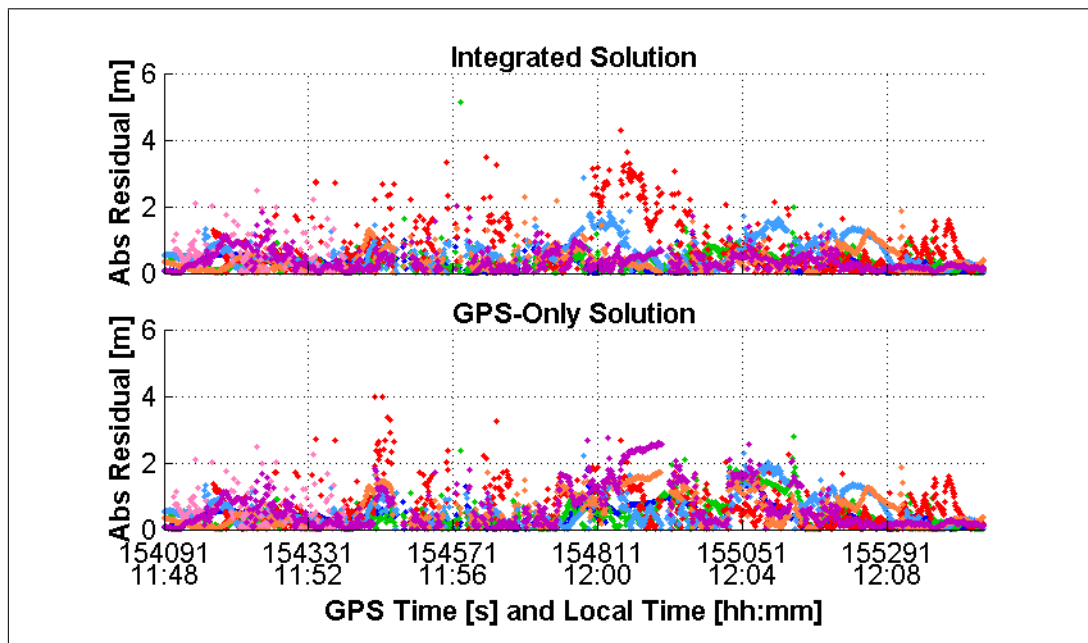
Figure 8.14: Code Residuals (Colour-Coded by PRN) for Real-Time Integrated Solution and Post-Mission GPS-Only Solution For Second Real-Time Test

indicate the quality of the carrier phase solution at those times. Specifically, assuming the carrier phase ambiguities are fixed correctly, the code residuals will essentially represent the errors in the code measurements. However, assuming the carrier phase ambiguities are fixed incorrectly, the resulting error in the position estimate will also be reflected in the code residuals, along with the actual code errors. It follows therefore that, on average, if the carrier phase ambiguities are fixed correctly, the code residuals should be of smaller magnitude than if the ambiguities are fixed incorrectly.

With this concept in mind, Figure 8.15 shows the code residuals during the time interval 154800–155160 in detail. To begin, consider the graph up to approximately GPS time 154920. Here, the three satellites' code residuals (orange, purple and dark blue) are clearly biased in the GPS-only case, with average values of about one metre or more. However, these same satellites for the integrated solution have residuals on
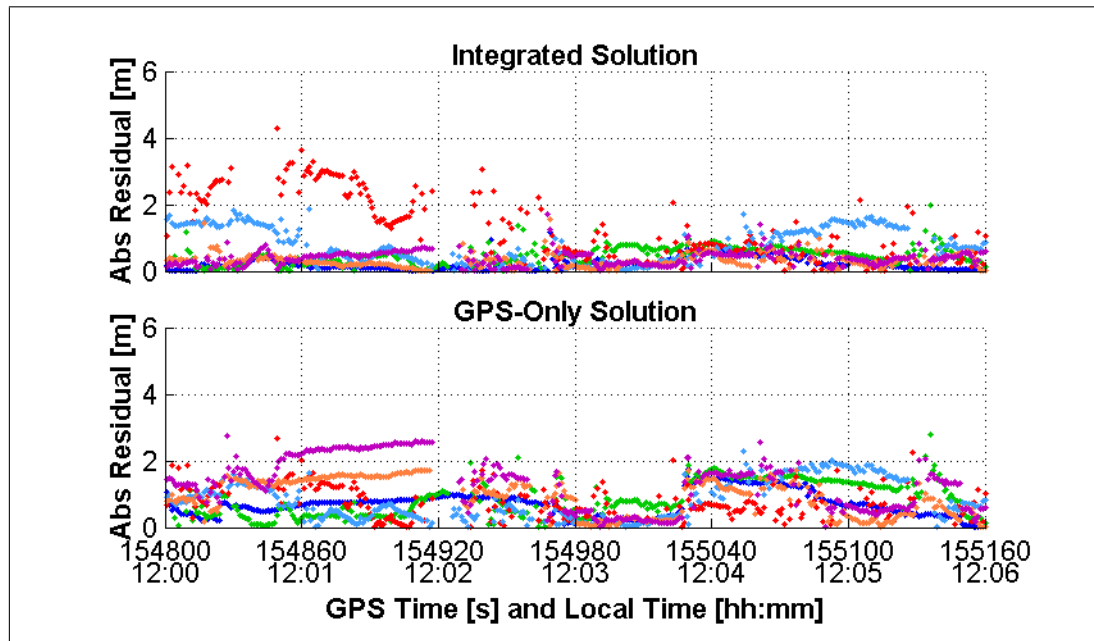
Figure 8.15: Selected Time Period Showing Code Residuals (Colour-Coded by PRN) for Real-Time Integrated Solution and Post-Mission GPS-Only Solution for Second Real-Time Test

the order of decimetres. In contrast, the red dots show an increased code residual for the integrated solution relative to the GPS-only solution. This is not unexpected, as it implies that that particular satellite is experiencing multipath errors that are being filtered out. Similar arguments can be made for the interval starting at GPS time 155040. Overall, the above analysis supports the conjecture that it is the GPS-only solution that is causing the differences seen in Figure 8.12.

While the above analysis is not conclusive, it does indicate that the integrated solution is more correct than that of GPS-only. Under this assumption, the position differences of Figure 8.12 are interpreted as the error in the GPS-only solution. This again shows that the integrated system is capable of improving overall accuracy and eliminating incorrect fixes which contaminate the GPS-only solution. Finally, Figure 8.16 shows that the estimated standard deviations of the integrated solution are

at the sub-decimetre level for the majority of the test, with some periods of approximately half-metre accuracy. Given the relatively adverse conditions under which the test was performed, these results are quite good and demonstrate that sub-decimetre positioning is possible under some adverse operational conditions.
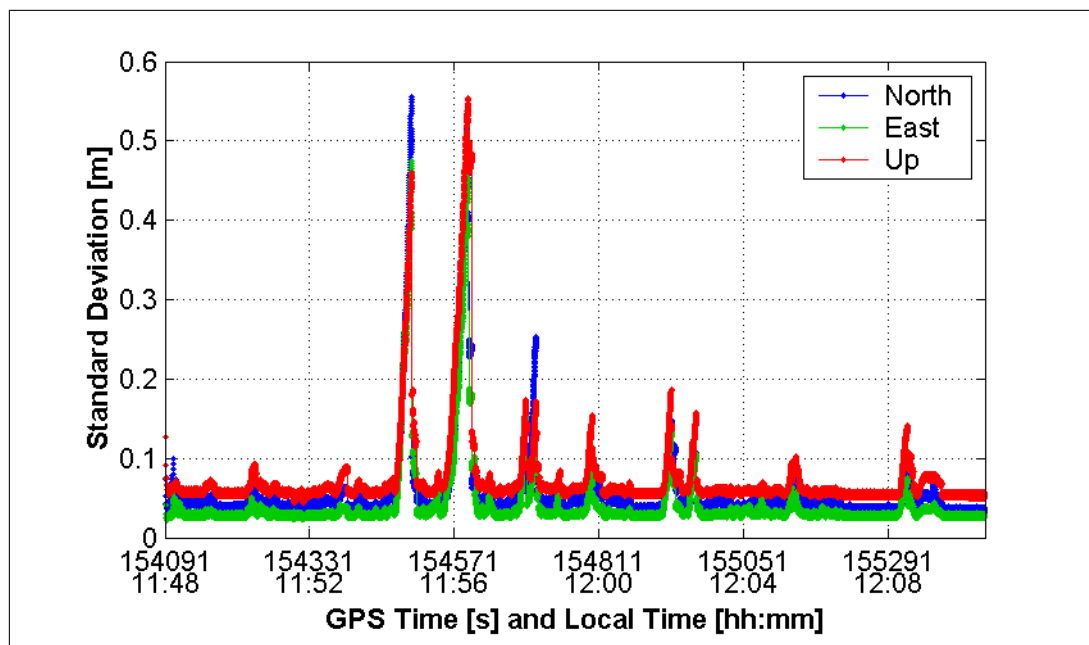

Figure 8.16: Estimated Position Standard Deviations From the Widelane Integrated Solution for Second Real-Time Test

8.4   Summary of Results

In this chapter, the output from two real-time runs were analyzed. The first run, collected under suburban conditions, showed that accurately resolving the L1 carrier phase ambiguities was not possible. However, compared with the GPS-only L1 solution, the integrated approach performed considerably better with a reduction of errors by over one metre in some cases.

The second run was collected in a pseudo-urban environment using widelane carrier phase data. Comparison with the GPS-only solution showed differences of several metres for extended periods. Although the fixed ambiguity carrier phase residuals for both solutions appeared reasonable, an analysis of the reliability parameters and the code residuals strongly suggests that it is the GPS-only solution that is causing the differences in the two solutions.

In general, results of the real-time testing indicate that the SAINT$^{\text{TM}}$ software is performing well and that sub-decimetre solutions are possible when using widelane carrier phase data, with exceptions occurring during periods of severe GPS signal masking.

Chapter 9

Conclusions and Recommendations

The contribution of this research was the thorough assessment of the performance of a tactical-grade IMU integrated with a GPS receiver for high-accuracy navigation. In this regard, a comparison of three integration strategies was also performed to assess their relative performance. In particular, loose integration, loose integration with INS seeding and tight integration strategies were considered with the latter providing the best results overall. The system tested used a NovAtel OEM4 GPS receiver and a Honeywell HG1700 AG11 IMU. A new software program named SAINT$^{\text{TM}}$ was also developed as part of this work and was used to prepare the results presented in previous chapters.

The performance parameters used to assess the above system included position accuracy during complete and partial GPS data outages, L1 and widelane ambiguity resolution capability after such data outages, as well as the overall statistical reliability of the system. With regard to the statistical reliability, the traditional reliability equations were reworked for use with more practical systems. Specifically, the equations for a reliability assessment of cascaded systems and systems using sequential measurement updates were developed.

The above performance parameters were also evaluated with a consideration for real-time applications with the ultimate goal being continuous sub-decimetre positioning capability. Real-time testing showed that this level of performance is possible most of the time when using widelane carrier phase updates. Other results served to illustrate

the limitations of the system under operational conditions. The following sections outline the major conclusions found in the course of this research and recommend possible improvements.

9.1 Conclusions

The integrated system showed better performance than GPS-only in all cases. Furthermore, the tight integration strategy outperformed the loose integration approach, although in some circumstances these differences were not significant. Below, details of the major conclusions of this dissertation are summarized in terms of the objectives set out in Chapter 1.

Accuracy During Data Outages

1. During complete simulated data outages, the integrated system was shown to provide sub-decimetre three-dimensional accuracy for data outages lasting up to about five seconds, in a root mean squre sense, when using L1 carrier phase updates in a tightly coupled system. The accuracy of the integrated solution degraded to the level of differential code solutions after approximately 30 seconds, and thus presents an significant advantage over GPS-only for data outages of up to this duration. The Kalman filter's estimate of this error was also shown to be a reasonable approximation to the actual system behaviour. These results were obtained under moderate vehicle dynamics.

2. Positioning accuracy during partial data outages was shown to be better than one decimetre for data outages lasting approximately 10–12 seconds when using

L1 carrier phase data in a tight integration approach. After 40 seconds, position accuracies degraded to only about 70 cm despite the poor GPS satellite geometry.

3. The tight integration approach outperformed the loose integration approaches in terms of overall system accuracy. Improvements of about 10 cm after 40 s were observed for complete data outages. For partial data outages, this improvement increased to about half a metre over the same time interval. This improvement is attributed to the reduced amount of process noise in the tight integration Kalman filter.

4. The widelane carrier phase observation provides poorer positioning performance than do the L1 observations for both complete and partial data outages. This is attributed to the increased measurement noise of the widelane measurements.

5. Using a tight integration approach, the velocity accuracy during the complete and partial data outages was shown to be good to approximately 11 cm/s and 4 cm/s after 40 seconds respectively.

Ambiguity Resolution

1. Using loose coupling with INS seeding significantly reduced the ambiguity resolution times after complete data outages relative to using GPS alone. In particular, 50% or better improvements in L1 ambiguity resolution times were observed for complete data outages lasting up to 20 seconds for two separate data collection runs. For widelane ambiguities, the percent improvements were even larger but the actual time needed to resolve the ambiguities with GPS-

only was already small and so the improvements are limited in a practical sense.

2. The tight integration strategy improved upon the L1 ambiguity resolution performance of the loose integration with INS seeding after complete data outages. In general, improvements were negligible for data outages lasting less than five, and longer than 30, seconds. For intermediate outage durations, the improvements of the tight integration over the loose integration with seeding were typically 40–70%. No significant differences were seen between the two integration strategies in terms of widelane ambiguity resolution, as both approaches provided instantaneous or near-instantaneous resolution at all times.

3. The integrated solutions are more robust in terms of L1 ambiguity resolution after complete data outages. Specifically, for one run the GPS-only solution was shown to incorrectly resolve the L1 carrier phase ambiguities. These incorrect fixes were mostly influenced by code errors. However, both integrated approaches were able to mitigate the effect of these errors and maintained a float ambiguity solution instead of fixing incorrectly. For partial data outages, these same code errors affected the GPS-only L1 and widelane ambiguity resolution process whereas the tight integration remained basically unaffected.

4. The usefulness of inertial data for ambiguity resolution is significant for data outages having durations over which the INS can provide more accurate solutions than DGPS alone (approximately 30 s for the system tested). For such data outages, the integrated approach can significantly improve GPS-only ambiguity resolution performance. These results are better than what was originally expected.

System Reliability

1. Use of tightly coupled GPS/INS system was shown to reduce the MDB of Doppler and L1 carrier phase measurements by decimetres per second and several centimetres respectively, relative to GPS alone. The magnitude of detectable code blunders was the same in both cases.

2. For the L1 carrier phase, the probability of detecting a one-cycle cycle slip was found to be greater than 50% at all times using the tight integration strategy. In contrast, using a GPS-only approach, some satellites had less than a 20% chance of detecting a cycle slip.

3. The effect of a code blunder on the estimated position, when fixed ambiguity carrier phase data is available, is negligible. Using GPS-only, RMS protection levels were found to be mostly below 1 cm. However, some satellites showed RMS protection levels of several centimetres when estimating several ambiguities as real values. Both the loose and tight integration approaches reduced the RMS protection levels to below 1 cm.

4. The GPS-only protection levels for the Doppler blunders were reduced from decimetres per second to a few millimetres per second using either integration strategy. The advantage of the tightly coupled over the loosely coupled approach was only a few millimetres per second.

5. The GPS-only L1 carrier phase protection levels were reduced by tens of centimetres in some cases when using an integrated approach. The tightly coupled approach was better than the loosely coupled approach by as much as 3 cm in each of the horizontal and vertical components. Given the estimated accu-

racy of the system (i.e. a few centimetres), these differences are significant and represent a significant advantage of the tight integration approach.

6. The difference in the statistical reliability parameters when using a simultaneous or sequential updating strategy was negligible. Maximum differences in the MDBs were found to be 1 mm or 1 mm/s for code and Doppler measurements respectively. Protection levels for the two approaches were consequently found to be identical to the millimetre and millimetre per second level respectively.

Real-Time Performance

1. Direct resolution of the L1 carrier phase ambiguities in a suburban environment could not be accomplished reliably with the system tested. Some incorrect fixes were detected yielding differences with respect to the widelane carrier phase solution of up to several decimetres. However, the L1 GPS-only solution showed differences at the metre-level indicating that the integrated approach was still beneficial. Poor characterization of the errors in the suburban setting is considered the major reason for the incorrect fixes.

2. In a pseudo-urban environment, the difference between the GPS-only and the integrated solution showed differences at the metre-level. Several wrong fixes were identified with the GPS-only solution. The absence of a truth trajectory limited the ability to confidently confirm that the integrated solution produced correct integer fixes throughout the run, but all indications suggest that the test was in fact successful.

3. Assuming the estimated widelane solutions are correct, the estimated uncertainty of the position was computed to be better than 10 cm for each coordinate

component except during complete data outages. A sub-decimetre accuracy system is therefore possible most of the time using the equipment tested.

9.2   Recommendations

Based on the results and conclusions of this research, the following recommendations can be made

1. Investigate the benefit of performing a laboratory and/or field calibration of the IMU prior to data collection. The system tested did not have a calibration performed in an effort to reduce the number of person-hours needed to prepare the system for operation. However, if simple calibration procedures were shown to be effective for high-accuracy applications, they could be implemented in later versions of the system to improve overall performance.

2. Investigate system performance in the presence of larger differential errors. Results shown in this dissertation are valid for baseline lengths up to about 7 km and differential errors on the order of 3 ppm, with some satellites showing effects as large as 9 ppm. By investigating the performance of the integrated system in the presence of larger error magnitudes, a better overall assessment will be obtained.

3. Assess the system accuracy during data outages when only float ambiguities are available prior to the data outages. The results shown herein used fixed ambiguities prior to data outages and therefore represent the ideal situation. However, it was also shown that as the observation uncertainty increases, when

using the widelane observable for example, the performance of the system during data outages is adversely affected. Since float ambiguity carrier phase measurements effectively contain less information than when the ambiguities are fixed, it follows that the system performance will be lower in this case. A full characterization of this situation is required to obtain the best overall assessment of the system.

4. Quantify the accuracy of the various integration approaches during the ambiguity resolution process. This dissertation was only concerned with duration of the ambiguity resolution process, and the veracity of the resulting integer ambiguities. However, system accuracy during the ambiguity resolution process is also a critical component of the overall system performance and therefore needs to be characterized.

5. A more thorough reliability assessment of the integrated system is required. The work shown herein served only to illustrate the potential benefits of using an integrated approach over GPS alone. Given the benefits that were identified, a more rigourous analysis would better characterize these improvements. In particular, a broader range of satellite geometries and vehicle dynamics should be tested. Also, an assessment of the reliability during periods when ambiguities are being estimated as real values should be performed.

6. Given the robustness of the widelane ambiguity resolution process relative to L1, a cascading approach whereby widelane ambiguities are fixed first, followed by an attempt to resolve the L1 ambiguities should be investigated. If L1 ambiguity resolution times and/or reliability could be improved by this process, the integrated system could take advantage of the robust widelane ambiguities

as a worst case, while maintaining the possibility of having a fixed L1 solution. Real-time applicability of such an approach should also be considered.

7. Perform a better characterization of the errors in suburban and pseudo-urban environments. In so doing, the performance of the current system may be improved. Specifically, if the integrated L1 solution could be made more reliable, the cost savings to the user in terms of GPS hardware could be significant.

8. Compare the integration of a tactical and navigation-grade system to better assess the INS performance between GPS updates. Such an analysis may identify means of improving the tactical-grade system beyond its current level.

9. Implement an algorithm to automatically detect and exploit zero-velocity conditions in real-time. This could potentially introduce high-accuracy observations to the system, even in the absence of good GPS satellite coverage. The resulting improvement in the INS error state estimation may then extend the capabilities of the system tested.

10. Investigate the potential benefits of the integrated system for post-mission applications. This should include an investigation of a backward processing strategy, the use of optimal smoothing algorithms and methods of interpolating system error during data outages (e.g. as in Nassar and Schwarz, 2001).

11. Investigate the possibility of lowering the dependence of the integrated solution on the GPS code observations. It was shown herein that code errors could significantly influence the ambiguity resolution process. It follows therefore, that if the integrated system could reduce its dependence on these measurements, the overall ambiguity resolution performance may be improved.

References

Baarda, W. (1967) Statistical Concepts in Geodesy. *Netherlands Geodetic Commission*, 4(2).

Baarda, W. (1968) A Testing Procedure For Use in Geodetic Networks. *Netherlands Geodetic Commission*, 5(2).

Böder, V. and G. Seeber (1997) Real-Time PDGPS Positioning, Attitude Determination and INS-Integration for Hydrographic Applications. *Proceedings of KIS 1997*, pp. 197–194. Department of Geomatics Engineering, The University of Calgary.

Brown, R. G. and P. Y. C. Hwang (1992) *Introduction To Random Signals and Applied Kalman Filtering*. John Wiley & Sons, Inc., second edition.

Cannon, M. E. (1991) *Airborne GPS/INS with an Application to Aerotriangulation*. Ph.D. thesis, The University of Calgary. UCGE Report 20040.

Chen, D. (1994) *Development of a Fast Ambiguity Search Filter (FASF) Method for GPS Carrier Phase Ambiguity Resolution*. Ph.D. thesis, The University of Calgary. UCGE Report 20071 (Available at: http://www.ensu.ucalgary.ca/links/GradTheses.html).

Counselman, C. C. and S. A. Gourevitch (1981) Miniature Interferometer Terminals for Earth Surveying: Ambiguity and Multipath with Global Positioning System. *IEEE Transactions on Geoscience and Remote Sensing*, GE-19(4).

Da, R. (1997a) Analysis of Test Results of AIMS GPS/INS System. *Proceedings of ION GPS 1997*, pp. 771–780. Institute Of Navigation.

197

Da, R. (1997b) Investigation of a Low-Cost and High-Accuracy GPS/IMU System. *Proceedings of ION NTM 1997*, pp. 955–963. Institute Of Navigation.

Da, R., G. Dedes, and K. Shubert (1996) Design and Analysis of a High-Accuracy Airborne GPS/INS System. *Proceedings of ION GPS 1996*, pp. 955–964. Institute Of Navigation.

de Jong, C. D., G. Lachapelle, S. Skone, and I. A. Elema (2002) *Hydrography*. Delft University Press.

El-Sheimy, N., K. P. Schwarz, M. Wei, and M. Lavigne (1995) VISAT: A Mobile City Survey System of High Accuracy. *Proceedings of ION GPS 1995*, pp. 1307–1315. Institute Of Navigation.

Farrell, J. A., T. D. Givargis, and M. J. Barth (2000) Real-Time Differential Carrier Phase GPS-Aided INS. *IEEE Transactions on Control Systems Technology*, 8(4), pp. 709–720.

Ford, T., J. Neumann, and M. Bobye (2001) OEM4 Inertial: An Inertial/GPS Navigation System on the OEM4 Receiver. *Proceedings of KIS 2001*, pp. 150–168. Department of Geomatics Engineering, The University of Calgary.

Fortes, L. P., M. E. Cannon, and G. Lachapelle (2000) Testing a Multi-Reference GPS Station Network for OTF Positioning in Brazil. *Proceedings of ION GPS 2000*, pp. 1133–1142. Institute Of Navigation.

Fortes, L. P., M. E. C. S. Skone, and G. Lachapelle (2001) Improving a Multi-Reference GPS Station Network Method for OTF Positioning in the St. Lawrence Seaway. *Proceedings of ION GPS 2001*, pp. 404–414. Institute Of Navigation.

Geier, G. J. (1998) GPS Integration with Low Cost Sensor Technology for Automotive Applications. ENGO 699.47 Lecture Notes (August 1998). Department of Geomatics Engineering, The University of Calgary.

Gelb, A. (1974) *Applied Optimal Estimation*. The M.I.T. Press.

GFZ-Potsdam (2003) Geomagnetic Kp Index (Webpage). Http://www.gfz-potsdam.de/pb2/pb23/GeoMag/niemegk/kp_index/kp.html.

Greenspan, R. L. (1996) GPS and Inertial Integration. B. Parkinson and J. J. Spilker, Jr., eds., *Global Positioning System: Theory And Applications*, volume 2, chapter 7. American Institute of Aeronautics and Astronautics, Inc., Washington D.C., USA.

Grejner-Brzezinska, D. A., R. Da, and C. Toth (1998) GPS error modeling and OTF ambiguity resolution for high-accuracy GPS/INS integrated system. *Journal of Geodesy*, 72, pp. 626–638.

Grewal, M. S. and A. P. Andrews (1993) *Kalman Filtering Theory and Practice*. Prentice Hall.

Han, S. and C. Rizos (1997) Comparing GPS Ambiguity Resolution Techniques. *GPS World*, pp. 54–61.

Hartman, R. G. (1988) An Integrated GPS/IRS Design Approach. *Navigation: Journal of The Institute Of Navigation*, 35(1), pp. 121–134.

Hatch, R. (1990) Instantaneous Ambiguity Resolution. *Proceedings of KIS 1990*, pp. 299–308. Department of Geomatics Engineering, The University of Calgary.

Hatch, R. (1994) Comparison of Several AROF Kinematic Techniques. *Proceedings of ION GPS 1994*, pp. 363–370. Institute Of Navigation.

Hein, G. and W. Werner (1995) Comparison of Different On-The-Fly Ambiguity Resolution Techniques. *Proceedings of ION GPS 1995*, pp. 1137–1144. Institute Of Naviation, Alexandria, VA., USA.

Honeywell (1997) Document DS34468-01 - Critical Item Development Specification HG1700AG Inertial Measurement Unit.

Jekeli, C. (2000) *Inertial Navigation Systems with Geodetic Applications*. Walter de Gruyter, New York, NY., USA.

Klobuchar, J. A., P. H. Doherty, and M. B. El-Arini (1995) Potential Ionospheric Limitations to GPS Wide-Area Augmentation System (WAAS). *Navigation: Journal of The Institute Of Navigation*, 42(2), pp. 353–370.

Koch, K. R. (1999) *Parameter Estimation and Hypothesis Testing in Linear Models*. Springer-Verlag, second edition.

Krakiwsky, E. J. (1990) The Method of Least-Squares: A Synthesis of Advances. UCGE Report 10003. Department of Geomatics Engineering, The University of Calgary.

Lachapelle, G. (1997) GPS Theory and Applications. ENGO 625 Lecture Notes. Department of Geomatics Engineering, The University of Calgary.

Lachapelle, G., P. Alves, L. P. Fortes, M. E. Cannon, and B. Townsend (2000) DGPS RTK Positioning Using a Reference Network. *Proceedings of ION GPS 2000*, pp. 1165–1171. Institute Of Navigation.

Lapucha, D. (1990) GPS/INS Trajectory Determination for Highway Surveying. *Kinematic Systems in Geodesy, Surveying, and Remote Sensing, Symposium No. 107*, pp. 372–381. Springer-Verlag.

Leick, A. (1995) *GPS Satellite Surveying*. John Wiley & Sons, Inc., second edition.

Leva, J. L., M. U. de Haag, and K. V. Dyke (1996) Performance of Standalone GPS. E. D. Kaplan, ed., *Understanding GPS Principles and Applications*, chapter 7. Artech House.

Liu, G. C. (2001) *Ionosphere Weighted Global Positioning System Carrier Phase Ambiguity Resolution*. Master's thesis, The University of Calgary. UCGE Report 20155 (Available at: http://www.ensu.ucalgary.ca/links/GradTheses.html).

Lu, G. (1991) *Quality Control for Differential Kinematic GPS Positioning*. Master's thesis, The University of Calgary. UCGE Report 20042 (Available at: http://www.ensu.ucalgary.ca/links/GradTheses.html).

Lu, G. and G. Lachapelle (1992) Statistical quality control for kinematic GPS positioning. *manuscripta geodaetica*, 17, pp. 270–281.

Masson, A., D. Burtin, and M. Sebe (1996) Kinematic DGPS and INS Hybridization for Precise Trajectory Determination. *Proceedings of ION GPS 1996*, pp. 965–973. Institute Of Naviation, Alexandria, VA., USA.

Mikhail, E. M. (1976) *Observations and Least Squares*. Harper & Row.

Misra, P. and P. Enge (2001) *Global Positioning System - Signals, Measurements, and Performance*. Ganga-Jamuna Press.

Mohamed, A. H. (1999) *Optimizing the Estimation Procedure in INS/GPS Integration for Kinematic Applications*. Ph.D. thesis, The University of Calgary. UCGE Report 20127.

Nassar, S. M. and K. P. Schwarz (2001) Bridging DGPS Outages in Kinematic Applications Using a Simple Algorithm for INS Bias Modeling. *Proceedings of KIS 2001*, pp. 401–408. Department of Geomatics Engineering, The University of Calgary.

Neumann, J. B., A. Manz, T. J. Ford, and O. Mulyk (1996) Test Results from a New 2 cm Real Time Kinematic GPS Positioning System. *Proceedings of ION GPS 1996*, pp. 873–882. Institute Of Naviation, Alexandria, VA., USA.

Parkinson, B. W. (1996) Introduction and Heritage of NAVSTAR, the Global Positioning System. B. Parkinson and J. J. Spilker, Jr., eds., *Global Positioning System: Theory And Applications*, volume 1, chapter 1. American Institute of Aeronautics and Astronautics, Inc., Washington D.C., USA.

Press, W. H., S. A. Teukolsky, W. T. Vetterling, and B. P. Flannery (1992) *Numerical Recipes in C*. Press Syndicate or the University of Cambridge, second edition.

Raquet, J. F. (1998) *Development of a Method for Kinematic GPS Carrier-Phase Ambiguity Resolution Using Multiple Reference Receivers*. Ph.D. thesis, The University of Calgary. UCGE Report 20116 (Available at: http://www.ensu.ucalgary.ca/links/GradTheses.html).

Ray, J. K. (2000) *Mitigation of GPS Code and Carrier Phase Multipath Effects Using a Multi-Antenna System*. Ph.D. thesis, The University of Calgary. UCGE Report 20136 (Available at: http://www.ensu.ucalgary.ca/links/GradTheses.html).

Ryan, S. J. (2002) *Augmentation of DGPS for Marine Navigation*. Ph.D. thesis, The Univerisity of Calgary. UCGE Report 20164 (Available at: http://www.ensu.ucalgary.ca/links/GradTheses.html).

Salychev, O. S., V. V. Voronov, M. E. Cannon, R. Nayak, and G. Lachapelle (2000) Low Cost INS/GPS Integration: Concepts and Testing. *Proceedings of ION NTM 2000*, pp. 98–105. Institute Of Naviation, Alexandria, VA., USA.

Salzmann, M. (1990) MDB: A Design Tool for Integrated Navigaiton Systems. *Proceedings of KIS 1990*, pp. 218–227. Department of Geomatics Engineering, The University of Calgary.

Savage, P. G. (1998a) Strapdown Inertial Navigation Integration Algorithm Design Part 1: Attitude Algorithms. *AIAA Journal of Guidance, Control, and Dynamics*, 21(1), pp. 19–28.

Savage, P. G. (1998b) Strapdown Inertial Navigation Integration Algorithm Design Part 2: Velocity and Position Algorithms. *AIAA Journal of Guidance, Control, and Dynamics*, 21(2), pp. 208–221.

Savage, P. G. (2000) *Strapdown Analytics*, volume 1. Strapdown Associates, Inc.

Scherzinger, B. M. (2000) Precise Robust Positioning with Inertial/GPS RTK. *Proceedings of ION GPS 2000*, pp. 155–162. Institute Of Naviation, Alexandria, VA., USA.

Scherzinger, B. M. (2001) Robust Inertially-Aided RTK Position Measurement. *Proceedings of KIS 2001*, pp. 265–272. Department of Geomatics Engineering, The University of Calgary.

Scherzinger, B. M. (2002a) Personal Conversation.

Scherzinger, B. M. (2002b) Robust Positioning with Single Frequency Inertially Aided RTK. *Proceedings of ION NTM 2002*, pp. 911–917. Institute Of Naviation, Alexandria, VA., USA.

Schwarz, K. P. (1996) Fundamentals of Geodesy. Lecture Notes for ENGO 421. Department of Geomatics Engineering, The University of Calgary.

Schwarz, K. P., M. E. Cannon, and R. V. C. Wong (1989) A comparison of GPS kinematic models for the determination of position and velocity along a trajectory. *manuscripta geodaetica*, 14, pp. 345–353.

Schwarz, K. P., N. El-Sheimy, and Z. Liu (1994a) Fixing GPS Cycle Slips by GPS/INS - Methods and Experience. *Proceedings of KIS 1994*, pp. 265–275. Department of Geomatics Engineering, The University of Calgary.

Schwarz, K. P. and M. Wei (1990) Efficient numerical formulas for the computation of normal gravity in a Cartesian frame. *manuscripta geodaetica*, 15, pp. 228–234.

Schwarz, K. P. and M. Wei (1999) INS/GPS Integration for Geodetic Applications. Partial Lecture Notes for ENGO 623. Department of Geomatics Engineering, The University of Calgary.

Schwarz, K. P., M. Wei, and M. Van Gelderen (1994b) Aided Versus Embedded A Comparison of Two Approaches to GPS/INS Integration. *Proceedings of IEEE PLANS 1994*, pp. 314–322. IEEE.

Schwarz, K. P. and G. Zhang (1994) Developement and Testing of a Low Cost In-

tegrated GPS/INS. *Proceedings of ION GPS 1994*, pp. 1137–1144. Institute Of Naviation, Alexandria, VA., USA.

Sennott, J. and D. Senffner (1997) Robustness of Tightly Coupled Integrations for Real-Time Centimeter GPS Positioning. *Proceedings of ION GPS 1997*, pp. 655–663. Institute Of Navigation.

Shi, J. and M. E. Cannon (1995) Critical Error Effects and Analysis in Carrier Phase-Based Airborne GPS Positioning Over Large Areas. *Bulletin Géodésique*, 69, pp. 261–273.

Shin, E. H. (2001) *Accuracy Improvement of Low Cost INS/GPS for Land Applications*. Master's thesis, The University of Calgary. UCGE Report 20156 (Available at: http://www.ensu.ucalgary.ca/links/GradTheses.html).

Skone, S. (1998) *Wide Area Ionospheric Grid Modeling in Auroral Region*. Ph.D. thesis, The University of Calgary. UCGE Report 20123.

Spilker, J. J., Jr. (1996) GPS Signal Structure and Theoretical Performance. B. Parkinson and J. J. Spilker, Jr., eds., *Global Positioning System: Theory And Applications*, volume 1, chapter 7. American Institute of Aeronautics and Astronautics, Inc., Washington D.C., USA.

Spilker, J. J., Jr. and B. W. Parkinson (1996) Overview of GPS Operation and Design. B. Parkinson and J. J. Spilker, Jr., eds., *Global Positioning System: Theory And Applications*, volume 1, chapter 2. American Institute of Aeronautics and Astronautics, Inc., Washington D.C., USA.

Sun, H. (1994) *GPS/INS Integration for Airborne Applications*. Master's thesis, The University of Calgary. UCGE Report 20069.

Sun, H., M. E. Cannon, T. E. Owen, and M. A. Meindl (1994) An Investigation of Airborne GPS/INS for High Accuracy Position and Velocity Determination. *Proceedings of ION NTM 1994*, pp. 801–809. Institute Of Naviation, Alexandria, VA., USA.

Teunissen, P. J. G. (1990a) An Integrity And Quality Control Procedure For Use In Multi Sensor Integration. *Proceedings of ION GPS 1990*, pp. 513–522. Institute Of Naviation, Alexandria, VA., USA.

Teunissen, P. J. G. (1990b) Quality Control In Integrated Navigation Systems. *Proceedings of IEEE PLANS 1990*, pp. 158–165. IEEE.

Teunissen, P. J. G. (1990c) Some Aspects of Real-Time Model Validation Techniques For Use In Integrated Systems. *Proceedings of KIS 1990*, pp. 191–200. Department of Geomatics Engineering, The University of Calgary.

Teunissen, P. J. G. (1997) Some Remarks On GPS Ambiguity Resolution. *Publications of the Delft Geodetic Computing Centre*, 32(3), pp. 13–23.

Teunissen, P. J. G. and D. Odijk (1997) Ambiguity Dilution Of Precision: Definition, Properties, and Application. *Proceedings of ION GPS 1990*, pp. 891–899. Institute Of Naviation, Alexandria, VA., USA.

Teunissen, P. J. G. and M. A. Salzmann (1989) A recursive slippage test for use in state-space filtering. *manuscripta geodaetica*, 14, pp. 383–390.

Teunissen, P. J. G. and C. C. J. M. Tiberius (1994) Integer Least-Squares Estimation of The GPS Phase Ambiguities. *Proceedings of KIS 1994*, pp. 221–231. Department of Geomatics Engineering, The University of Calgary.

Vaníček, P. and E. J. Krakiwsky (1986) *Geodesy: The Concepts*. Elsevier, second edition.

Škaloud, J. (1998) Reducing The GPS Ambiguity Search Space By Including Inertial Data. *Proceedings of ION GPS 1998*, pp. 2073–2080. Institute Of Naviation, Alexandria, VA., USA.

Wanninger, L. (1993) Effects of the Equatorial Ionosphere on GPS. *GPS World*, pp. 48–54.

Ward, P. (1996) GPS Satellite Signal Characteristics. E. D. Kaplan, ed., *Understanding GPS Principles and Applications*, chapter 4. Artech House.

Wei, M., D. Lapucha, and H. Martell (1990) Fault Detection And Estimation In Dynamic Systems. *Proceedings of KIS 1990*, pp. 201–217. Department of Geomatics Engineering, The University of Calgary.

Wei, M. and K. P. Schwarz (1990a) A Strapdown Inertial Algroithm Using an Earth-Fixed Cartesian Frame. *Navigation: Journal of The Institute Of Navigation*, 37(2), pp. 153–167.

Wei, M. and K. P. Schwarz (1990b) Testing A Decentralized Filter for GPS/INS Integration. *Proceedings of IEEE PLANS 1990*, pp. 429–435. IEEE.

Yang, Y., J. Farrell, and M. Barth (2000) High-Accuracy Differential Carrier Phase GPS Aided Low-Cost INS. *IEEE Position Location and Navigation Symposium 2000*, pp. 148–155. IEEE.

Zhang, J. (1999) *Investigations into the Estimation of Residual Tropospheric Delays*

in a GPS Network. Master's thesis, The University of Calgary. UCGE Report 20132 (Available at: http://www.ensu.ucalgary.ca/links/GradTheses.html).

Appendix A

Equivalence of Simultaneous and Sequential Measurement Updates

This appendix derives the mathematical equivalence of using simultaneous and sequential processing strategies to update a Kalman filter. An alternate form of the Kalman filter is shown for this purpose. Equivalence is first shown using only two sets of observations before considering the more generic case.

A.1   Alternate Kalman Filter Algorithm

The Kalman filter algorithm shown in Chapter 2 is only one of two forms. The other form can be summarized using the following equations (Brown and Hwang, 1992)

$$\hat{x}_{k+1}^- = \Phi_{k,k+1}\hat{x}_k \tag{A.1}$$

$$C_{\hat{x}_{k+1}}^- = \Phi_{k,k+1}C_{\hat{x}_k}\Phi_{k,k+1}^T + Q_k \tag{A.2}$$

$$C_{\hat{x}_k}^+ = \left((C_{\hat{x}_k}^-)^{-1} + H_k^T C_{z_k}^{-1} H_k\right)^{-1} \tag{A.3}$$

$$K_k = C_{\hat{x}_k}^+ H_k^T C_{z_k}^{-1} \tag{A.4}$$

$$\hat{x}_k^+ = \hat{x}_k^- + K_k\left(z_k - H_k\hat{x}_k^-\right) \tag{A.5}$$

This algorithm is essentially a combination of least-squares with weighted parameters and a prediction step. As can be seen, most of the steps are the same as in the

original algorithm. The gain matrix using both approaches is also identical (Brown and Hwang, 1992) however, both formulations will be used below for convenience.

A.2 Equivalence of Update Strategies

The derivation presented below utilizes the notation developed in Section 6.1. In this regard, some symbols that did not use this notation before are included here. At these locations, the symbol is defined, but the notation is not explained in detail as it is obvious from the context.

A.2.1 Equivalence Using Two Observation Sets

The proof begins by assuming two sets of statistically independent observations

$$z_1 \quad = \quad H_1 x + v_1$$

$$z_2 \quad = \quad H_2 x + v_2$$

By assuming the observations are processed both simultaneously and sequentially, the equivalence of the two approaches can be shown.

Sequential Updates

Assume that the first set of observations are processed to give

$$\hat{x}^{(1)} \quad = \quad \hat{x}^{(0)} + K_1^{(0)} \nu_1^{(0)} \tag{A.6}$$

$$= \quad \hat{x}^{(0)} + \chi_1^{(0)} \tag{A.7}$$

where, in general

$$\chi_i^{(j,k,\dots)} = K_i^{(j,k,\dots)} \nu_i^{(j,k,\dots)} \tag{A.8}$$

represents the corrections to the estimated parameters using the ith set of observations.

Next, assume the second set of observations is processed to yield

$$\hat{x}^{(2)} = \hat{x}^{(1)} + K_2^{(1)} \nu_2^{(1)} \tag{A.9}$$

$$= \hat{x}^{(1)} + \chi_2^{(1)} \tag{A.10}$$

where the innovation sequence is given by

$$\nu_2^{(1)} = z_k - H_2 \hat{x}^{(1)}$$

$$= z_k - H_2 \left(\hat{x}^{(0)} + K_2^{(1)} \nu_1^{(0)} \right)$$

$$= \nu_2^{(0)} - H_2 K_2^{(1)} \nu_1^{(0)} \tag{A.11}$$

From the above two processing steps, the cumulative correction applied to $\hat{x}^{(0)}$ is given by

$$\chi_{1,2}^{(0)} = \chi_1^{(0)} + \chi_2^{(1)}$$

$$= K_1^{(0)} \nu_1^{(0)} + K_2^{(1)} \nu_2^{(1)}$$

$$= K_1^{(0)} \nu_1^{(0)} + K_2^{(1)} \left(\nu_2^{(0)} - H_2 K_2^{(1)} \nu_1^{(0)} \right)$$

$$= \left(I - K_2^{(1)} H_2 \right) K_1^{(0)} \nu_1^{(0)} + K_2^{(1)} \nu_2^{(0)} \tag{A.12}$$

Simultaneous Update

In contrast to above, consider the case where both observations are processed simultaneously. In this case, the gain matrix is given by

$$
\begin{aligned}
K_{1,2}^{(0)} &= \left((C_{\hat{x}}^{(0)})^{-1} + H_1^T C_{z_1}^{-1} H_1 + H_2^T C_{z_2}^{-1} H_2 \right)^{-1} \left[\begin{array}{cc} H_1^T C_{z_1}^{-1} & H_2^T C_{z_2}^{-1} \end{array} \right] \\[2mm]
&= \left((C_{\hat{x}}^{(1)})^{-1} + H_2^T C_{z_2}^{-1} H_2 \right)^{-1} \left[\begin{array}{cc} H_1^T C_{z_1}^{-1} & H_2^T C_{z_2}^{-1} \end{array} \right] \\[2mm]
&= (C_{\hat{x}}^{(1,2)})^{-1} \left[\begin{array}{cc} H_1^T C_{z_1}^{-1} & H_2^T C_{z_2}^{-1} \end{array} \right]
\end{aligned}
$$

where Equation A.3 was used to obtain the second and then the third lines. Next, assuming the innovation sequences for the two sets of observations can be denoted $\nu_{1,2}^{(0)} = \left[\begin{array}{cc} \nu_1^{(0)} & \nu_2^{(0)} \end{array} \right]^T$, the corrections to the initial state vector can be computed as

$$
\begin{aligned}
\chi_{1,2}^{(0)} &= K_{1,2}^{(0)} \nu_{1,2}^{(0)} \\[2mm]
&= C_{\hat{x}}^{(1,2)} H_1^T C_{z_1}^{-1} \nu_1^{(0)} + C_{\hat{x}}^{(1,2)} H_2^T C_{z_2}^{-1} \nu_2^{(0)} \\[2mm]
&= \left(I - K_2^{(1)} H_2 \right) C_{\hat{x}}^{(1)} H_1^T C_{z_1}^{-1} \nu_1^{(0)} + K_2^{(1)} \nu_2^{(0)} \\[2mm]
&= \left(I - K_2^{(1)} H_2 \right) K_1^{(0)} \nu_1^{(0)} + K_2^{(1)} \nu_2^{(0)} \qquad (\text{A.13})
\end{aligned}
$$

where the following substitutions were made

- $C_{\hat{x}}^{(1,2)} = \left(I - K_2^{(1)} H_2 \right) C_{\hat{x}}^{(1)}$ from line 2 to 3

- $C_{\hat{x}}^{(1,2)} H_2^T C_{z_2}^{-1} = K_2^{(1)}$ from line 2 to 3

- $C_{\hat{x}}^{(1)} H_1^T C_{z_1}^{-1} = K_1^{(0)}$ from lines 3 to 4

Finally, comparing Equations A.12 and A.13, the two approaches are shown to be identical, as desired.

A.2.2 Equivalence Using Arbitrary Number of Observation Sets

The previous section only showed the desired equivalence for the case of two observation sets. To expand this, first consider the case with three observation sets, z_1, z_2 and z_3. The first two sets of observations can be grouped together as $z_{1,2}$ and processed simultaneously without affecting the estimated states, as shown above. This leaves two observation sets $z_{1,2}$ and z_3 which can also be processed using either approach to arrive at the same result. Recursive application of the same logic to an arbitrary number of observation sets proves the that in general, simultaneous and sequential processing are numerically equivalent.

Appendix B

Dynamics Matrix for INS Error States

The state-space form of the INS error equations is shown in Chapter 4. It is reproduced here along with details of the individual matrices as follows

$$
\begin{bmatrix} \delta\dot{r}^e \\ \delta\dot{v}^e \\ \dot{\varepsilon}^e \\ \delta\dot{b}^b \\ \delta\dot{d}^b \end{bmatrix} = \begin{bmatrix} 0 & I & 0 & 0 & 0 \\ N^e & -2\Omega_{ie}^e & -F^e & R_b^e & 0 \\ 0 & 0 & -\Omega_{ie}^e & 0 & R_b^e \\ 0 & 0 & 0 & -diag(\alpha_i) & 0 \\ 0 & 0 & 0 & 0 & -diag(\beta_i) \end{bmatrix} \begin{bmatrix} \delta r^e \\ \delta v^e \\ \varepsilon^e \\ \delta b^b \\ \delta d^b \end{bmatrix}
$$

$$
+ \begin{bmatrix} 0 & 0 & 0 & 0 \\ R_b^e & 0 & 0 & 0 \\ 0 & R_b^e & 0 & 0 \\ 0 & 0 & I & 0 \\ 0 & 0 & 0 & I \end{bmatrix} \begin{bmatrix} w_f \\ w_\omega \\ w_b \\ w_d \end{bmatrix}
$$

where R_b^e is the rotation matrix from the body-frame to the ECEF-frame, $diag(\alpha_i)$ and $diag(\beta_i)$ are diagonal matrices for modeling the bias states are first-order Gauss-Markov processes. The remaining elements are given by

$$
N^e = \begin{bmatrix} \frac{kM}{R^3}\left(\frac{3r_x^2}{R^2}-1\right)+\omega_e^2 & \frac{kM}{R^3}\frac{3r_xr_y}{R^2} & \frac{kM}{R^3}\frac{3r_xr_z}{R^2} \\ \frac{kM}{R^3}\frac{3r_xr_y}{R^2} & \frac{kM}{R^3}\left(\frac{3r_y^2}{R^2}-1\right)+\omega_e^2 & \frac{kM}{R^3}\frac{3r_yr_z}{R^2} \\ \frac{kM}{R^3}\frac{3r_xr_z}{R^2} & \frac{kM}{R^3}\frac{3r_yr_z}{R^2} & \frac{kM}{R^3}\left(\frac{3r_z^2}{R^2}-1\right) \end{bmatrix}
$$

$$-\Omega_{ie}^{e} = \begin{bmatrix} 0 & \omega_e & 0 \\ \omega_e & 0 & 0 \\ 0 & 0 & 0 \end{bmatrix}$$

$$-F^e = \begin{bmatrix} 0 & f_z & -f_y \\ -f_z & 0 & f_x \\ f_y & -f_x & 0 \end{bmatrix}$$

where

k is the gravitational constant,

M is the mass of the Earth,

r is the position along the subscripted axis,

w_e is the rotation rate of the Earth, and

f is the specific force measured along the subscripted axis.

Appendix C

Matrix Inversion by Partitioning

If a matrix A is invertible and is given by

$$A = \begin{bmatrix} A_{11} & A_{12} \\ A_{21} & A_{22} \end{bmatrix}$$

then its inverse can be shown to be given by a matrix B with the form

$$B = \begin{bmatrix} B_{11} & B_{12} \\ B_{21} & B_{22} \end{bmatrix}$$

where (Mikhail, 1976)

$$
\begin{aligned}
B_{11} &= \left(A_{11} - A_{12} A_{22}^{-1} A_{21} \right)^{-1} \\[2mm]
B_{12} &= -B_{11} A_{12} A_{22}^{-1} \\[2mm]
&= \left(A_{12} A_{22}^{-1} A_{21} - A_{11} \right)^{-1} A_{12} A_{22}^{-1} \\[2mm]
B_{21} &= -A_{22}^{-1} A_{21} B_{11} \\[2mm]
&= A_{22}^{-1} A_{21} \left(A_{12} A_{22}^{-1} A_{21} - A_{11} \right)^{-1} \\[2mm]
B_{22} &= A_{22}^{-1} - A_{22}^{-1} A_{21} B_{12} \\[2mm]
&= A_{22}^{-1} + A_{22}^{-1} A_{21} B_{11} A_{12} A_{22}^{-1} \\[2mm]
&= A_{22}^{-1} + A_{22}^{-1} A_{21} \left(A_{11} - A_{12} A_{22}^{-1} A_{21} \right)^{-1} A_{12} A_{22}^{-1}
\end{aligned}
$$

Appendix D

Simulated Data Outages

The data outages simulated for post-mission analysis are shown in detail here. Specifically, on each of the following pages, a closeup of the trajectory during the data outage is shown, along with the approximate accelerations during the data outage. The trajectories are shown relative to the base station to facilitate baseline length computations. The accelerations were obtained as the time difference of the velocity and are thus quite noisy. However, the general trends are sufficient for identifying the overall dynamics of the vehicle during the data outages.
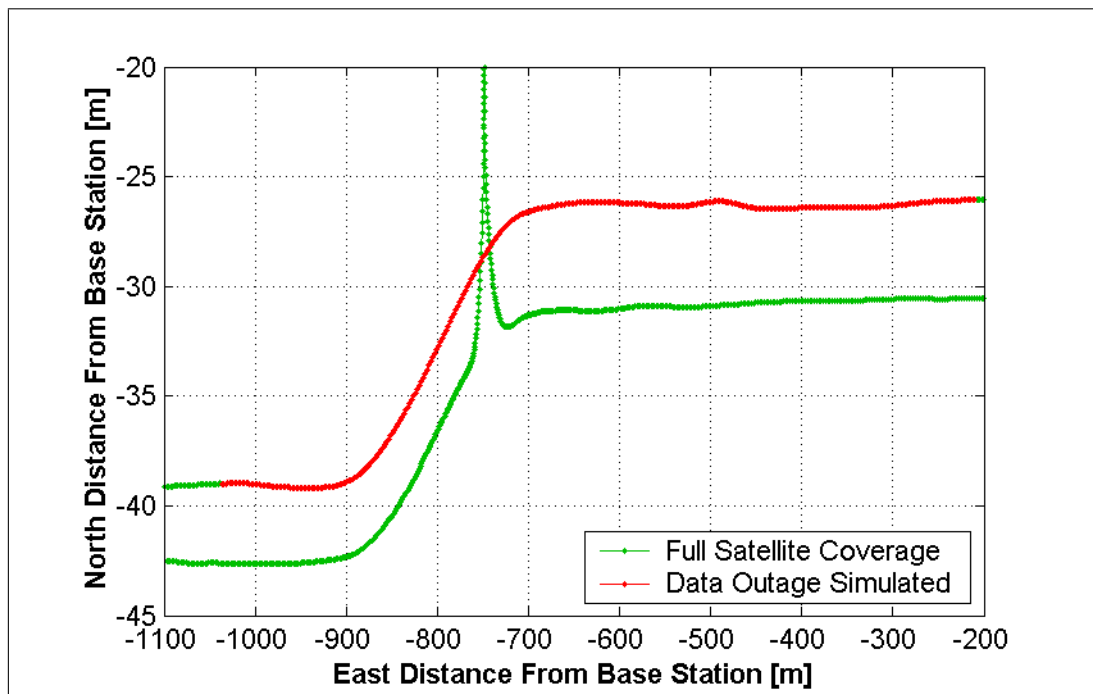
Figure D.1: Trajectory During Data Outage #1, Run #1
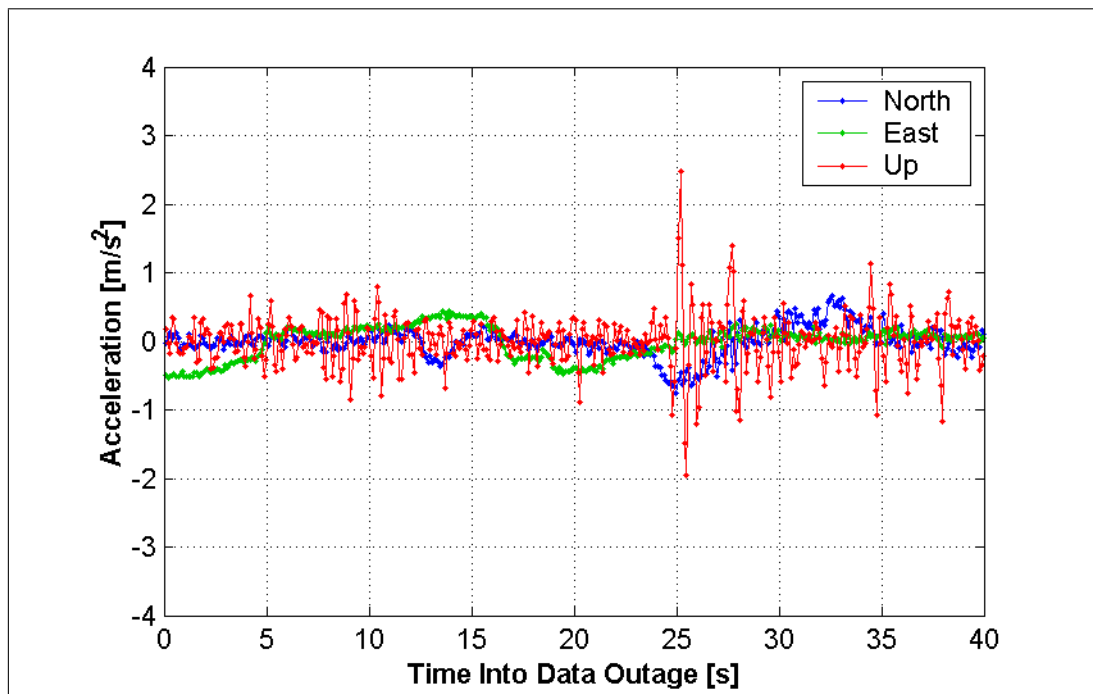
Figure D.2: Approximate Vehicle Accelerations During Data Outage #1, Run #1
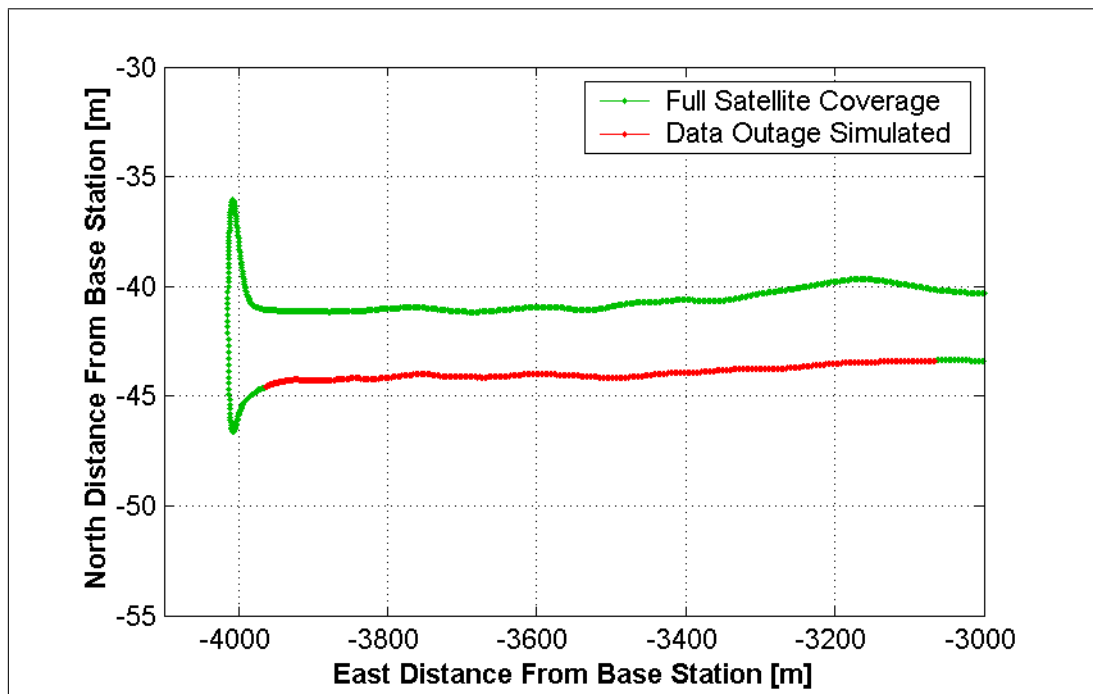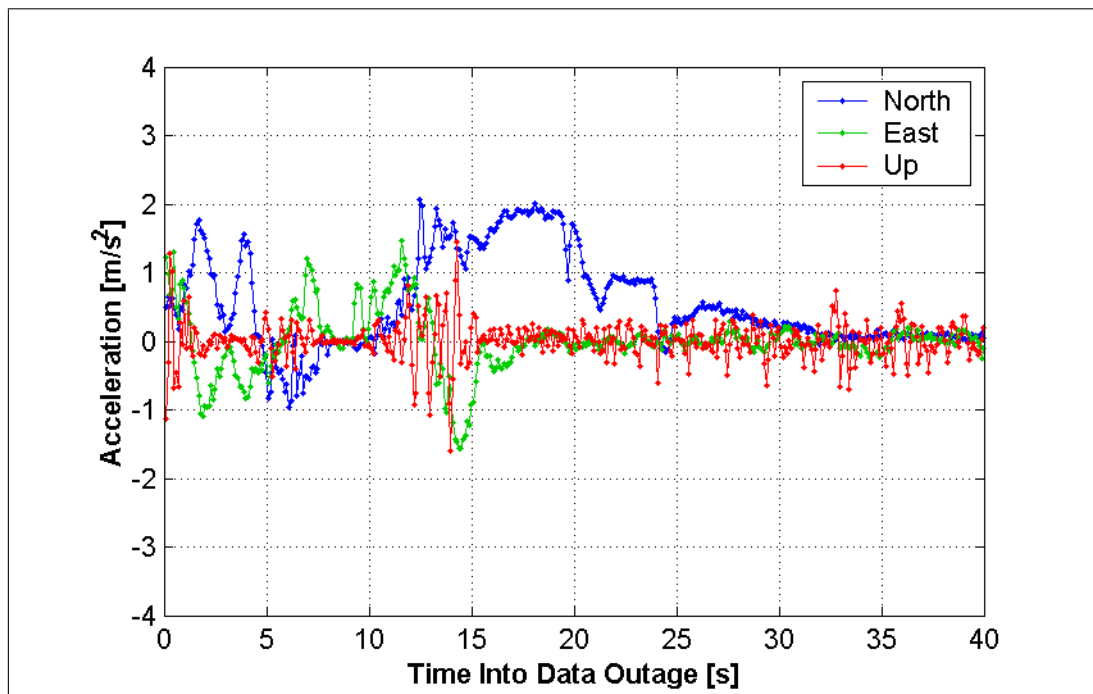
Figure D.3: Trajectory During Data Outage #2, Run #1
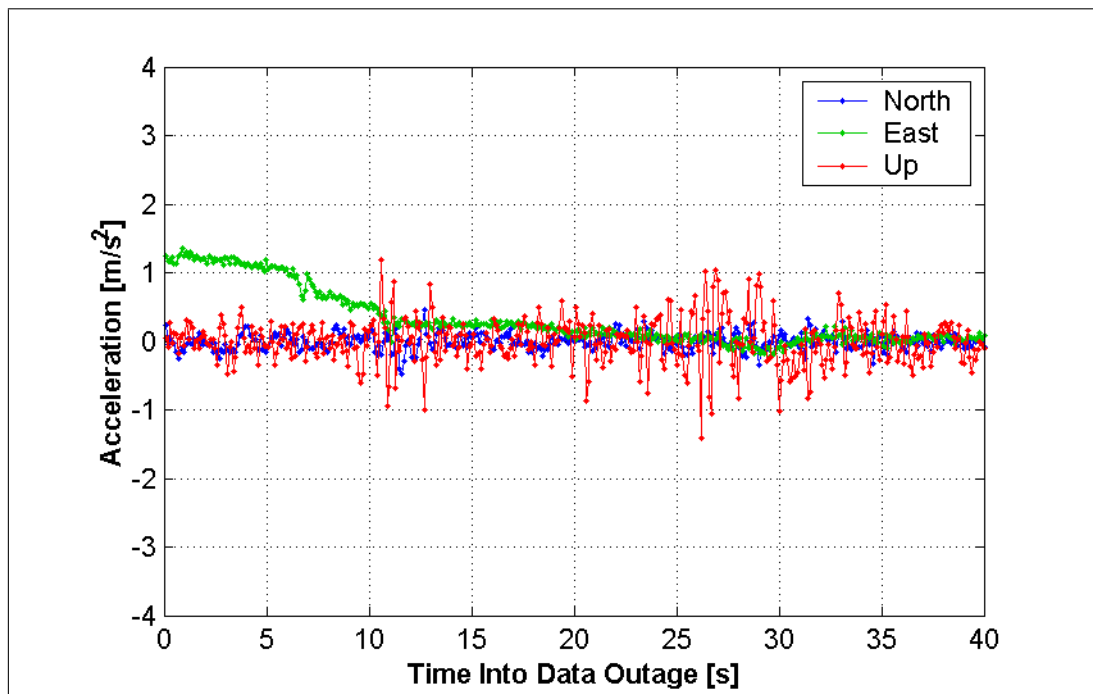
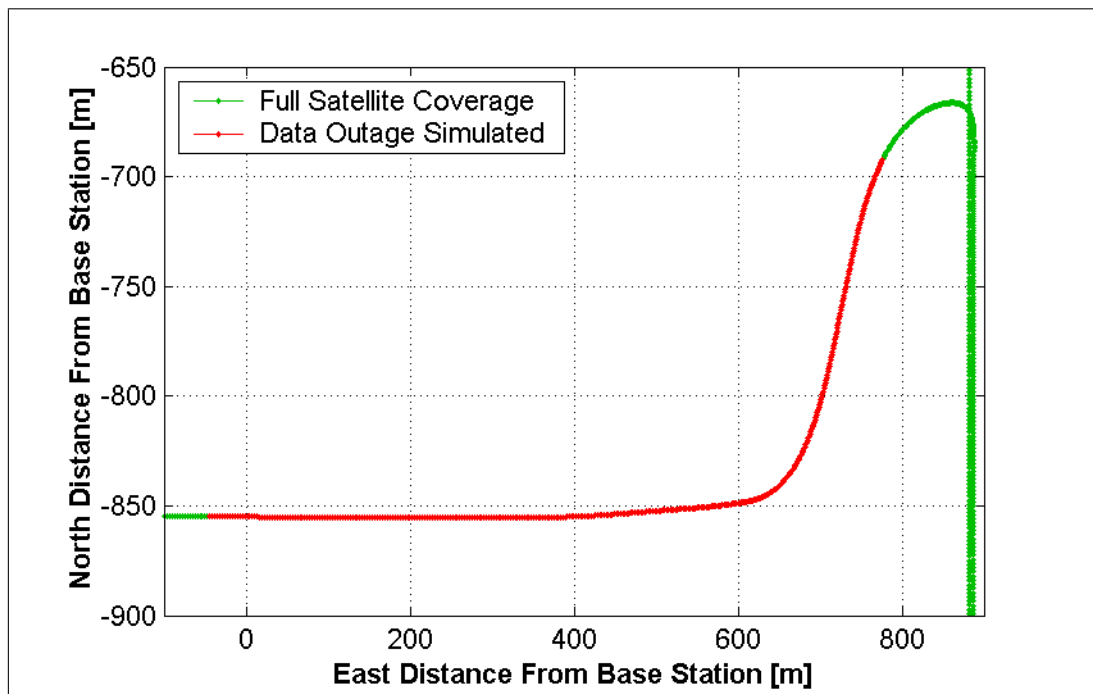Figure D.4: Approximate Vehicle Accelerations During Data Outage #2, Run #1
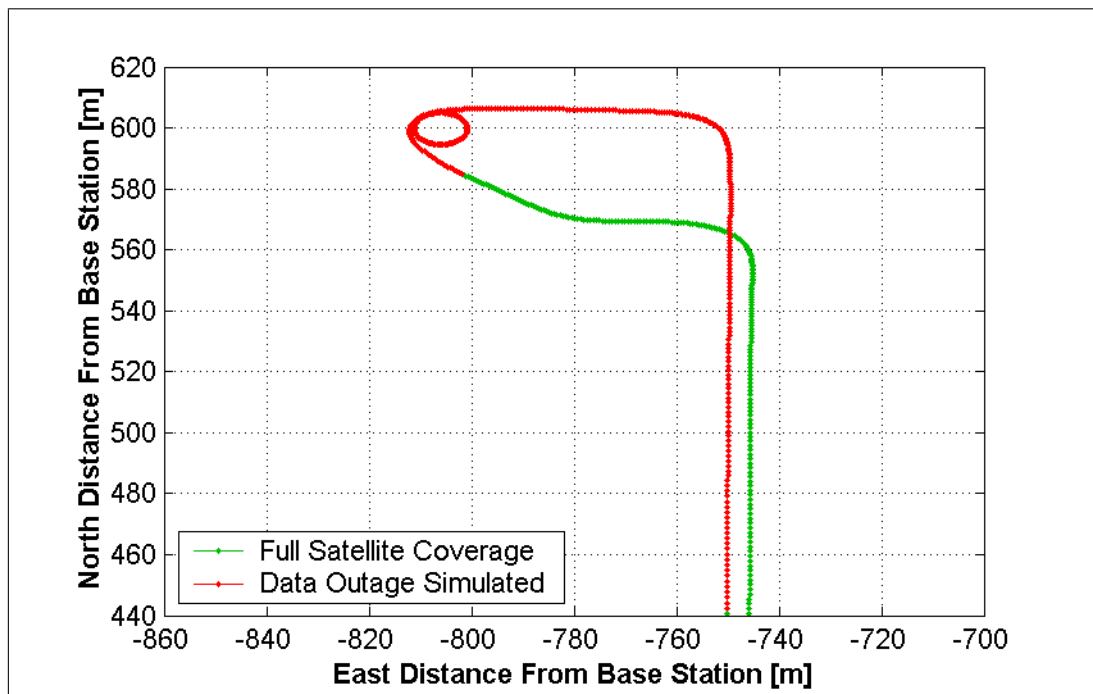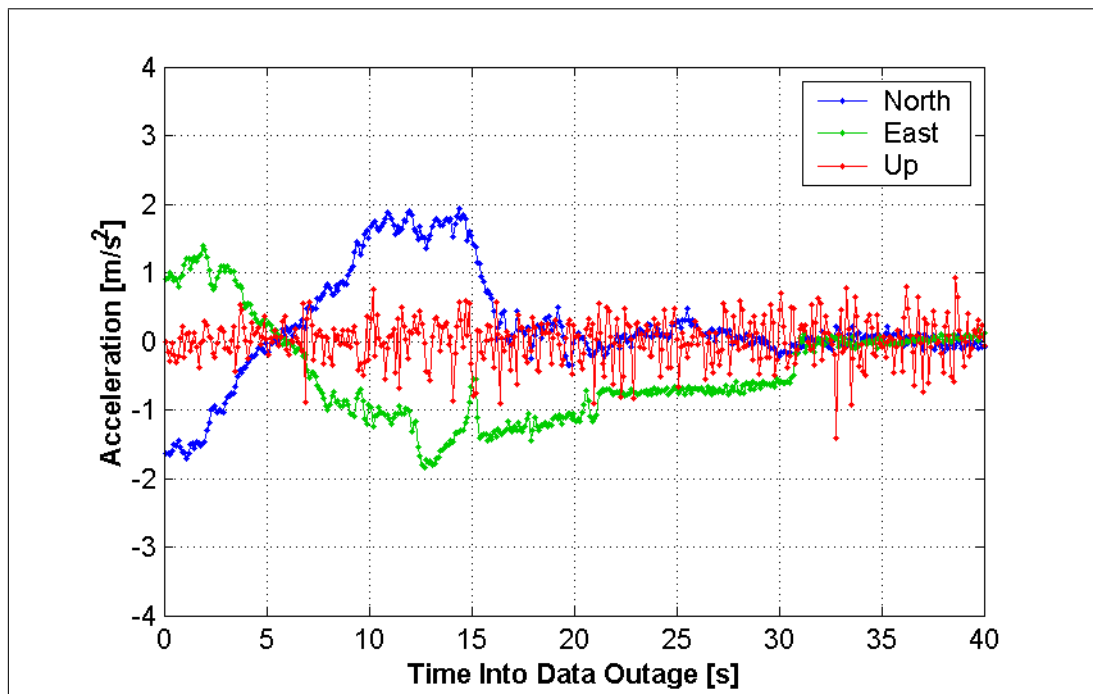
Figure D.5: Trajectory During Data Outage #3, Run #1
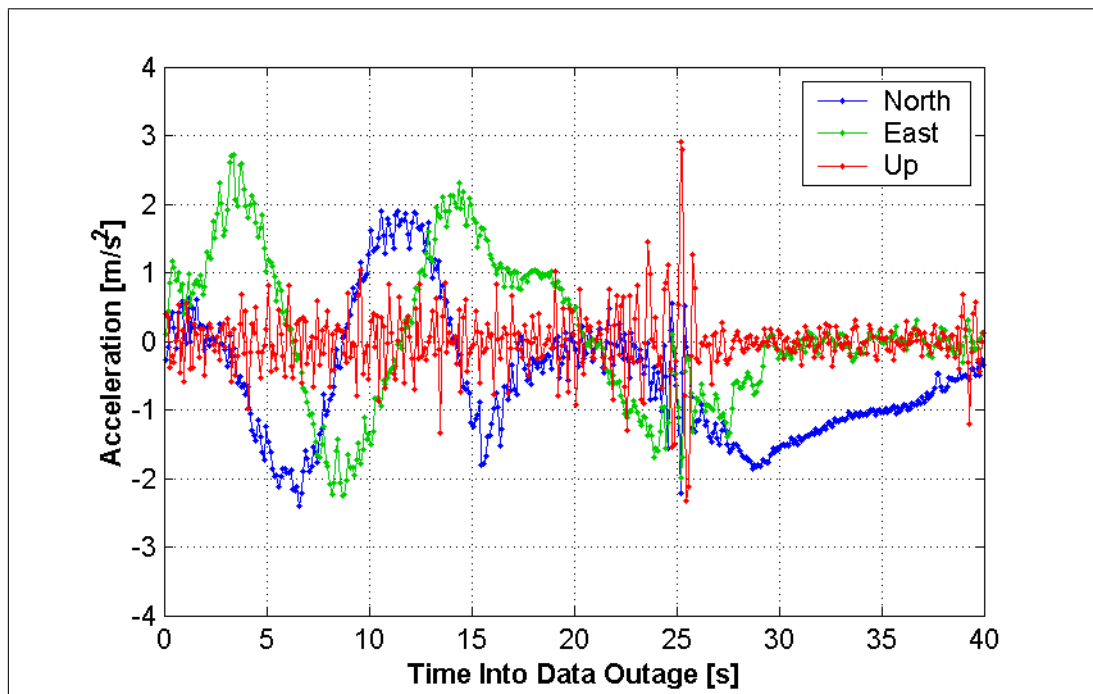
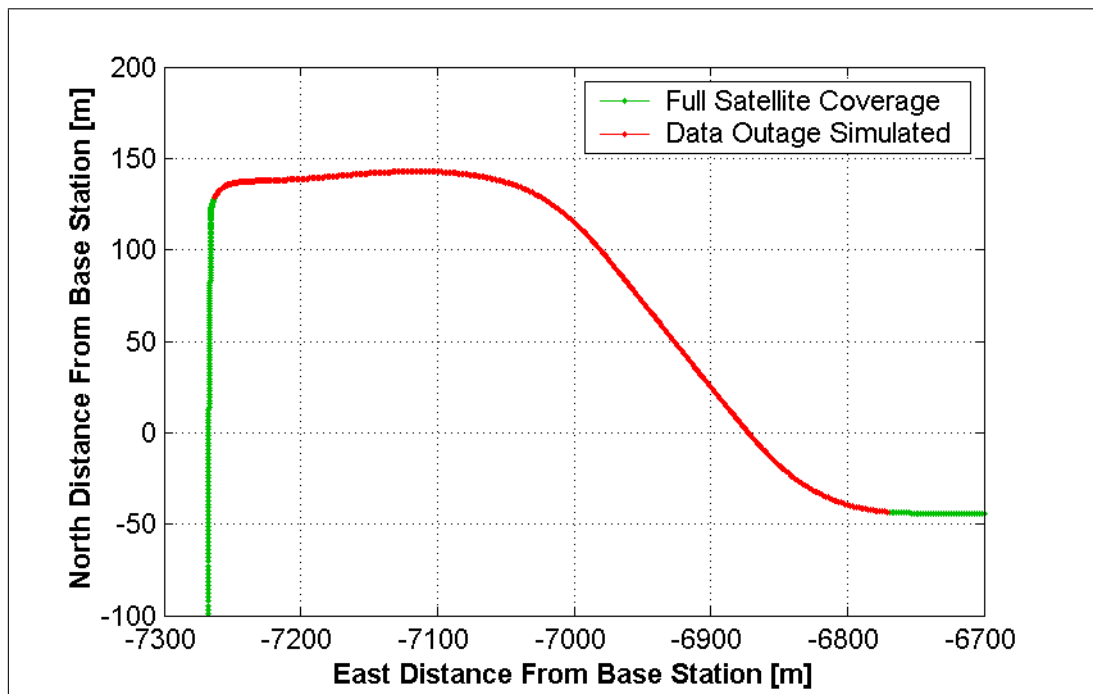Figure D.6: Approximate Vehicle Accelerations During Data Outage #3, Run #1
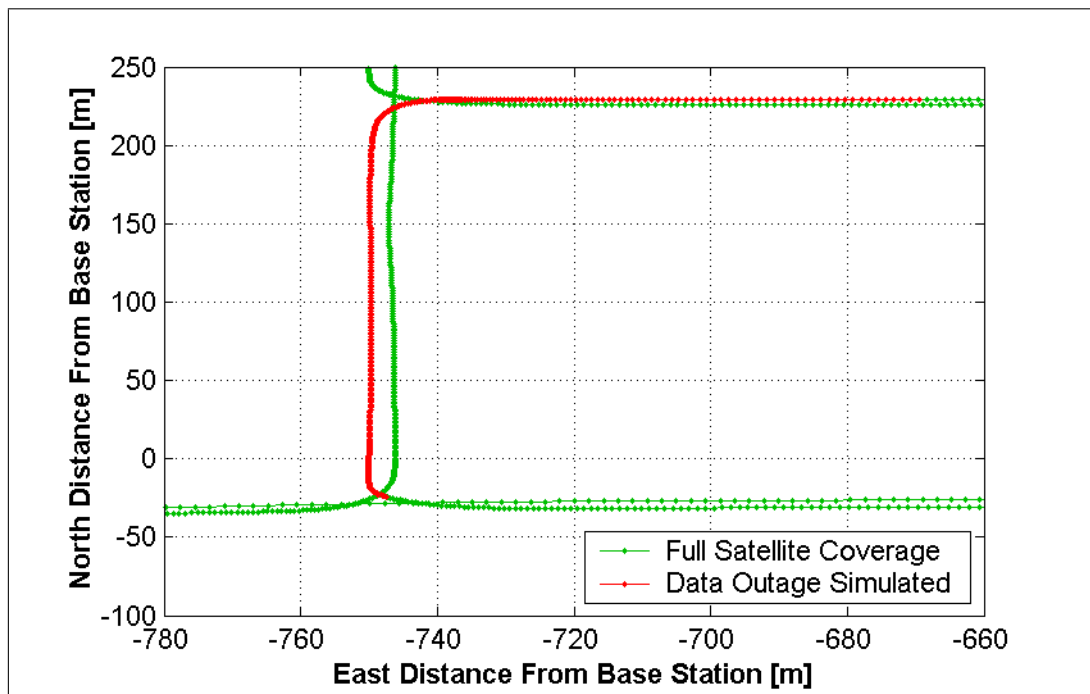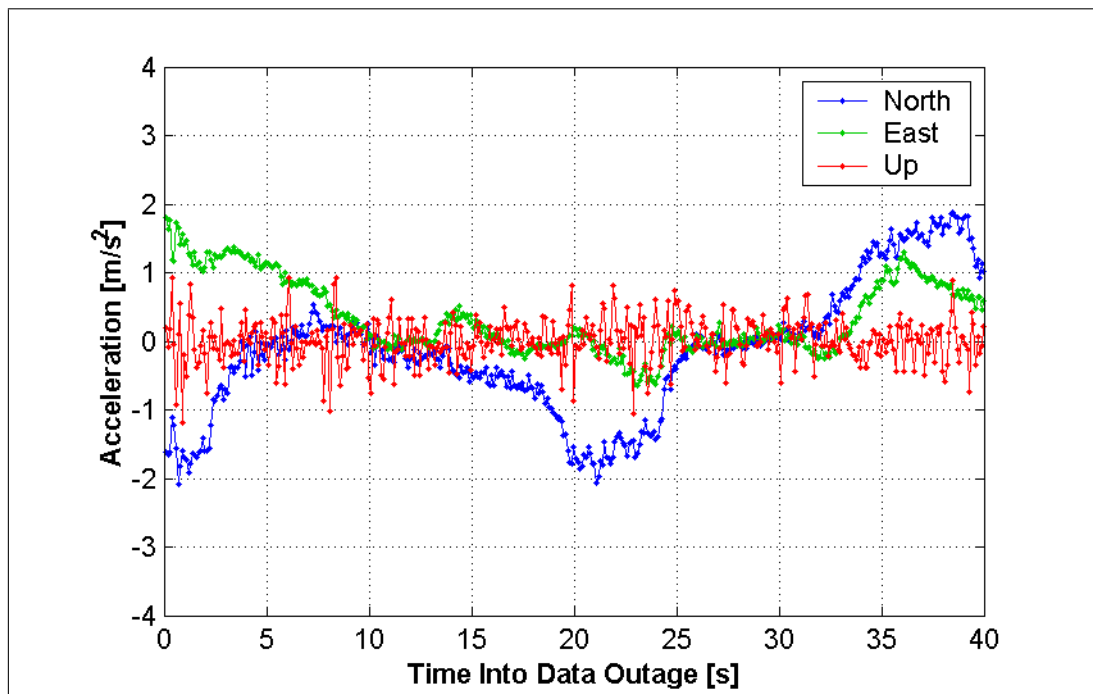
Figure D.7: Trajectory During Data Outage #4, Run #1
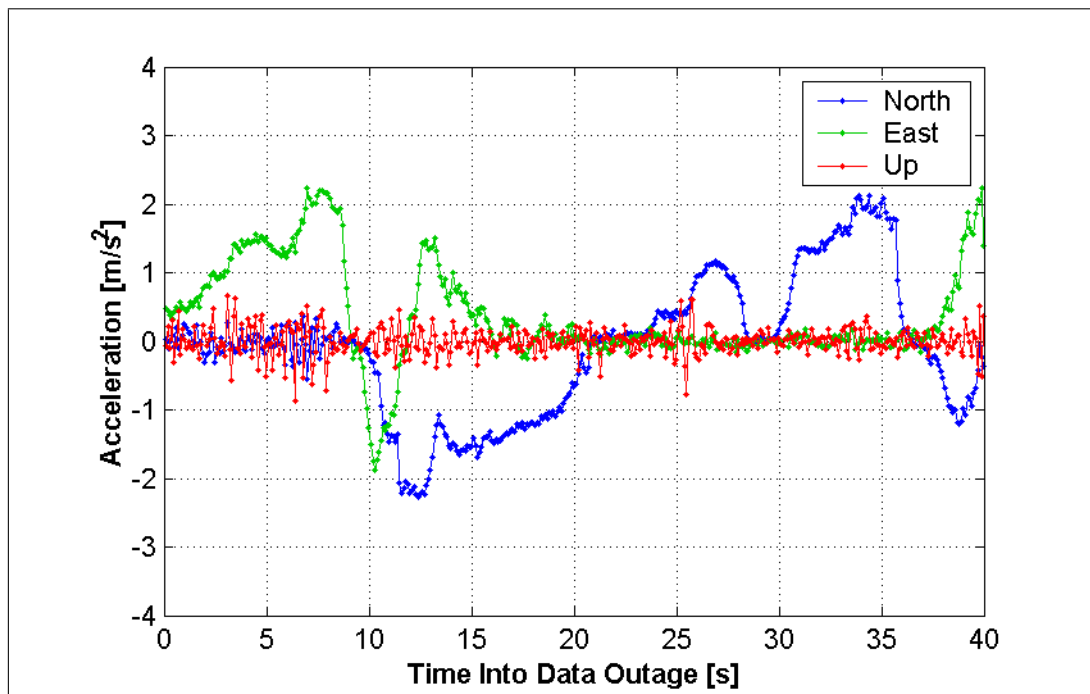
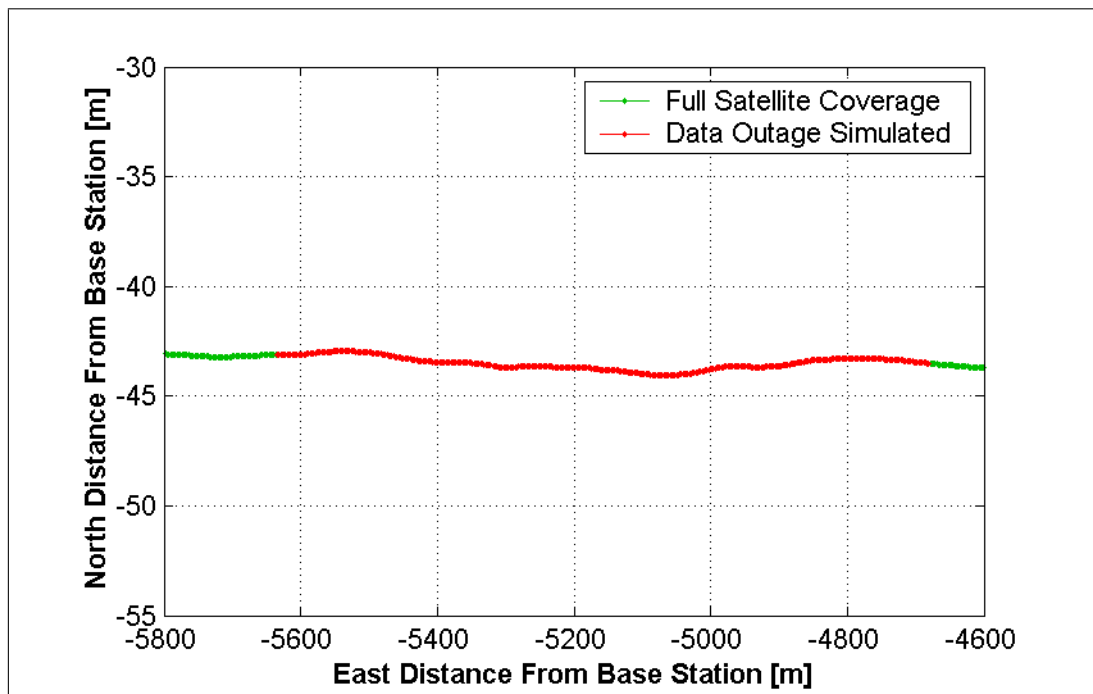Figure D.8: Approximate Vehicle Accelerations During Data Outage #4, Run #1
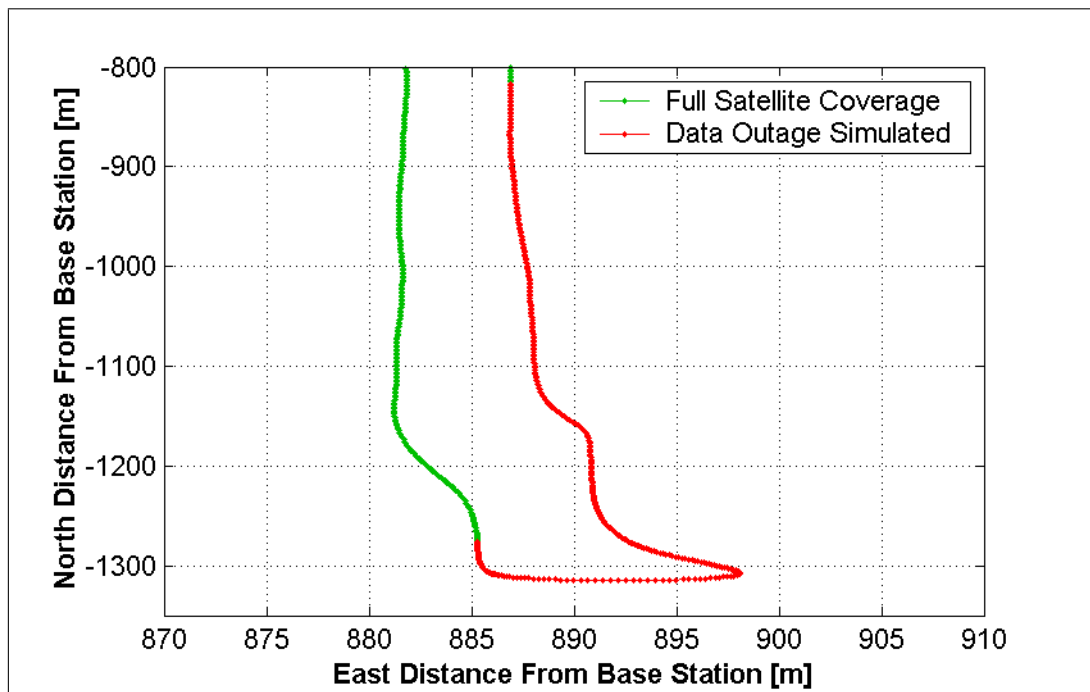
Figure D.9: Trajectory During Data Outage #5, Run #1
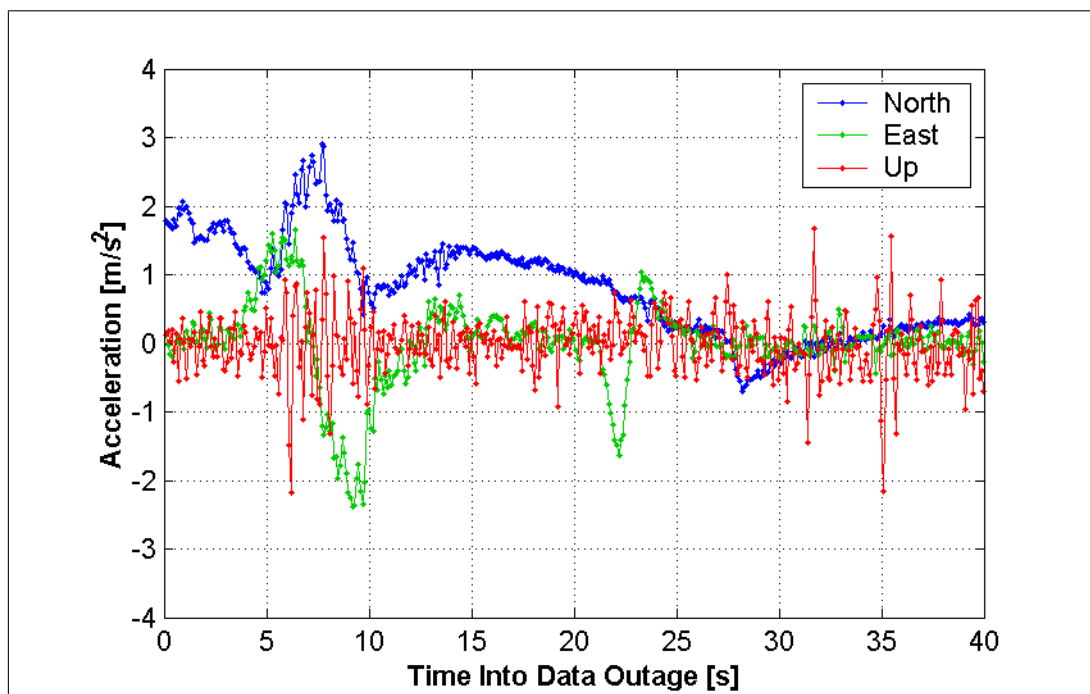
Figure D.10: Approximate Vehicle Accelerations During Data Outage #5, Run #1
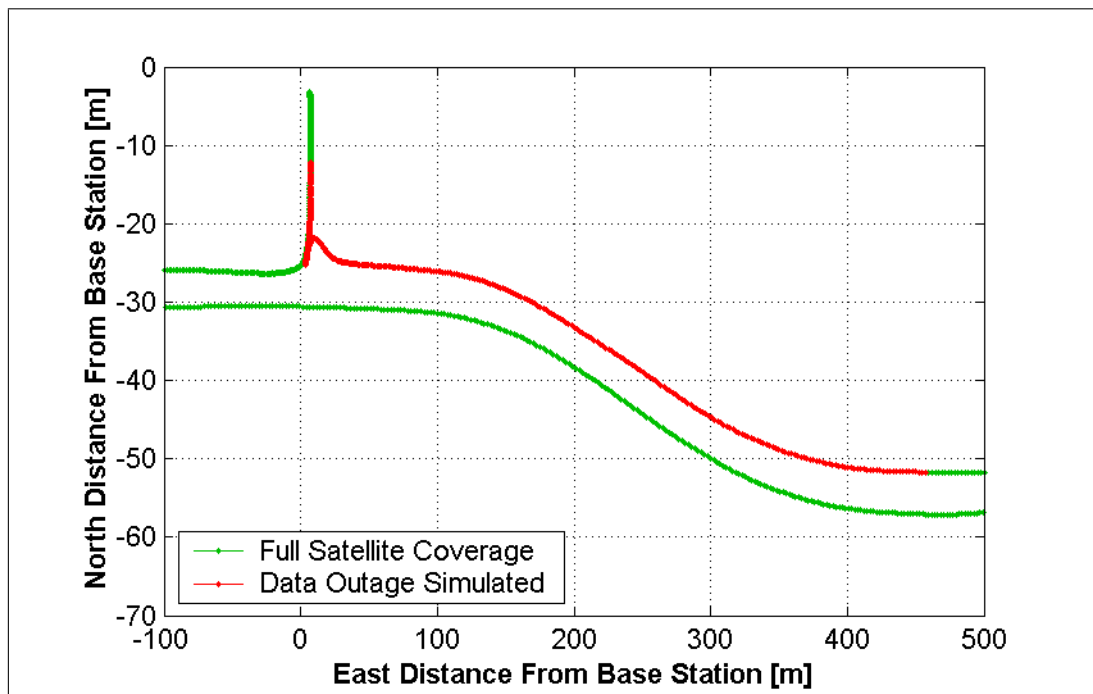
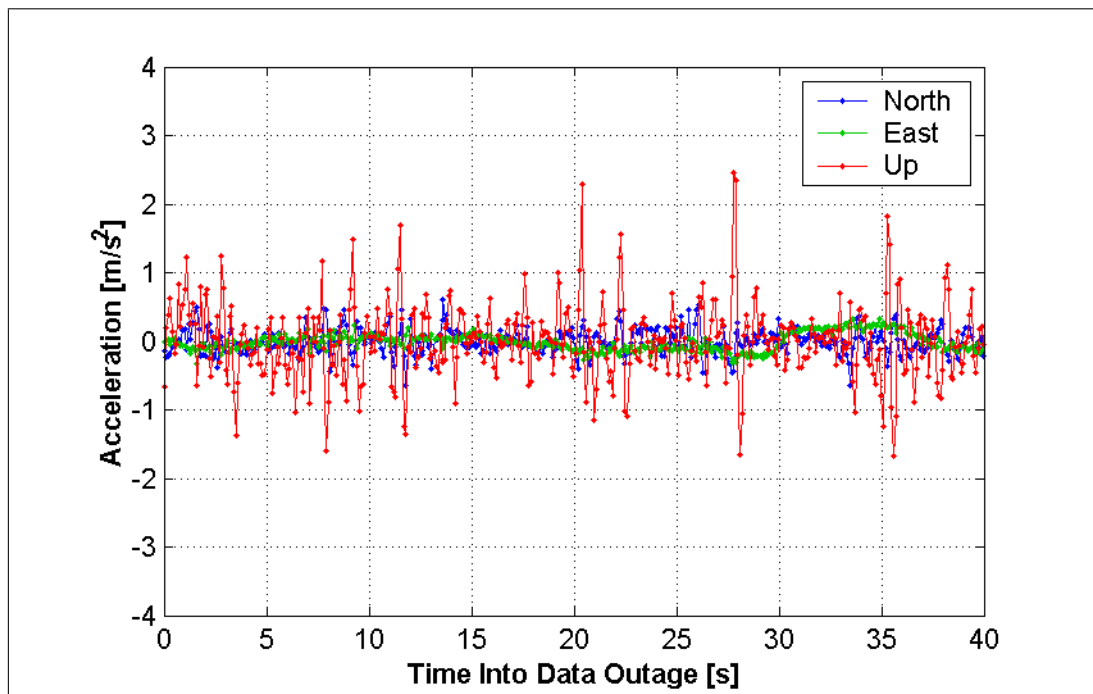Figure D.11: Trajectory During Data Outage #6, Run #1
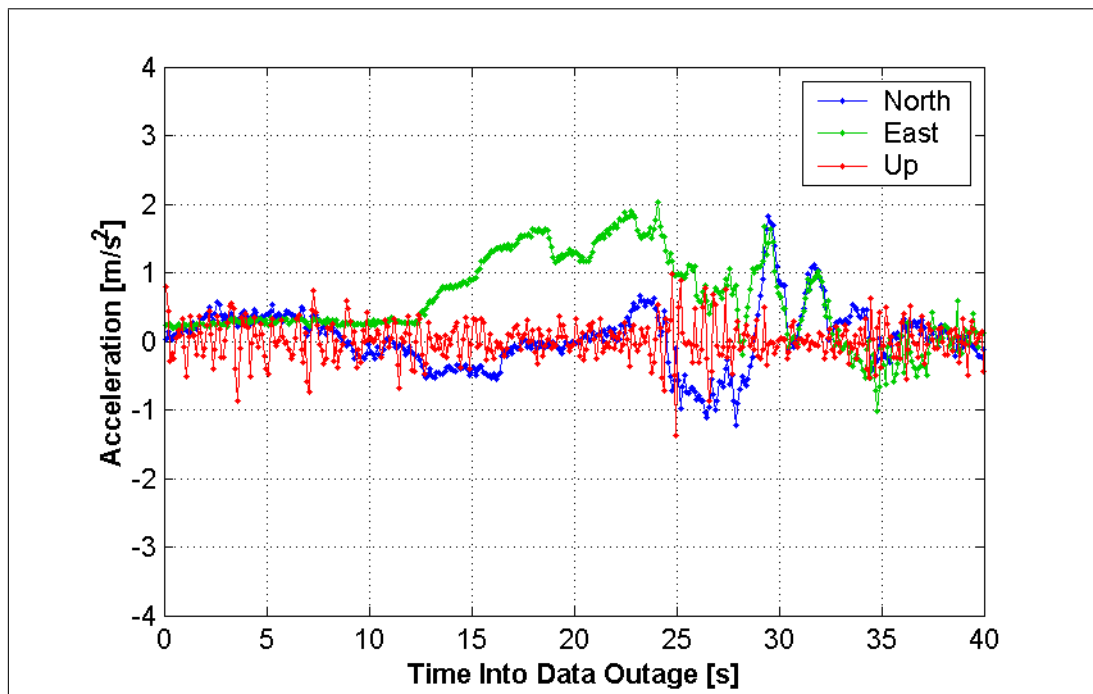
Figure D.12: Approximate Vehicle Accelerations During Data Outage #6, Run #1
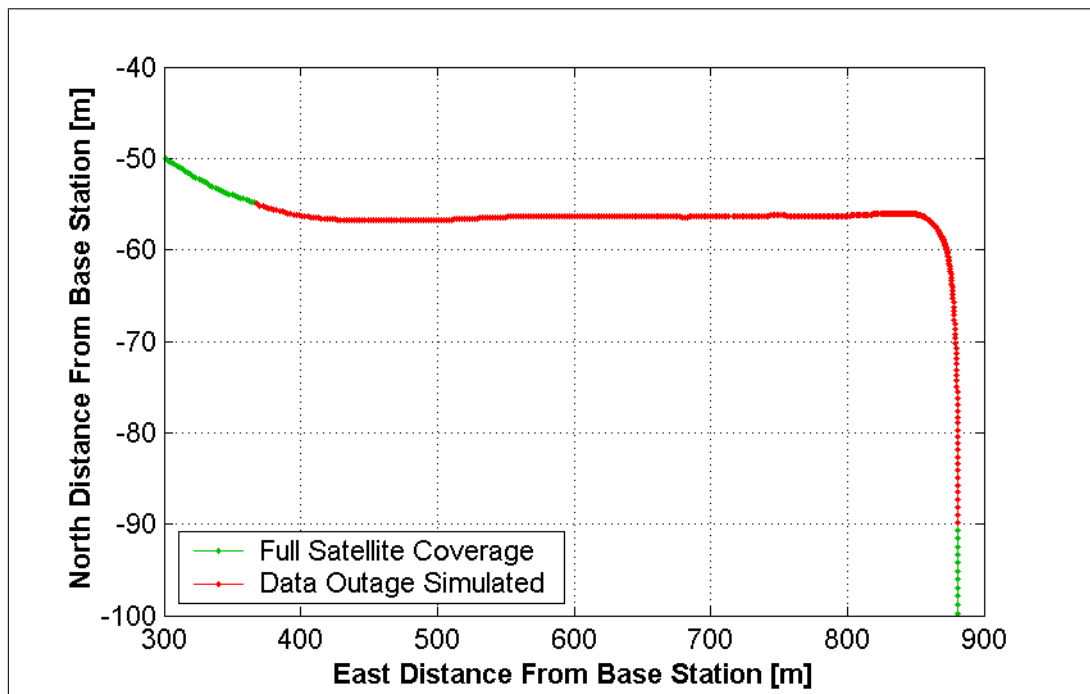
Figure D.13: Trajectory During Data Outage #1, Run #2
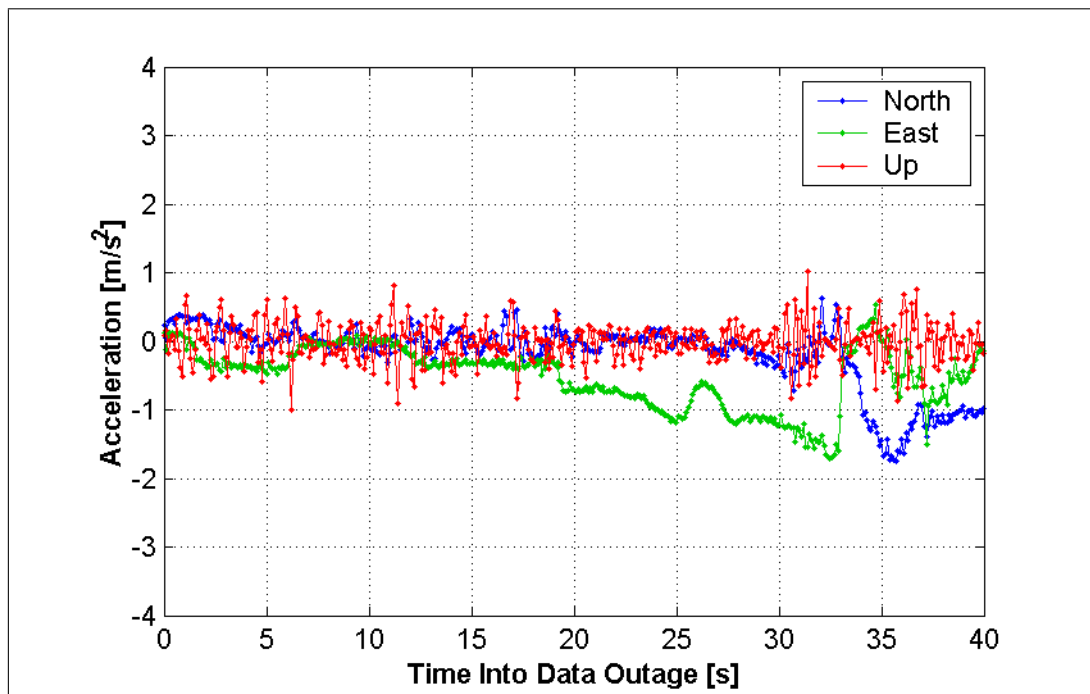
Figure D.14: Approximate Vehicle Accelerations During Data Outage #1, Run #2
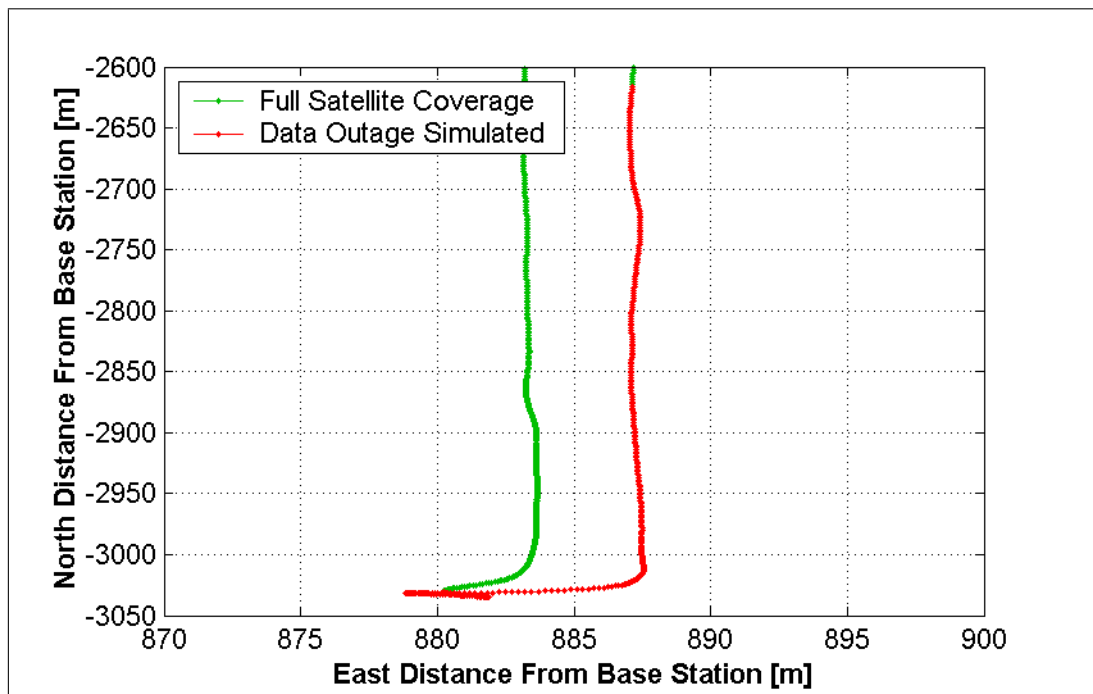
Figure D.15: Trajectory During Data Outage #2, Run #2

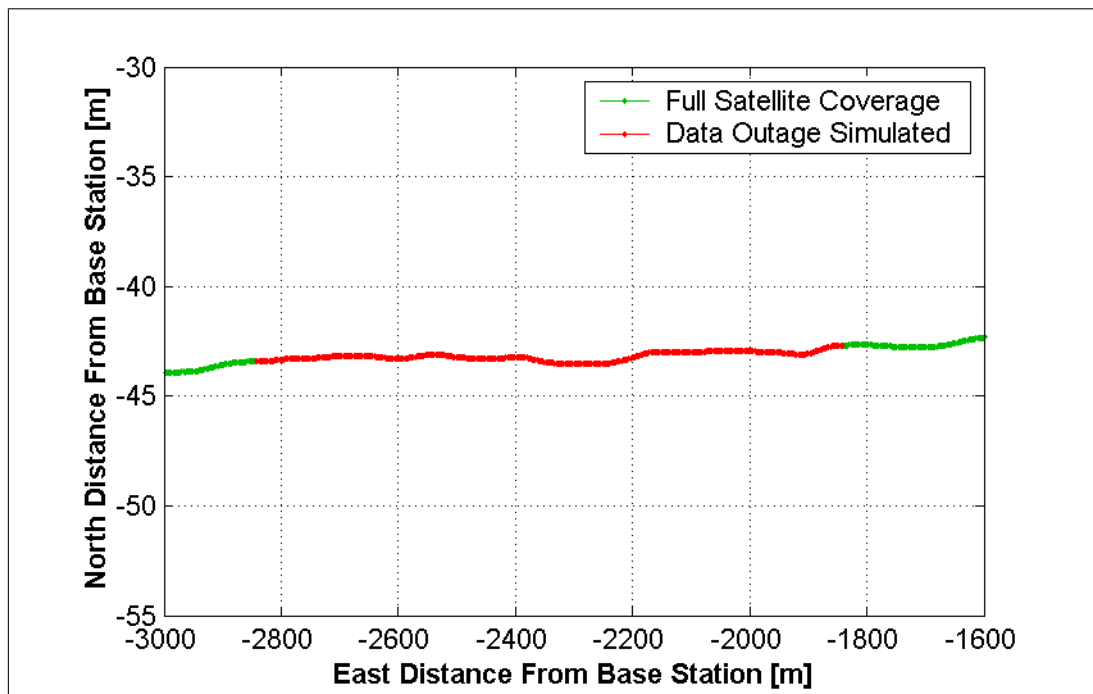Figure D.16: Approximate Vehicle Accelerations During Data Outage #2, Run #2

Figure D.17: Trajectory During Data Outage #3, Run #2

Figure D.18: Approximate Vehicle Accelerations During Data Outage #3, Run #2

Figure D.19: Trajectory During Data Outage #4, Run #2

Figure D.20: Approximate Vehicle Accelerations During Data Outage #4, Run #2

Figure D.21: Trajectory During Data Outage #5, Run #2

Figure D.22: Approximate Vehicle Accelerations During Data Outage #5, Run #2

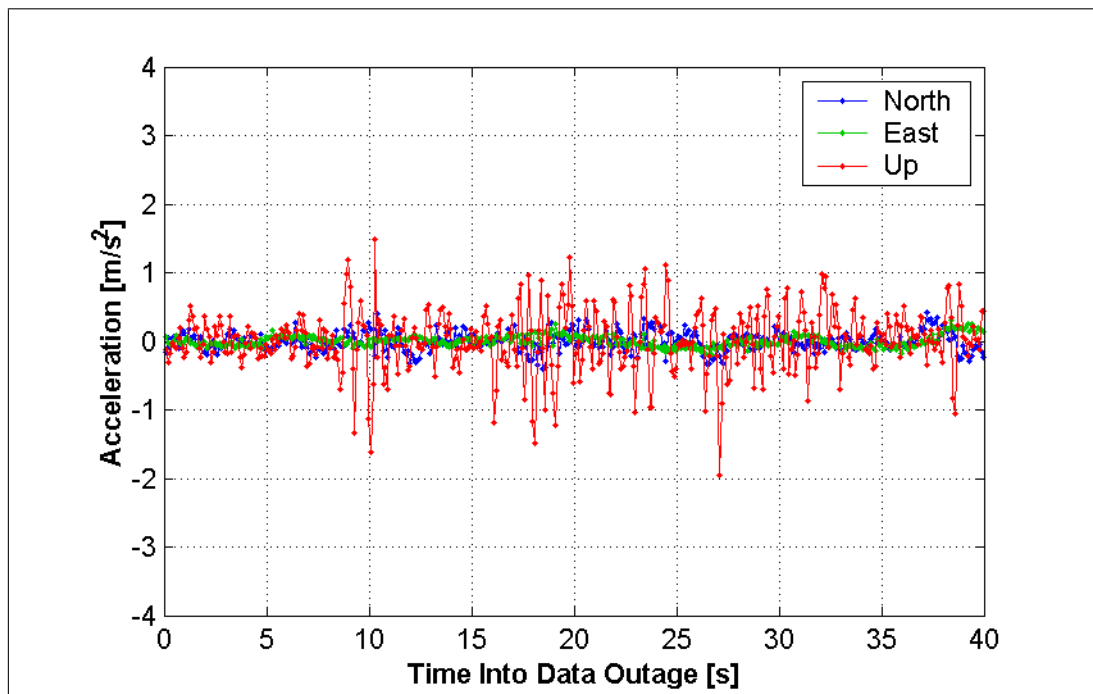Figure D.23: Trajectory During Data Outage #6, Run #2

Figure D.24: Approximate Vehicle Accelerations During Data Outage #6, Run #2

Appendix E

Pictures of First Real-Time Run

This appendix contains pictures taken from various locations along the first real-time test run. The figures are labeled according to the street names and the direction in which the camera was pointing when the picture was taken. For convenience, the overall trajectory is shown in Figure E.1.
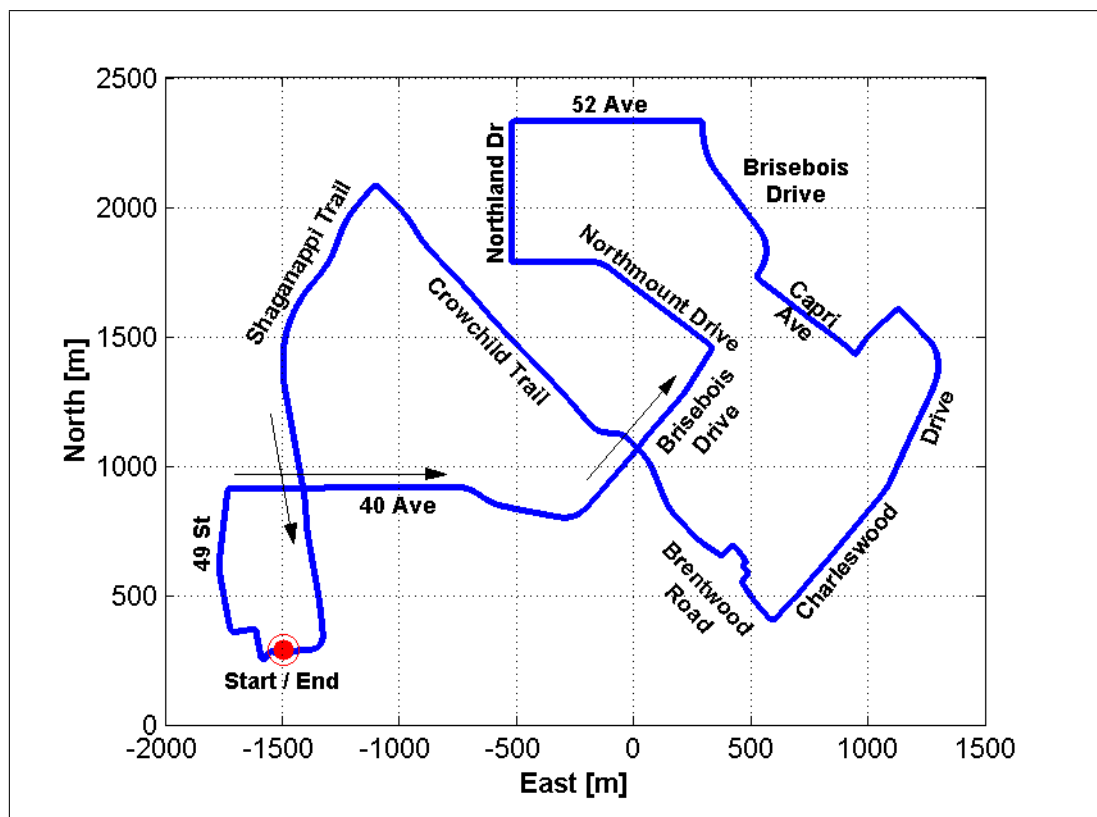

Figure E.1: Trajectory of First Real-Time Run Relative to Base Station

Figure E.2: 49 Street Looking North

Figure E.3: 40 Avenue Just East of Shaganappi Trail Looking East

Figure E.4: 40 Avenue Looking Northeast at Crowchild Trail Overpass

Figure E.5: Brisebois Drive Just Northeast of Crowchild Trial Looking Northeast

Figure E.6: Northmount Drive Looking Northwest

Figure E.7: 52 Avenue Looking East

Figure E.8: Capri Avenue Looking Southwest

Figure E.9: Charleswood Drive Looking Southeast

Figure E.10: Brentwood Road Looking Northwest

Figure E.11: Crowchild Trail Looking Northwest at Northland Drive Overpass

Figure E.12: Shaganappi Trail Looking South

Appendix F

Pictures of Second Real-Time Run

This appendix contains pictures taken from various locations along the second real-time test run. The figures are labeled according to the street names and the direction in which the camera was pointing when the picture was taken. For convenience, the overall trajectory is shown in Figure F.1.
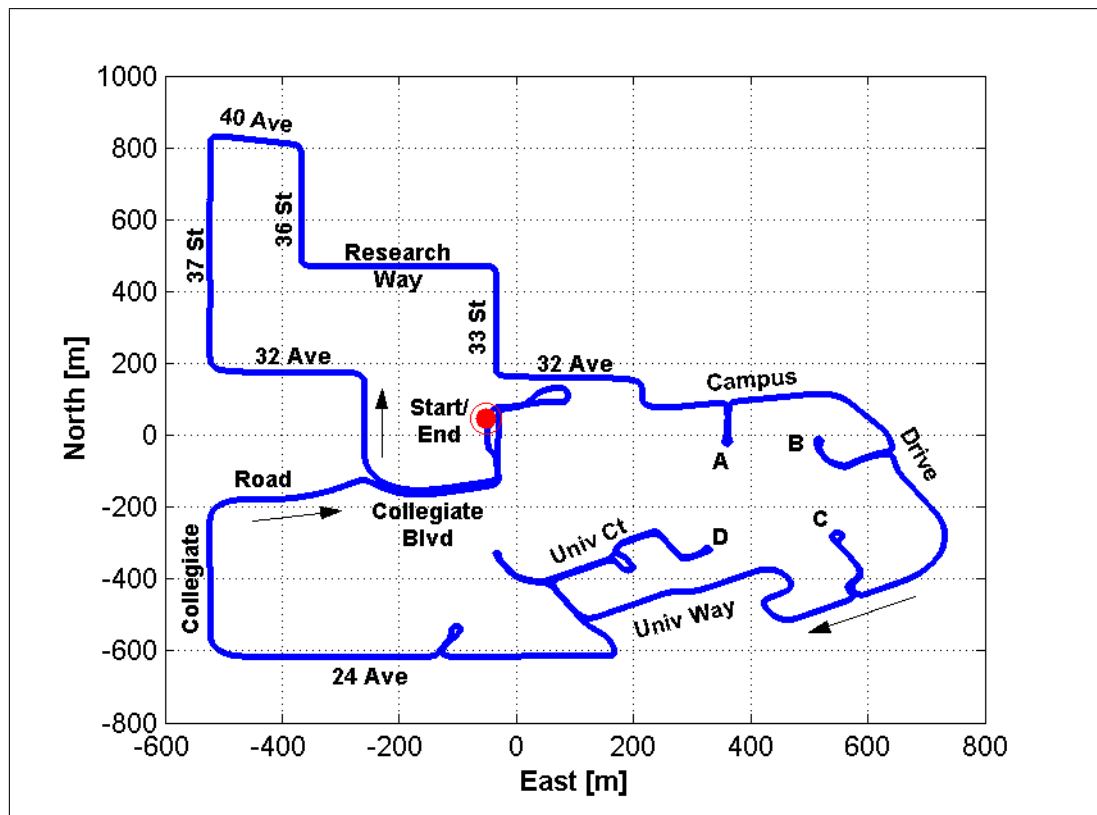

Figure F.1: Trajectory of Second Real-Time Run Relative to Base Station

Figure F.2: 37 Street Looking North

Figure F.3: 36 Street Looking South

Figure F.4: Research Way Looking East

Figure F.5: 33 Street Looking South

Figure F.6: Campus Drive Near Point "A" Looking East

Figure F.7: Campus Drive Looking South Towards Point "A"

Figure F.8: Point "A" Looking North

Figure F.9: Point "B" Looking South

Figure F.10: Point "C" Looking South

Figure F.11: University Way Looking West

Figure F.12: University Court Near Point "D" Looking Southeast

Figure F.13: Point "D" Looking South

Figure F.14: 24 Avenue Looking West

Figure F.15: Collegiate Road Looking North